The Thesis Committee for Eric Clinton Schulz
Certifies that this is the approved version of the following thesis:

Conductivity of Proppant Mixtures

APPROVED BY
SUPERVISING COMMITTEE:

Supervisor:

Kishore K. Mohanty

Kenneth E. Gray

Conductivity of Proppant Mixtures

by

Eric Clinton Schulz, B.S.P.E.

Thesis

Presented to the Faculty of the Graduate School of

The University of Texas at Austin

in Partial Fulfillment

of the Requirements

for the Degree of

Master of Science in Engineering

The University of Texas at Austin

May 2014

Dedication

To my mother, father, and sisters

Acknowledgements

I would like to thank Dr. Kishore Mohanty for providing me with his guidance and support, as well as the opportunity to work in his research group. I would also like to express my gratitude towards Dr. Eric Dao and Dr. Ming Gu for their assistance in setting up and debugging the experimental setup. Much thanks goes to Songyang Tong for very graciously performing experiments when I was unable to be at the lab. Finally, this work would not have been possible without the generous donation of proppants by U.S. Silica and Carbo Ceramics.

Abstract

Conductivity of Proppant Mixtures

Eric Clinton Schulz, M.S.E

The University of Texas at Austin, 2014

Supervisor: Kishore K. Mohanty

Hydraulic fracturing is a physically complex phenomenon, and there are many variables, both environmental and operational, that affect the overall success of a fracture treatment. Amongst the operational variables, the process of proppant selection is key to ensuring that the induced fractures remain open and permeable. A variety of physical mechanisms act to degrade the permeability of a given proppant packing after deposition in a fracture, the most important of which is the magnitude of the confining stress. The goal of this work is to understand how mixtures of unlike proppants behave under various stress conditions. Specifically, the permeability and conductivity of various mixtures of unlike proppants are measured as a function of confining stress. A secondary investigation is also made into the dependence of permeability on the areal concentration of proppant. Choices of proppants are restricted to those which are currently most common in industry, in terms of both material and size. To that end, mixtures consisted

of primarily ceramics and sands with appropriate grain size distributions. Additionally, a light-weight plastic proppant was included in the study.

Simple laboratory methods are employed to measure the permeability of the various proppant packings. Values obtained from direct experimentation are compared with values obtained from an independent analytical model. Given the assumptions which are inherent in the analytical model, the experimental and analytical results are in satisfactory agreement. Also, a correlation is developed for single proppants and binary mixtures which predicts permeability as a function of stress, grain size, material, and weight fraction.

One key conclusion is that for a binary mixture of proppants, the mixture permeability will not generally be a weighted linear combination of the pure proppant permeabilities. In other words, the permeability of a mixture comprised of 50% (by weight) of one component and 50% of the second component will generally not be halfway between the permeabilities of the single components. A hypothesis is presented which posits that there are threshold weight fractions for each proppant pair that control the permeability of the mixture.

Table of Contents

List of Tables

List of Figures

Chapter 1: Introduction

It is no secret that hydraulic fracturing is a practical and effective way to produce from the so-called unconventional shales, and thus has been the subject of much research in academia and much interest in industry. There are many variables, both operational and environmental, that control the degree of difficulty and the ultimate success of a fracture treatment, and abundant field trials and laboratory studies have been conducted over the course of the last few decades to attempt to reveal the optimum treatment strategy for a given formation.

The success of hydraulic fracturing can be credited to its ability to create flow channels within the formation, which facilitate flow of in-situ fluids into the wellbore and ultimately up to the surface. These flow channels can be viewed as streaks of high permeability which, ideally, form a dense and inter-connected network within the rock. However, it is common knowledge that once fractures have been created, if nothing else is done then they will close upon relaxation of the fluid pressure and effectively nothing will be accomplished. In order to prevent fracture closure, granular solids, known as proppants in the industry vernacular, are pumped into the system in the hope that they will populate the fracture network and prop the fractures. Therefore, it is apparent that the overall proppant strategy for a particular treatment is a critical operational parameter.

Proppant selection is often an exercise in optimization, as it must balance the competing desires of proppant transport and placement, and permeability retention after deposition (Gidley et al. 1989). Typically, lighter, low density materials are easier to

transport, but are weaker when exposed to stress and thus have relatively low permeability compared to heavier materials. Proppant transport has been extensively studied, but it is outside of the scope of this work and is not reviewed here; rather, this work focuses on characterization and understanding of permeability of heterogeneous proppant packs.

Proppant permeability is a function of many variables; because of this, exact replication of reservoir conditions in the laboratory is, if not impossible, certainly not practical. As is commonly done with multivariate systems, all of the parameters except for one can be held constant so that the effect of the single variable upon the overall outcome can be examined. The laboratory setting provides a controlled environment in which this kind of testing can be performed.

MOTIVATION

Surprisingly, despite the abundant studies that have been performed on the topic of proppant characterization, little attention has been paid to the dependence of proppant permeability on mixing of unlike proppants. Thus, the goal of this work is to understand how mixtures of proppants affect the permeability of the resultant packing. The permeabilities (and conductivities) of mixtures of several commonly used grain sizes and materials were measured by direct experimentation. One may question the utility in testing different materials, as the permeability of a medium is not dependent on the makeup of the medium (assuming that there is no chemical interaction between the fluid and the medium). The reason for testing different materials is simply because they will

behave differently upon exposure to stress. Historically, several different materials have been used as propping agents in fracture treatments, including glass beads, walnut hulls, metal shot, ceramics, and most traditionally, sand (Rickards et al. 2003). The artificial ceramic proppants and the naturally-occurring sand have withstood the test of time and are currently the most prevalent in industry; and as such they will be the primary focus of this study. An artificial light-weight proppant is also included in some experiments. The light-weight proppants are typically plastic materials, and as such they have poor crush resistance.

Because the term 'ceramic' is an umbrella which covers many different things, it is necessary at this point to define it more precisely. The ceramic proppants used in this study consist of approximately three-fourths by weight aluminum oxide, about one-tenth by weight silicon dioxide (silica), and the remaining portions consist of iron oxide, titanium dioxide, and a few others substances are present in small amounts (Carbo Ceramics). Likewise, the term 'sand' is somewhat ambiguous. The mineralogy of sand is generally understood to be overwhelmingly silica, but other substances can be present, depending on the locale in which the sand was sourced. For the purposes of this study, the differences amongst sands will be considered negligible compared to the differences between sands and ceramics. The grain sizes used in the experiments are governed by familiar standardized mesh sizes that have been endorsed by the American Society for Testing and Materials (ASTM).

OVERVIEW

Scientific research is typically performed by direct experimentation, computer modelling and simulation, development of purely theoretical mathematical models, or some combination of the three. Because these are three independent methods of obtaining information about a physical system, each can be used to validate the results of the others. For example, if the result of an experiment that models a particular process is in reasonable agreement with the result of a simulation of the same process, then we can be confident that both the simulation and the experimental setup and methods are valid. This study is primarily carried out through experimentation, but results are compared with those of an analytical model provided by Panda and Lake (1994). Discrete finite element models have been developed to describe the response of granular packings to the application of stress, but those are outside of the scope of this work and were not considered, although they could be a useful tool.

This work was conducted by first performing a literature review of studies and papers that are relevant to the subject. These include topics such as the behavior and properties of granular packings and characterization of proppant performance at reservoir conditions. Then, the experimental setup was constructed and debugged as necessary. Experiments were carried out and results were compared with the predictions of the analytical model. Finally, a correlation was developed that may be used to predict mixture permeability for any arbitrary proppant pack. This thesis contains a thorough description of all procedures and results, and closes with a discussion of the findings and recommendations for future work on this subject.

Chapter 2: Literature Review

This chapter is intended to present an overview of previous research in the area of permeability characterization and proppant performance. The first section describes work that is aimed at gaining general understanding of the properties of granular packings. The second section discusses work that is intended to help understand the specific factors which affect in-situ proppant degradation and the degree of applicability of standardized laboratory experimentation. The third section discusses standards and recommended procedures for proppant testing; and finally, there is a brief discussion on previous testing of proppant mixtures.

HETEROGENEOUS GRANULAR PACKINGS

Since proppant mixtures can simply be viewed as unconsolidated heterogeneous granular packings, any study of this type of packing can lend insight to the problem at hand. Characterization of the macroscopic properties of porous media such as porosity and permeability can be difficult, and unfortunately the concept of permeability itself is somewhat nebulous. For this reason, it is imperative to understand the nature of permeability in a thorough manner. The work performed by Henry Darcy in 1856 is often cited as the original investigation into fluid flow through porous media. Darcy empirically observed that, for modest flow rates, the volumetric flow rate through a fixed, rigid porous medium varies linearly with the imposed pressure difference and that the volumetric flow rate is proportional to the cross-sectional area open to flow. The

constant of proportionality which relates the flow rate to the pressure drop and cross-sectional area was called the permeability, and was considered to be an intrinsic property of the porous medium. Barree et al. (2003) takes issue with this notion and argues that permeability is not an intrinsic property of the medium, but actually just an empirical constant with contrived units that was defined out of experimental convenience. They further argue that permeability depends on the experimental conditions, and is therefore not an intrinsic property. Hubbert (1940) recognized the need for a rigorous definition of permeability and presented a method of deriving a theoretical relationship which agrees with Darcy's empirical law and is more general. Hubbert begins his analysis with the assumption that the porous medium is chemically inert, i.e. does not react with the invading fluid. He notices that many others assume that pressure is the physical quantity that drives fluid flow; in other words, the prevailing assumption is that fluid flow always occurs from regions of high pressure to regions of low pressure. This assumption is valid for many situations, but is not generally true. Hubbert observes that the actual quantity that controls fluid flow is the mechanical energy per unit mass, which he calls the potential. The mathematical definition of the fluid potential arises from the realization that the potential of a fluid is equal to the amount of work required to bring the fluid from some standard state to its current state. The potential is then provided by the mechanical energy balance:

$$\Phi = gz - p_0 V_0 + \int_V^{V_0} p\, dV + pV + \frac{v^2}{2} \tag{2.1}$$

where Φ is the potential, g is the gravitational constant of acceleration, p is the fluid pressure, V is the specific volume of the fluid, z is the height of the element of fluid in the gravitational field with respect to some datum, v is the velocity of the fluid, and the 0 subscript denotes the conditions at the standard state. By some mathematical manipulation, it can be shown that the potential can also be expressed by:

$$\Phi = gz + \int_{p_0}^{p} V\, dp + \frac{v^2}{2} \tag{2.2}$$

By recognizing that the specific volume is the inverse of density, this can be rewritten as:

$$\Phi = gz + \int_{p_0}^{p} \frac{dp}{\rho} + \frac{v^2}{2} \tag{2.3}$$

where ρ is the fluid density. Next, by assuming the fluid is incompressible (valid for liquids) and that the velocity term is so small relative to the others that it can be neglected, (generally valid for flow in porous media) the expression simplifies to:

$$\Phi = gz + \frac{p - p_0}{\rho} \tag{2.4}$$

Hubbert then proceeds to utilize a microscopic force balance to derive an expression which relates the fluid flow rate to the potential; the mathematical details will not be outlined here, but the interested reader is referred to Hubbert's paper. The result of his analysis is as follows:

$$u = \frac{-Nd^2\rho}{\mu} \frac{\partial \Phi}{\partial x} \tag{2.5}$$

where u is the velocity of the fluid and x is the spatial variable (the other variables will be defined shortly). Other authors have independently come to this conclusion, albeit in

different ways and using different notation, such as Neuman (1975) and Mokadam (1961), who derived the relation using a thermodynamic approach. The empirical constant of proportionality observed by Darcy is recovered in Hubbert's analysis, but is revealed to be a function of five independent parameters: the gravitational constant of acceleration, the viscosity of the fluid, the density of the fluid, a characteristic grain diameter, and a dimensionless numerical coefficient (*N)* that depends on the internal geometry of the porous medium. Since gravitational effects can be ignored for situations where flow is horizontal, the gravitational term *gz* in the expression for potential vanishes and the equation reduces to:

$$u = \frac{-Nd^2}{\mu} \frac{\partial p}{\partial x} \tag{2.6}$$

This result is identical to Darcy's equation, and the constant of proportionality *K* is:

$$K = \frac{Nd^2}{\mu} \tag{2.7}$$

where d is a characteristic grain diameter, μ is the fluid viscosity, and N is the aforementioned numerical coefficient. Of these three parameters, N and d are properties of the porous medium. Therefore, it is convenient to define the permeability k of a porous medium to be the numerator of Equation 2.7:

$$k = Nd^2 \tag{2.8}$$

The coefficient N is typically considered to include effects of tortuosity, porosity, and irregularities in grain shape (Shepherd 1989). The notion that permeability varies with the square of some average grain diameter has been verified experimentally by several

investigators. It follows from the above equation that if the logarithm of permeability is plotted against the logarithm of grain diameter, the curve should be linear with a slope of two. The following plot is a summary of the experimental work which was assimilated by Shepherd:

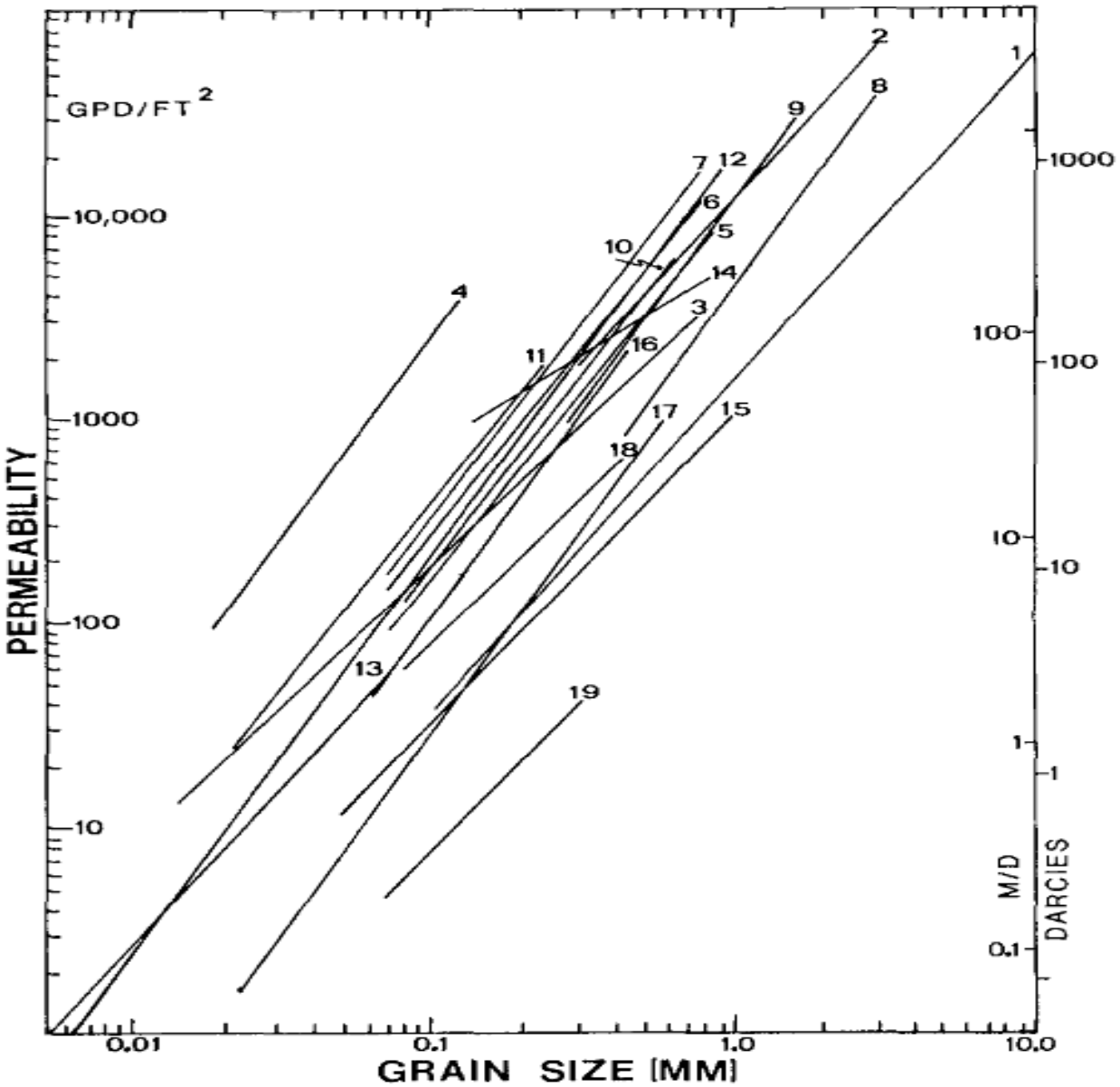

Figure 2.1: Permeability as a function of grain sizes for various samples (Shepherd 1989)

It is apparent by inspection that the slope of each line is approximately two (log cycles per log cycle), and so we can be confident that Hubbert's model is valid. Bedinger provides another verifying example:

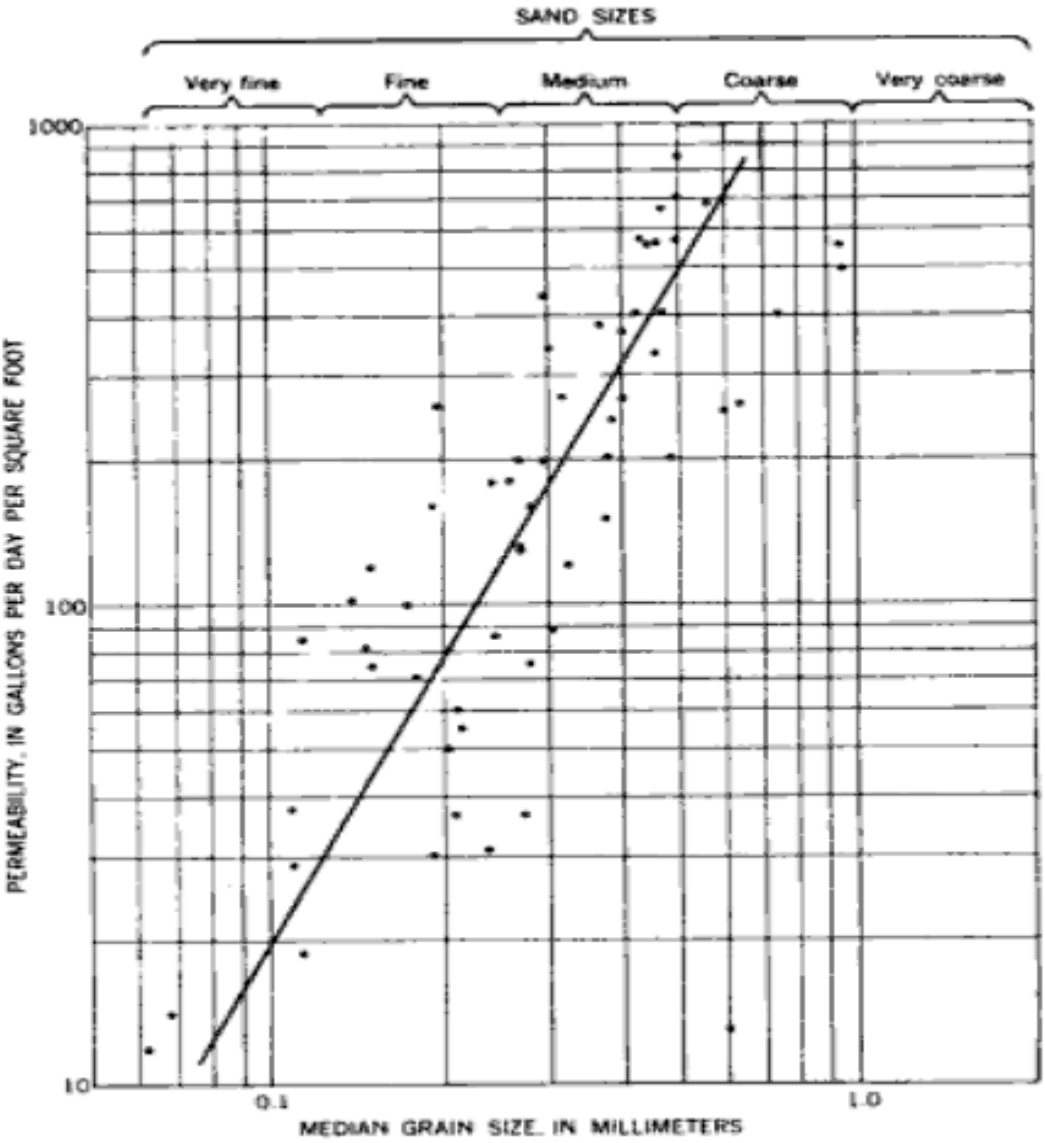

Figure 2.2: Permeability as function of median grain size for a single grain type (Bedinger 1961)

Once again, the log-log plot of median grain size versus permeability exhibits a slope of two.

Keech and Rosene performed a similar study, but they plotted the characteristic grain size on the ordinate and 'coefficient of permeability' on the abscissa:

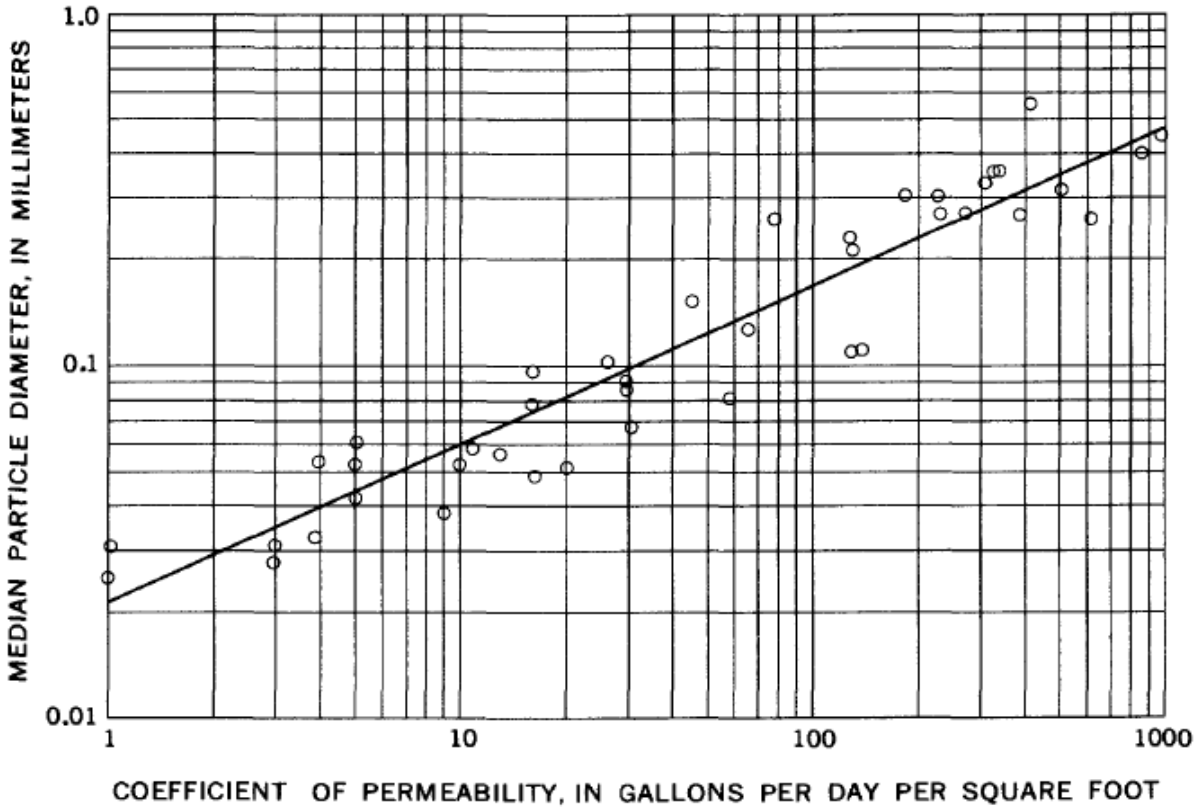

Figure 2.3: Plot of particle diameter as function of coefficient of permeability (Keech & Rosene 1964)

If the permeability varies as the square of some average grain diameter, then a log-log plot of grain diameter as a function of permeability should have a one-half slope. Keech and Rosene's plot (Figure 2.3) does indeed have a one-half slope. Keech and Rosene's coefficient of permeability is simply a proxy for the intrinsic permeability and behaves in the same manner as the intrinsic permeability if the flow is horizontal and the fluid viscosity is approximately constant.

Beard and Weyl (1973) conducted a well-known study in which they examined the influence of grain characteristics on the porosity and permeability of the bulk packing. According to them, there are five important properties to consider: grain size, sorting, sphericity, angularity, and packing arrangement. Sphericity and angularity may seem to be dependent on each other, but sphericity is the degree to which the grain approximates a spherical shape while angularity is a measure of the sharpness of the edges and corners, and so angularity is independent of shape. They constructed a table of permeability as a function of the median grain diameter and the Trask sorting coefficient from which the following plot was constructed for easier visualization:

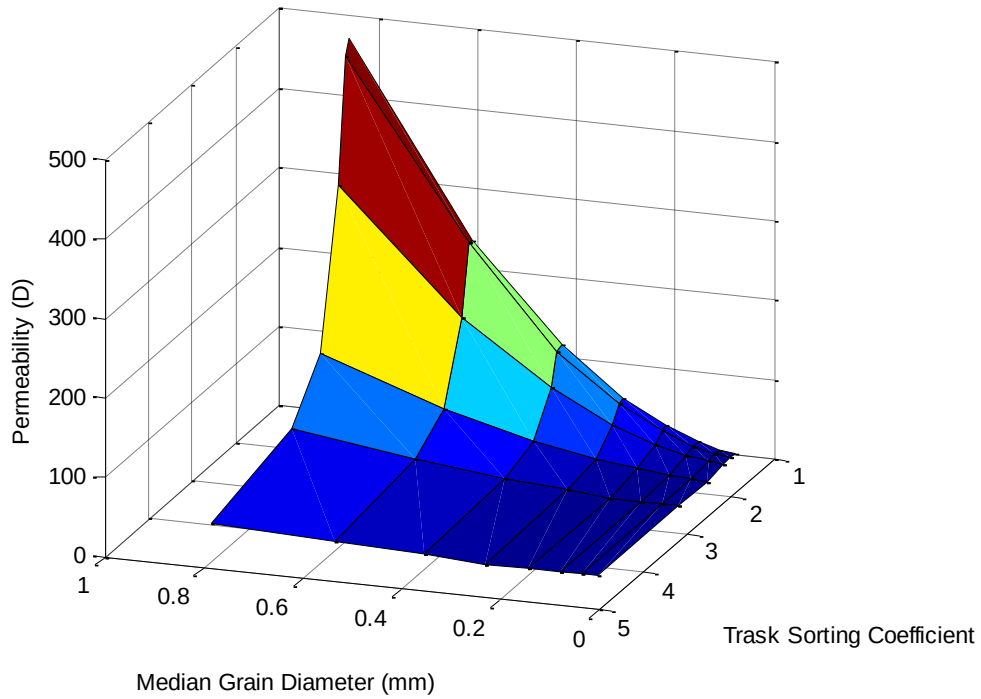

Figure 2.4: 3-D plot of permeability as a function of grain diameter and Trask sorting coefficient (data from Beard & Weyl)

The Trask sorting coefficient is defined as the square root of the ratio of the grain size that falls on the third quartile of the grain size distribution to the grain size that falls on the first quartile of the distribution (Friedman 1962). Thus, a Trask sorting coefficient of one indicates uniform grain sizes and therefore a very high degree of sorting, and as values increase away from one the degree of sorting decreases. The plot clearly indicates that permeability attains a maximum for large grain sizes and uniform size distributions and quickly decays as the grains get smaller and the size distribution broadens.

The sphericity and angularity of grains are difficult to quantify; and are highly laborious to measure, as hundreds of grains would have to be examined individually. For these reasons, Beard and Weyl did not perform a quantitative analysis on the effect of sphericity and angularity on permeability. However, they do predict that low sphericity and high angularity probably increase the permeability of the packing. Krumbein and Monk (1942) also investigated the response of permeability to changes in grain size distributions. They artificially mixed sands into convenient distributions and tested the dependence of permeability on the parameters of the grain size distribution, such as the standard deviation. Unfortunately, they were not able to produce general conclusions, other than the fact that the permeability decreases as the spread of the size distribution increases.

Naturally, several efforts have been made to produce analytical equations which predict permeability. These predictions can help in the understanding of the controls on permeability and in validation of experimental results. Kozeny (1927) was the first to present such a model, and shortly thereafter Carman (1939) confirmed and enhanced

Kozeny's effort. Their rather well-known result is referred to, appropriately, as the Carman-Kozeny equation and it serves as a relatively simple way to predict permeability. Dvorkin (2009) provides a nice review of the development of the model. It begins with the supposition that a porous medium can be thought of as a bundle of tubes that cross through the interior of some otherwise impermeable material. It can be shown (Bird, Stewart, Lightfoot p. 51) that, for a circular tube, the flow rate is related to the pressure drop across the tube by the following relation (known as the Hagen-Poiseulle equation):

$$Q = \frac{-\pi r^4}{8\mu}\frac{\Delta P}{L} \tag{2.9}$$

where r is the radius of the tubes, Q is the volumetric flow rate through the tube, P is pressure, L is the length of the tubes, and μ is the viscosity of the fluid. It is now convenient to introduce the parameter known as tortuosity, symbolized by τ, and defined as simply the ratio of the length of the tubes to the length of the medium. If the tubes are perfectly horizontal, then the tortuosity is equal to unity, but if the tubes are angled away from horizontal or twisted in any way, the tortuosity attains some value above one. By introducing the tortuosity into the above equation and summing the flow rates of the individual tubes, the flow rate across a medium of N tubes is:

$$Q = \frac{-N\pi r^4}{8\mu}\frac{\Delta P}{L\tau} \tag{2.10}$$

It is easy to define the porosity of such a system, as it simply the collective volume of the N tubes divided by the bulk volume of the rectangular prism AL where A is the cross-sectional area open to flow. Mathematically, it can be expressed as:

$$\emptyset = \frac{N\pi r^2 \tau}{A} \tag{2.11}$$

Combining this with the Equation 2.10, it is evident that the total flow rate can be expressed as:

$$Q = \frac{-\emptyset r^2 A}{8\mu}\frac{\Delta P}{L\tau^2} \tag{2.12}$$

By comparison with Darcy's law, it is also evident that the permeability *k* can then be expressed as:

$$k = \frac{\emptyset r^2}{8\tau^2} \tag{2.13}$$

This result tells us that permeability increases with the square of the tube radius and increases proportionally with the porosity, i.e. the number of tubes. In some papers and texts, the tortuosity term is not squared, however it is of little importance here, since it is dimensionless. The importance of the tortuosity lies in the fact that it captures the effect of tortuous conduits and that it is just a dimensionless numerical coefficient so it can be represented as either τ or τ^2 with equal validity. Not surprisingly, the permeability decreases as the tortuosity increases; this can be attributed to increased frictional pressure losses that are associated with tortuous conduits.

Unfortunately, this equation only describes the fictional scenario of a "bundle of tubes" and is not directly applicable to porous media. One major pitfall of the analysis is that it does not allow for crossflow between the "tubes", which undoubtedly occurs in porous media. However, this analysis may still be carried further. Following Dvorkin, we can define the specific surface area of the medium as the ratio of the internal surface

area to the total volume of the system and denote it with *s*. It is easy to show that the specific surface area for the 'bundle of tubes' model can be represented by:

$$s = \frac{2\pi N r \tau}{A} = \frac{2\emptyset}{r} \tag{2.14}$$

It follows that:

$$r = \frac{2\emptyset}{s} \tag{2.15}$$

This can be substituted into Equation 2.13 to yield:

$$k = \frac{1}{2}\frac{\emptyset^3}{s^2\tau^2} \tag{2.16}$$

If we now take the porous medium to be a packing of identical spheres, then it is trivial to show, using the well-known formulas for the volume and surface area of a sphere, that *s* for such a packing is:

$$s = \frac{6(1-\emptyset)}{d} \tag{2.17}$$

where *d* is the diameter of the spheres and is equal to twice the radius. Finally, by substituting Equation 2.17 into Equation 2.16, we arrive at:

$$k = \frac{\emptyset^3}{72\tau(1-\emptyset)^2} d^2 \tag{2.18}$$

In this result, I have chosen to discard the square on the tortuosity term τ for aesthetic reasons, which as mentioned earlier, is valid as long as we understand that the tortuosity is simply a coefficient that accounts for nonlinear flow pathways. This result is strikingly similar to that of Hubbert's, especially given that each equation was derived using distinct and independent methodologies. The most obvious similarity is the fact that both

models predict that the permeability increases proportionally to the square of some characteristic grain diameter; and, as mentioned earlier, this was also verified empirically. Another, perhaps more subtle, feature is that the constant of proportionality in both models is simply a dimensionless numerical coefficient. This is easily verified by inspection of the Carman-Kozeny (CK) result, as the porosity and tortuosity are both dimensionless, and therefore the coefficient is dimensionless. Further confirmation of the legitimacy of the CK result lies in the fact that as the porosity approaches unity, the permeability approaches infinity; which is tractable considering that it is difficult to imagine a porous medium with a porosity of one, but if such a medium were to exist, it would have infinite permeability.

Panda and Lake (1994) expanded upon the CK result by considering how the distribution of grain sizes affects the resultant permeability. Essentially, this was accomplished by relating parameters of the grain size distribution to the specific surface area *s*. The only assumption is that the grains must be spherical; but, as Lake points out, even this is not overly restrictive, as the effect of nonspherical grains affects not the specific surface area *s*, but primarily the porosity, which is explicitly accounted for in the final equation. The details will be skipped here, but the result is as follows:

$$k = \left[\frac{(\gamma\varphi^3 + 3\varphi^2 + 1)^2}{(1+\varphi^2)^2}\right]\frac{\emptyset^3}{72\tau(1-\emptyset)^2}\bar{d}^2 \tag{2.19}$$

where γ is the skewness of the particle size distribution, $\bar{d}$ is the mean particle diameter, and φ is the ratio of the standard deviation of the distribution σ and the mean particle diameter $\bar{d}$, $\sigma/\bar{d}$. This rather elegant result can be seen as a correction to the classic CK

equation, as the term in brackets introduces more generality in the equation, in that it allows for non-uniform particle size distributions.

It is now established that the permeability associated with a given porous medium is indeed an intrinsic property of said medium. Also, the permeability of a given medium varies with the square of a characteristic grain diameter; this has been suggested by at least two independent analytical models and verified empirically. The constant of proportionality which relates the permeability to the square of the grain diameter is itself a function of the grain size distribution, porosity, tortuosity, and to a lesser extent, irregularities in grain shape and angularity. Furthermore, it is not only possible but perfectly acceptable to measure the permeability of a porous medium by direct experimentation using Darcy's law.

IN-SITU PROPPANT DAMAGE

Not surprisingly, there are a variety of physical phenomena that can affect the performance of a proppant pack in an actual fracture. In no particular order, the most common culprits are:

- Embedment of proppant into the reservoir rock
- Non Darcy flow regimes (high velocity flow)
- Multiphase flow (water, oil, gas)
- Residual gel deposition
- Geochemical precipitation
- Reservoir fines migration

- Cyclic stress
- Magnitude and duration of stress

The most important factor affecting in-situ proppant permeability is the magnitude of the confining stress. Individual proppant grains will deform, fail, and rearrange themselves when they are exposed to stress, and this effectively reduces the permeability of the proppant pack. The confining stress, or closure stress, is equal to the difference between the minimum principal stress in the rock and the fluid pressure in the fracture. For normal faulting regimes, the minimum principal stress is horizontal; and so to estimate the closure stress, we must determine the value of this horizontal stress. It is generally accepted (Hubbert and Willis 1956) that the vertical stress gradient is approximately 1 psi/ft; and we know that the minimum horizontal stress must be less than the vertical stress (for normal faulting regimes). Common values for the minimum horizontal stress gradient range from 0.6 to 0.9 psi/ft (Zoback 2010). Since most fracture jobs are performed with water, we can assume a fluid gradient of about 0.45 psi/ft; subtracting this from typical minimum horizontal stress values gives a closure stress gradient range of 0.15 psi/ft to 0.45 psi/ft. If we further assume that a well is drilled to ten thousand feet of depth, then this gives a confining stress somewhere within the range of 1,500 to 4,500 psi. Of course, there are exceptions to these rules of thumb and wells can be drilled deeper, and so confining stresses can rise up to the 8,000 or even 10,000 psi range. Schubarth et al. (1997) have found that there is an extra stress that exists in addition to the so-called 'far-field' stresses, and its magnitude ranges from a couple of hundred of psi to about 1,500 psi, depending on the thickness of the pay interval and the Young's

modulus of the rock. The main takeaway from this is that expected confining stresses will be on the order of several thousand psi, and laboratory experiments should be designed accordingly. A plot of conductivity as a function of closure stress taken from Cutler (1983) is shown below, as an example; it should be noted here that many authors report data in terms of conductivity, which is simply the product of permeability and width.

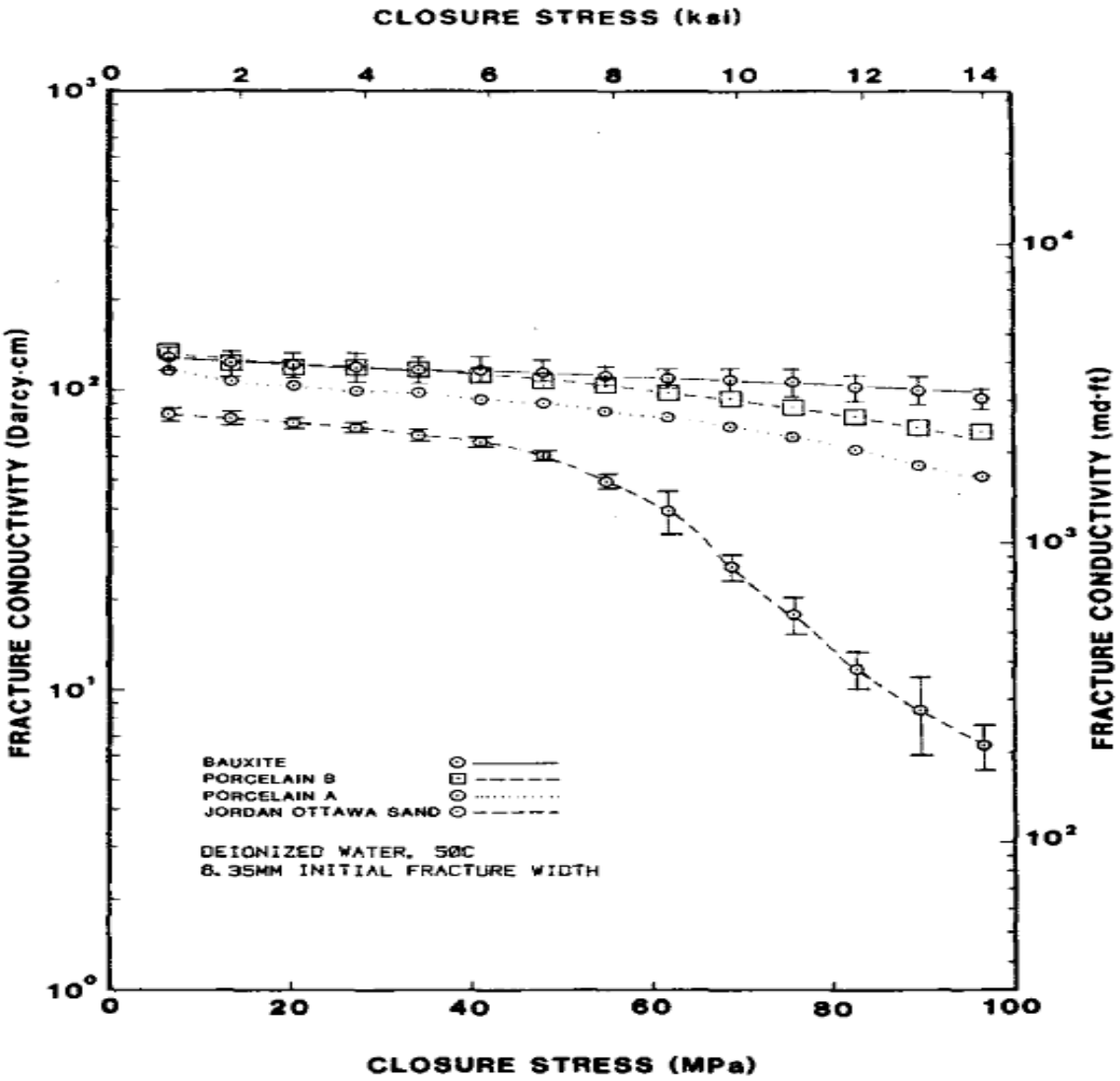

Figure 2.5: Typical plot of fracture conductivity as a function of closure stress (Cutler 1983)

Note that the conductivity was measured for stress values ranging from 1,000 to 14,000 psi, which is consistent with the reasoning above.

The amount of time that the proppant is exposed to stress affects the conductivity. Several authors, including McDaniel (1986) and Cobb and Farrell (1986), have reported that the conductivity of a proppant packing degrades in a continuous manner as time passes. As McDaniel's plot shows, the conductivity can drop by as much as ninety percent in just two weeks:

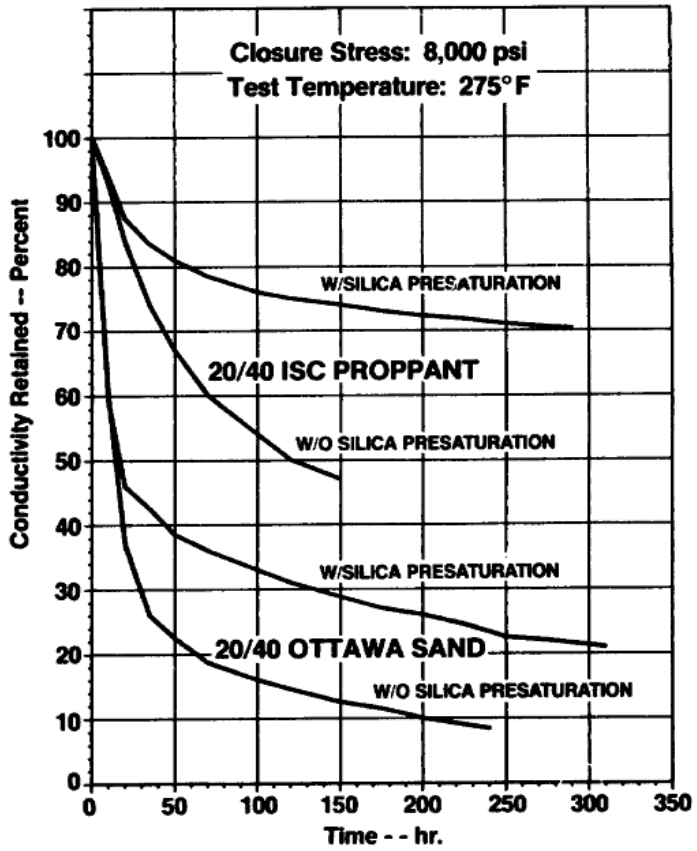

Figure 2.6: Plot illustrating loss of conductivity with time (McDaniel 1986)

Embedment of proppant into the reservoir rock is obviously a negative effect, as it reduces the width of the fracture, which in turn reduces its conductivity. The degree of

embedment is largely controlled by the Young's modulus of the rock, which is a proxy for stiffness (Alramahi 2012). The Young's modulus is itself a strong function of the mineralogy of the rock, as rocks with higher clay content, such as shales, tend to have lower Young's moduli and therefore exhibit a higher degree of embedment than rocks with lesser clay content, such as sandstones (Zoback 2010). Alramahi and Sundberg have performed a study dedicated solely to this issue, and some of the results are displayed in the plot below:

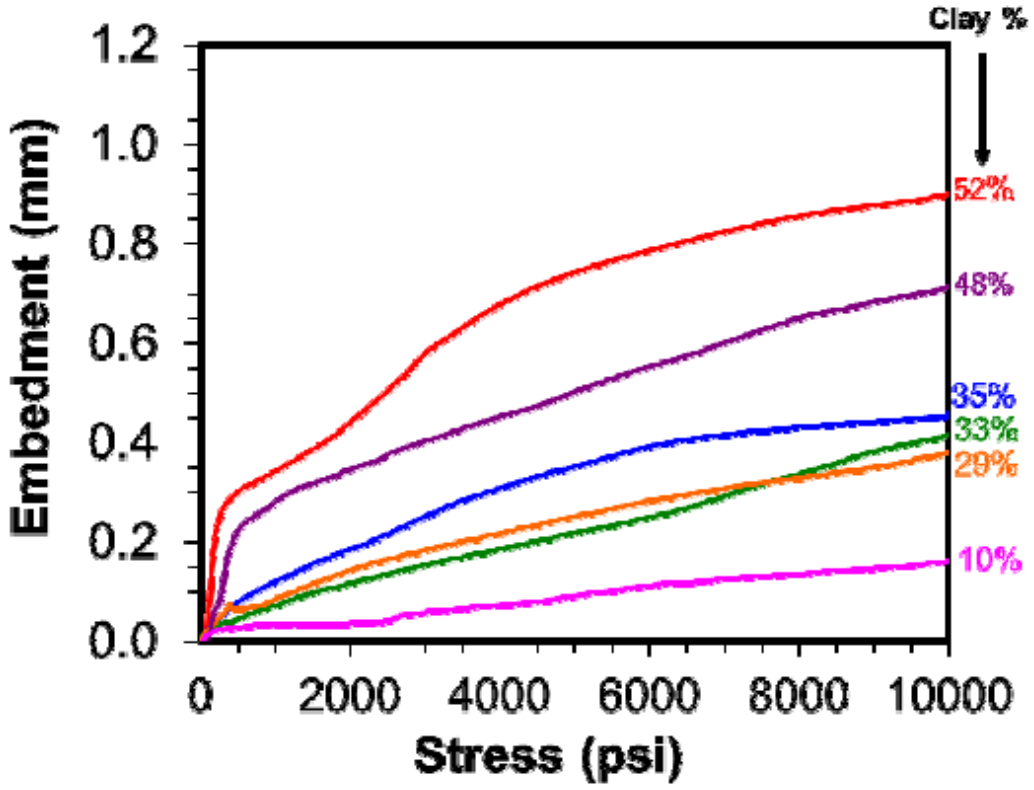

Figure 2.7: Degree of embedment as function of closure stress and clay content (Alramahi & Sundberg 2012)

This data agrees with Zoback's assertion that embedment is a strong function of clay content. Another important takeaway from this plot is that the actual degree of

embedment ranges from negligible to approximately 900 μm. Most proppants in use in the field range from a couple hundred to two thousand micrometers in diameter; so depending on the situation, it is possible that some proppants could be completely engulfed by the reservoir rock. For these scenarios, it is important to consider how many "layers" of proppant were deposited into the fracture. If there are multiple layers which comprise the proppant pack, perhaps on the order of four or five layers, then the loss of one layer to embedment will not be as deleterious as if there was only one layer to begin with.

Another detrimental effect that can occur during production is the exposure of proppant to stress cycles. Essentially, since we can safely assume that the stress in the rock is constant, cyclic stress occurs when the fluid pressure in the fracture changes significantly. This would happen if the well is ever shut in and sufficient surface pressure is not maintained, as the fluid pressure in the fracture should decrease due to the absence of frictional pressure losses. Stephens et al. (2007) investigated the dependence of permeability/conductivity on cyclic stress. Figure 2.8 shows their results:

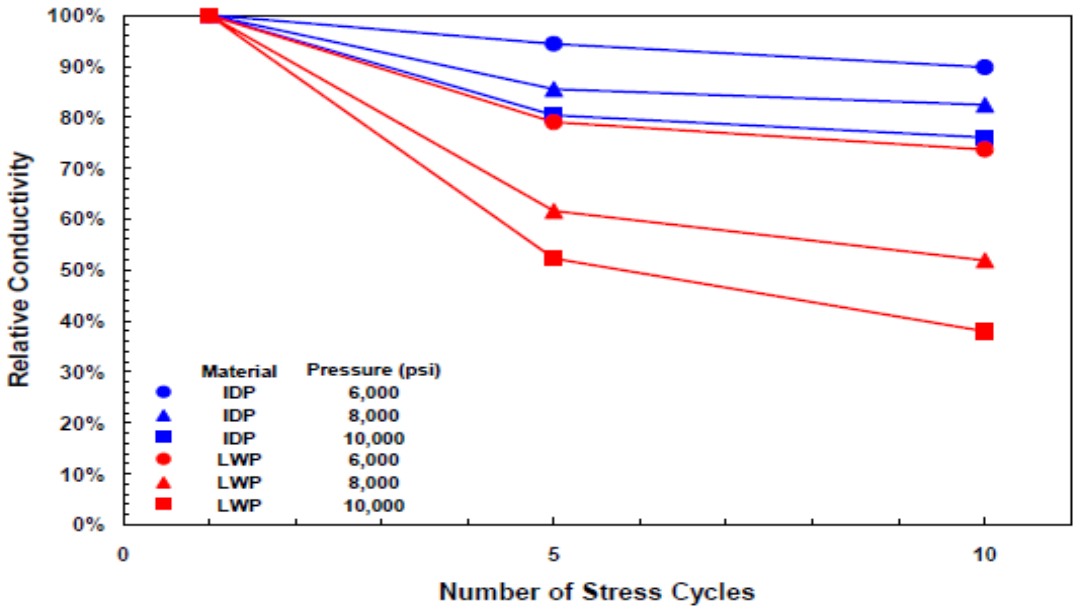

Figure 2.8: Conductivity loss as function of number of stress cycles (Stephens et al. 2007)

It is also believed (Barree et al. 2003, Lehman et al. 1999) that effects such as multiphase flow, non-Darcy flow, geochemical precipitation and scaling, and gel blocking contribute to the degradation of permeability. However, because it is difficult to isolate these effects from others in the laboratory, few, if any, studies have been performed on these effects.

LABORATORY TESTING METHODS

Since the advent of the technique of hydraulic fracturing, there has been a healthy interest in measuring the conductivity of proppants. Various methodologies and strategies have been used to perform these measurements in laboratory settings. However, these have been subject to vocal criticism because laboratory results are generally considered inapplicable to the field (Barree et al. 2003). This disconnect

between the laboratory and the field is caused by all of the mechanisms described in the previous section (non-Darcy flow, multiphase effects, etc.). Naturally, one would wonder why laboratory experiments are not modified in such a way that they produce more applicable results. The simple reason for this lies in the difficulty of creating an experimental setup which is capable of accounting for all of the physical mechanisms that act to degrade in-situ proppant permeability. In addition, it would be essentially impossible to isolate the effects from one another; so that, for example, if one were measuring the effect of non-Darcy flow, multiphase effects, and geochemical precipitation reactions, what portion of the permeability loss would be assigned to which mechanism? At this point, it is natural to question the value of laboratory measurements. However, there is useful information that can be mined from experimentation. First, it gives insight on how the system reacts to a change in one variable, e.g. the manner in which permeability changes with applied stress. Second, as all of the aforementioned effects are deleterious, laboratory measurements provide upper bounds on the parameter in question. Third, systems can be compared to one another, e.g. a sand pack with larger grains can be compared to a ceramic pack with smaller grains.

Gidley et al. (1989) provide a nice summary of the progression of laboratory techniques of conductivity measurement. All of the following methods are devised so that Darcy's law can be applied to calculate permeability. The first setup is shown in the following figure:

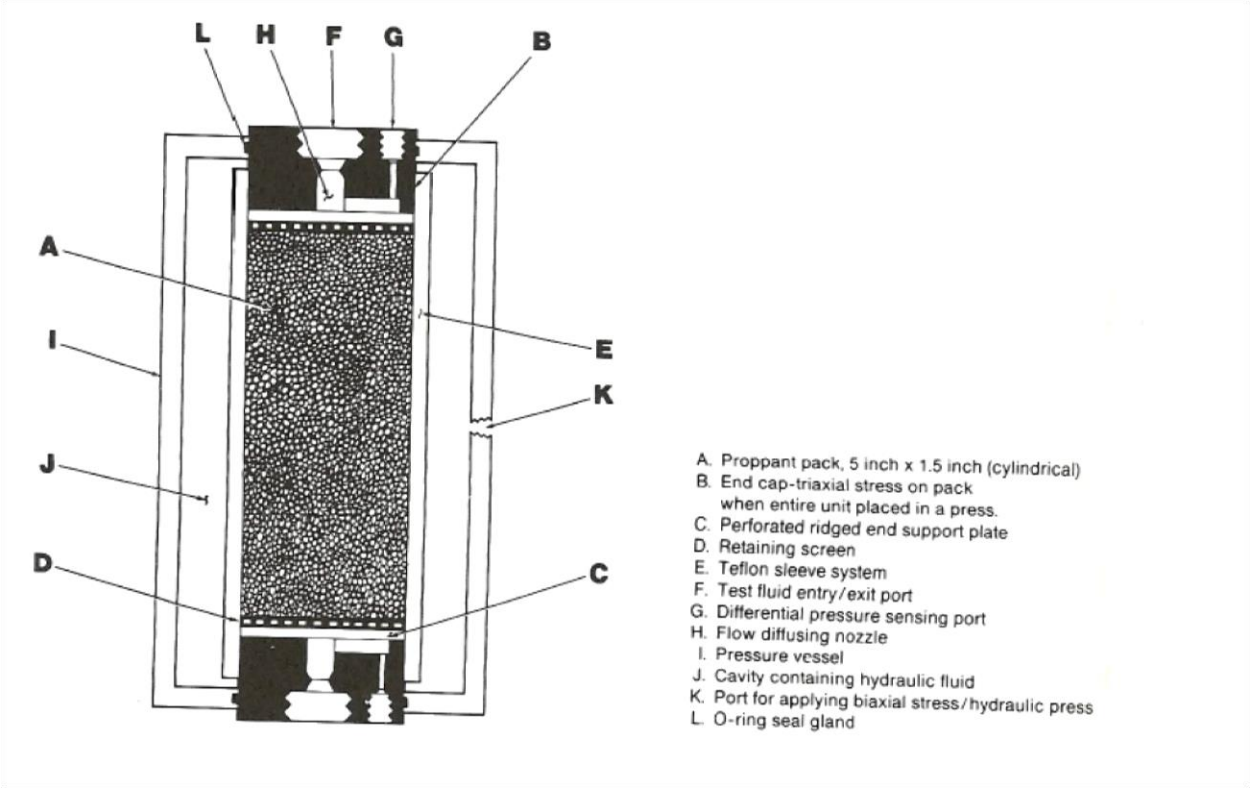

Figure 2.9: Schematic of Hassler sleeve permeameter (Gidley et al. 1989)

In this setup, known as the Hassler sleeve permeameter, the proppant is loaded into a cylindrical sleeve and confining stress is applied via the port labeled ‘K’ in the diagram. Then, test fluid is pumped through the packing and the differential pressure is measured. However, the setup was flawed in that the cross-sectional area is not constant and the cylindrical proppant packing does not imitate the rectangular geometry of a fracture.

Amoco then used an apparatus that was designed to induce radial flow instead of linear flow. The setup is outlined in the following diagram:

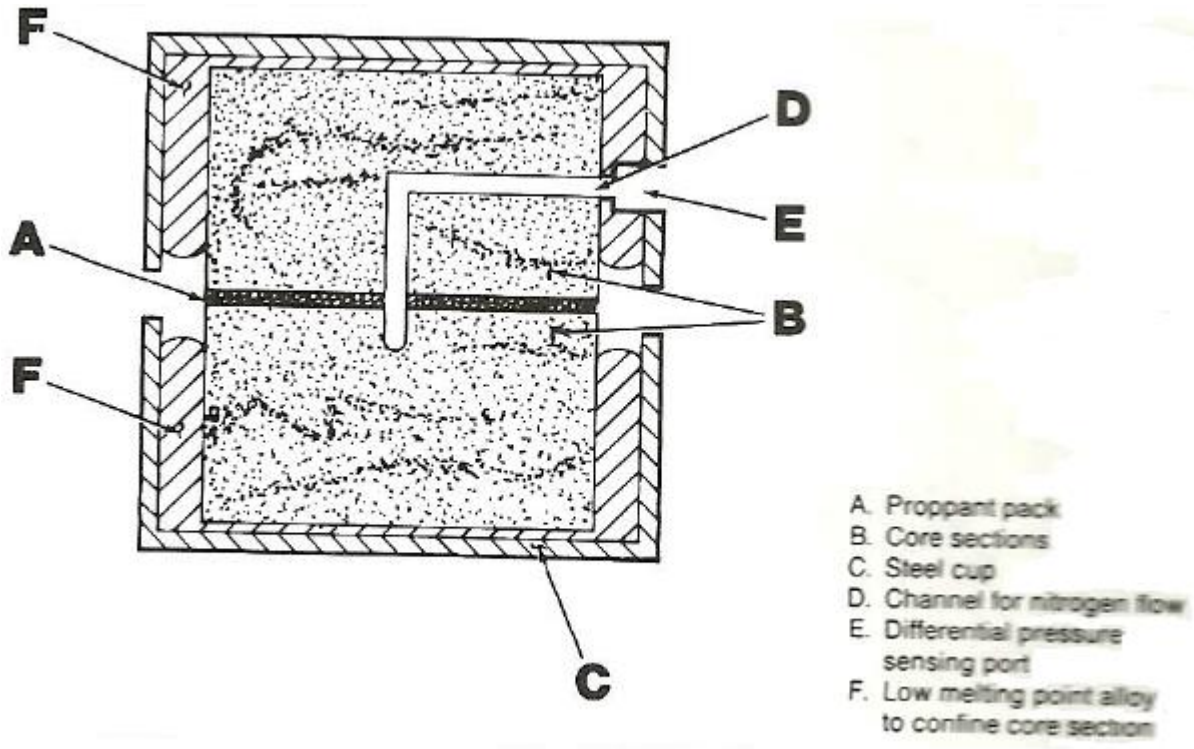

Figure 2.10: Schematic of Amoco conductivity cell Amoco (Gidley et al. 1989)

Test fluid is injected at port ‘D’ and is allowed to escape along the outer edge of the cylinder, marked by ‘A’. The difference in pressure between the center of the pack and the edge is measured, and the radial analog of Darcy’s law is used to calculate

permeability. The Amoco cell is superior to the Hassler permeameter because its cross-sectional area is more realistic. However, due to its radial setup, the cross-sectional area that the fluid moves through increases as the fluid migrates away from the center. This gives rise to abnormally high fluid velocities near the center and much slower fluid velocities at the edge, and the high velocities are likely to cause turbulent flow and therefore invalidate Darcy's law.

Another entity, Gulf, devised an apparatus to measure proppant permeability. This one discards a radial geometry in favor of a linear geometry and is a noticeable improvement over the previous efforts. Its diagram is shown below:

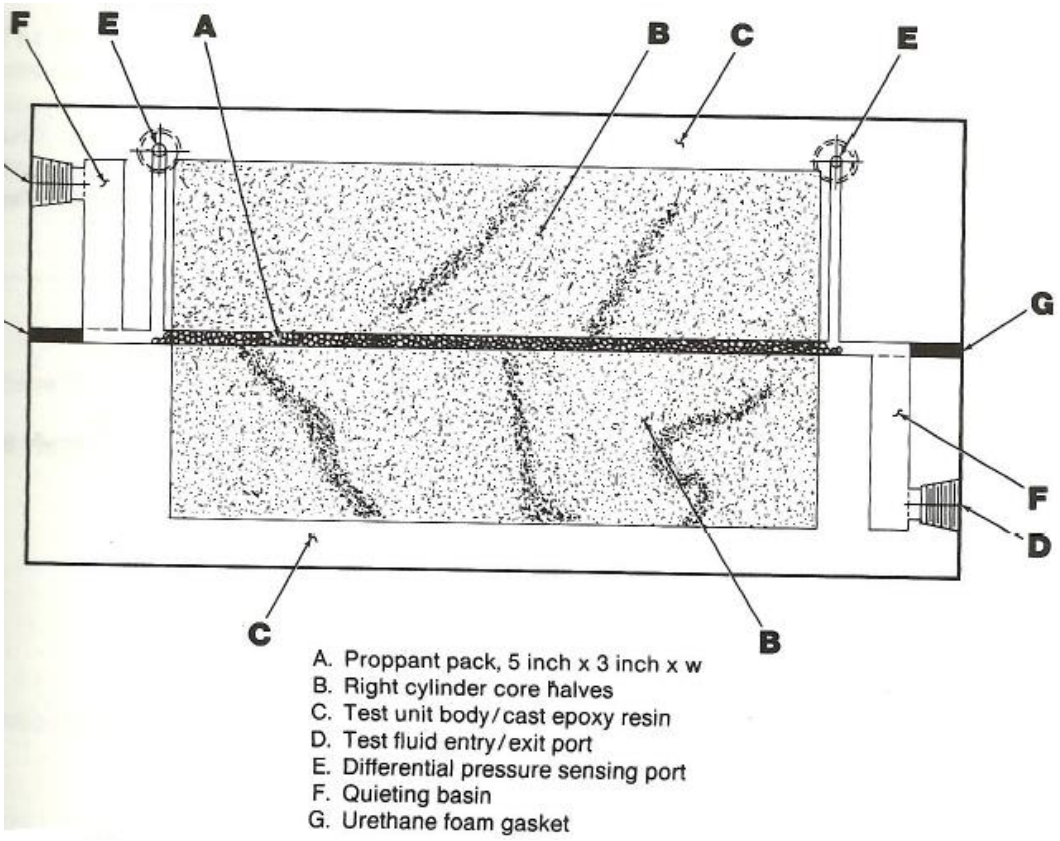

Figure 2.11: Schematic of conductivity testing apparatus as designed by Gulf (Gidley et al. 1989)

The major disadvantage of this setup is that it was not known how much of the confining stress was supported by the proppant pack and how much was supported by the two gaskets, denoted at the right end by 'G'.

Finally, the API recognized the need for a standardized test procedure that eliminates or minimizes the flaws that are associated with the previous schemes. The new setup was designed to have a linear geometry, a cross-sectional area which more closely resembles that of a fracture, and a simple setup that allows the proppant packing to absorb all of the confining stress. The API conductivity cell is shown in an exploded view below:

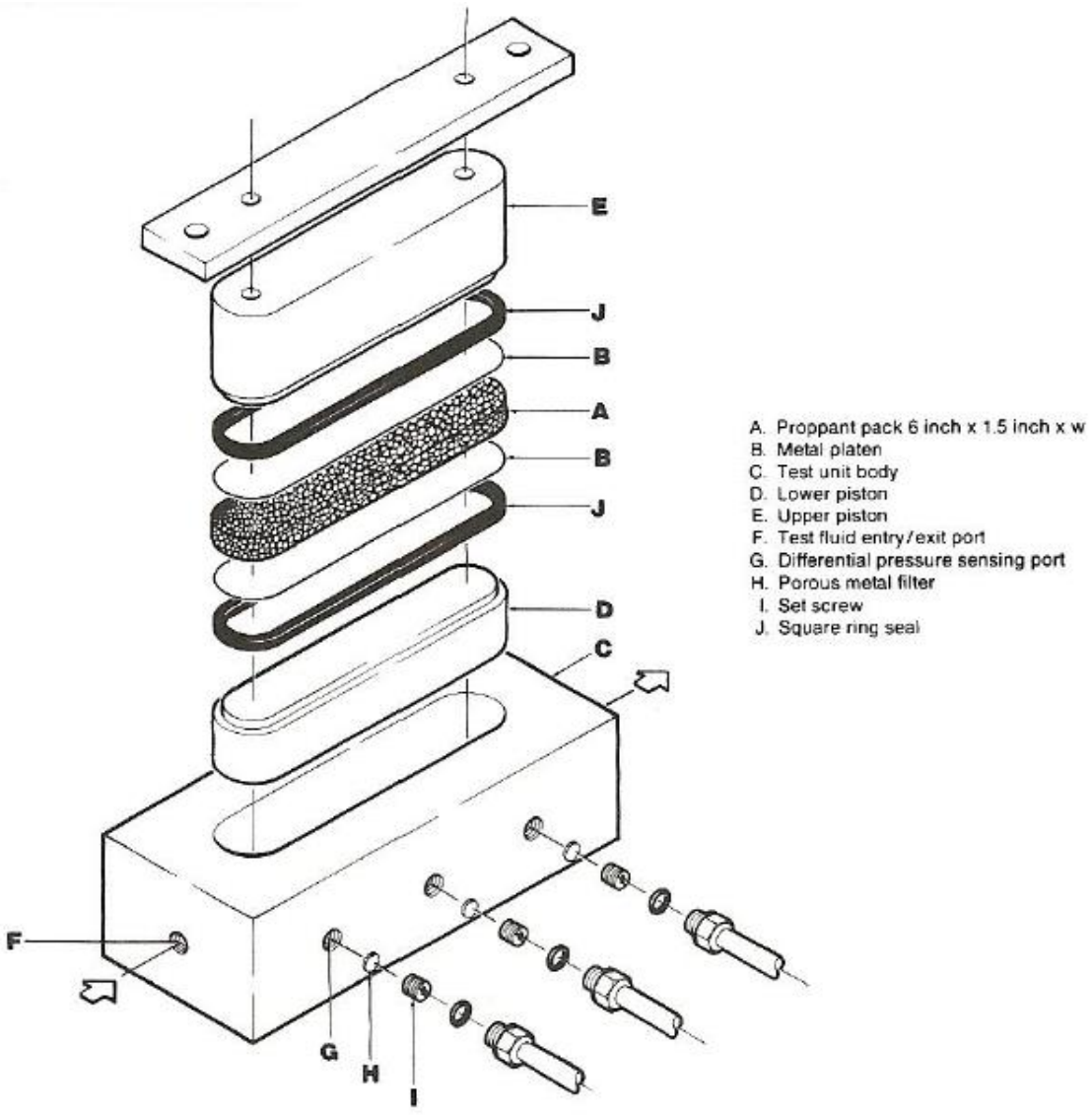

Figure 2.12: Exploded view of current API endorsed conductivity cell (Gidley et al. 1989)

This apparatus is simple, accurate, and is not prohibitively expensive, making it an ideal candidate for laboratory testing. Fluid enters the cell at 'F', moves through the packing, and exits at the opposite end. There are three pressure taps; the middle tap is to measure the fluid pressure in the packing, and the outer taps are for measuring the differential pressure. Since fluid leakage is a common problem for this unit, elliptical rubber gaskets

are placed around the inner groove of the pistons. When stress is applied, the rubber is compressed and forced up against the walls of the cell, which effectively traps the fluid inside the cell. For the experiments performed in this study, an additional rubber shim was placed in between the metal shim and the piston on both sides to provide additional leakage resistance. Also, small diameter tubes were placed in each of the "holes" of the cell so that individual proppant grains did not exit the cell and so that the proppant pack would stay aligned with the inlet and outlet ports.

PROPPANT MIXTURES

Despite their widespread usage, few studies have been performed on the behavior of mixtures of unlike proppants. After investigation, it seems that the only conspicuous paper that is explicitly dedicated to proppant mixtures belongs to McDaniel and Willingham (1978). They examined mixtures consisting of glass beads, sintered bauxite (ceramic), and sands which were sourced from various locales. Figure 2.13 shows the results of mixtures of sand and glass beads:

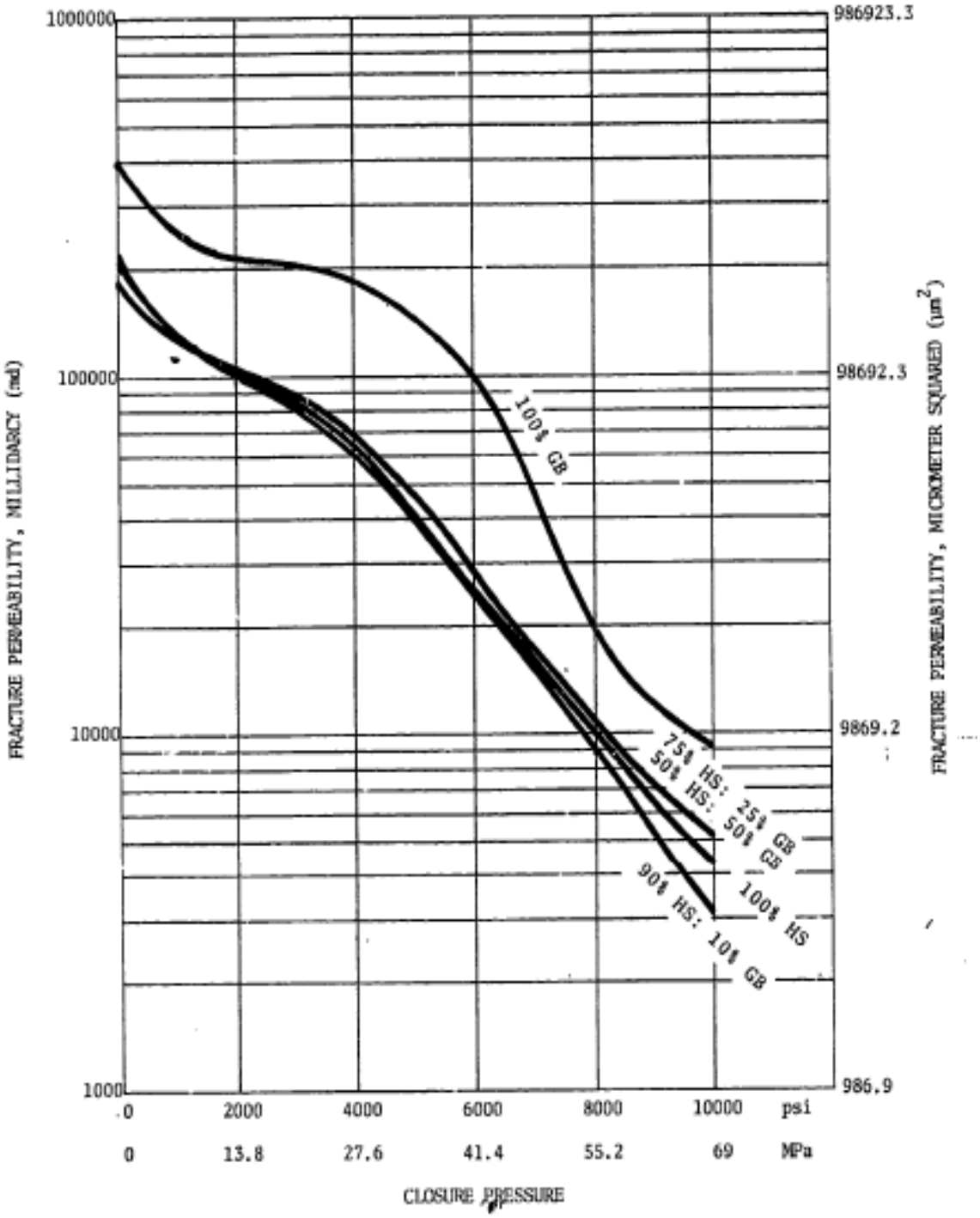

Figure 2.13: Plot of conductivity as a function of closure stress for mixtures of sand and glass beads (McDaniel & Willingham 1978)

Here, the 20-40 and 12-20 designations refer to the size distribution of the particles; this will be explained in detail later but now it will suffice to say that the smaller numbers indicate larger particles. In this instance, the 12-20 glass beads are larger than the 20-40 hickory sand grains. Examining the plot, it is evident that even for the case in which the proppants are mixed at equal ratios, the resultant permeability is much closer to the pure 20-40 hickory sand than the 12-20 glass beads. This result suggests that the permeability of a binary mixture of proppants is not simply a linear interpolation between the permeabilities of the pure component proppant packings. In another set of experiments, McDaniel and Willingham examined the effect of including grains whose size are indicated by the 100 mesh label; these grains are significantly smaller than the 12-20 and 20-40 mesh labels. Figure 2.14 shows the results.

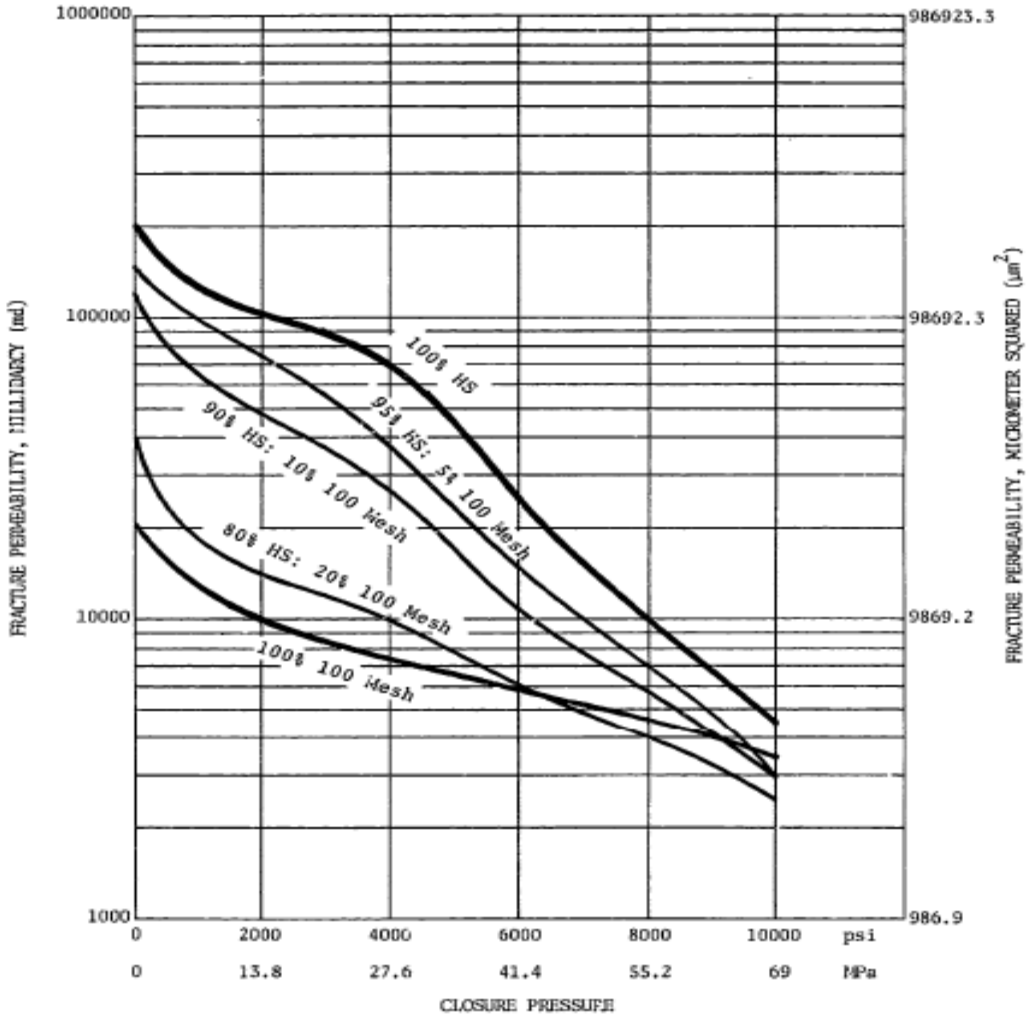

Figure 2.14: Permeability as a function of closure stress for mixtures of 20/40 mesh sand and 100 mesh sand (McDaniel & Willingham 1978)

In this instance, even a mixture with only five percent of the smaller 100 mesh sand causes a significant drop in permeability. Similarly, the permeability of the mixture of 80 percent 20-40 mesh sand and 20 percent 100 mesh sand lies much closer to the 100 mesh sand permeability than it does the 20-40 sand permeability.

SUMMARY

This chapter has established that the permeability of a porous medium is, in fact, an intrinsic property of the medium. Furthermore, according to both analytical and empirical evidence, the permeability is directly related to the grain size distribution and is proportional to the square of some characteristic grain diameter. The constant of proportionality which governs the relationship between permeability and grain size is itself a function of the porosity, tortuosity, grain size distribution parameters, and packing arrangement of the medium.

Acknowledgement is made of the fact that there are multiple physical mechanisms which degrade proppant permeability that are not accounted for in laboratory experiments. Experimental work can provide us with upper bounds on the permeabilities, and can lend insight into how proppants perform relative to each other. The most important in-situ effect, magnitude of closure stress, is explicitly included in all conductivity experiments. Also, previous methods of conductivity measurement are investigated and the apparatus recommended by the API is determined to be the most capable.

Finally, a previous study on proppant mixtures is considered, and the primary conclusion is that the inclusion of even a small amount of fine grains can severely degrade the permeability of the overall mixture.

Chapter 3: Methodology

The purpose of this chapter is to delineate in full detail the methods and assumptions that were employed in the measurements of proppant permeability and conductivity.

EXPERIMENTAL SETUP

The aforementioned Darcy's law permits the calculation of permeability from measurements of pressure, dimensions, and viscosity. Its origin and derivations are discussed in Chapter 2. In its range of applicability, it simply states that the flow rate of a fluid through a porous medium varies linearly with the pressure drop across the medium. In symbolic form, the relation can be stated as follows:

$$q = \frac{-kA}{\mu}\frac{\Delta p}{\Delta x} \tag{3.1}$$

where q represents the volumetric flow rate, k represents the permeability of the medium, A is the cross-sectional area open to flow, Δp is the pressure drop, μ is the viscosity of the fluid, and Δx is the length across which the pressure drop is occurring. There are several implicit assumptions that have been made with the relation as it is presented above; first, it is only applicable for a one-dimensional, i.e. linear, geometry. The second assumption is that the fluid is in a single phase, and it is incompressible. Also, the flow must be steady-state, meaning that the physical properties of the system do not change with time, and it must reside in the laminar flow regime. Finally, in Equation 3.1, gravitational effects are neglected. The difficulty of measuring permeability then becomes apparent,

because although the technique is conceptually simple, it is a challenge to ensure that the experiments are conducted in a way that is consistent with all of the assumptions.

The apparatus that houses the proppant, known as the API conductivity cell (Figure 2.12), is designed for small-scale testing for laboratory convenience. The test cell is depicted in Figures 3.1, 3.2, 3.7, and 3.8.

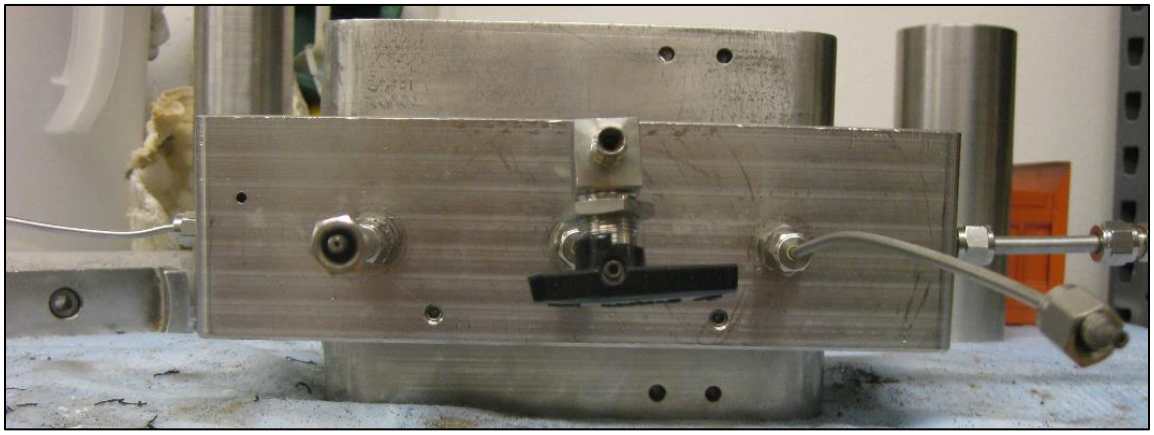

Figure 3.1: Front view of API cell. Pressure taps in foreground.

The geometry of the cell is such that the flow is dominantly in one horizontal direction, which eliminates gravitational effects and provides a linear flow path and thus satisfies two of the original assumptions. The API guidelines (Kaufman et al. 2007) suggest using a solution of deionized water and 2% potassium chloride (KCl) as the test fluid. In the current work, both tap water and deionized water (without KCl) were used; there was no noticeable difference on the results. The most important properties of the test fluid are its low compressibility and its state of aggregation at the test conditions; because water is nearly incompressible, safely remains in a single phase at test conditions, and is readily accessible, it is an ideal test fluid. The steady-state requirement

of Darcy's law is easily met by imposing a constant flow rate and allowing the system to equilibrate.

The final assumption to satisfy is the restriction of the flow to a laminar flow regime. Generally, for flow in a porous medium, the flow can be characterized by either Darcy's law or Forchheimer's equation. The latter is simply an extension of Darcy's law and effectively makes the pressure drop across the medium a quadratic function of the flow rate instead of a linear function of the flow rate. Laminar Stokes flow is associated with Darcy's law; inertial and turbulent flow is associated with the Forchheimer equation. The distinction between the flow regimes is governed by the value of the Reynolds number, which is a dimensionless quantity that represents the ratio of inertial forces to viscous forces. Generally speaking, the Reynolds number is just the product of the fluid density, fluid velocity, and a characteristic length scale divided by the fluid viscosity. For flow in a pipe, the characteristic length scale is usually taken to be the pipe diameter. However, the choice of a characteristic length in a porous medium is not as obvious. Huang and Ayoub (2007) provide the following possible definitions of the Reynolds number for a porous medium:

$$Re_{grain} = \frac{\rho V d_g}{\mu} \tag{3.2}$$

$$Re_{interstitial} = \frac{\rho V d_g}{\Phi \mu} \tag{3.3}$$

$$Re_k = \frac{\rho V \sqrt{k}}{\mu} \tag{3.4}$$

where ρ is the fluid density, V is the fluid velocity, d_g is some characteristic grain diameter, μ is the fluid viscosity, Φ is the porosity, and k is the permeability. They conclude that Reynolds numbers less than 4.3 can be considered fully Darcy (laminar) flow, and Reynolds numbers up to 180 can be adequately characterized by the Forchheimer equation. To ensure that the experiments are conducted as close to the laminar boundary as possible, the Reynolds number is calculated for each proppant pack at each flow rate. A range of possible Reynolds numbers is generated due to the fact that proppant packs have a certain grain size distribution associated with them and that multiple flow rates, and hence multiple velocities, were used in the experiments. The maximum Reynolds number for a particular data point was calculated with the highest flow rate used and the highest grain size in the pack; analogously for the minimum Reynolds number. The grain-based Reynolds number (Eq. 3.2) was chosen for use because of its relative simplicity. Most experiments had Reynolds numbers that fell between 1 and 20; so while they may not have been strictly in the laminar window, they were reasonably close. Flow regimes in porous media can also be verified by simply examining plots of pressure drop versus flow rate; if the relationship is linear, then it is most likely laminar flow, and if the relationship is quadratic or otherwise nonlinear, it is probably an indication of non-laminar flow. Diagnostic plots for most tests which were run as part of this study are included in Appendix A.

The experimental setup is guided by the recommendations of the API, which has published a set of standards for conductivity testing (Kaufman et al. 2007). While many of the conditions were met, some were not due to time constraints and equipment

constraints. The first recommendation is that stress should be applied to the proppant pack for 50 hours. This requirement was not met because there was simply not enough time to implement it. In the present setup, stress was applied for 24 ± 3 hours at each stress level. It should be noted that the 50 hour requirement is essentially arbitrary, and while it is aimed at allowing the proppant pack enough time to come to a semi-equilibrium state, it should be remembered that in the field, proppant can be subjected to stress over the producing life of a well, which could be several years. It is apparent that applying stress to proppant in a laboratory setting at this time scale is simply not practical, and in choosing the duration of stress one must balance the competing desires of saving time versus allowing a sufficient amount of time so that the effect of crushing is adequately captured.

The API recommendations also state that the tests should be run at a temperature of 250°F to better imitate in-situ reservoir conditions. This stipulation was not met; the tests were performed at ambient temperature. Temperature effects are important for curable resin-coated proppants which require time at temperature, but for proppants without resin, temperature should not have an appreciable physical effect on the permeability of a given proppant pack. Another guideline suggests using sandstone or shale cores in lieu of metal shims so that the effect of proppant embedment is taken into account; however, because this study is not focused on embedment effects, and due to the difficulty and cost of obtaining fresh core samples, the experiments in this work were performed with metal shims for simplicity. Finally, the API recommends using a back pressure regulator that applies 300 to 500 psi on the back end of the system to ensure that

any gases that may be present in the test fluid remain in the liquid phase. This recommendation was implemented and a back pressure of approximately 350 psi was applied to the system.

The measurements were performed by rearranging Darcy's law so that the permeability term is isolated, as follows (negative sign is ignored because it only indicates directionality):

$$k = \frac{q\mu\Delta x}{A\Delta p} \tag{3.5}$$

where the symbols are the same as before. For this situation, the cross sectional area A is rectangular and can be broken into two dimensions, w and L, so that $A = wL$. The parameter w represents the thickness of the proppant pack in the vertical direction, and L represents the horizontal width of the proppant pack in the direction perpendicular to flow. With these definitions, Darcy's law can now be written as:

$$k = \frac{q\mu\Delta x}{wL\Delta p} \tag{3.6}$$

The following image depicts the test cell as seen from above, and defines visually the parameters Δx and L.

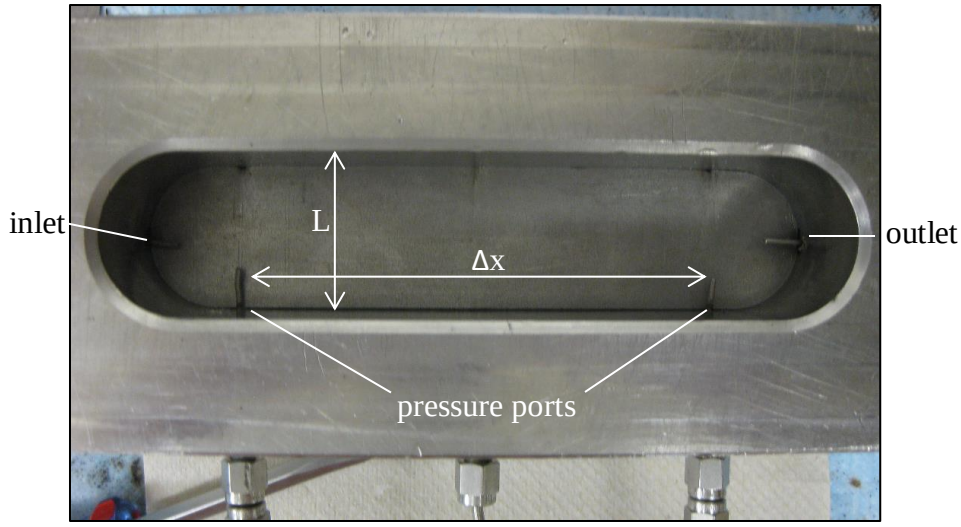

Figure 3.2: API cell with one piston as viewed from above.

The vertical width of the proppant pack, *w*, could not be measured directly; it was obtained by measuring the width of the entire apparatus (difference between the top of the upper platen and bottom of the lower platen) both with and without proppant inside the test cell and taking the difference between the lengths. This idea is represented diagrammatically below.

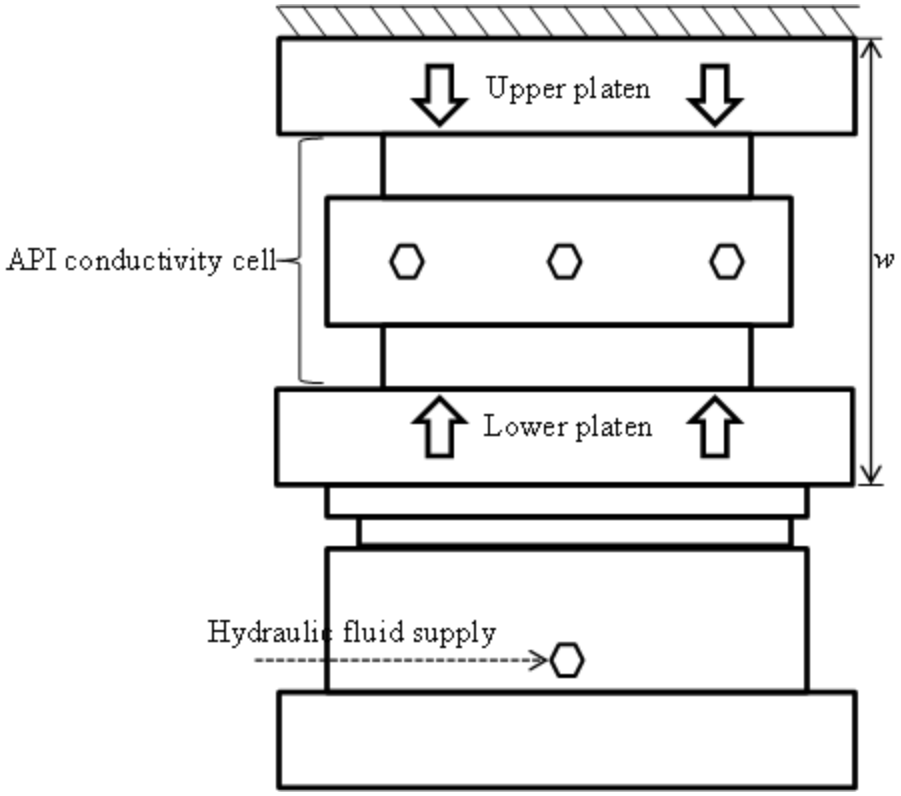

Figure 3.3: Schematic of entire assembly. Width of proppant pack is obtained by measuring *w*, as illustrated above, when the cell contains everything except proppant, and subtracting that from measuring *w* when the cell contains proppant.

Another reason that water was chosen as the test fluid is that its physical properties are well known and widely documented, which eased the process of obtaining an accurate value of water viscosity. Likhachev (2002) introduced an equation of state that provides a first-order approximation for the viscosity of water as a function of temperature and pressure. The relationship is as follows:

$$\mu = \eta \, exp\left[ap + \frac{E - bp}{R(T - \theta - cp)}\right] \tag{3.7}$$

where μ is the viscosity of water, η, a, b, c, θ, and E are constants, T is temperature, p is pressure, and R is the universal gas constant. The viscosity of water as predicted by this equation is most sensitive to temperature and very weakly dependent on pressure. Since

all of the experiments were performed at room temperature, a value of 25°C (298 K) was used for the temperature. Because a back pressure of 350 psi was applied to the system, the internal pressure ranged from about 350 to 500 psi. Inputting these values for pressure into the equation of state, along with a temperature of 298 K, resulted in viscosity predictions ranging from 0.890415 centipoise to 0.890379 centipoise. The precision of these viscosity predictions helped to keep experimental measurement errors to a minimum.

At this point, Darcy's law can be rewritten as:

$$k = \frac{q\mu\Delta x}{(w - w_{ref})L(p - p_{ref})} \tag{3.8}$$

where p is the differential pressure and p_{ref} is the differential pressure with no flow rate, i.e. reference pressure. The reference pressure variable is introduced because differential pressure transducers may display a nonzero value for the pressure difference, even when there is obviously no pressure difference. This does not mean they are defective, it just means that the reference pressure is nonzero. For a given proppant pack subjected to a particular closure stress, multiple flow rates are imposed across the medium and their associated pressure drops are recorded. We can rearrange Darcy's law once again to obtain:

$$\frac{1}{(p - p_{ref})} = k\frac{(w - w_{ref})L}{Cq\mu\Delta x} \tag{3.9}$$

where C is a constant that takes care of all unit conversions. If pressure is measured in psi, lengths in inches, flow rate in milliliters per minute, viscosity in centipoise, and permeability in Darcies, then C is 0.095179. The reason for writing the equation in this

form is that it can now be recognized as a linear function with an intercept of zero, where *k* is the slope of the line. Therefore, multiple flow rates can be imposed, and a plot can be constructed so that the right hand side of the equation (without *k*) is placed on the abscissa and the left hand side is placed on the ordinate. Then a least squares regression can be performed on the data, and the slope of the resultant best-fit line is equivalent to the permeability of the proppant pack. There are three reasons for calculating the permeability in this manner; first, it is a robust way to average the permeabilities that would be calculated at each individual flow rate. Secondly, if the plot is significantly nonlinear, then the flow behavior is most likely not laminar, which would invalidate Darcy's law. Finally, it validates the functionality of the pressure transducers, and of the entire experimental setup. An example of such a plot is shown below:

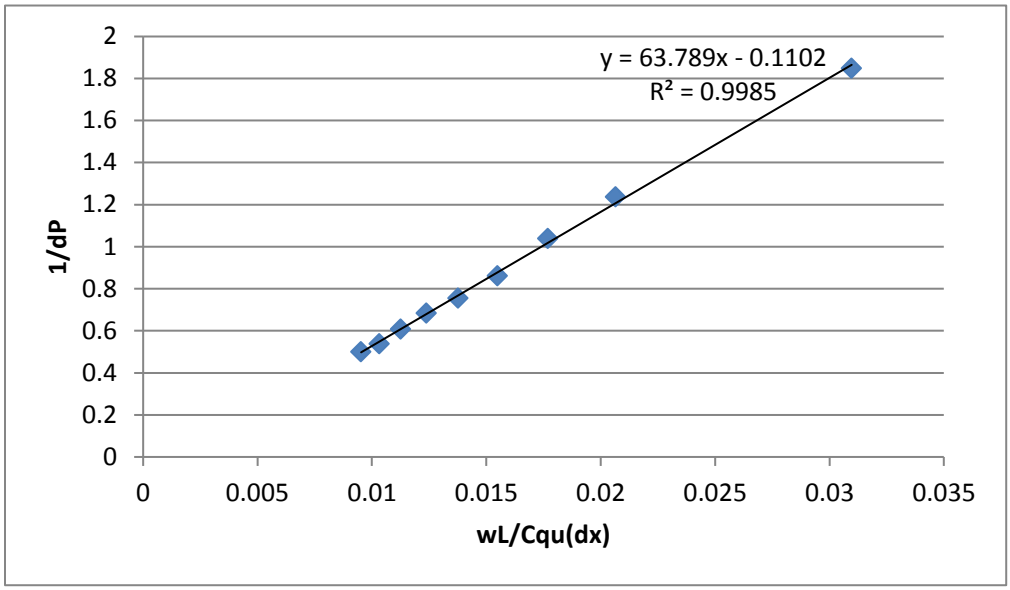

Figure 3.4: Example of a diagnostic plot for a proppant sample at a particular level of stress.

Again, each point is representative of a particular flow rate/pressure drop pair, and the permeability of this proppant pack at this level of stress is about 63.8 Darcies.

The propagation of uncertainties that are associated with measurements was also performed and error bars were calculated for each data point. The general formula for error propagation was used, and in this particular application it can be expressed as:

$$\Delta k = \left|\frac{\partial k}{\partial q}\right| \Delta q + \left|\frac{\partial k}{\partial p}\right| \Delta p + \left|\frac{\partial k}{\partial \mu}\right| \Delta \mu + \left|\frac{\partial k}{\partial (\Delta x)}\right| \Delta(\Delta x) + \left|\frac{\partial k}{\partial w}\right| \Delta w + \left|\frac{\partial k}{\partial L}\right| \Delta L + \left|\frac{\partial k}{\partial p_{ref}}\right| \Delta p_{ref} + \left|\frac{\partial k}{\partial w_{ref}}\right| \Delta w_{ref} \tag{3.10}$$

Equation 3.10 states that the error in permeability (Δk) can be calculated as the sum of the absolute value of the partial derivatives of the permeability with respect to each independent variable multiplied by its associated uncertainty. Evaluating all of the derivatives, we arrive at the working form of the equation:

$$\Delta k = \frac{\mu \Delta x}{(w - w_{ref})L(p - p_{ref})}\Delta q + \frac{q\mu \Delta x}{(w - w_{ref})L(p - p_{ref})^2}\Delta p$$
$$+ \frac{q\Delta x}{(w - w_{ref})L(p - p_{ref})}\Delta \mu$$
$$+ \frac{q\mu}{(w - w_{ref})L(p - p_{ref})}\Delta(\Delta x)$$
$$+ \frac{q\mu \Delta x}{(w - w_{ref})^2 L(p - p_{ref})}\Delta w \qquad (3.11)$$
$$+ \frac{q\mu \Delta x}{(w - w_{ref})L^2(p - p_{ref})}\Delta L$$
$$+ \frac{q\mu \Delta x}{(w - w_{ref})L(p - p_{ref})^2}\Delta p_{ref}$$
$$+ \frac{q\mu \Delta x}{(w - w_{ref})^2 L(p - p_{ref})}\Delta w_{ref}$$

Any negative signs that arose from differentiation were disposed of by the absolute value signs. The uncertainty propagation, when evaluated in this manner, is the most pessimistic method in that it estimates the maximum possible uncertainty in the measurement. The uncertainties for each quantity are dictated by the precision of the measuring instrument. For example, a pair of digital calipers capable of measuring in increments of 0.0005 inches was used to measure each length quantity. The associated uncertainty is half of that value, so for this case it would be 0.00025 inches. Because the viscosity was predicted by an equation of state, a sensitivity analysis was performed with values of temperature and pressure that are in the vicinity of the experimental conditions, and there was little variation in the predictions, so an error of 0.01 centipoise was

assumed. The pump used to impose flow has an uncertainty of 0.0005 milliliters per minute. Due to the small magnitude of the pressure drops incurred in these experiments, several pressure values were recorded for each flow rate. The average of these was reported as the actual value, and the standard deviation of the set was taken as the uncertainty. The reference pressure usually settled down to a single value, and because the digital transducer measures pressure in increments of 0.0001 psi, its uncertainty was taken as 0.00005 psi. The reference width proved to be problematic, as it is a function of closure stress because the rubber shims that were used as seals are compressible, and decrease in width as stress is applied. As stated earlier, the reference width was obtained by measuring the width of the entire apparatus sans proppant. Ten trials were performed at each stress level, an average was taken at each stress level, and an equation was fit to the data. The results are shown in Figure 3.5.

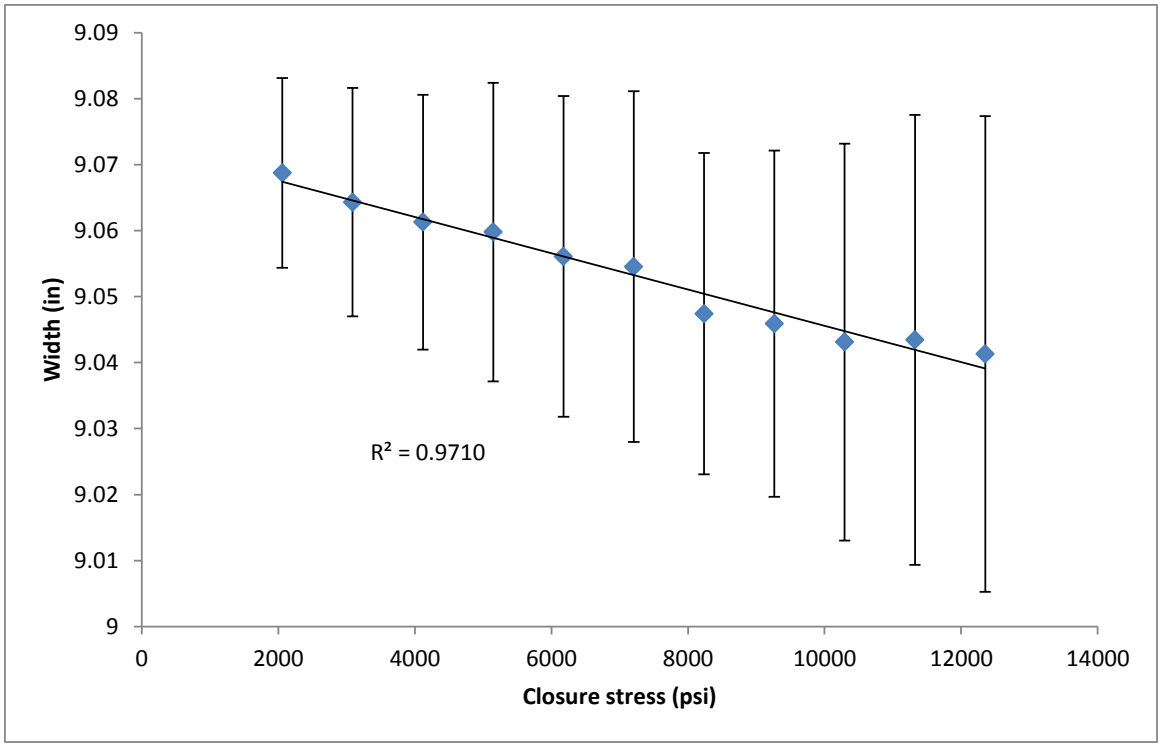

Figure 3.5: Reference widths as a function of closure stress. Proppant pack width is calculated by subtracting the reference widths from the measured width at the time of testing.

The error bars in this plot represent the standard deviation of the ten measurements made at each stress level. The plot makes them seem large, but their magnitude is only about 0.02 to 0.08 inches. Therefore, the reference widths and their associated uncertainties are functions of closure stress.

EXECUTION

Prior to running any experiments, the method of applying closure stress to the proppant was conceptualized and implemented. A simple hydraulic pump, shown in Figure 3.6, was utilized to create suitable fluid pressures.

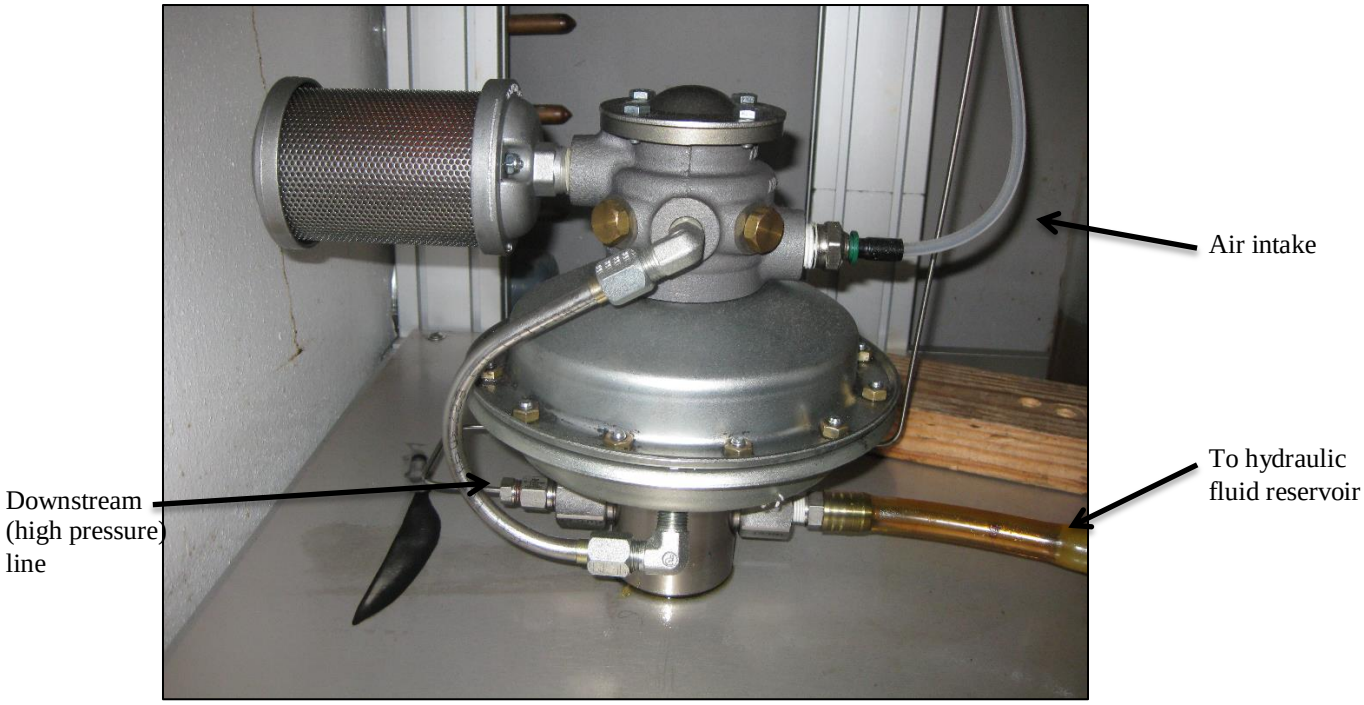

Figure 3.6: Hydraulic pump which supplied confining stress.

The pump intake was configured to accept air at a pressure of 100 psi, and the pump converted that into downstream pressures of up to 10,000 psi. The downstream line was connected to the bottom of a piston which was situated at the bottom of the press, as shown in Figure 3.7.

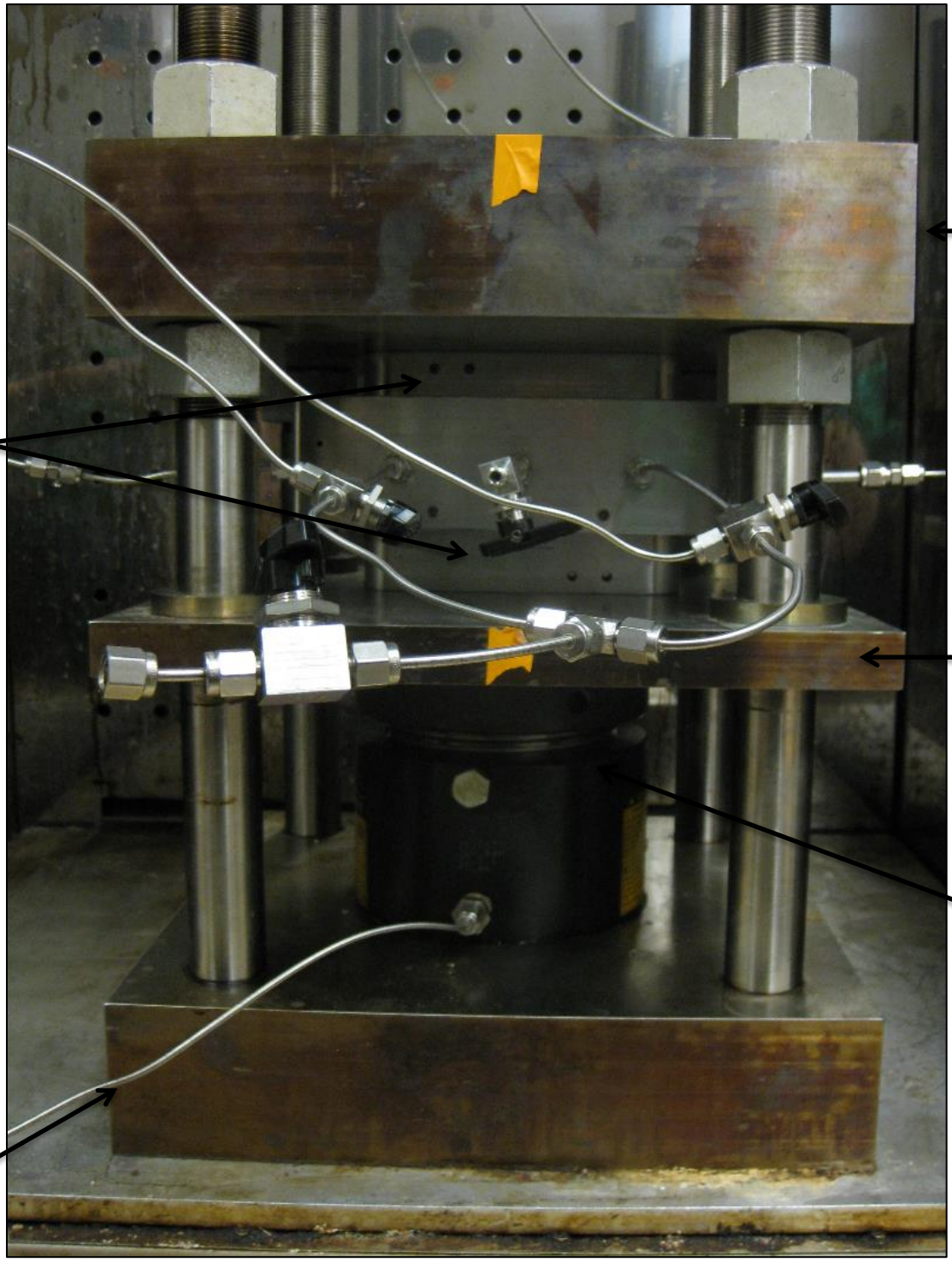

Figure 3.7: Front view of overall assembly. Hydraulic piston at bottom of press accepts high pressure fluid from the pump and transmits it through the moveable platen to the API cell.

It is evident from Figure 3.7 that the circular area of the hydraulic piston is not equal to the elliptical area of the pistons in the API conductivity cell. This means that the pressure in the hydraulic fluid is not equal to the stress being applied to the proppant packing. The force from the hydraulic fluid is being transmitted through the movable platen from the circular hydraulic piston to the smaller API cell pistons, and so the stress on the proppant pack is higher than the hydraulic fluid pressure. The areas of each piston were measured and it was determined that the hydraulic piston area is about 2.058 times larger than the area of the API pistons, and so the closure stress was calculated by multiplying the pressure of the hydraulic fluid by 2.058.

The amount of proppant placed in the cell, as measured by its areal concentration, is another parameter that is available for tuning or tweaking in these experiments. Because this study is focused on mixtures, the areal concentration was kept at a constant 2 lbm/ft^2. This value was chosen because it follows the recommendation of the API guidelines on conductivity testing and it results in realistic pack widths. The API cell requires a mass of 63 grams of proppant to maintain an areal concentration of 2 lbm/ft^2. When mixtures were tested, the proppants were measured so that the total mass was 63 grams; e.g. if a mixture required fifty percent of a particular proppant, 31.5 grams of that component were placed into the mixture. An example of a prepared mixture in the cell is shown in Figure 3.8.

Figure 3.8: Fifty fifty mixture of 20/40 sand and 40/70 ceramic before testing.

After loading the proppant, the upper piston assembly was placed onto the packing and the cell was placed onto the moveable platen, as shown in Figure 3.7. Then, stress was applied to the cell, beginning with 2,000 psi closure stress (~972 psi hydraulic fluid pressure). The inlet, outlet, and pressure gauge flow lines were hooked up to the cell, and it was exposed to stress for approximately 24 hours. Finally, water was pumped through the system at various flow rates and differential pressure readings were obtained at each flow rate. After a satisfactory number of flow rates were used, the stress was increased by an increment of 2,000 psi closure stress, so that the next stress level would be at 4,000

psi. This process was repeated until the proppant pack had been tested at 10,000 psi closure stress.

The algorithm for measuring permeability at a given closure stress is to impose a volumetric flow rate q, then record values for w, p, $p_{ref,}$ and μ, (Eq. 3.9) keeping in mind that L and Δx only need to be measured once. Flow rates ranged from 10 mL/min to 190 mL/min. Higher flow rates were sometimes necessary because high permeability packings produce low pressure drops, which can be difficult to measure accurately. For example, the 20/40 ceramic packing would exhibit pressure differentials of approximately 0.05 psi at low flow rates, and measurements at that level of precision dramatically increase the experimental uncertainty as calculated by Equation 3.11.

A schematic of the experimental setup is shown in Figure 3.9:

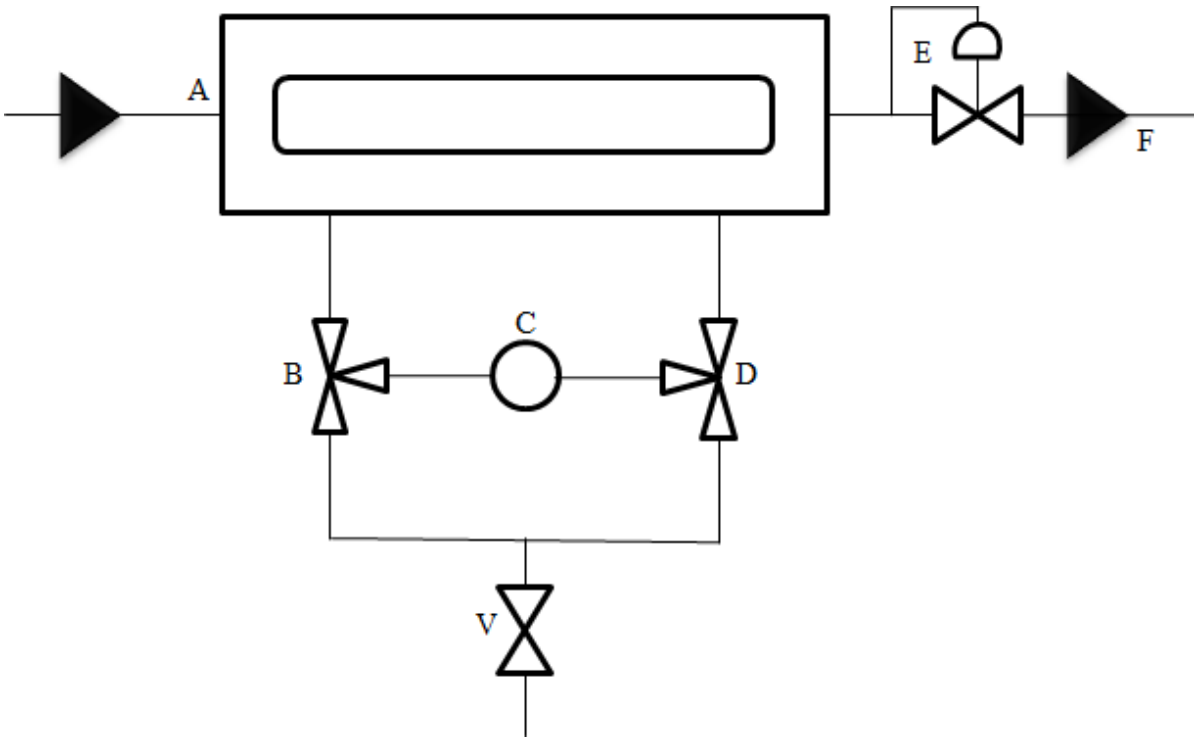

Figure 3.9: Schematic of flow loop used in experimentation.

In the diagram, B and D represent three-way valves, C represents a differential pressure gauge, and E represents a back pressure regulator. There is a valve installed at point V to allow venting. Before beginning a trial, the reference pressure is recorded. This is accomplished by pumping water into the system at point V and manipulating the three-way valves at B and D so that the fluid occupies only the portion of the system delineated by B, C, D and V. By then closing the valve at V, a pressure equalization circuit is created and it is guaranteed that the pressure on either side of the gauge is the same. The pressure reading at this point in time is the reference, or 'zero', pressure. After this, water is pumped into the API cell at the entry point A and moves through the back pressure regulator at E and leaves the system at point F. The back pressure regulator is set at a pressure of 350 psi. This ensures that the internal system pressure is at least 350 psi which prevents any gas bubbles that may be present in the water from coming out of solution. When steady state flow is established between A and F, the three-way valves at B and D are switched so that the pressure gauge at C is now connected to the cell instead of the pressure equalization circuit. Finally, the circuit is visually inspected for any leaks and pressure readings are recorded for processing.

Chapter 4: Results

This chapter reveals the results of permeability and conductivity measurements of the proppants under consideration. Analysis and conclusions will be deferred to Chapters 6 and 8 of this thesis. The goal of this work is to understand how mixtures of proppants of varying materials, sizes, and mixing proportions affect the overall permeability of the packing. Sand, ceramic, and ULW (polymeric) were the only three materials considered, as they are the dominant types of proppant used in current wells. The grain sizes which were tested are also consistent with the sizes of proppants used in industry. Mixing proportions are stated in terms of weight percentage, i.e. a 25% - 75% mixture of two unlike components consist of 15.75 grams of the first component and 47.25 grams of the second component, as the total amount must equal 63 grams to ensure that an areal concentration of 2 lbm/sq ft is achieved.

Clarification of the size nomenclature is necessary before discussing the results. Because it is impractical to mine or manufacture grains of precisely the same diameter, grain sizes are specified by two bounding dimensions. A simple and effective way to sort grains by size is through the use of sieves; so it is natural to describe the size of a sample of grains by their larger diameter and smaller diameter. The American Society for Testing and Materials (ASTM) has created a standardized progression of grain sizes that is adhered to by most, if not all, proppant suppliers. The grain sizes are approximately logarithmically spaced and can be generated by successively multiplying the smallest grain size (20 μm) by the fourth root of two. However, instead of using the grain diameters, the so-called mesh sizes are used. As outlined in ASTM's standards, the mesh

number for a particular sieve is defined as the number of wires or openings per linear inch counted from the center of any wire. Therefore, the mesh numbers are associated with one and only one grain diameter. Table 4.1 displays each mesh number and its associated aperture as defined by ASTM.

Table 4.1: Mesh numbers and their associated apertures (ASTM)

Mesh number	Aperture (μm)	Mesh number (cont'd)	Aperture (μm) (cont'd)
635	20	100	150
500	25	80	180
450	32	70	212
400	38	60	250
325	45	50	300
270	53	45	355
230	63	40	425
200	75	35	500
170	90	30	600
140	106	25	710
120	125	20	850

There are several sieve sizes which are coarser than the 20 mesh sieve, but are not listed in Table 4.1 because they were not used in this study. Sizes of a proppant pack are typically notated as X/Y, where X and Y are mesh numbers. For example, if a proppant

pack is described as 20/40 sand, then the sample consists of sand grains that were trapped between the 20 mesh sieve and the 40 mesh sieve. In that case, each sand grain must have a diameter between 425 μm and 850 μm. Unfortunately, nothing is known about the shape of the distribution in between the two bounding diameters, although it is common to assume a uniform distribution. It should be noted here that smaller mesh numbers correspond to larger grain sizes.

SINGLE COMPONENT RESULTS

Experiments were performed first on the 'pure' component proppants to establish reference data for comparison with the mixture data, and to serve as a quality check on the experimental setup and procedure. As mentioned in a previous chapter, it is common to report the results of these experiments in terms of conductivity instead of permeability. Conductivity is defined as the product of the permeability and the width of the pack. The results of the single component tests will be presented in terms of both permeability and conductivity.

20/40 Sand

The first packing under consideration is 20/40 sand. The term 'sand' is somewhat of a blanket term; traditionally, distinctions are made based on where the sand was sourced, and names such as Ottawa sand, Brady sand, etc. are common in the literature. The mineralogy of sand can vary somewhat (although silica is the most common mineral), and therefore the material properties of different sands can vary. However, for the purposes of this study, the differences among sands will be considered negligible

compared to the differences between sand and ceramic. Permeability and conductivity measurements for 20/40 sand as a function of closure stress are shown in Figure 4.1.

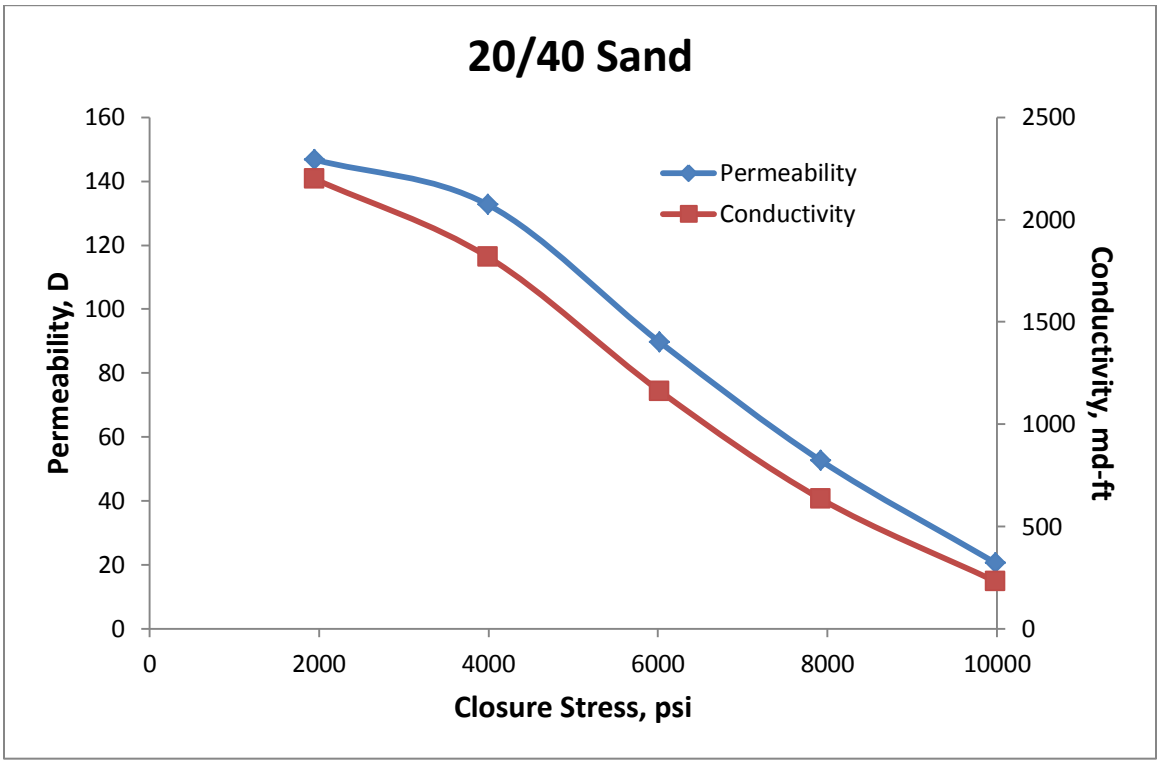

Figure 4.1: Permeability and conductivity as function of closure stress for 20/40 sand.

Pictures of the sand pack after exposure to stress are shown in Figures 4.2 and 4.3.

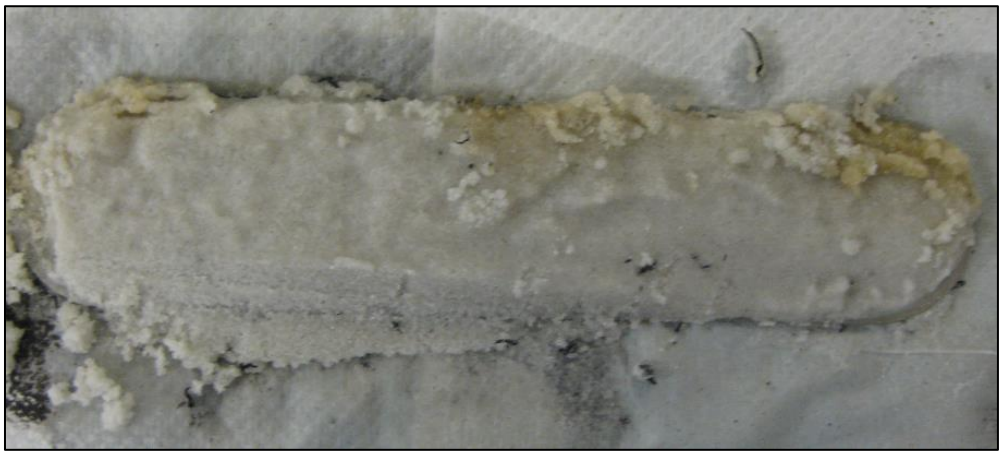

Figure 4.2: 20/40 sand pack after exposure to stress.

Figure 4.3: Cross-sectional view of 20/40 sand pack after exposure to stress. The key is included for scale.

40/70 Sand

The results for 40/70 sand are below:

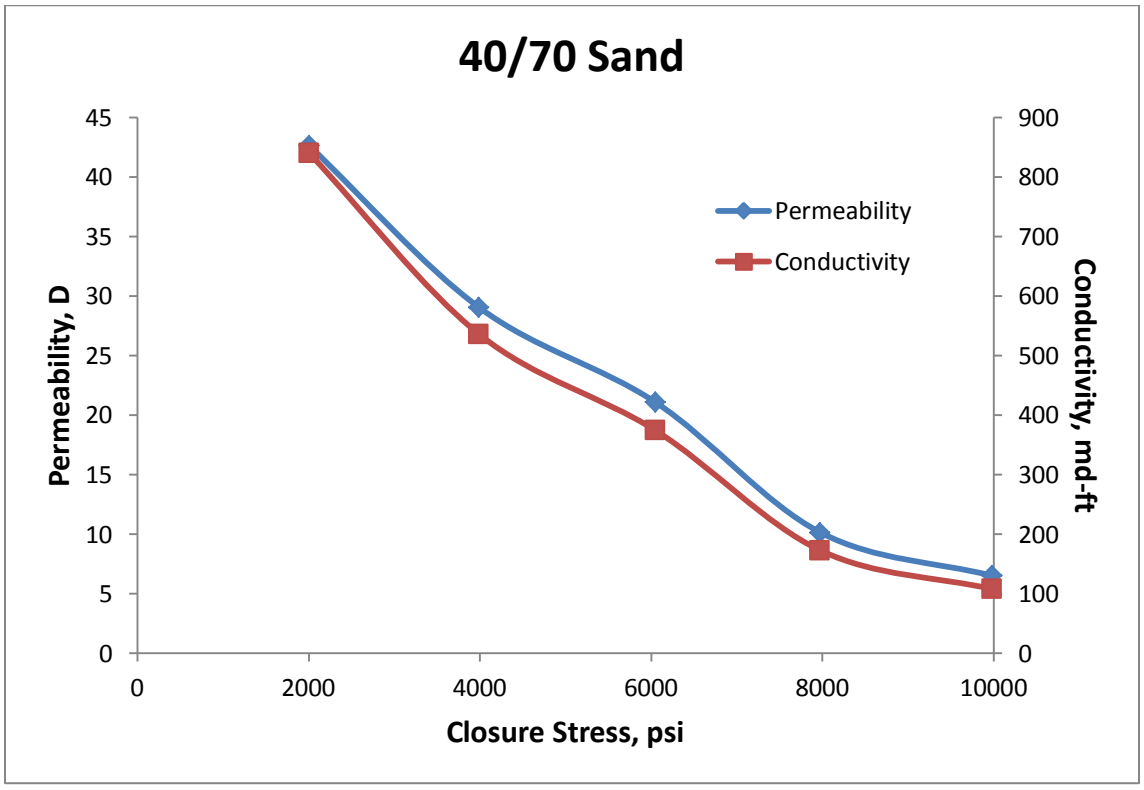

Figure 4.4: Permeability and conductivity as function of closure stress for 40/70 sand.

20/40 Ceramic

The results for 20/40 ceramic are shown below:

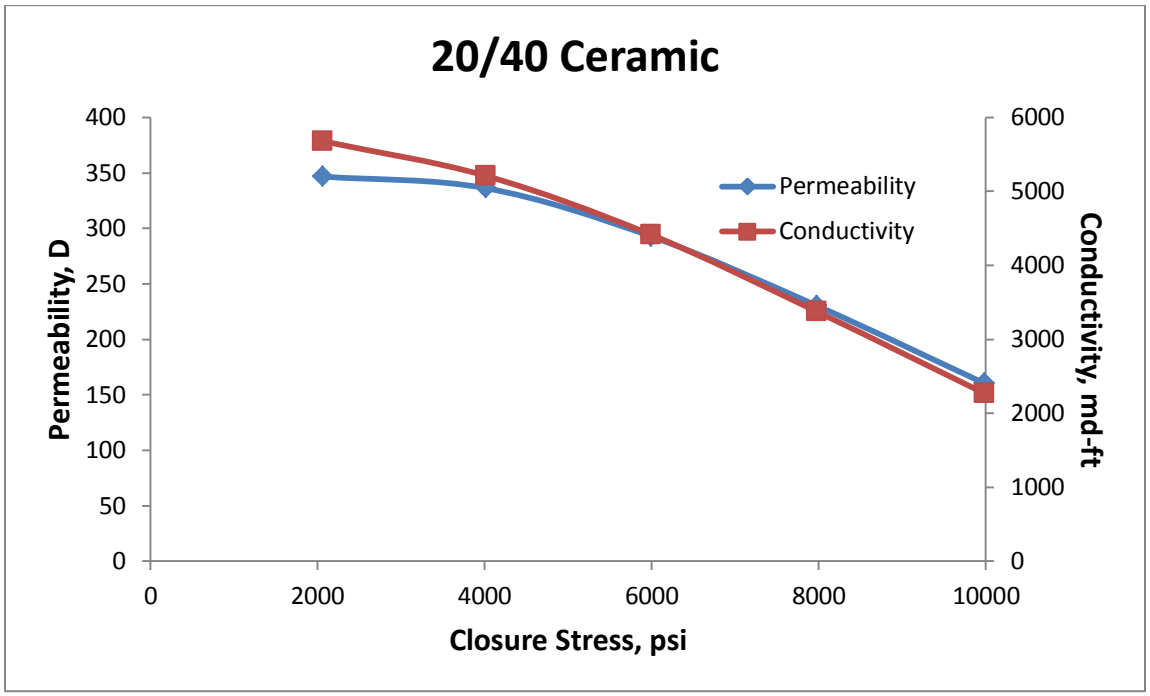

Figure 4.5: Permeability and conductivity as function of closure stress for 20/40 ceramic.

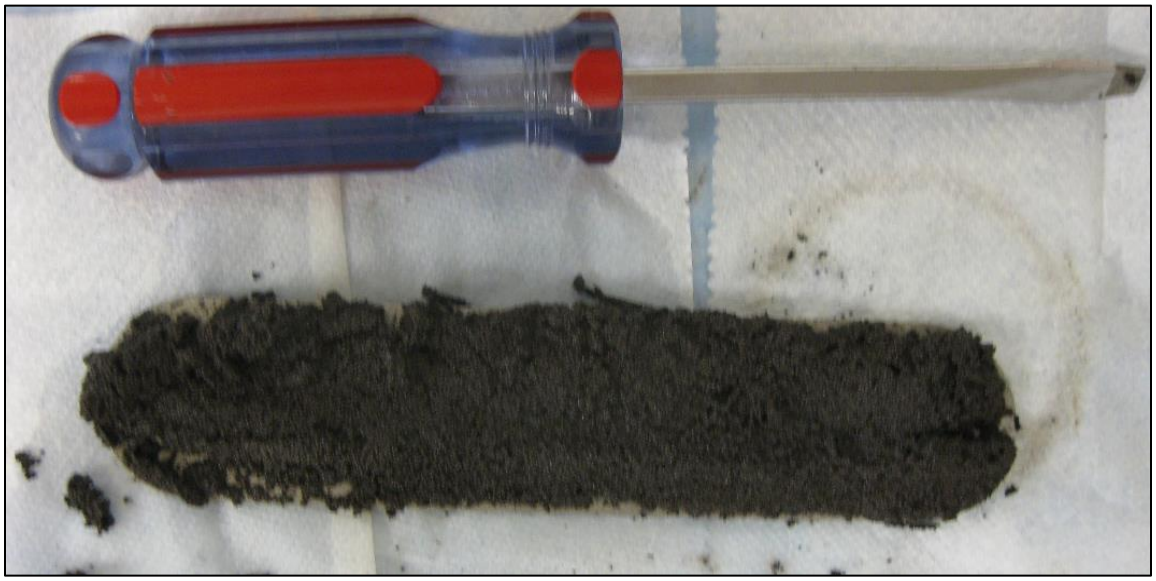

Figure 4.6: 20/40 ceramic pack after exposure to stress. The screwdriver is included for scale.

40/70 Ceramic

The results for 40/70 ceramic are shown below:

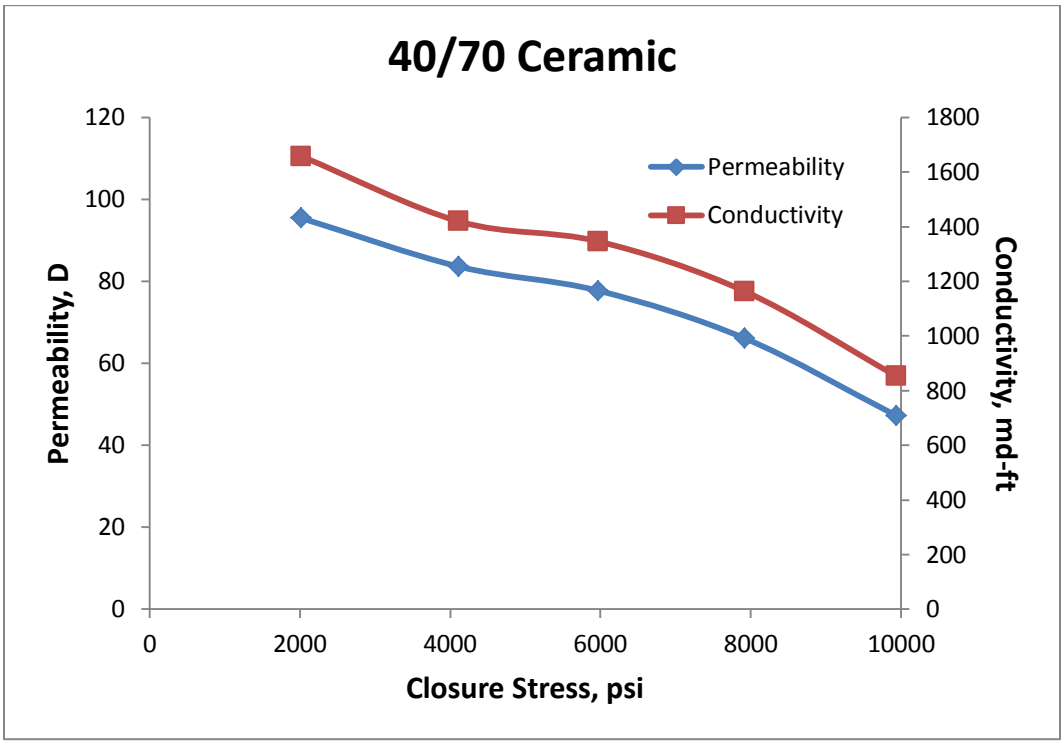

Figure 4.7: Permeability and conductivity as function of closure stress for 40/70 ceramic.

Figure 4.8: 40/70 ceramic pack after exposure to stress. The screwdriver is included for scale.

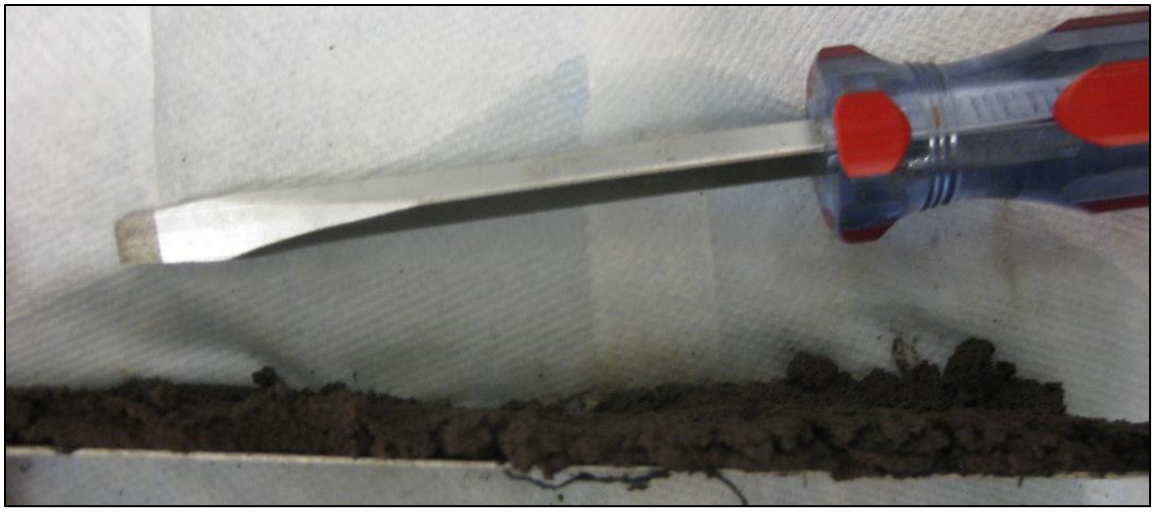

Figure 4.9: Cross-sectional view of 40/70 ceramic pack after exposure to stress. Screwdriver included for scale.

20/40 ULW 1

An artificial light weight proppant was also tested, referred to as ULW 1 (ultra-light weight #1). Its density is very nearly that of water; Gaurav (2010) reports that its specific gravity is 0.95. To confirm this, a small sample was placed in water, and most of the particles floated on the water, which seems to confirm that this sample is indeed less dense than water. Due to its light weight, the usual 2 pounds per square foot concentration was reduced to 1 pound per square foot else the packing would exceed the dimensions of the API cell. Results are shown in Figure 4.10:

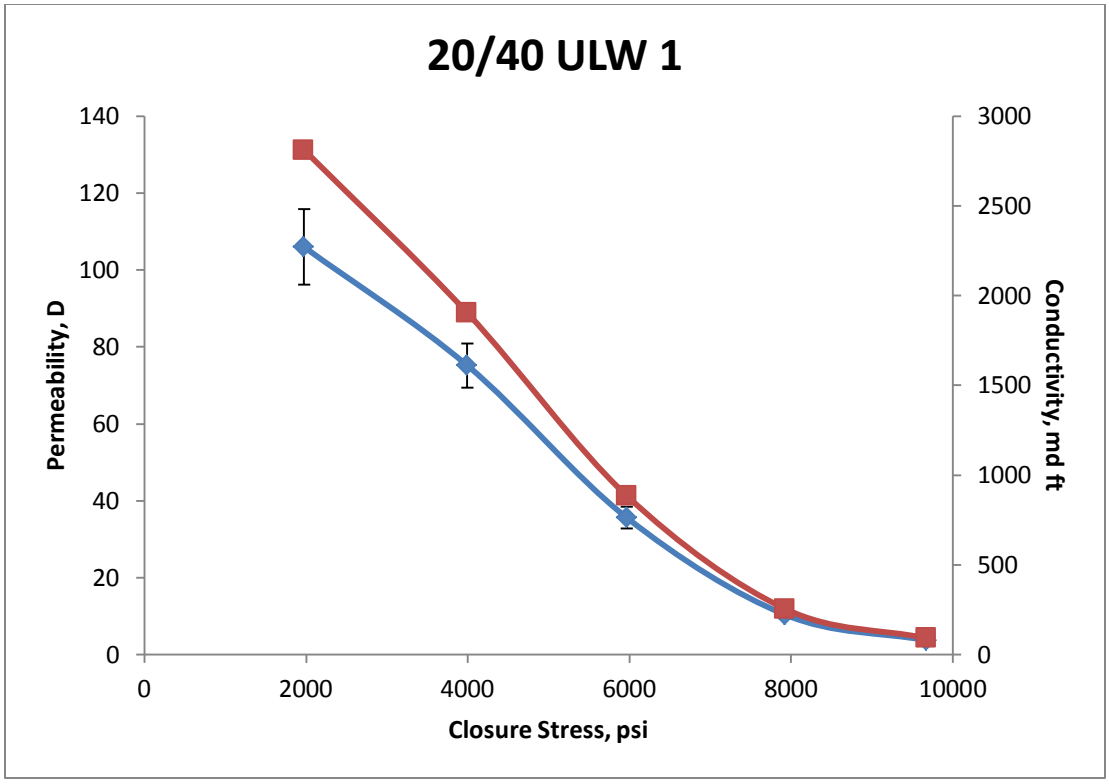

Figure 4.10: Permeability and conductivity as function of closure stress for 20/40 ULW 1.

MIXTURES

Mixture results are shown in terms of both permeability and conductivity and compared to the single-component reference cases. To keep the plots from being overly crowded, the permeability and conductivity data are displayed in separate plots. It may seem redundant to show the conductivity data in addition to the permeability as the trends will be similar, but it is helpful to know the actual values of conductivity.

20/40 Sand & 20/40 Ceramic

The results of two mixtures of 20/40 sand and 20/40 ceramic are shown below. The error bars shown in the permeability plots are calculated from Equation 3.11.

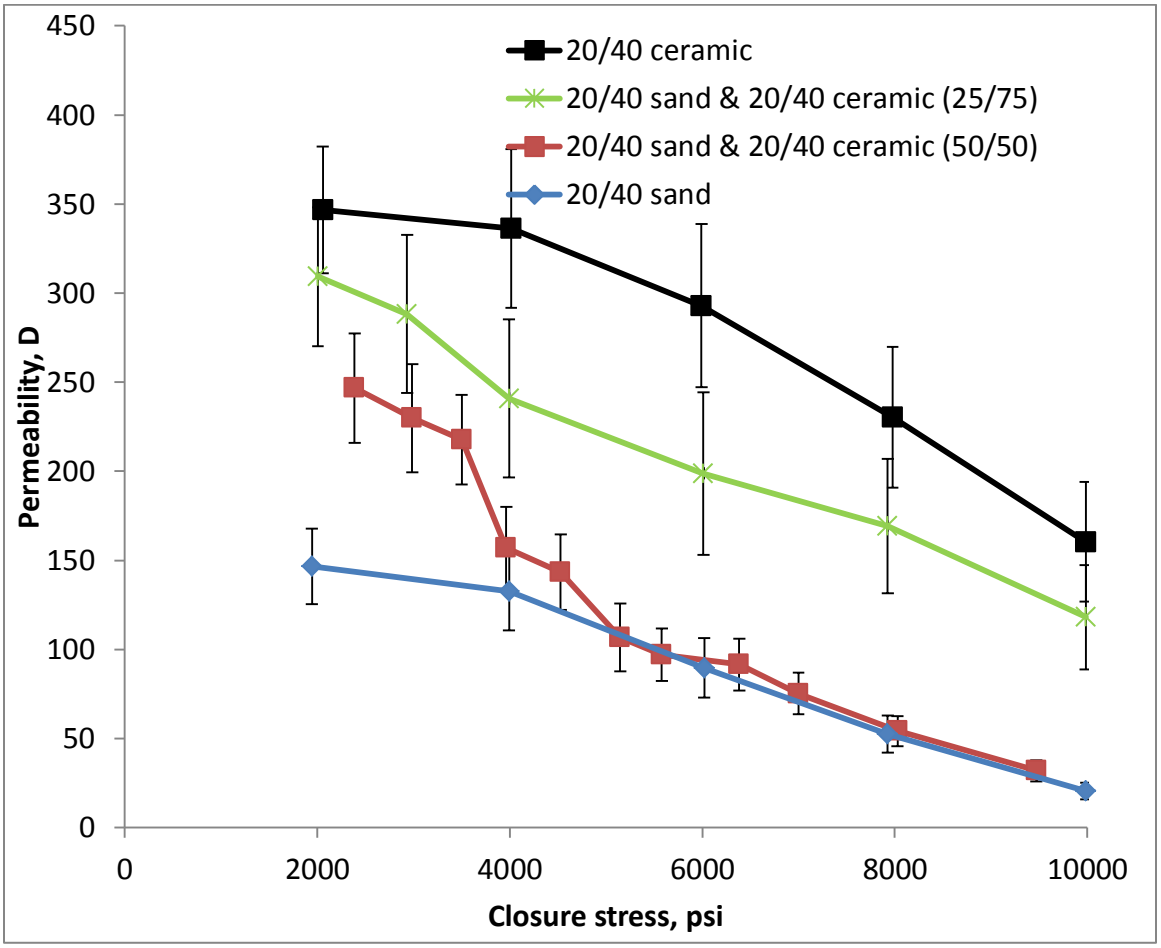

Figure 4.11: Permeability as a function of closure stress for samples consisting of 20/40 ceramic and/or 20/40 sand.

In Figure 4.10, the green curve is a mixture of 25% 20/40 sand and 75% 20/40 ceramic; again, these are weight percentages. The red curve is a mixture of equal weight percentages. Error bars are smaller for lower permeabilities because these exhibit higher pressure drops, which are easier to measure and therefore reduces the measurement

uncertainty. The conductivity plot is shown below; error bars were not calculated for conductivities.

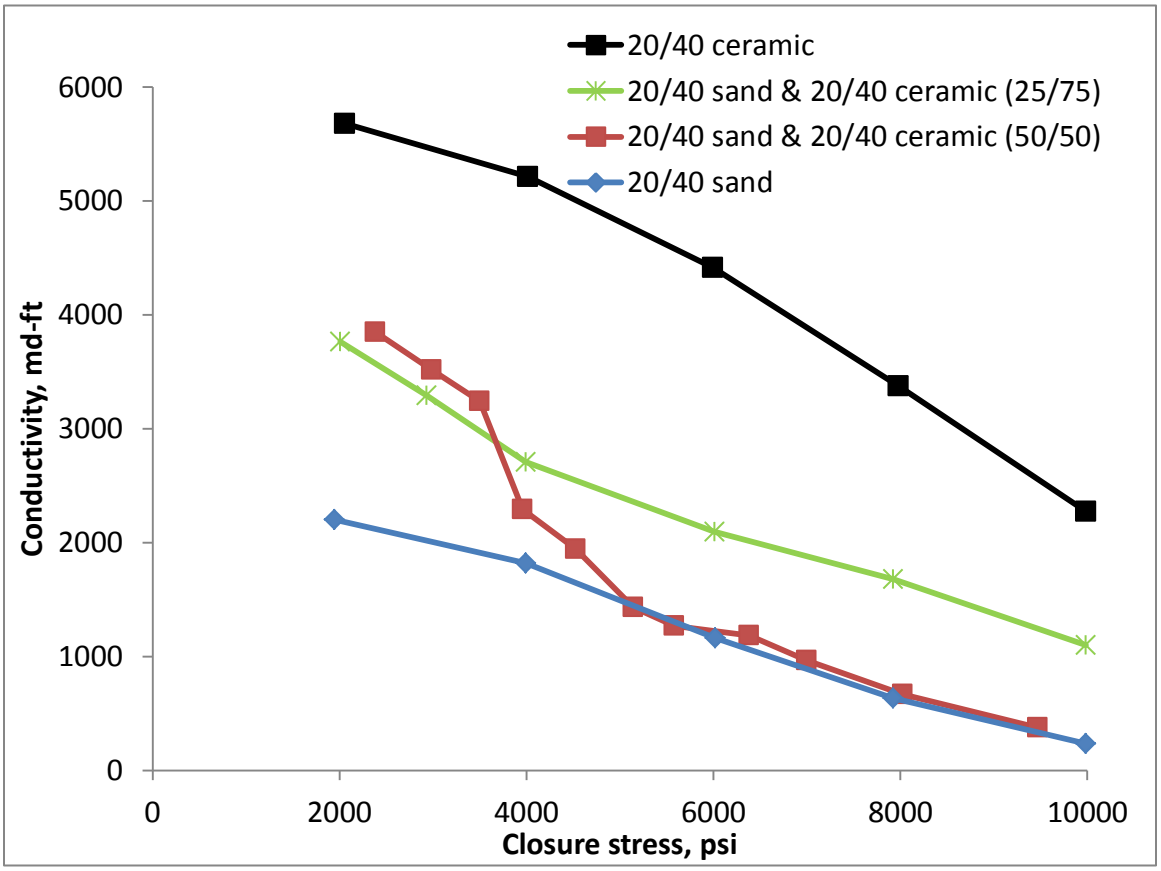

Figure 4.12: Conductivity as function of closure stress for mixtures of 20/40 sand and/or 20/40 ceramic.

Figure 4.13: Mixture of 50% 20/40 sand and 50% 20/40 ceramic after exposure to stress. The marker is included for scale.

Figure 4.14: Cross-sectional view of mixture of 50% 20/40 sand and 50% 20/40 ceramic after exposure to stress. The marker is included for scale.

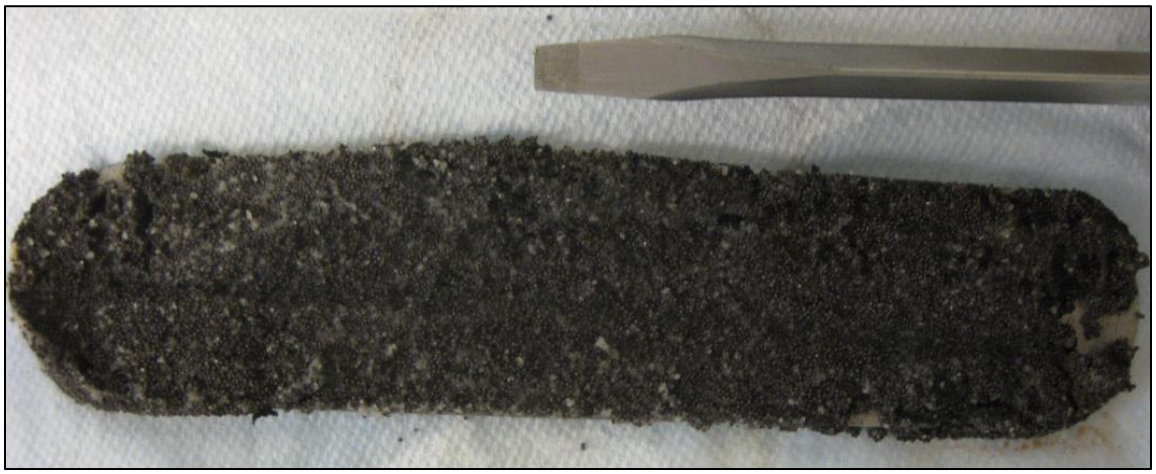

Figure 4.15: Mixture of 25% 20/40 sand and 75% 20/40 ceramic after exposure to stress. The screwdriver is included for scale.

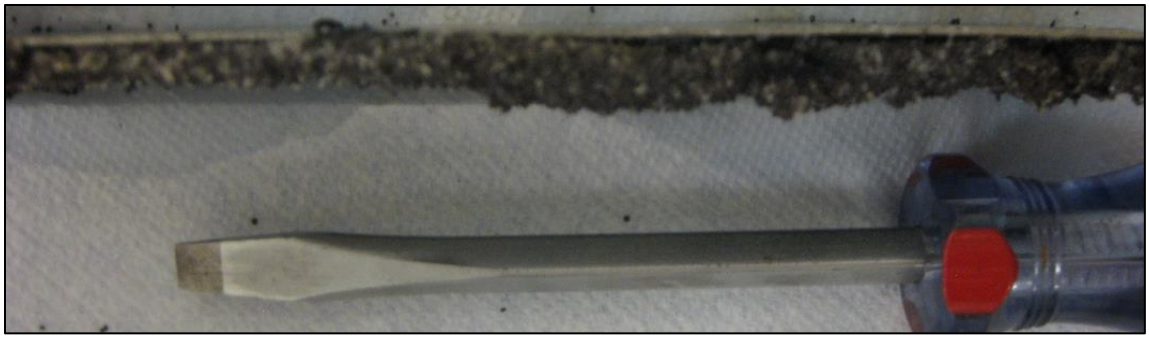

Figure 4.16: Cross-sectional view of mixture of 25% 20/40 sand and 75% 20/40 ceramic after exposure to stress. The screwdriver is included for scale.

20/40 Sand & 40/70 Sand

The results for an equal mixture of 20/40 sand and 40/70 sand are shown below:

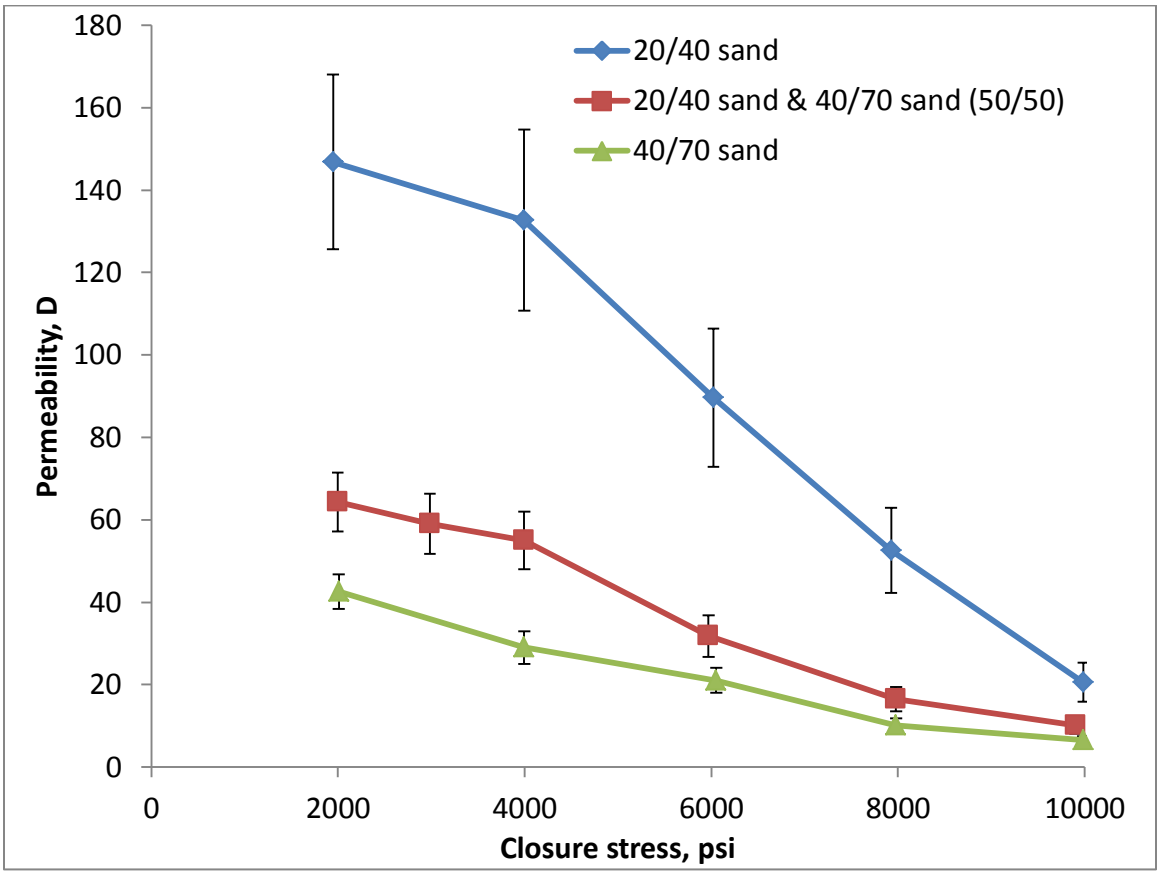

Figure 4.17: Permeability as function of closure stress for samples consisting of 20/40 sand and/or 40/70 sand.

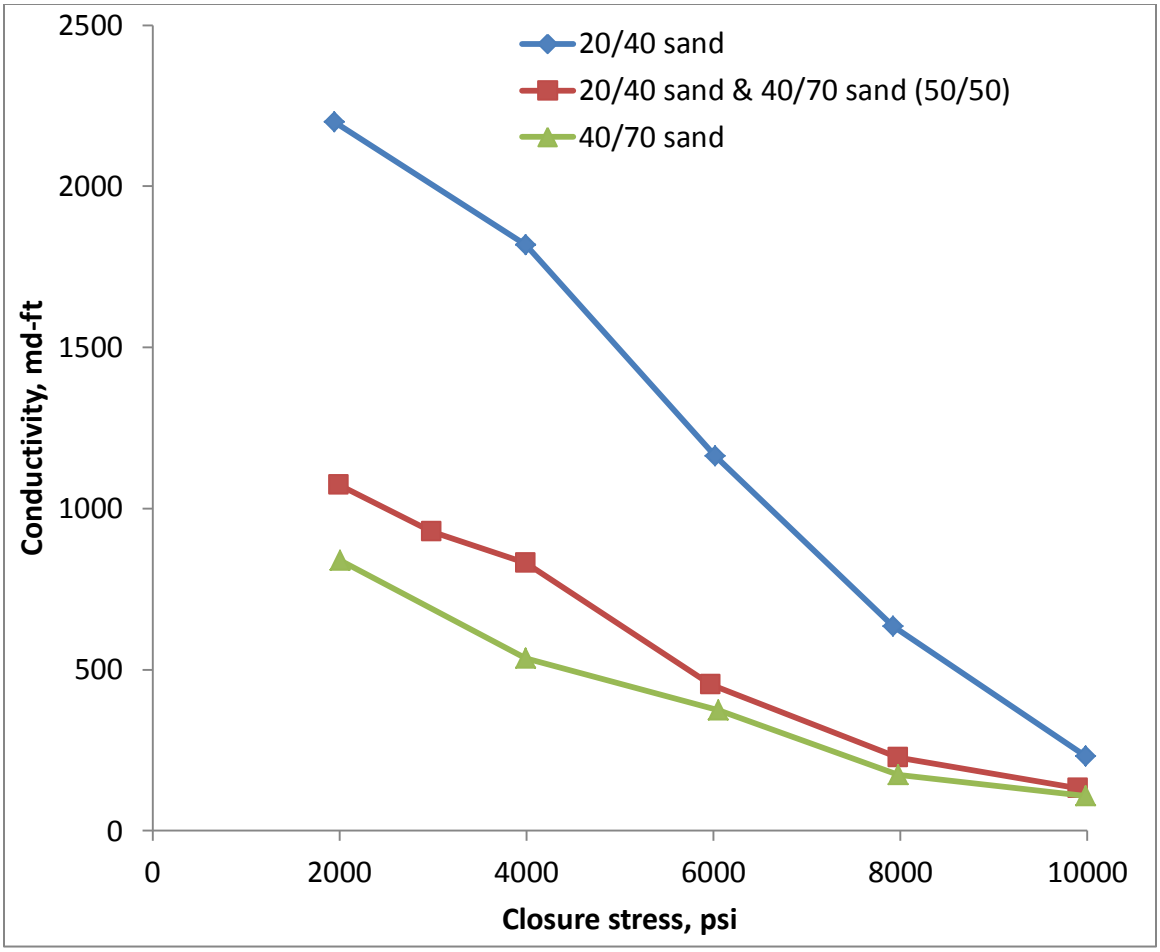

Figure 4.18: Conductivity as function of closure stress for samples consisting of 20/40 sand and/or 40/70 sand.

20/40 Sand & 40/70 Ceramic

The results for mixtures of 20/40 sand and 40/70 ceramic are shown below:

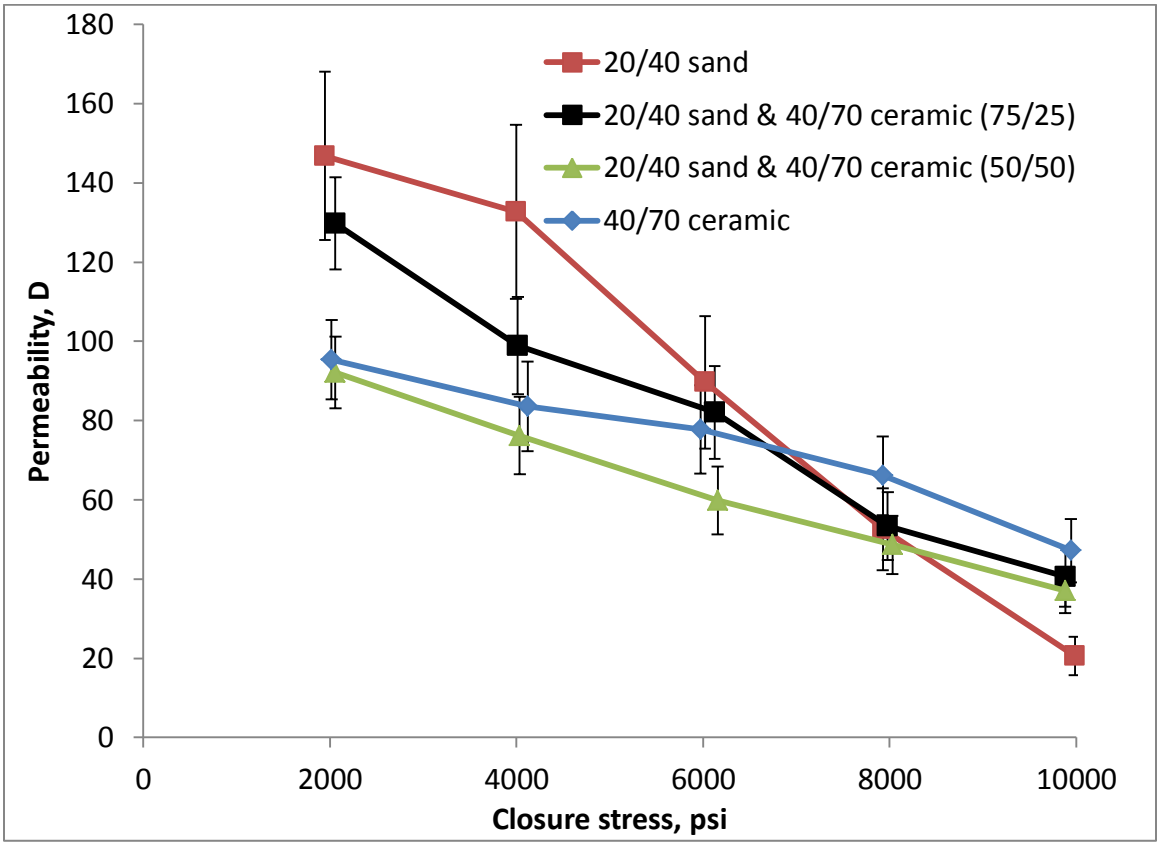

Figure 4.19: Permeability as function of closure stress for samples consisting of 20/40 sand and/or 40/70 ceramic.

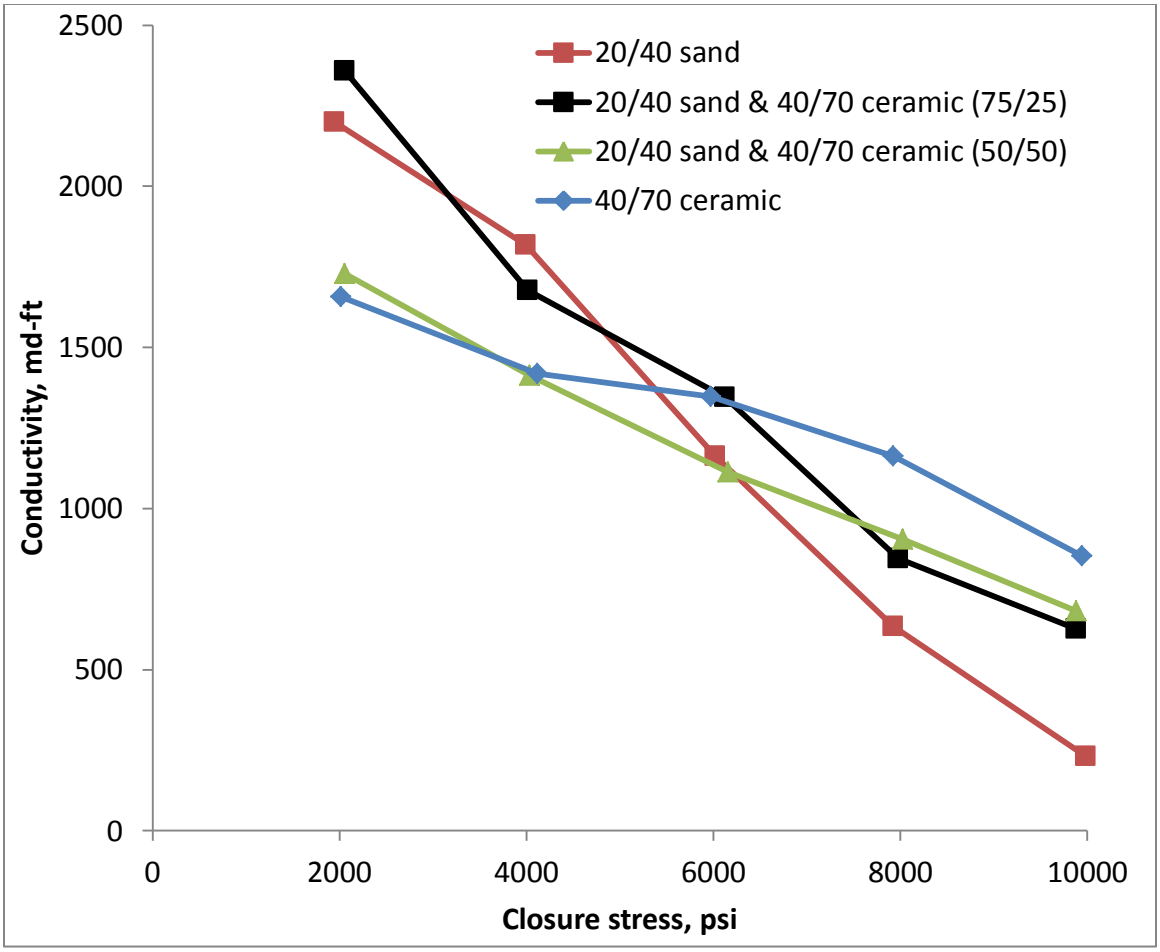

Figure 4.20: Conductivity as a function of closure stress for samples consisting of 20/40 sand and/or 40/70 ceramic.

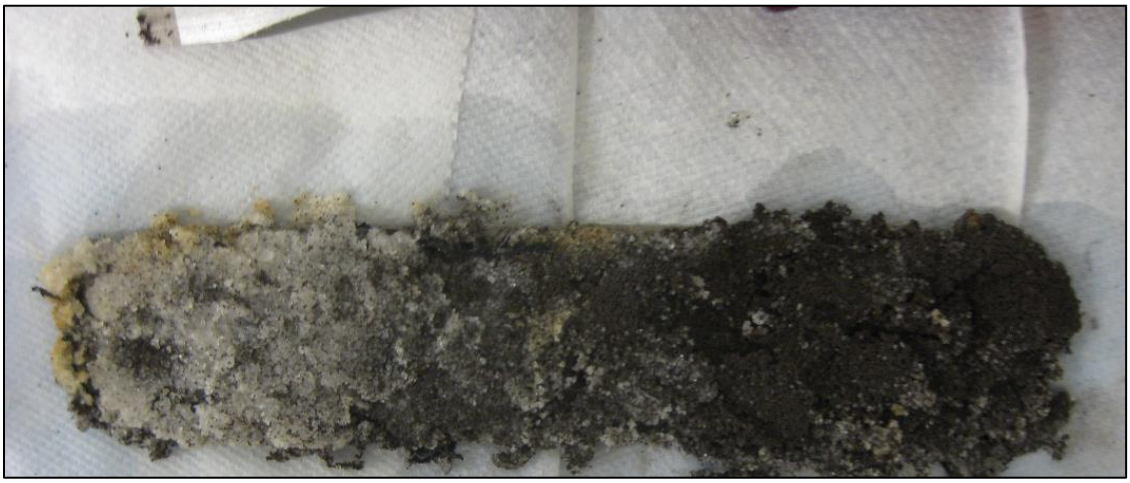

Figure 4.21: Mixture of 50% 20/40 sand and 50% 40/70 ceramic after exposure to stress. The screwdriver is included for scale.

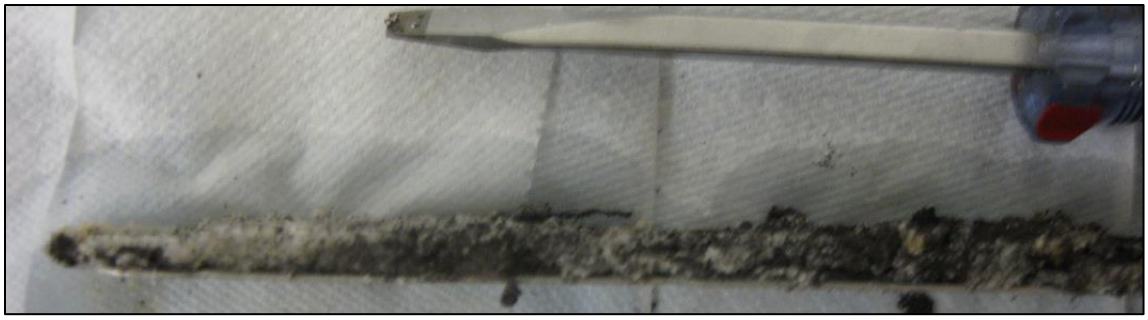

Figure 4.22: Cross-sectional view of mixture of 50% 20/40 sand and 50% 40/70 ceramic after exposure to stress. The screwdriver is included for scale.

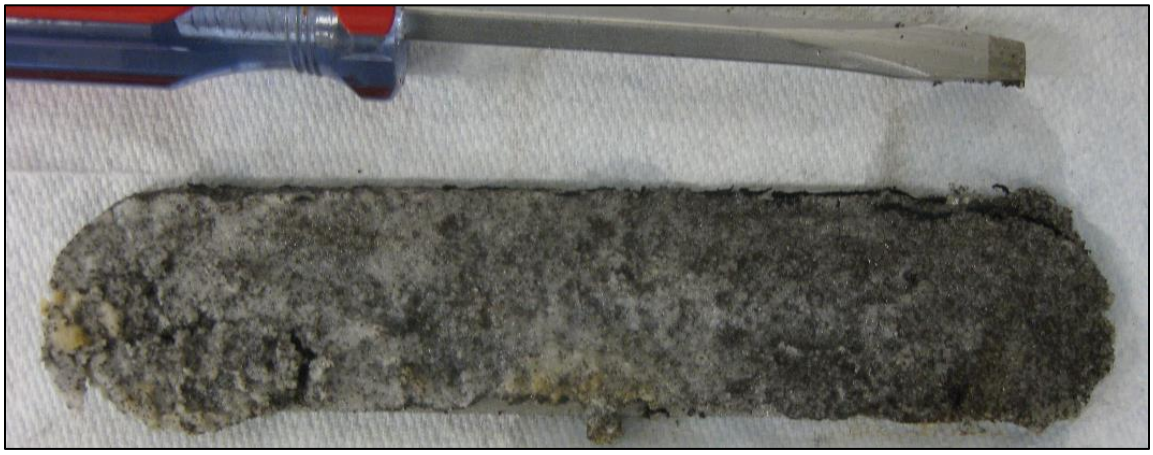

Figure 4.23: Mixture of 75% 20/40 sand and 25% 40/70 ceramic after exposure to stress. The screwdriver is included for scale.

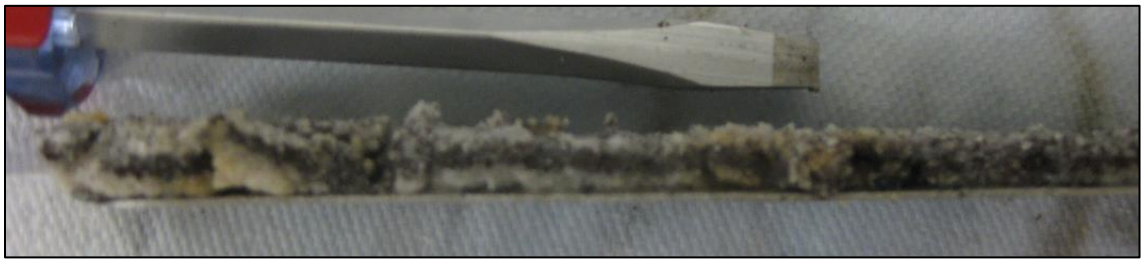

Figure 4.24: Cross-sectional view of mixture of 75% 20/40 sand and 25% 40/70 ceramic after exposure to stress. The screwdriver is included for scale.

20/40 Ceramic & 40/70 Sand

The results for mixtures of 20/40 ceramic and 40/70 sand are shown below:

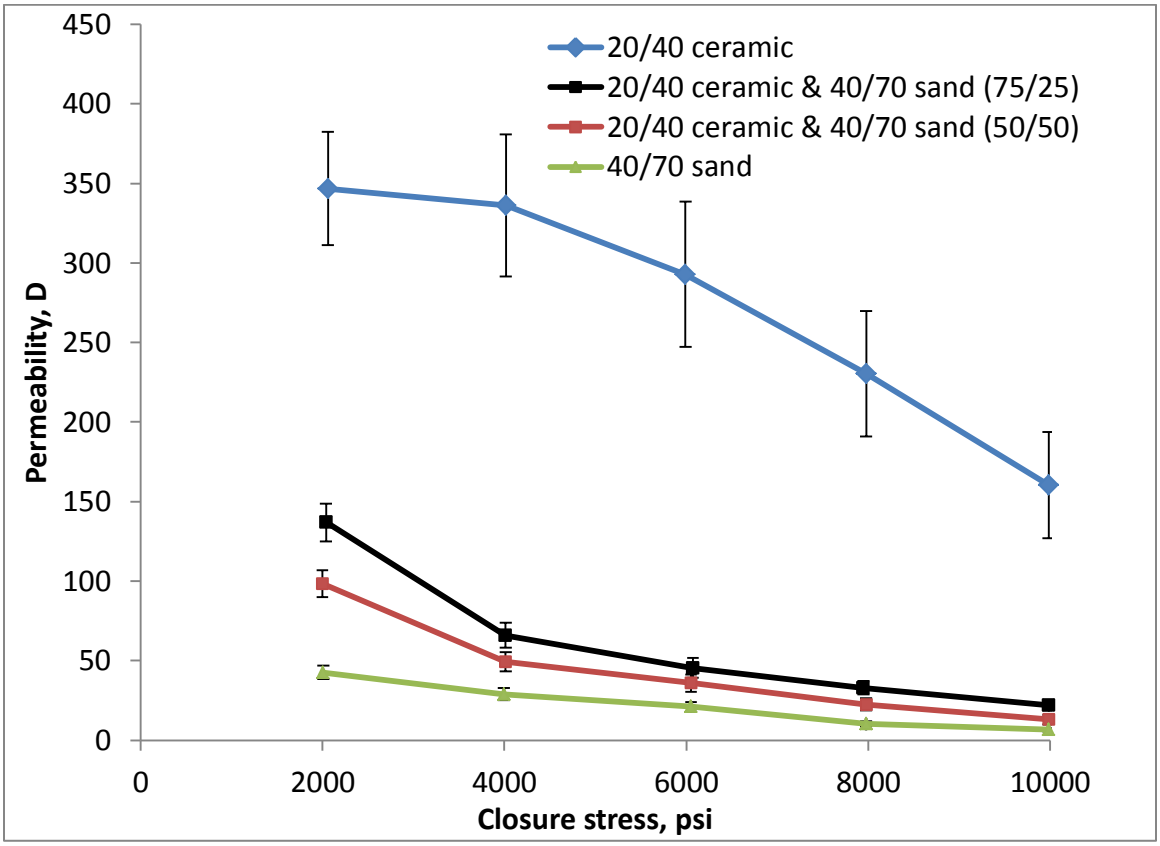

Figure 4.25: Permeability as function of closure stress for samples consisting of 20/40 ceramic and/or 40/70 sand.

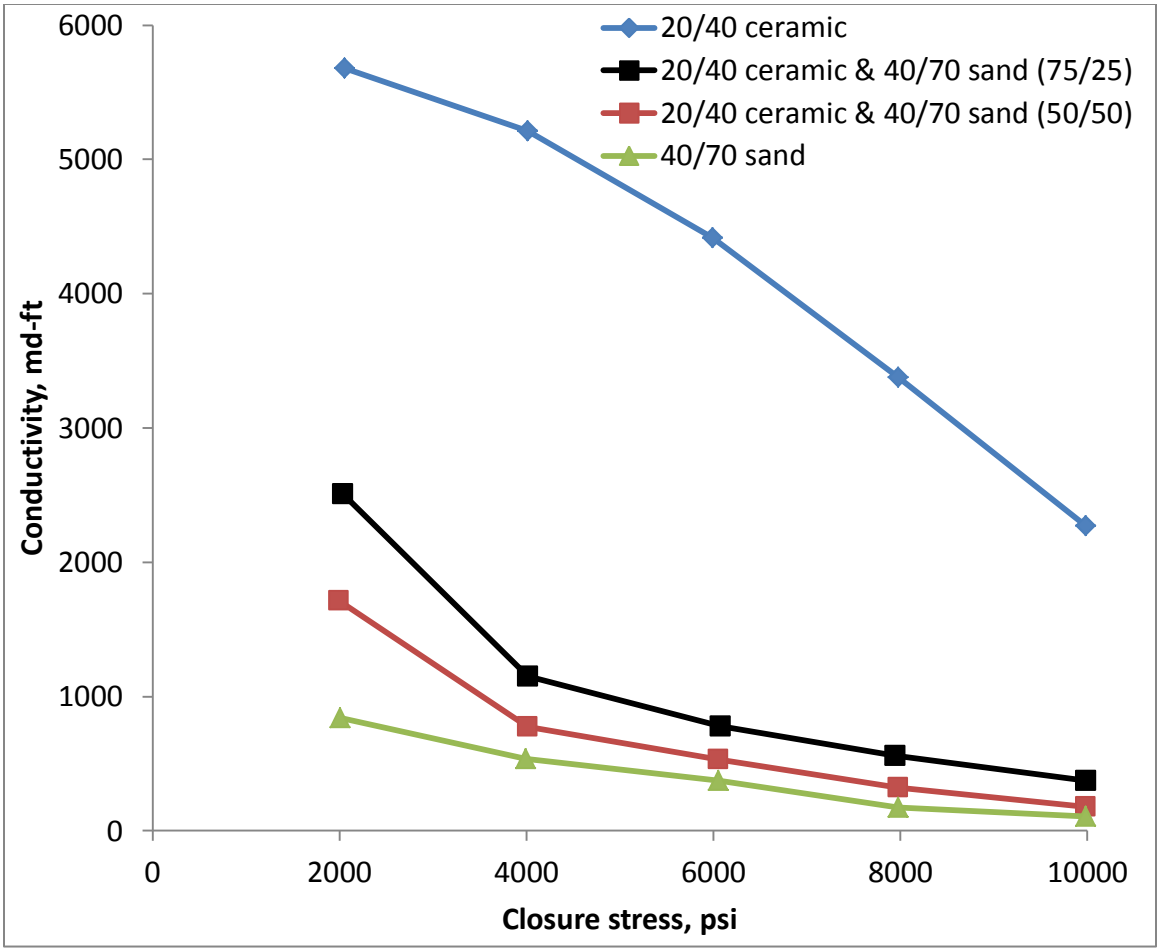

Figure 4.26: Conductivity as function of closure stress for samples consisting of 20/40 ceramic and/or 40/70 sand.

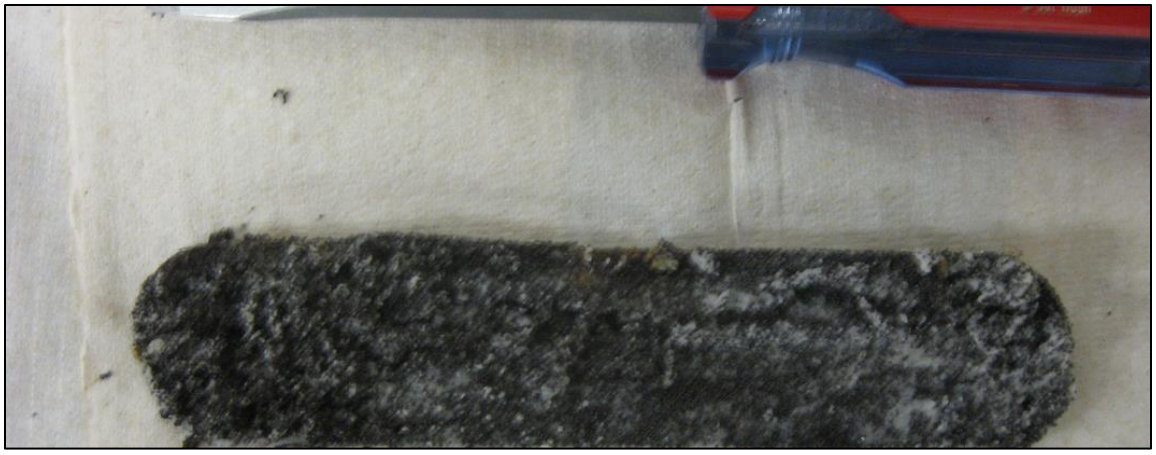

Figure 4.27: Mixture of 50% 20/40 ceramic and 50% 40/70 sand after exposure to stress. The screwdriver is included for scale.

Figure 4.28: Cross-sectional view of mixture of 50% 20/40 ceramic and 50% 40/70 sand after exposure to stress. The screwdriver is included for scale.

Figure 4.29: Mixture of 75% 20/40 ceramic and 25% 40/70 sand after exposure to stress. The screwdriver is included for scale.

Figure 4.30: Cross-sectional view of mixture of 75% 20/40 ceramic and 25% 40/70 sand after exposure to stress. The screwdriver is included for scale.

40/70 Ceramic & 40/70 Sand

The results for mixtures of 40/70 ceramic and 40/70 sand are shown below:

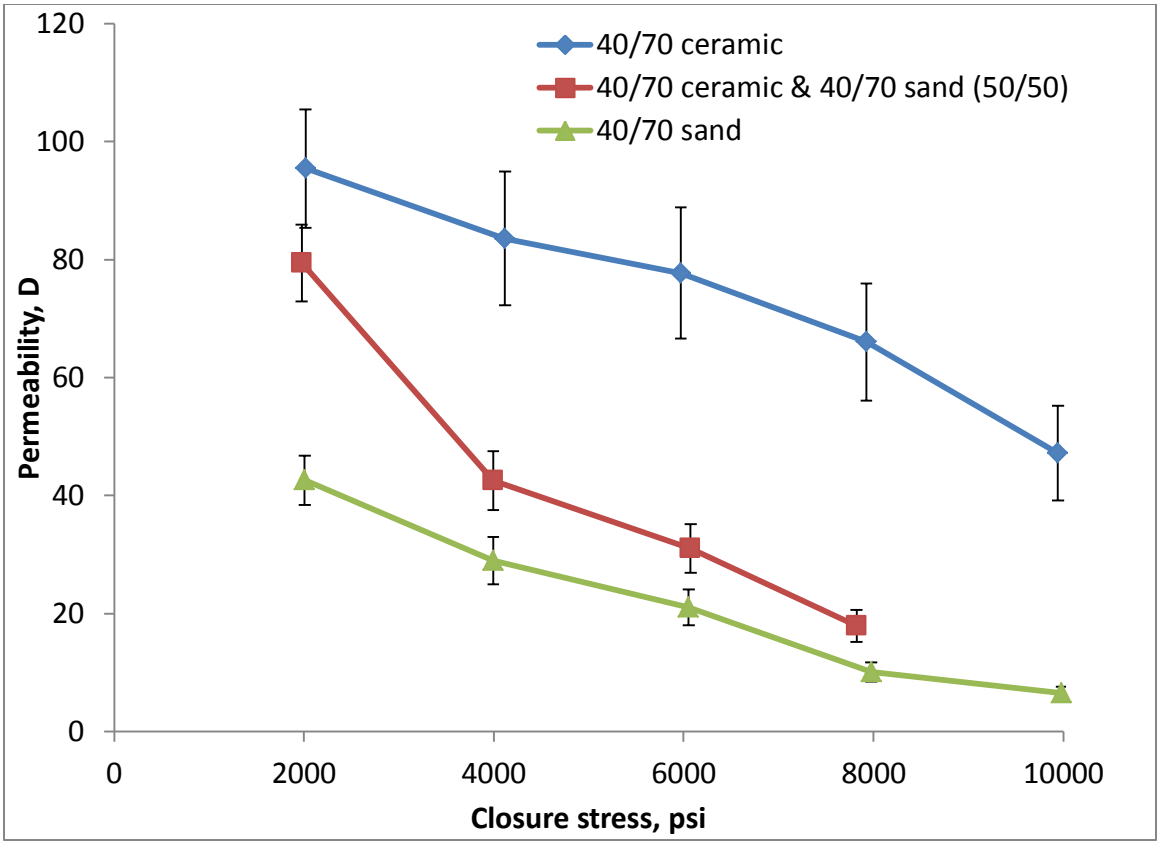

Figure 4.31: Permeability as function of closure stress for samples consisting of 40/70 ceramic and/or 40/70 sand.

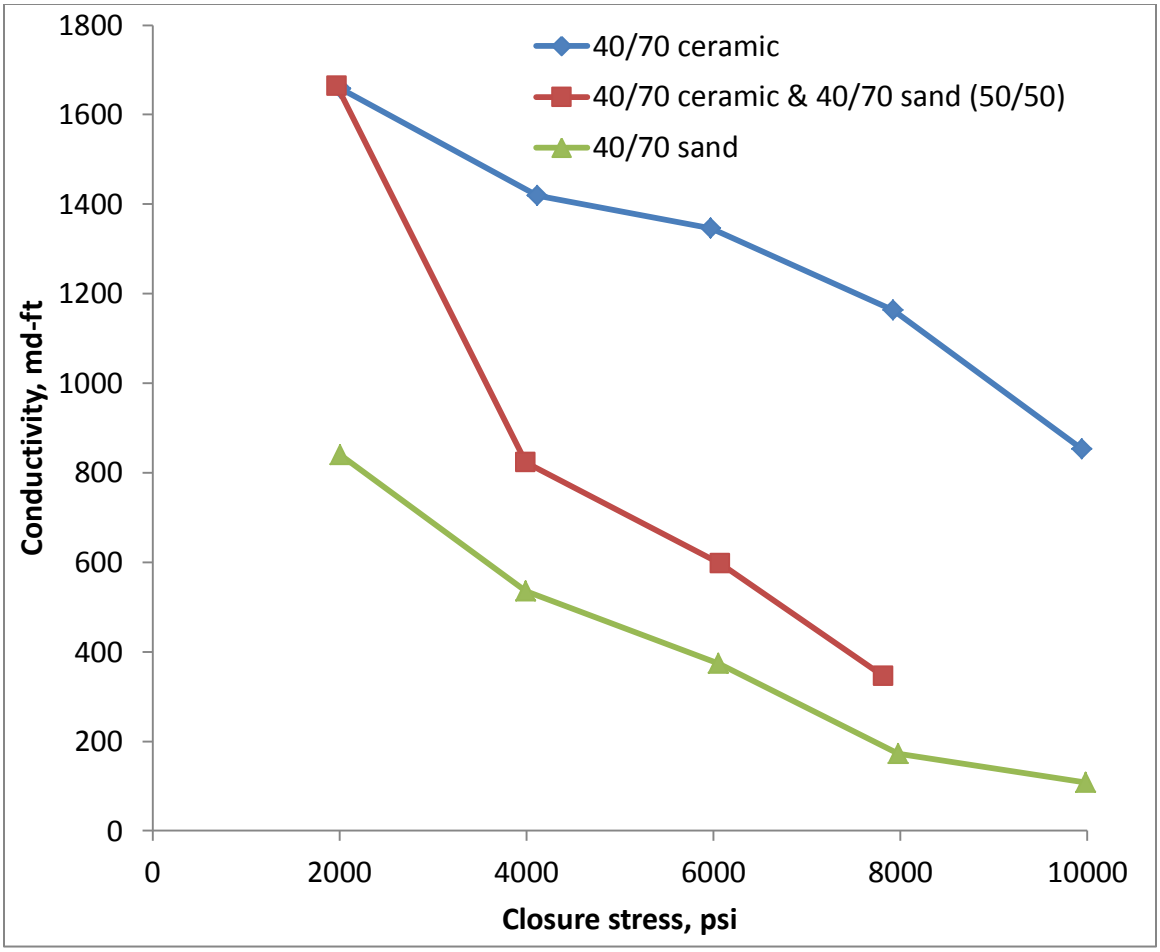

Figure 4.32: Conductivity as function of closure stress for samples consisting of 40/70 ceramic and/or 40/70 sand.

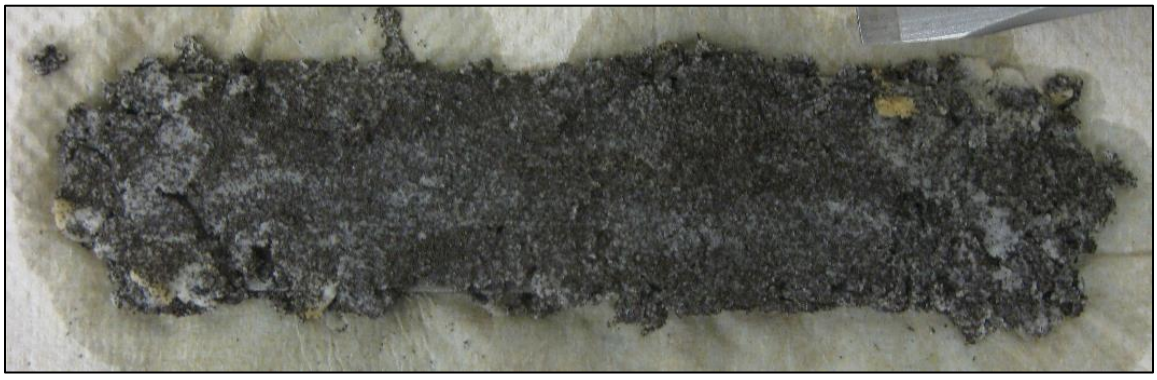

Figure 4.33: Mixture of 50% 40/70 ceramic and 50% 40/70 sand after exposure to stress. The screwdriver is included for scale.

Figure 4.34: Cross-sectional view of mixture of 50% 40/70 ceramic and 50% 40/70 sand after exposure to stress. The screwdriver is included for scale.

20/40 Sand & 20/40 ULW 1

The results for an equivalent weight mixture of 20/40 sand and 20/40 ULW 1 are shown below:

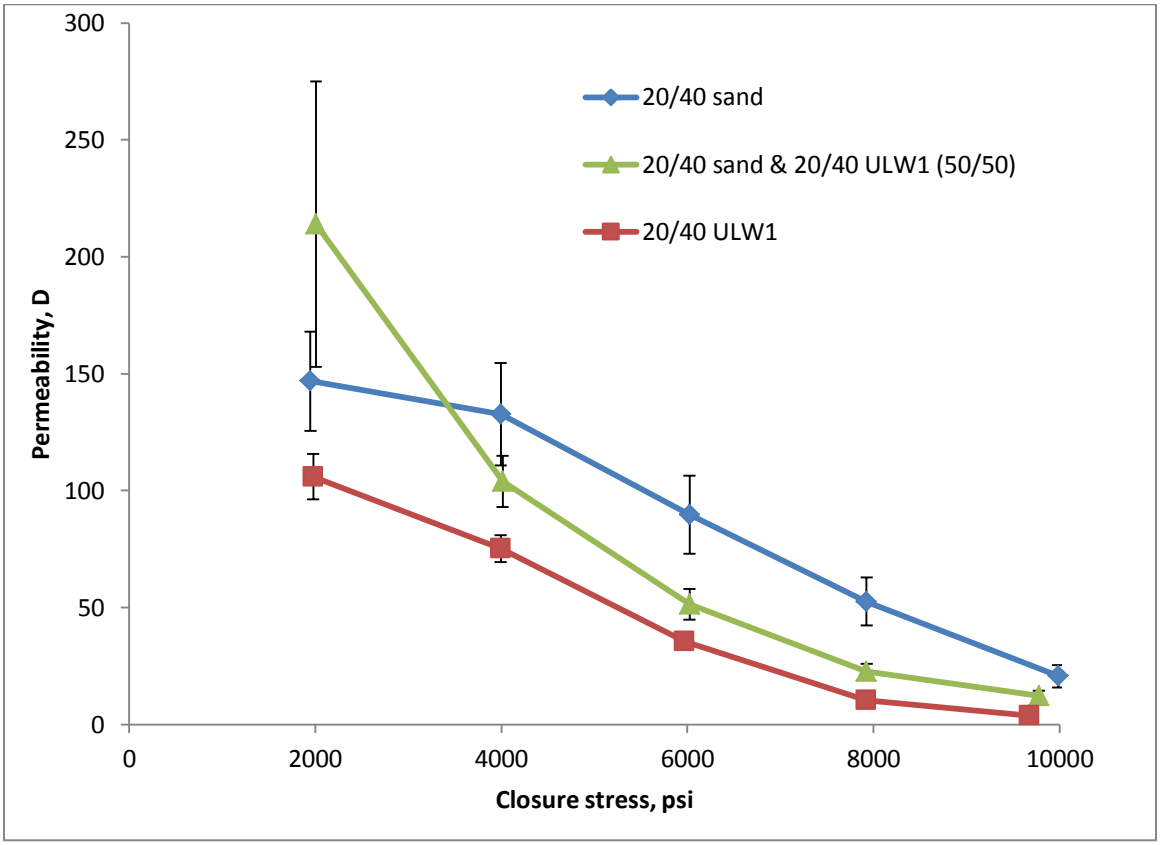

Figure 4.35: Permeability as function of closure stress for samples consisting of 20/40 sand and/or 20/40 ULW 1.

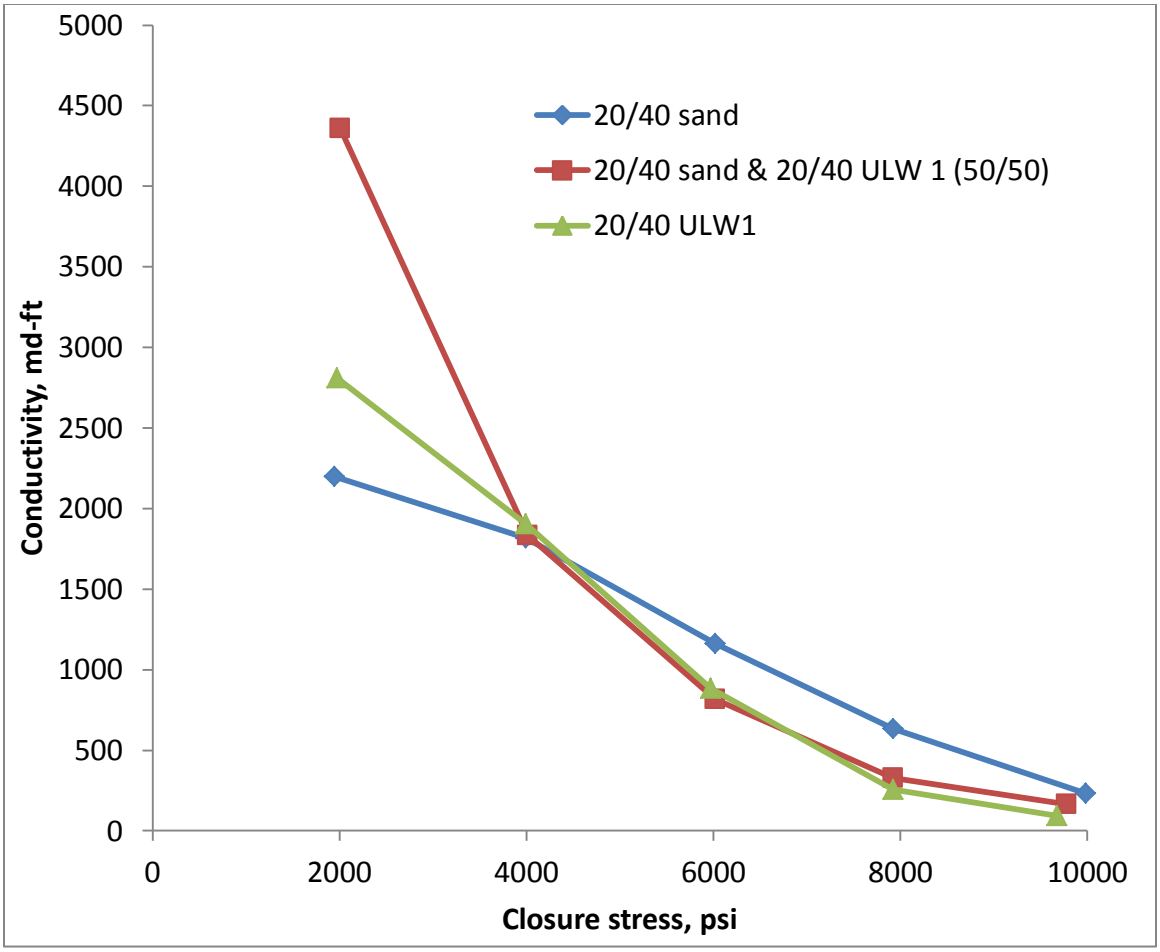

Figure 4.36: Conductivity as function of closure stress for samples consisting of 20/40 sand and/or 20/40 ULW 1.

AREAL CONCENTRATION

As promised in the abstract and introduction, an investigation into the effect of areal concentration was carried out. The idea is that the permeability of the proppant pack will depend upon how many layers of the pack are deposited, for which the areal concentration is a proxy. It is thought that a partial monolayer of proppant is preferential to a full single layer, due to the partial monolayer having much more space in between grains than the full monolayer. Brannon et al. (2004) provide the following pictogram which compares the partial monolayer to the full monolayer:

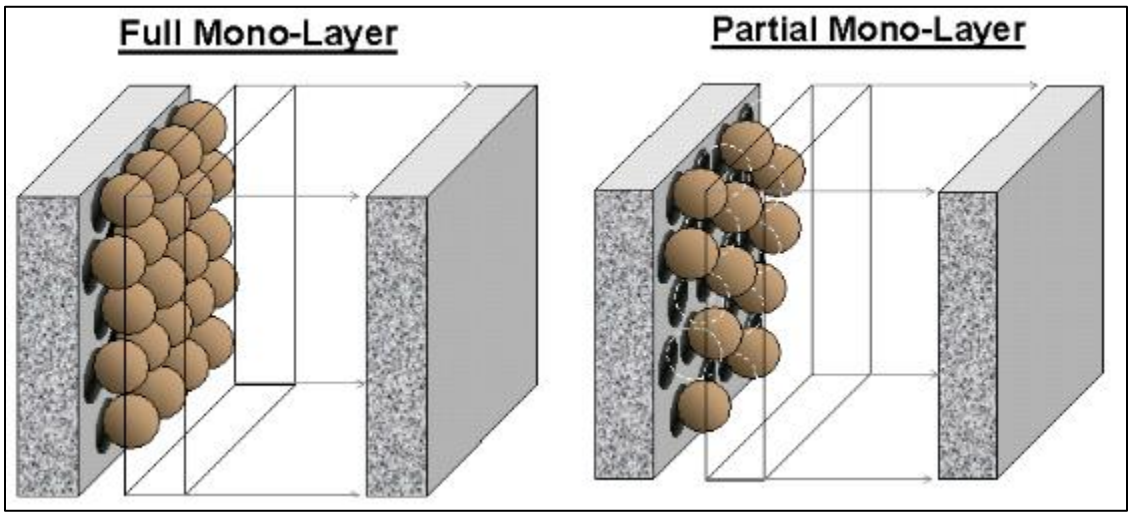

Figure 4.37: Comparison of partial monolayer to full monolayer (Brannon et al. 2004).

It is speculated that the partial monolayer may be even more desirable than a thick, multilayer packing due to its sparse packing. However, it must be remembered that embedment effects are much more pronounced on monolayers, which can result in significant deformation and permeability degradation. Also, it should be expected that after a certain number of layers, there will be no further permeability increase with increasing number of layers, i.e. there is some limiting permeability that cannot be eclipsed by simply adding more proppant. Several experiments were conducted to test the validity of these theories.

The material selected for the areal concentration testing was 40/70 sand. All variables were kept constant except for the areal concentration, which was measured in terms of pounds mass per square foot. Approximately 5,000 psi stress was applied for 24 hours to each different concentration. The results for the 40/70 sand are shown below:

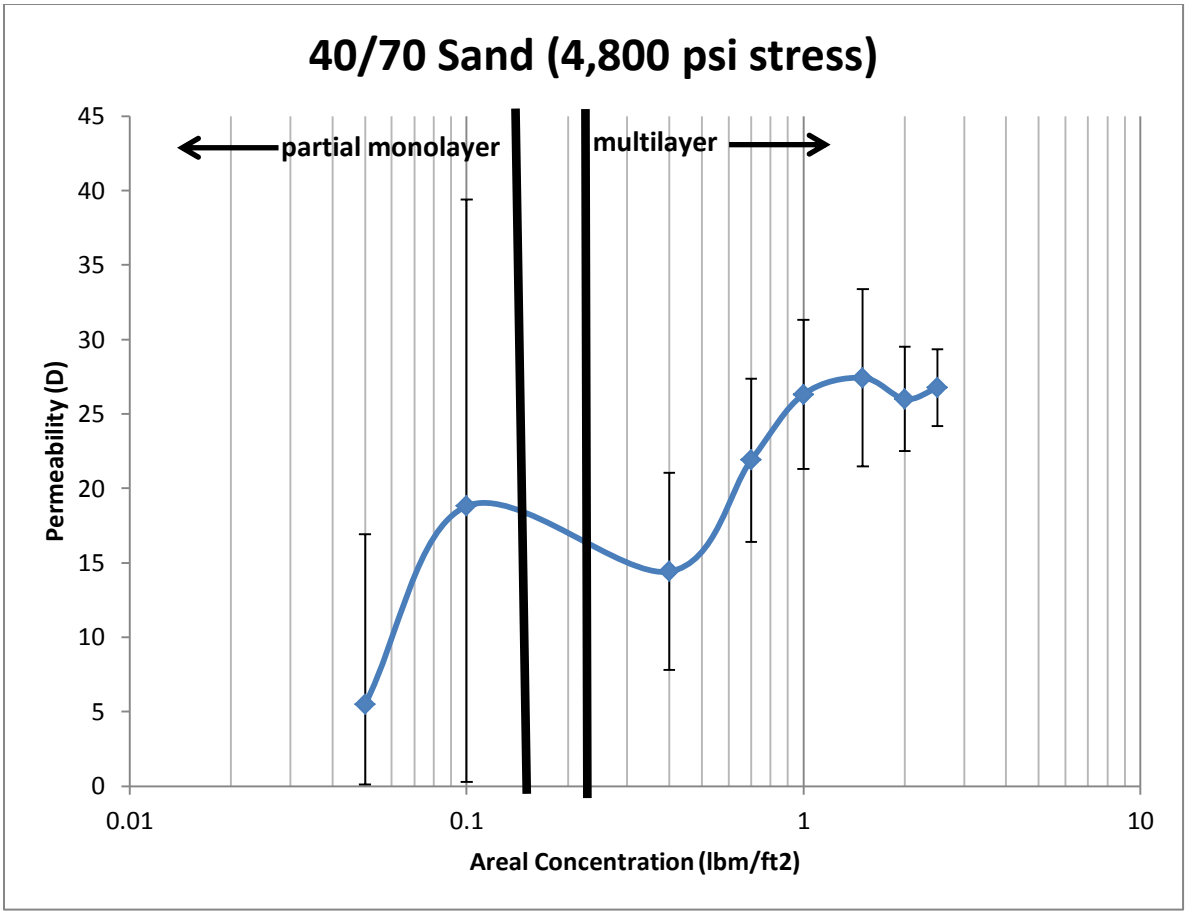

Figure 4.38: Permeability of 40/70 sand as function of areal concentration. Note the logarithmic scale.

The solid black lines delineating the concentrations which constitute a full monolayer and two full monolayers are approximate. The relationship between areal concentration and the number of layers depends on the density and size of the grains, and thus will vary amongst different proppants; the ones shown on Figure 4.38 are valid for 40/70 sand. The data support the notion that a limiting maximum permeability is reached after a certain number of layers is achieved. For 40/70 sand, this critical amount is achieved at a concentration of about 1 lbm/ft^2, which corresponds to approximately 8 to 10 layers. The data also show that the appropriate partial monolayer is indeed preferable to the full

monolayer, but there still must be about 90% coverage; because, as the plot shows, a 50% partial monolayer displays an abysmal permeability, which falls significantly below the full monolayer permeability. Interestingly, the permeability of a 90% partial monolayer is equivalent to the permeability of about 5 full layers of proppant.

REPEATABILITY

The validity of a study in which the conclusions are predicated on experimental results is significantly enhanced if the results are repeatable. As such, an effort was made to duplicate the results of one of the samples. Due to its importance, the mixture of 50% 20/40 sand and 50% 20/40 ceramic was chosen for retesting. The results are shown below:

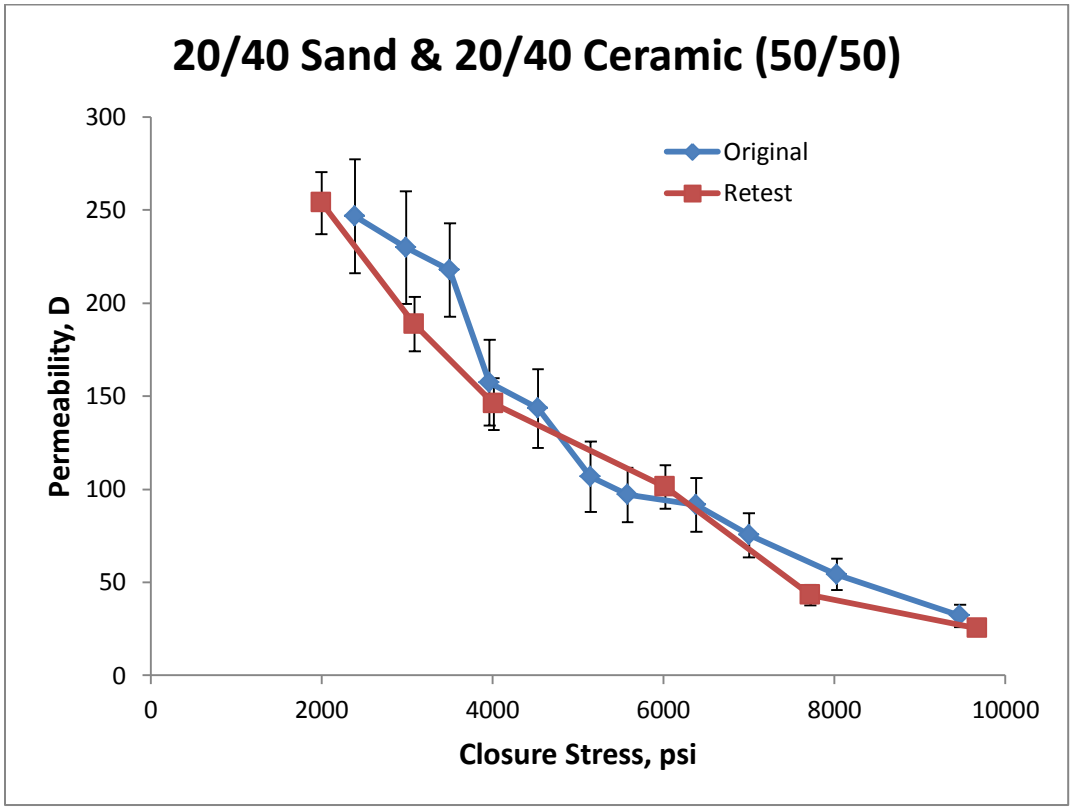

Figure 4.39: Comparison of results for two trials of 50% 20/40 sand and 50% 20/40 ceramic.

The data show that there is some slight disagreement between the original trial and the second trial; however, the two curves are mostly contained within each other's error bars. Deviations can be attributed to normal experimental error and also differences in the porous media themselves; the size distributions of the two mixtures will be slightly different, and the packing arrangement will not be exactly the same, and therefore we should expect that the measured permeability will not be quite the same. So, in the author's estimation, the two results are in satisfactory agreement and the repeatability test is passed.

Chapter 5: Permeability Modeling

The analytical model developed by Panda and Lake (1994) is used in this study to test the validity of the experimental methods and results. The origin of the model (Eq. 2.19) is discussed in Chapter 2 of this thesis, but the equation will be repeated here for convenience:

$$k = \left[\frac{(\gamma\varphi^3 + 3\varphi^2 + 1)^2}{(1+\varphi^2)^2}\right]\frac{\emptyset^3}{72\tau(1-\emptyset)^2}\bar{d}^2 \tag{5.1}$$

where γ is the skewness of the particle size distribution, $\bar{d}$ is the mean particle diameter, and φ is the ratio of the standard deviation of the distribution σ and the mean particle diameter $\bar{d}$, $\sigma/\bar{d}$. This equation requires measurement or knowledge of the grain size distribution, porosity, and tortuosity. This chapter will focus first on the methods that were used to obtain the necessary parameters, and then will show the results of the analytical model for several proppant packings.

METHODOLOGY

The measurement of grain size distribution will be considered first, followed by the measurement of porosity.

Grain Size Distribution

Several techniques exist for measurement of a particle size distribution: sieve analysis, sedimentation procedures, electrical resistance tests, laser diffraction methods, and direct particle by particle examination (Fieller, Flenley, Olbricht 1990). Fieller et al.

correctly point out that measurement of size distributions through sieving does not give any information about the distribution in between sieve sizes, it only provides upper and lower bounds. Moreover, sieving gives the weight fraction distribution instead of the number fraction distribution, the latter being necessary for use in Equation 5.1. Also, if the particles are not perfectly spherical, then irregularly shaped particles can pass through smaller sieves if they are oriented in an opportune manner. Finally, dust-sized particles are difficult to account for, as there is a physical limit to the level of fineness that can be achieved with a sieve. Despite these setbacks, sieve analysis was used in this study for the sake of simplicity and ease of measurement.

Sieves for all of the mesh numbers listed in Table 4.1 were used in characterization of the size distributions. The samples were placed into the stackable sieves, the assembly was agitated to allow settling of the particles, and the weight retained on each sieve was recorded. To convert the weight fraction distribution into the number frequency distribution, it was assumed that the grains were all spherical particles. Using the definition of density and the formula for the volume of a sphere, the number of grains N on a particular sieve can be estimated by:

$$N = \frac{6m}{\pi \rho d^3} \tag{5.2}$$

where m is the total mass, ρ is the density of the grains, and d is the diameter of the grains. However, because the sieve only provides upper and lower boundaries on the diameters of a particular collection of grains, a slight difficulty is introduced in Equation 5.2, in that it is not clear which value to use for d. The most obvious choice to make in

this situation is the median value between the bounding diameters. For example, for particles which were trapped on the 40 mesh sieve, *d* was taken to be 462.5 μm, which is intermediate between the 425 μm associated with the 40 mesh sieve and the 500 μm associated with the 35 mesh sieve. Another complication that arises with this method is that if grains with different densities are involved, they must first be separated from each other before application of Equation 5.2 and then recombined. There are not many practical ways to separate grains with different densities; one method is to immerse the grains in a liquid which has a density intermediate between the two grain densities. In this case, the typical ceramic proppant has a density of approximately 3.24 grams per cubic centimeter and the typical sand grain has a density of approximately 2.65 grams per cubic centimeter. There are some liquids which exhibit densities between 2.65 and 3.24 grams per cubic centimeter, but they are not easily attainable.

At this point, the number of grains within a certain 'bin' is known for a variety of bins. However, this still does not lend itself to direct calculation of the mean, standard deviation, and skewness of the distribution. One way to remedy this is to treat the number fraction of each bin as a probability, and then use statistical techniques or curve-fitting algorithms to fit a suitable probability distribution function (pdf) to the data. Once the parameters of the distribution are determined, then the mean, standard deviation, and skewness can be easily computed. However, this method can be computationally difficult and some size distributions have irregular shapes that are not well approximated by any analytical pdf's. Also, some pdf's, such as the Levy distribution, have undefined skewness, and others, such as the Pareto distribution, have a skewness that is only

defined for certain conditions. Because it is required in Equation 5.1, if the skewness is unknown, the model cannot be used. An alternative way to obtain the mean, standard deviation and skewness from the available data is to simply assume that there is a uniform distribution of grains within a particular bin. This method allows the generation of a series of numbers where each number represents the diameter of a grain. This will not be the true grain size distribution, but it will honor the known data and will approximate the distribution to a satisfactory degree. It is simple to calculate the mean, standard deviation, and skewness of a set of numbers by using the following equations:

$$\mu = \frac{1}{N}\sum_{i=1}^{N} d_i \tag{5.3}$$

$$\sigma = \sqrt{\frac{1}{N}\sum_{i=1}^{N}(d_i - \mu)^2} \tag{5.4}$$

$$\gamma = \frac{N}{(N-1)(N-2)}\sum_{i=1}^{N}\left(\frac{d_i - \mu}{\sigma}\right)^3 \tag{5.5}$$

where μ is the mean, σ is the standard deviation, γ is the skewness, N is the total number of grains, and d_i is the diameter of the individual grain indexed with i. There are alternative ways to calculate the skewness of a distribution, but Equation 5.5 was chosen for usage. The latter method was used in this study so that the difficulties associated with fitting probability distribution functions to single-valued histograms could be avoided. A Matlab function file was created that accepts the weight on each sieve, porosity, tortuosity, and range of meshes, assumes a uniform distribution within bins, and

uses Equations 5.2 – 5.5 to estimate the parameters of the size distribution and finally uses Equation 5.1 to estimate the permeability. A copy of the code is included in Appendix B.

Porosity

The porosity of a given medium is simply the ratio of the void volume to the bulk volume. In this study, the porosity was measured by placing the proppant into a cylindrical holder whose dimensions are known. A piston is then slid into the cylinder, and the length of the cylinder without the piston is subtracted from the length of the cylinder with the piston to obtain the height of the proppant pack. When the height is recorded, the void volume is obtained by removing the piston from the cylinder and pouring water into the packing until there is a slight film of water covering the top of the packing. The bulk volume of the packing is calculated by using the basic equation for the volume of a cylinder, and the porosity is calculated by dividing the void volume by the bulk volume.

RESULTS

Measurements were performed on proppant samples before they were exposed to any stress and after they were exposed to a complete stress cycle starting at 2,000 psi and ending at 10,000 psi. Because of the difficulty of separating the ceramic grains from the sand grains, no size distribution measurements were performed on these mixtures after exposure to stress. The permeability value for the crushed proppants predicted by the analytical model is compared to the permeability measured by the techniques described in Chapter 3. The analytical prediction for the non-crushed proppants is compared to the measured permeability at 2,000 psi closure stress because no permeability measurements were made in the absence of stress, due to leakage issues.

Generally, it is not possible to directly measure the tortuosity of a porous medium. According to Panda and Lake (1994), the tortuosity for high-permeability media usually exhibits a value between 2 and 3. In the present work, the tortuosity is tuned, subject to the bounding values 2 and 3, to provide the closest match between the analytical prediction and the experimental measurement as possible.

20/40 Ceramic

The weight fraction and number frequency distribution for the 20/40 ceramic packing before and after exposure to stress is shown below:

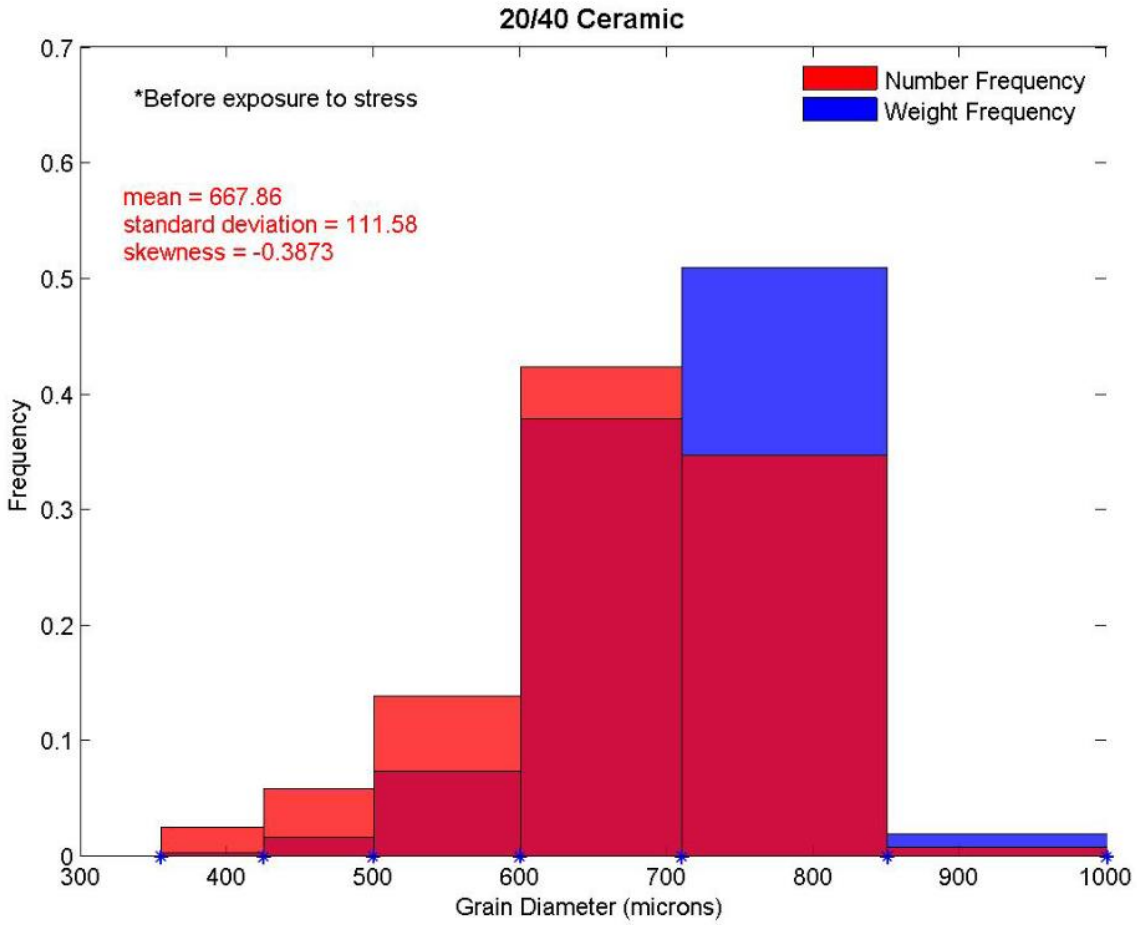

Figure 5.1: Number and weight frequency distributions of 20/40 ceramic before exposure to stress.

In Figure 5.1, the dark shade of red represents overlap between the two distributions. The number frequency distribution tends to the left of its associated weight frequency distribution. The parameters of the distribution shown in the plot are color coded, so in this case they refer to the number frequency distribution.

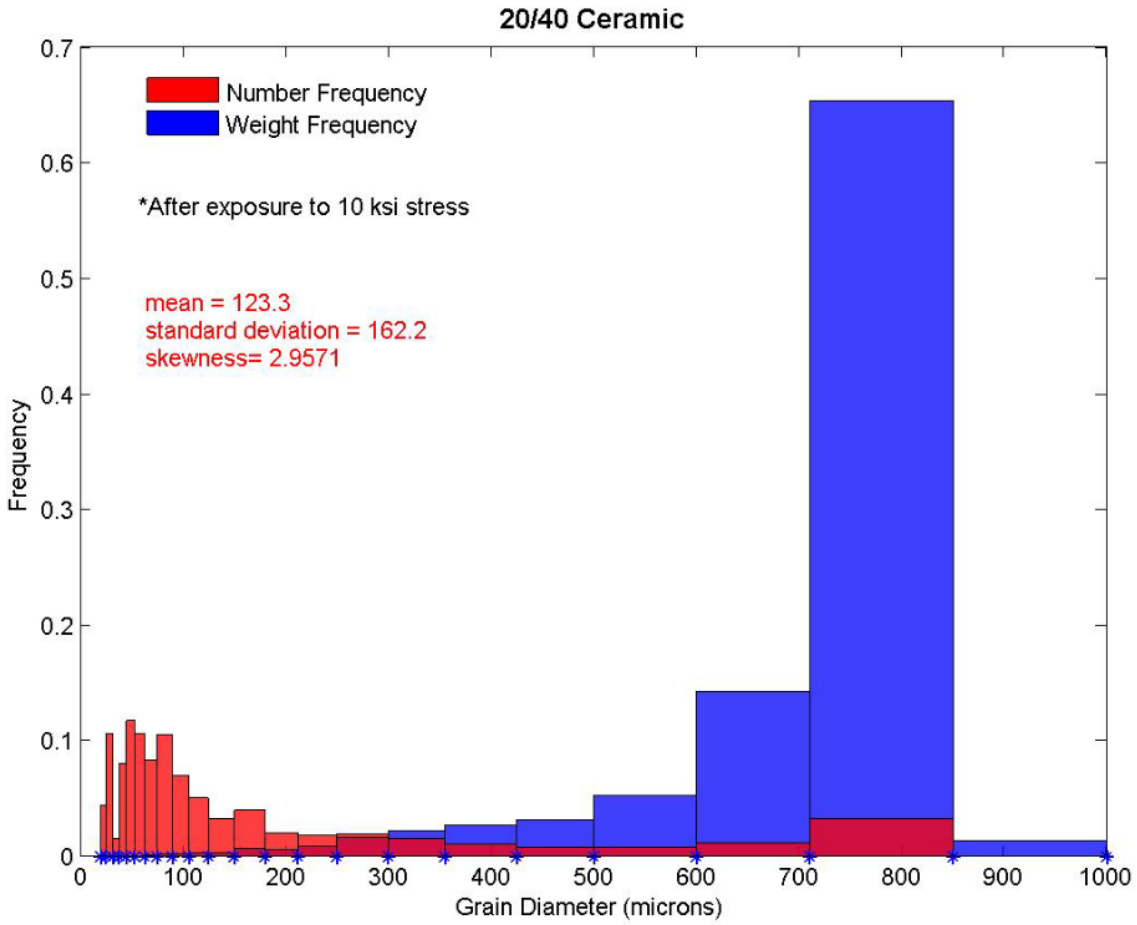

Figure 5.2: Number and weight frequency distributions of 20/40 ceramic after exposure to stress.

After exposure to stress, the number frequency distribution is drastically different from its associated weight fraction distribution. As Figure 5.2 shows, there is considerably less overlap amongst the two distributions compared to the pre-stressed data.

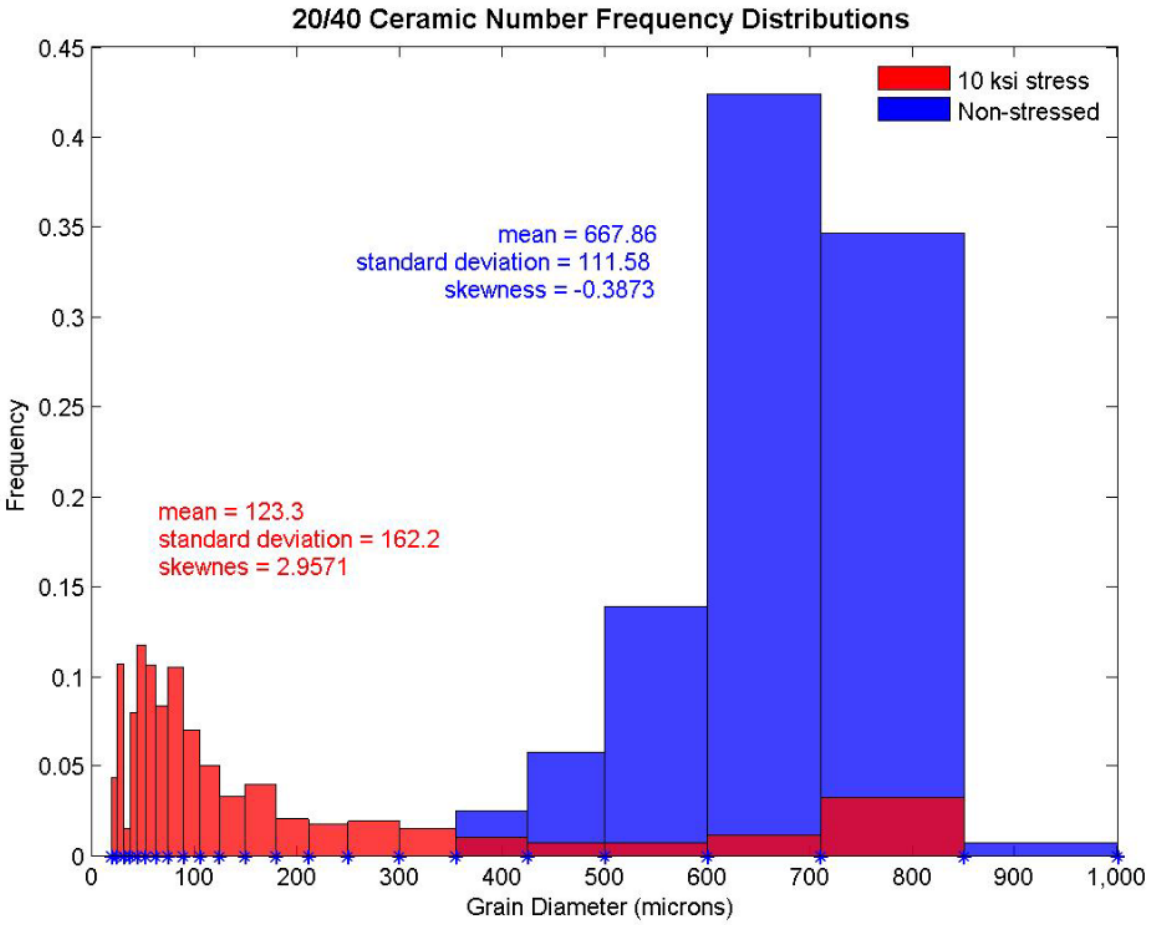

Figure 5.3: Number frequency distributions of 20/40 ceramic before and after exposure to stress.

In Figure 5.3, the number frequency distributions of 20/40 ceramic are compared to each other; the relevant size distribution parameters are color coded. Not surprisingly, there is a drastic difference in the particle size distributions of the stressed and non-stressed samples.

Since no direct permeability measurements were made on samples without applied stress, comparison of the non-stressed analytical prediction with the stressed measurements must suffice. It stands to reason that the pack should have the highest

permeability in its unstressed state, and so the analytical prediction should be higher than the measurements. The permeability was calculated assuming tortuosity values of 2 and 3, and both results are compared with the measurements of the stressed packing. Figure 5.5 shows the results of the analytical predictions for a tortuosity value of 2 and a tortuosity value 3 compared with the measured values.

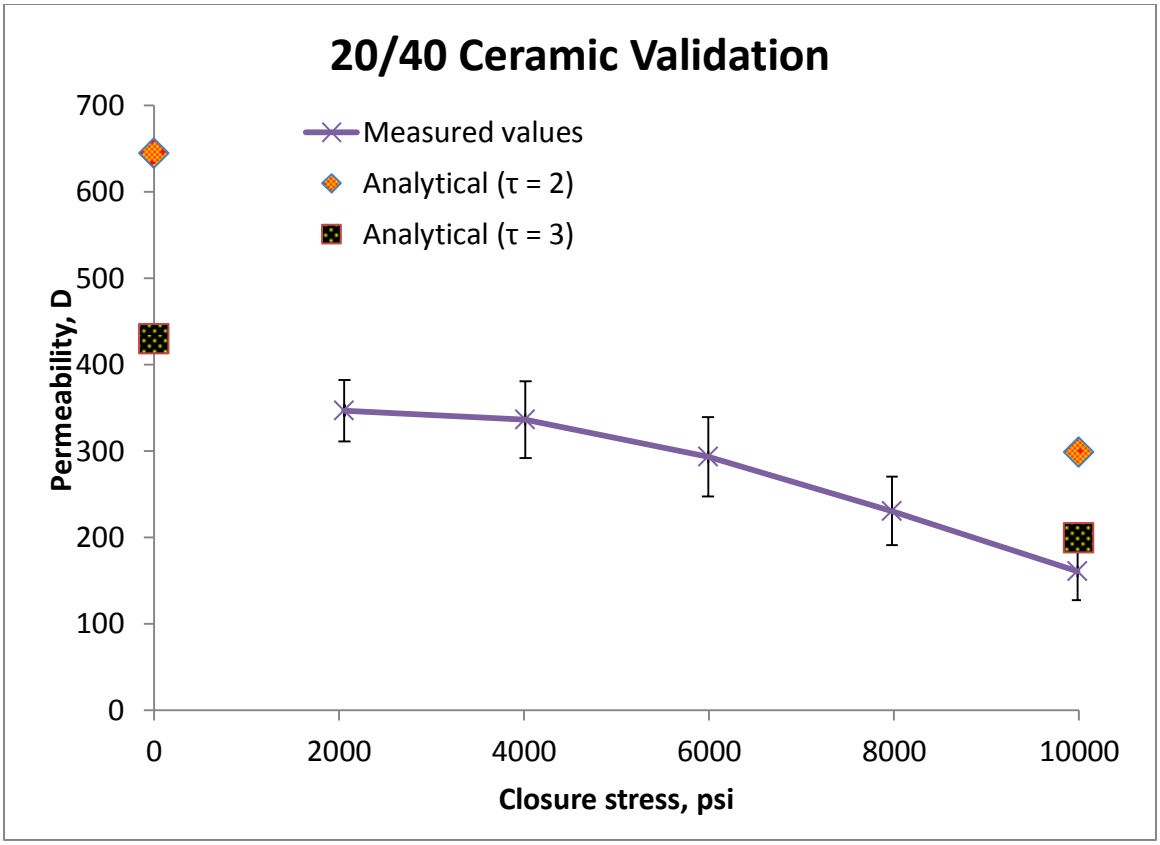

Figure 5.4: Comparison of analytical predictions with measured values for 20/40 ceramic.

In the unstressed case, the analytical predictions using both values of tortuosity are higher than the measured values, as expected. The analytical prediction agrees quite well with the prevailing trend if the tortuosity is set equal to 3. At 10,000 psi applied stress, the analytical predictions agree well with the measured value.

40/70 Ceramic

The weight and number frequency distribution for the 40/70 ceramic packing before and after exposure to stress is shown below:

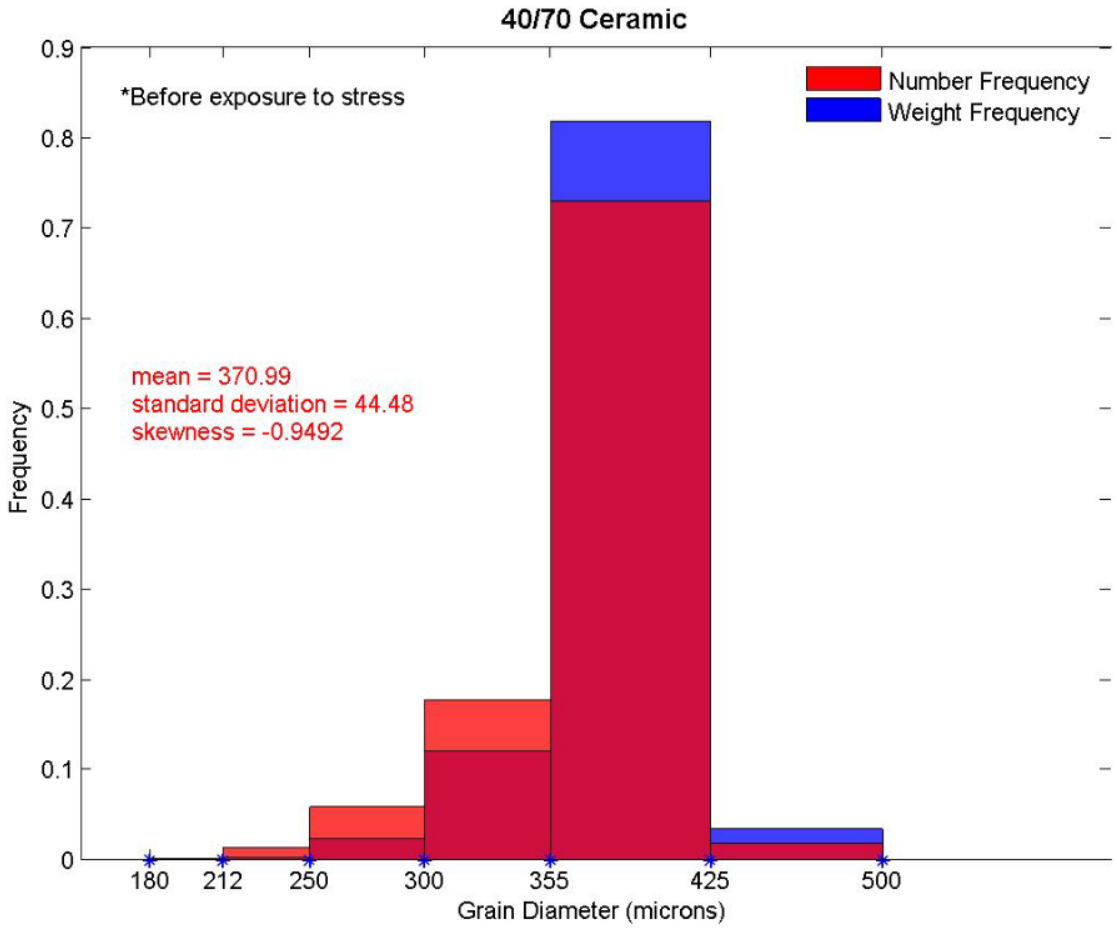

Figure 5.5: Number and weight frequency distributions of 40/70 ceramic before exposure to stress.

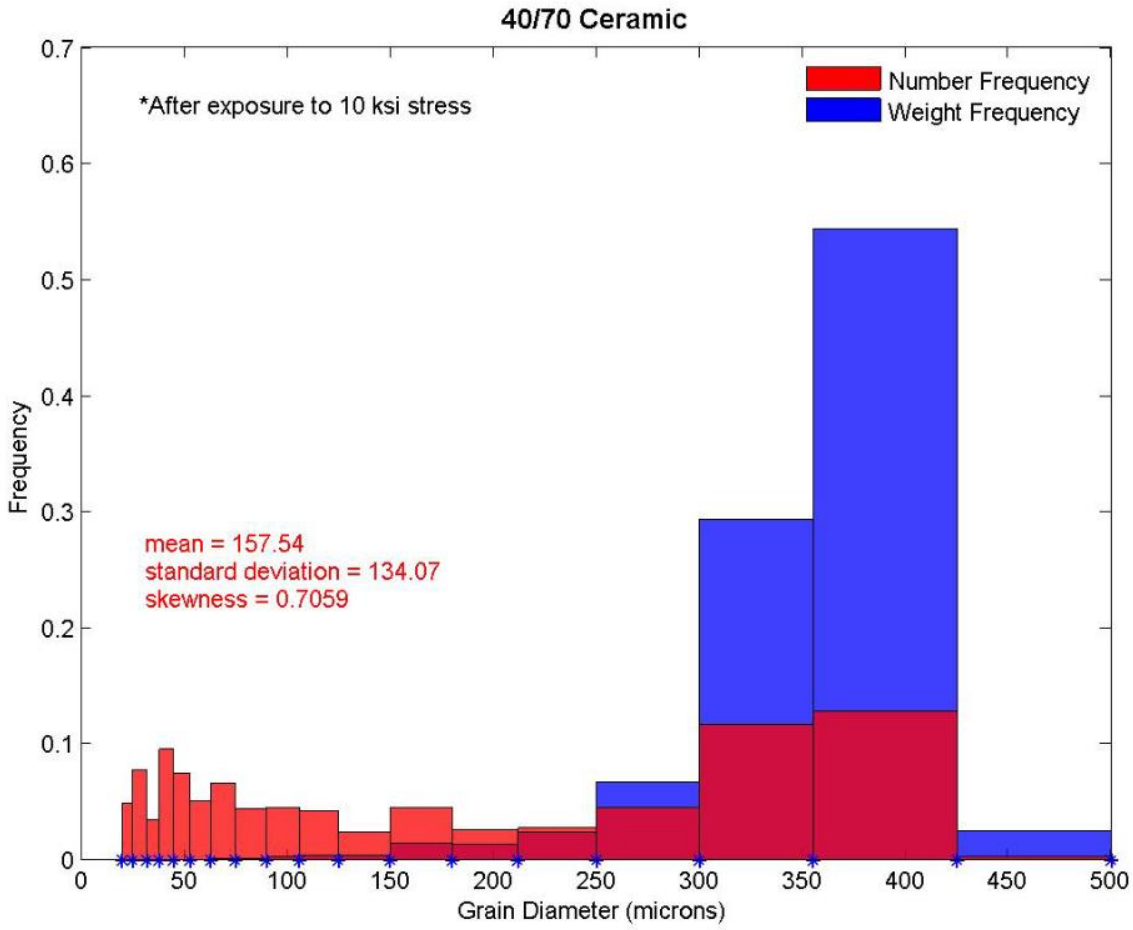

Figure 5.6: Number and weight frequency distributions of 40/70 ceramic after exposure to stress.

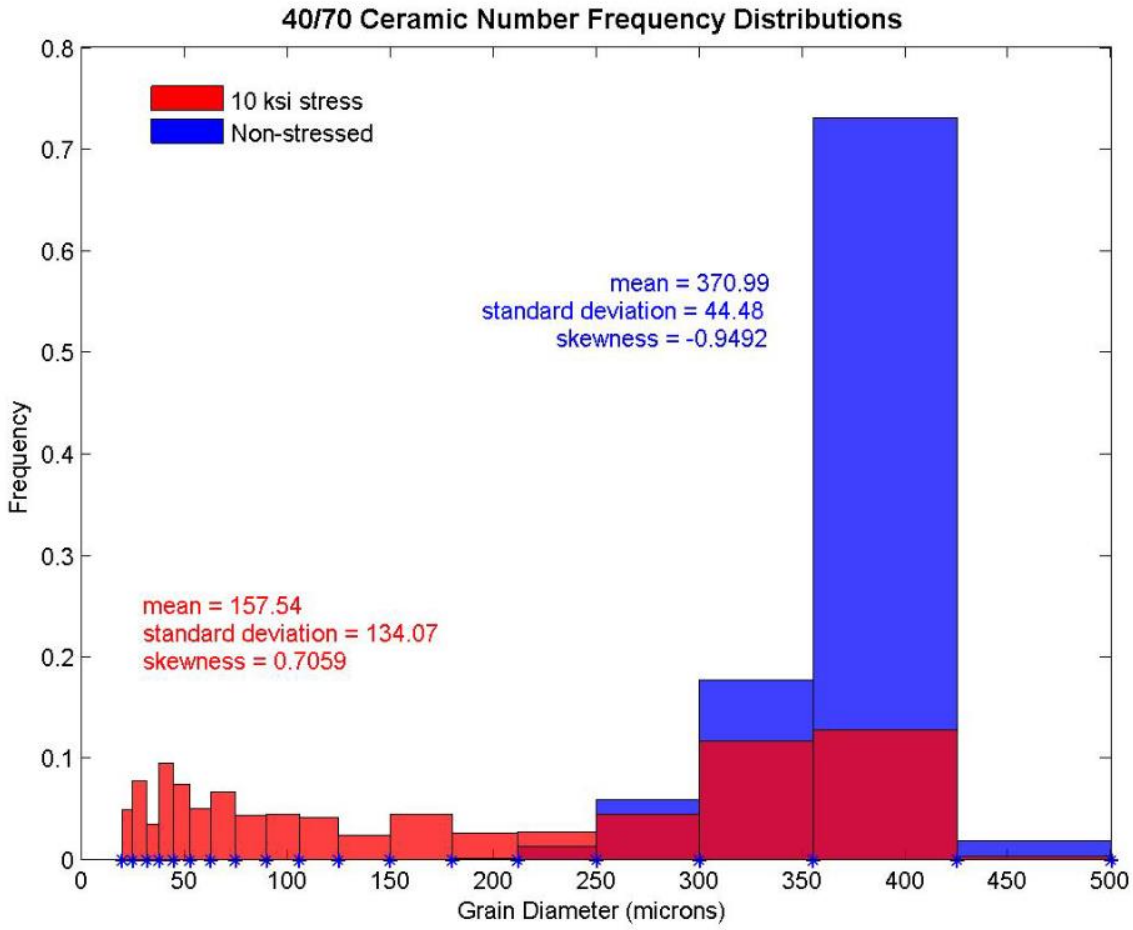

Figure 5.7: Number frequency distributions of 40/70 ceramic before and after exposure to stress.

Figure 5.8 shows the comparison of the analytical results and the experimental measurements:

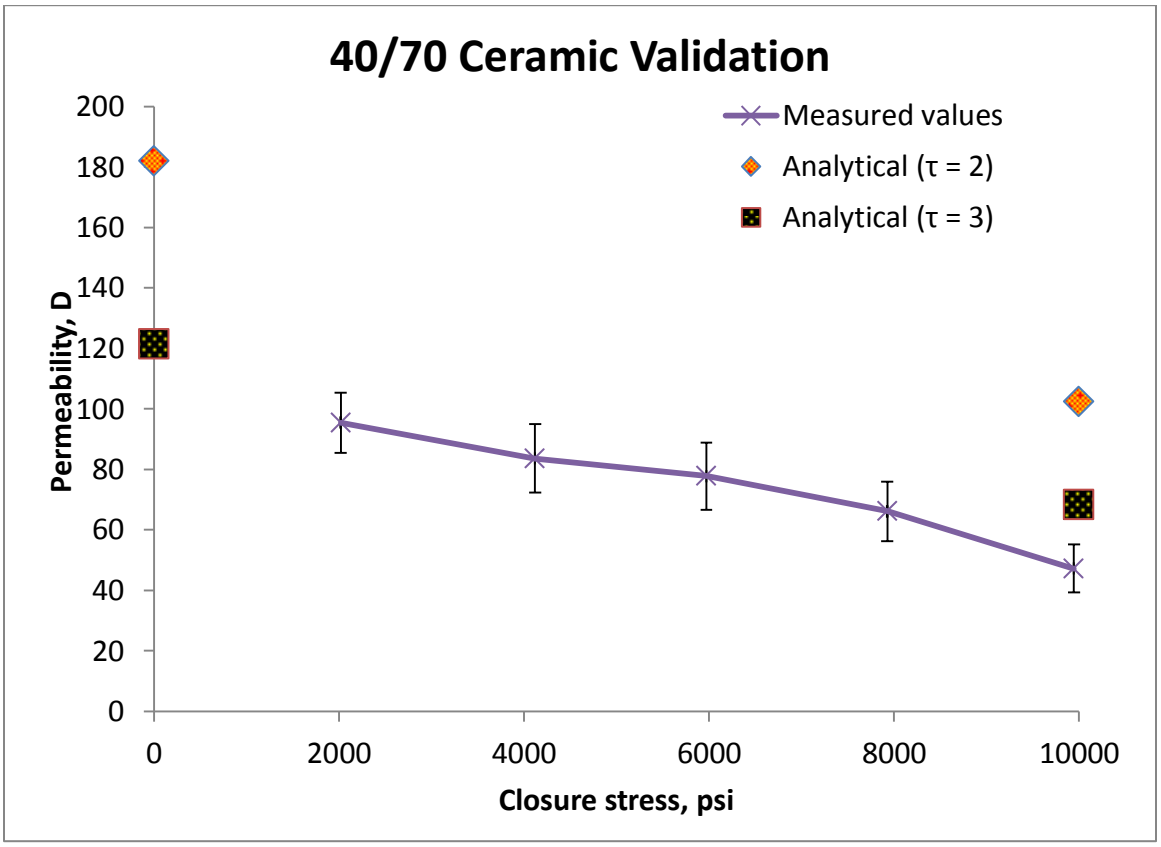

Figure 5.8: Comparison of analytical predictions with measured values for 40/70 ceramic.

The analytical values slightly overestimate the permeability, but the results are generally in good agreement with the experimental values.

20/40 Sand

The weight fraction and number frequency distribution for the 20/40 sand packing before and after exposure to stress is shown below. This packing was measured at a level of 4,800 psi stress instead of the usual 10,000 psi stress.

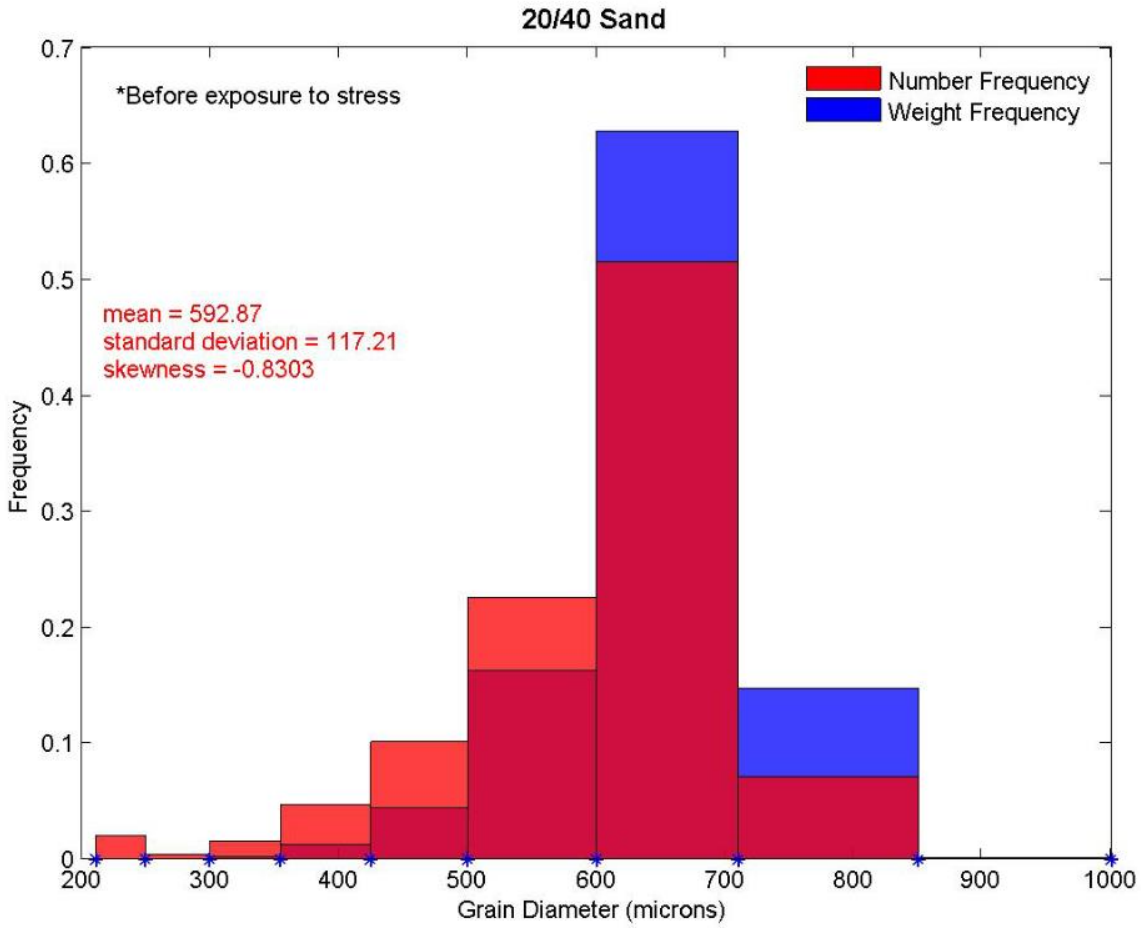

Figure 5.9: Number and weight frequency distributions of 20/40 sand before exposure to stress.

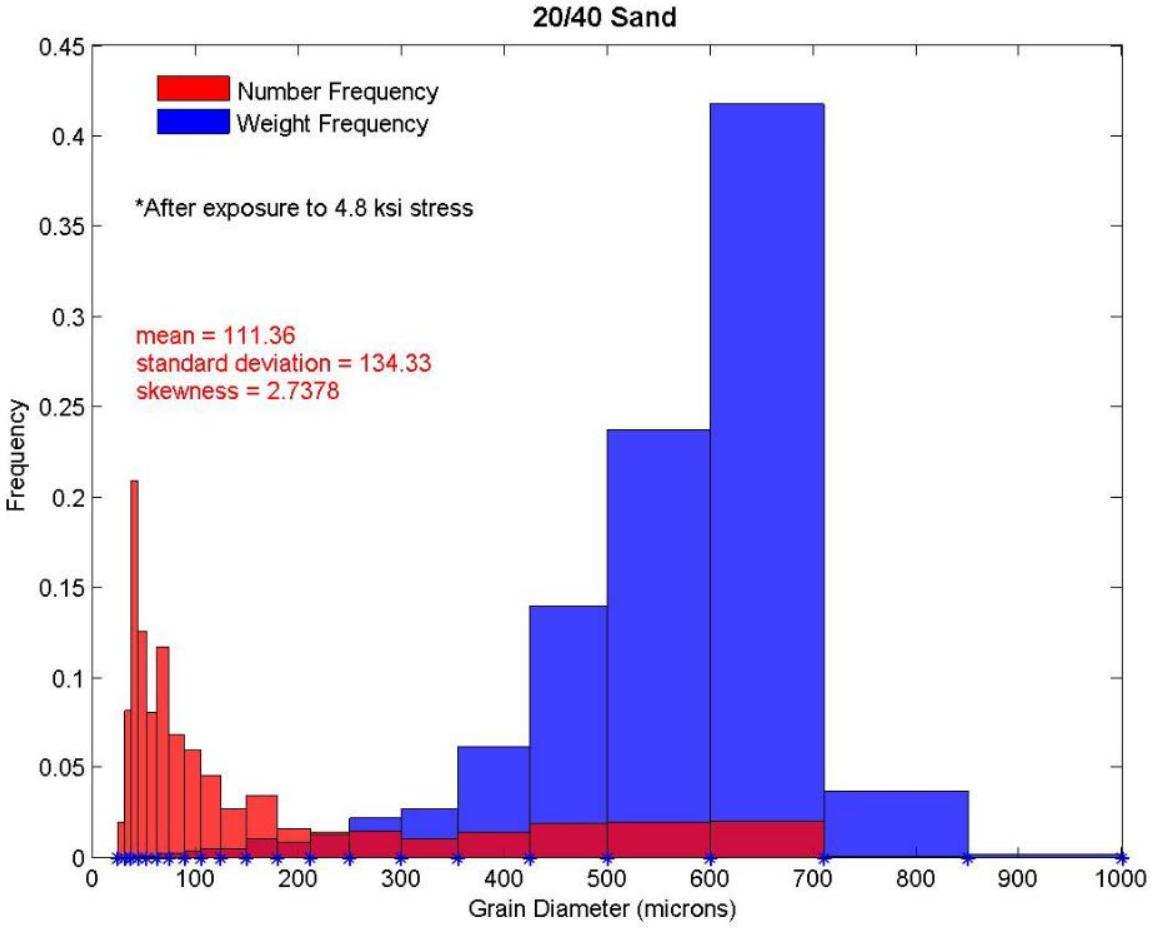

Figure 5.10: Number and weight frequency distributions of 20/40 sand after exposure to stress.

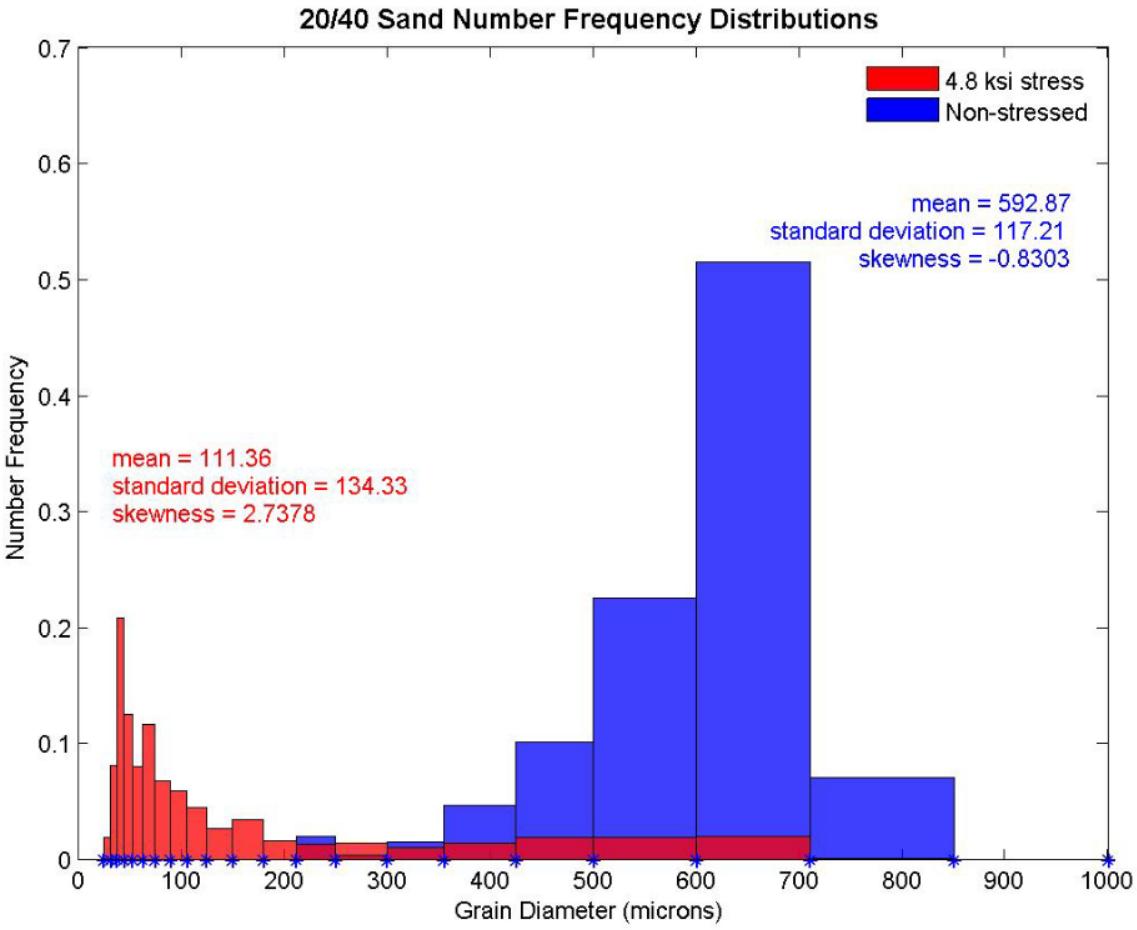

Figure 5.11: Number frequency distributions of 20/40 sand before and after exposure to stress.

Figure 5.12 shows the comparison of the analytical results and the experimental measurements:

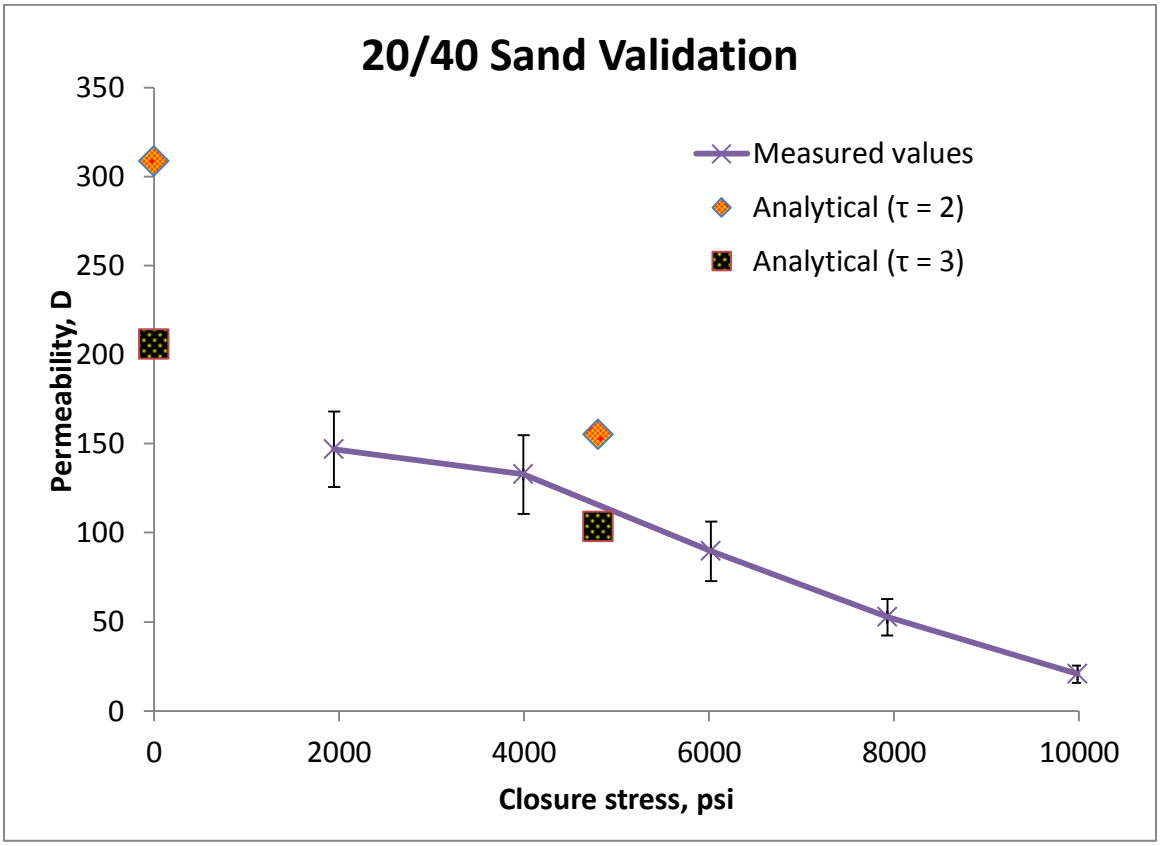

Figure 5.12: Comparison of analytical predictions with measured values for 20/40 sand.

For this case, the predictions are in excellent agreement with the experimental results, especially if the tortuosity is set equal to three.

40/70 Sand

The weight fraction and number frequency distribution for the 40/70 sand packing before and after exposure to stress is shown below:

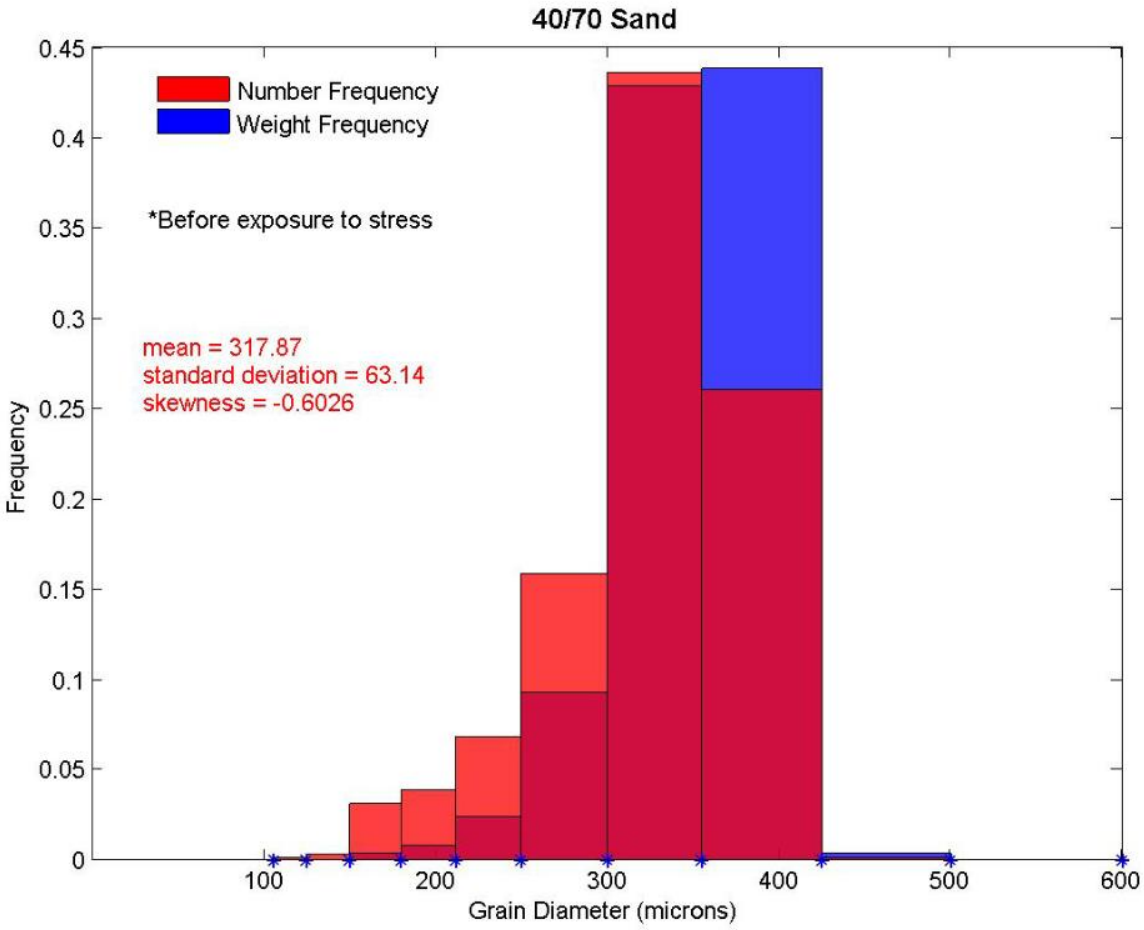

Figure 5.13: Number and weight frequency distributions of 40/70 sand before exposure to stress.

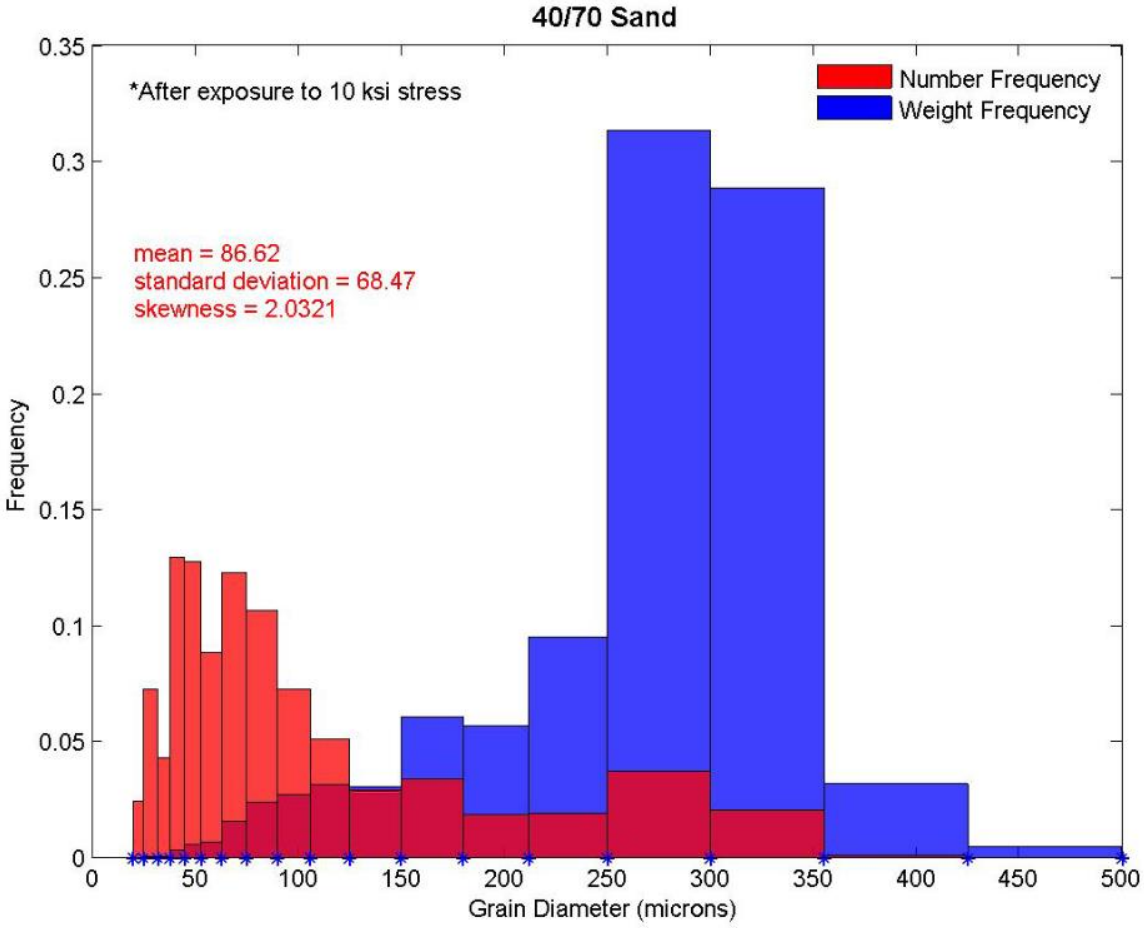

Figure 5.14: Number and weight frequency distributions of 40/70 sand after exposure to stress.

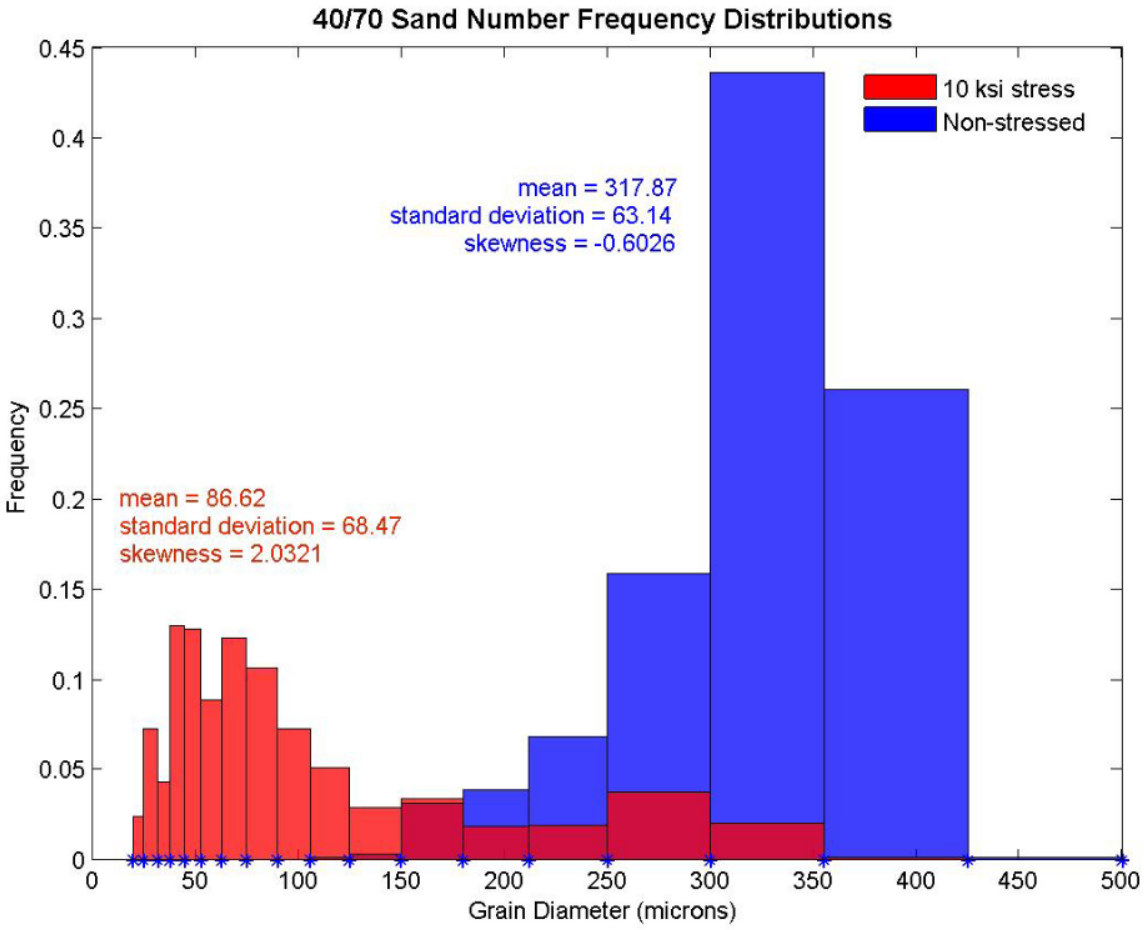

Figure 5.15: Number frequency distributions of 40/70 sand before and after exposure to stress.

Figure 5.20 shows the comparison of the analytical results and the experimental measurements:

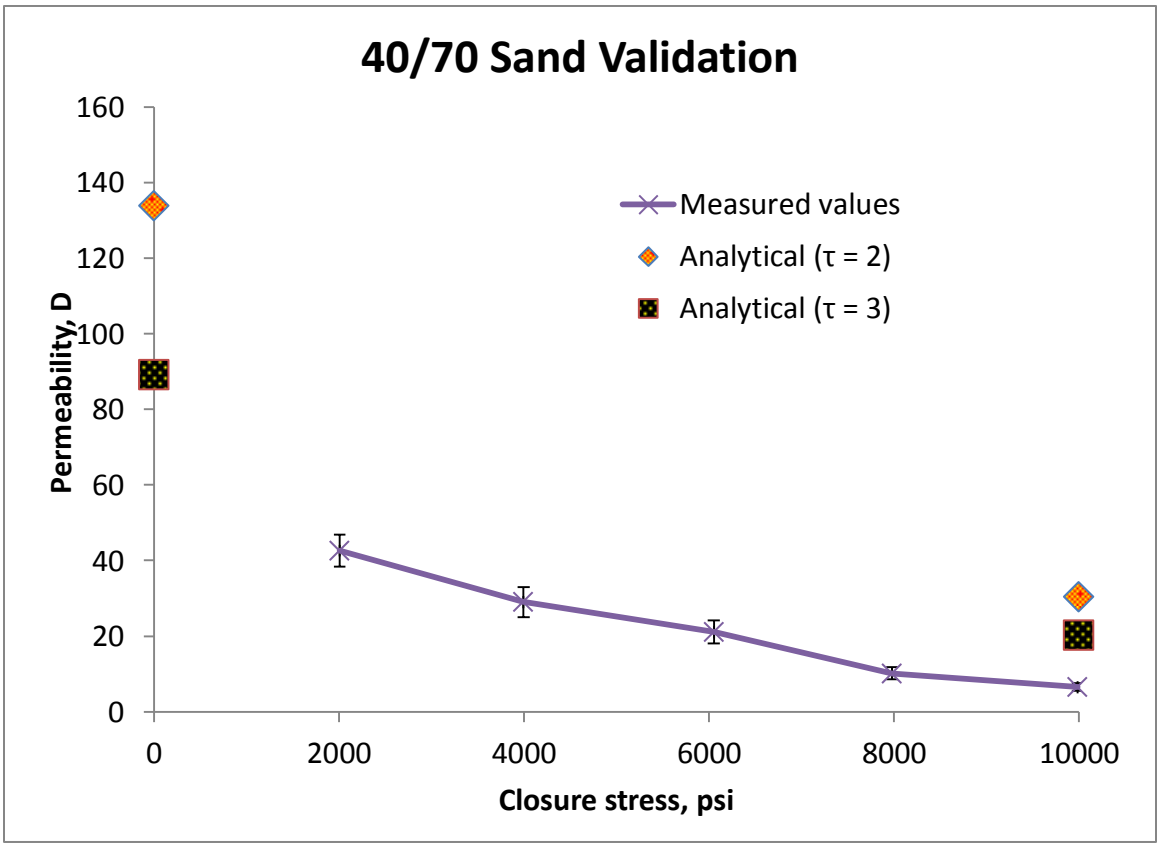

Figure 5.16: Comparison of analytical predictions with measured values for 40/70 sand.

Once again, good agreement is evident, especially at the 10,000 psi stress level. The non-stressed predictions appear to be higher than the experimental results, if the trend is extrapolated.

20/40 Ceramic & 40/70 Sand

In addition to the single component proppants, the analytical model was applied to the mixture of 75% 20/40 ceramic and 25% 40/70 sand before any stress was applied. The grain size distribution was measured before the sand and ceramic grains were combined to avoid the difficulty of density separation. The results are shown below:

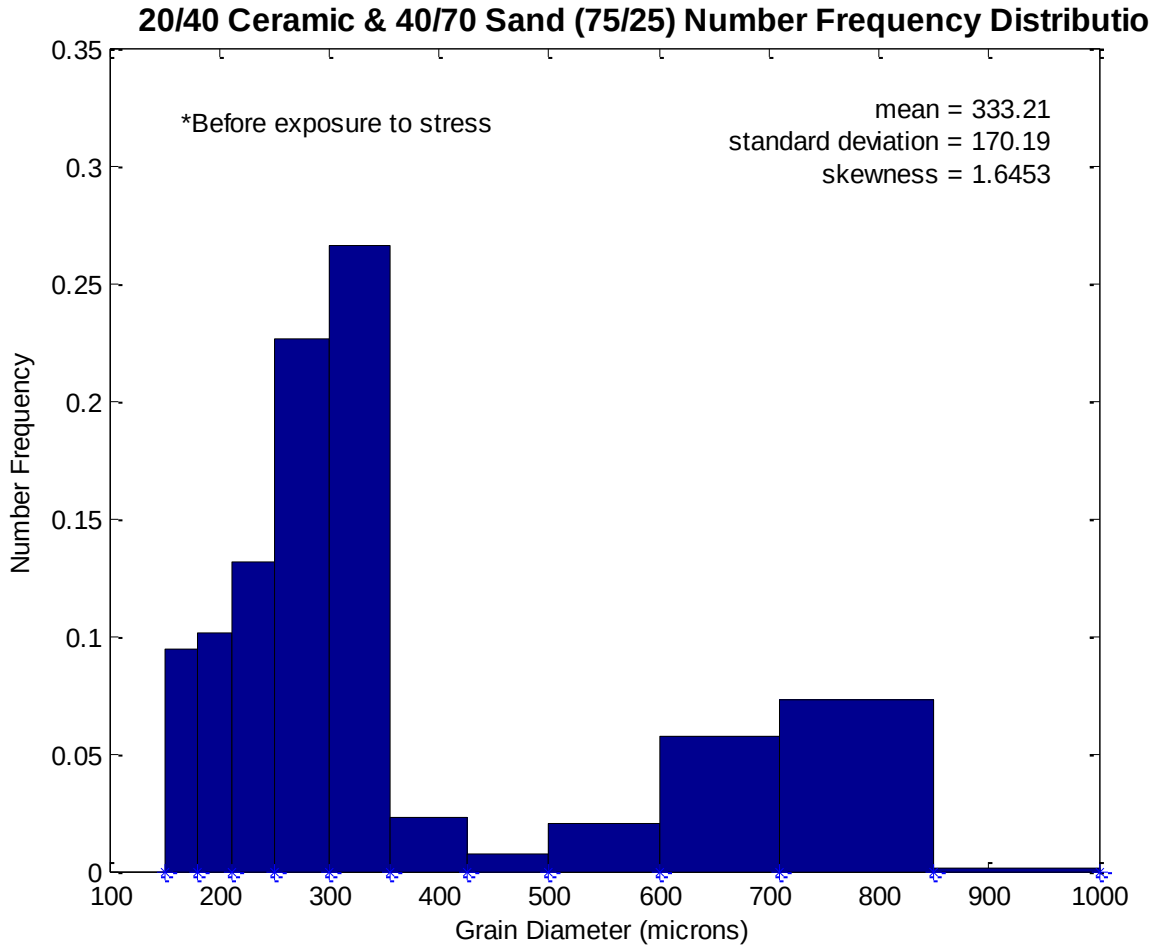

Figure 5.17: Number frequency distribution of mixture of 75% 20/40 ceramic and 25% 40/70 sand before exposure to stress.

Figure 5.18 shows the comparison of the analytical results and the experimental measurements:

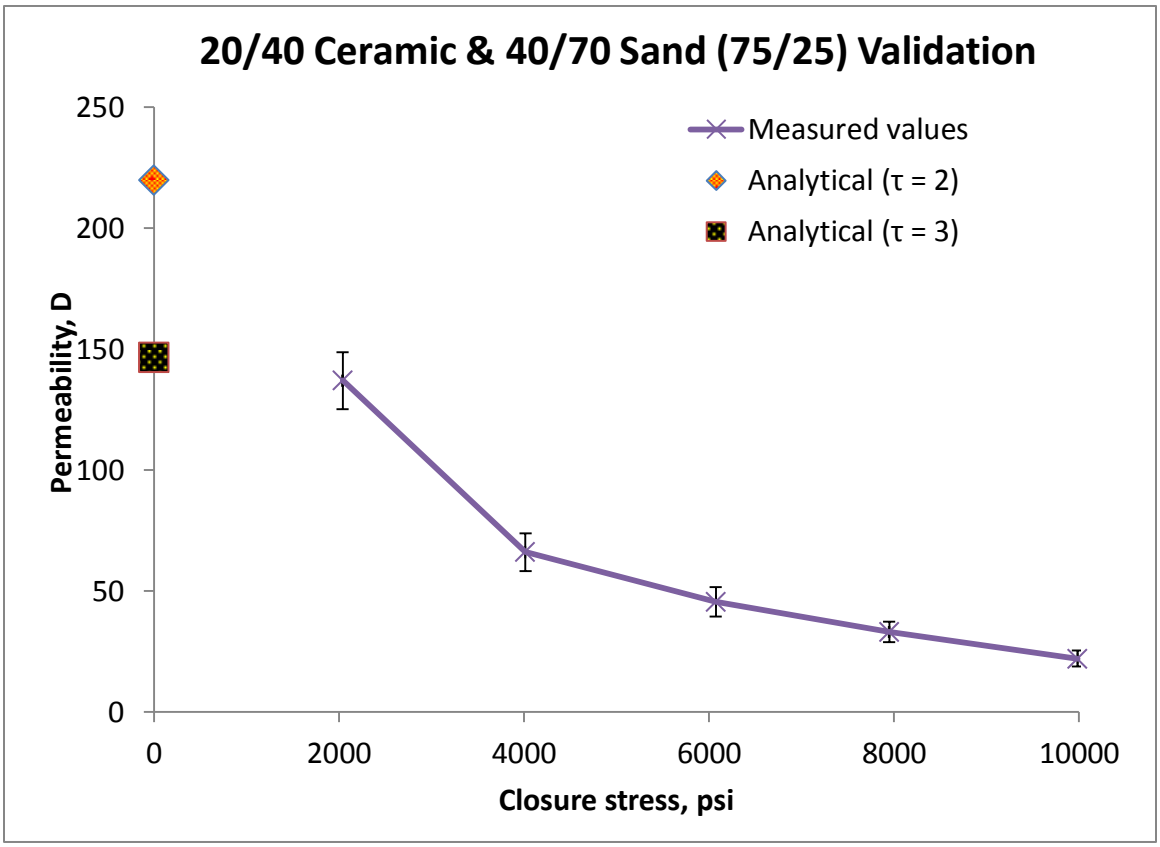

Figure 5.18: Comparison of analytical predictions with measured values for the mixture of 75% 20/40 ceramic and 25% 40/70 sand.

The predictions for this sample are in good agreement with the trend which is exhibited by the experimental results.

SUMMARY

The number frequency distributions of similarly sized sand and ceramic packs after exposure to stress are shown below:

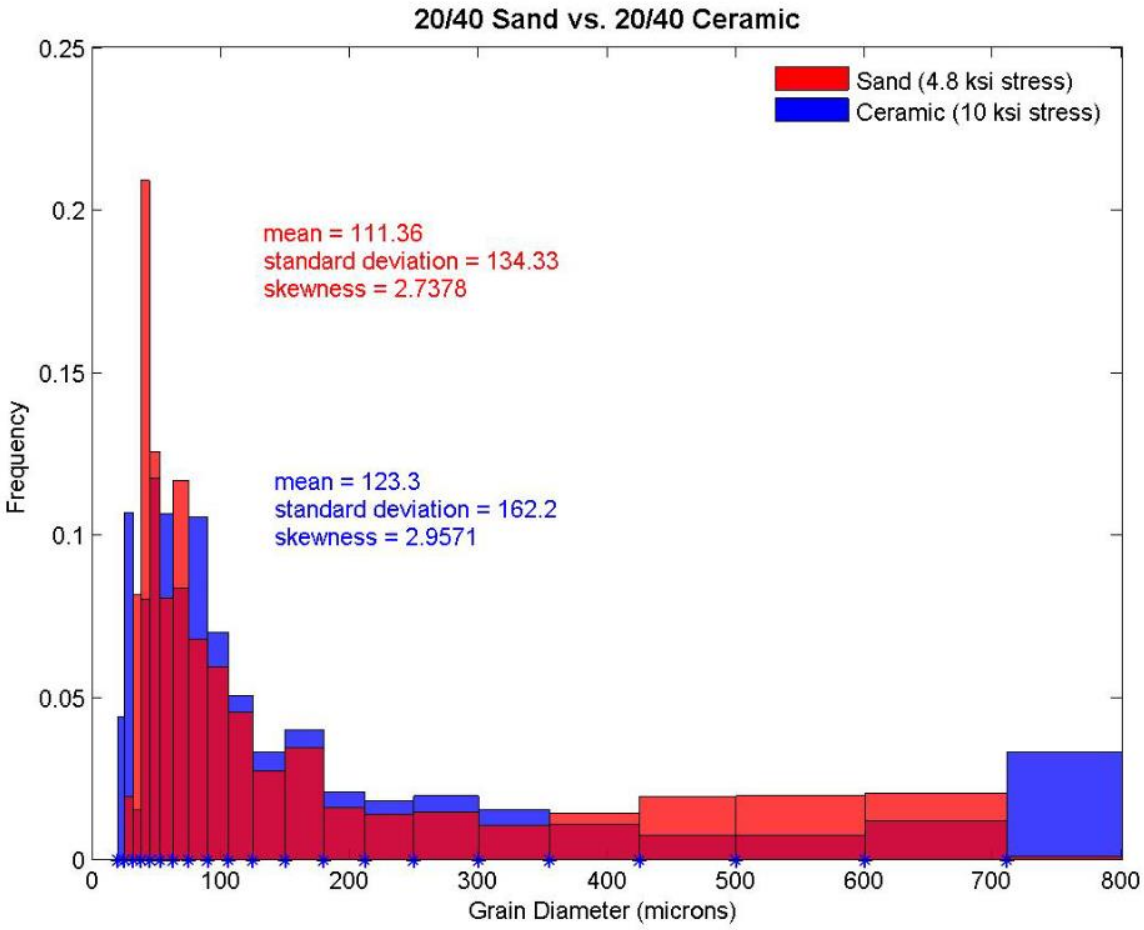

Figure 5.19: Comparison of number frequency distributions of 20/40 sand and 20/40 ceramic after exposure to stress.

It should be noted in Figure 5.19 that the sand packing was exposed to only 4,800 psi stress while the ceramic packing was exposed to 10,000 psi stress. Despite this, the ceramic packing still exhibits a size distribution with larger particles.

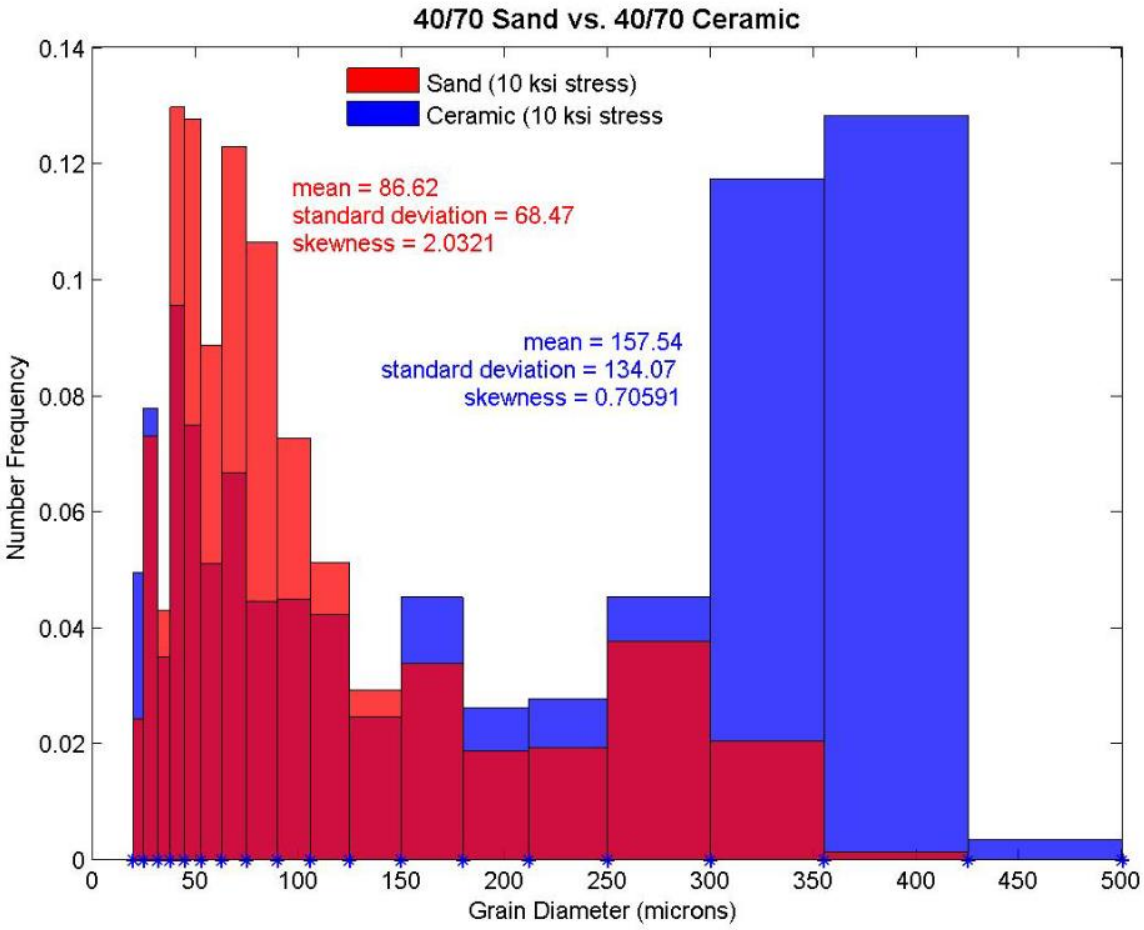

Figure 5.20: Comparison of number frequency distributions of 40/70 sand and 40/70 ceramic after exposure to stress

Figure 5.21 shows the analytical predictions versus the measured values for the single-component proppant packings after exposure to stress. The 20/40 sand was evaluated at 4,800 psi while the others were evaluated at 10,000 psi. It is evident that remarkably good agreement is attained when setting the tortuosity equal to three.

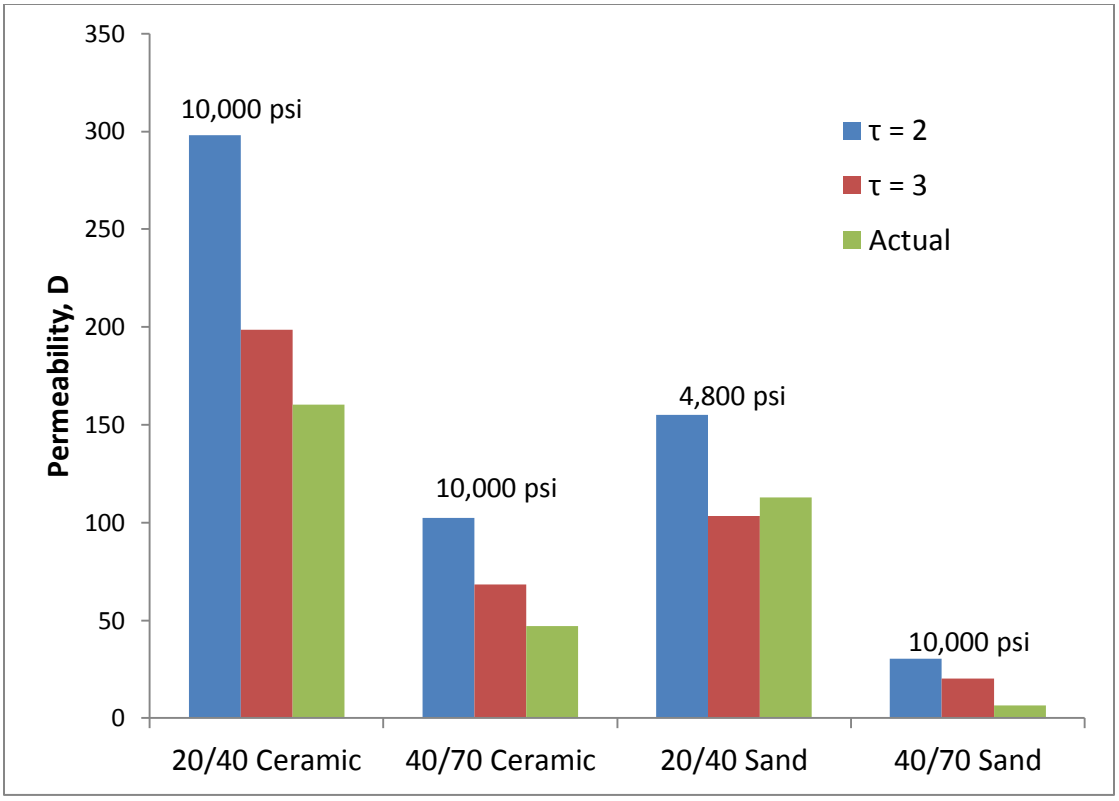

Figure 5.21: Comparison of analytical predictions versus measured values for the single-component proppant packs.

Chapter 6: Discussion

The results are presented and validated in the previous two chapters; the purpose of this chapter is to analyze the results and discover their implications and any underlying physical mechanisms that control these systems. First, the validation of the results is discussed, followed by a thorough discussion of the quantitative nature of the results and any general statements that can be made based on the data.

VALIDATION

Comparisons of the analytical predictions with the measured values are shown in the previous chapter. Generally, the first and most important requirement for verification of experimental results is to have the analytical predictions (or simulations) be within an order of magnitude of the experimental results. This hurdle is clearly met in this study, as most of the predictions deviate from the associated measured value by about twenty percent. In fact, some deviation is expected, because analytical predictions are often derived from idealized cases. Several assumptions were made in this case, both in the model itself and in the measurement of grain size distribution, which undoubtedly affect the accuracy of the predictions. The analytical model used in this study is rooted in the assumption that all of the grains can be considered perfectly spherical, which of course will not be the case, although it is a good approximation, especially for the ceramic grains.

The analytical predictions are further contaminated by simple measurement error, especially in measurement of the grain size distributions. It is difficult to accurately

collect and weigh particles that have diameters on the order of tens of microns, and so most of the number frequency distributions in Chapter 5 (after exposure to stress) probably underestimate the influence of very small particles. Also, in the conversion from weight fraction distributions to number frequency distributions, the assumption that all grains can be considered to have the median diameter between the two bounding sieve diameters is a liability. Then, a uniform distribution of grain sizes is assumed between the two bounding sieve diameters for the purpose of calculating distribution parameters, which is a direct contradiction to the assumption of all grains having the median diameter. Despite these obvious flaws, the measured size distributions do honor the data and they are still good approximations of the real distributions.

Generally, the analytical predictions marginally overestimate the actual permeability; this could be partially attributed to the underestimation of the amount of very fine particles. There is one instance where the permeability is underestimated - the 20/40 sand at 4,800 psi stress. But, when considered with all of the assumptions and idealizations mentioned above, the analytical predictions agree remarkably well with the experimental results. Therefore, the experimental results for the single component proppant packs are valid and, by extension, the mixture results are also valid.

FINDINGS

The two main properties of proppants under focus in this study are size and material. It has been established that the permeability of a porous medium is significantly influenced by the size distribution of the particles; to put it simply, the larger

the particles, the larger the permeability. Fundamentally, the permeability of a porous medium does not depend on the material makeup of the solid medium itself. Of course, in this study, the materials are subjected to stress, which alters the initial grain size distribution and porosity, and therefore alters the permeability. All else being equal, the expectation is that ceramic packings will exhibit higher permeability at a given stress level than sand packings, due to the fact that ceramics are more resistant to crushing effects. As for binary mixtures, the kind considered in this study, the naïve expectation is that the permeability of the mixture will simply be a linear interpolation of the two 'pure' permeabilities, i.e. the permeability of an equal mixture of A and B will be exactly halfway between the permeabilities of A by itself and B by itself.

20/40 Ceramic & 20/40 Sand

The first mixtures under consideration are those involving 20/40 ceramic and 20/40 sand. Based on the reasoning above, the expectation is that because the sizes are initially the same, the ceramic packing should exhibit higher permeability at all levels of stress. Figure 4.10 confirms that this is the case. Also, the permeability of the mixture of 75% ceramic and 25% sand does appear to be consistent with the hypothesis that the mixture permeability is a linear function of the mass fraction; in other words, the permeability of the mixture is three-fourths of the distance between the sand permeability and the ceramic permeability. However, the mixture of 50% sand and 50% ceramic only exhibits this behavior from 2,000 psi stress to about 3,500 psi stress, after which its permeability rapidly collapses down to that of the pure sand packing. This could mean

that the 50% sand and 50% ceramic mixture has a similar grain size distribution to the pure sand at sufficiently high stresses; however this is unlikely, as the ceramic particles should be considerably less deformed than the sand particles. It is more likely that the porosity of the mixture is notably lower than the porosity of the pure sand, as porosity is a strong function of grain sorting, and the grains in the pure sand pack are probably more well sorted than the grains in the mixture. Generally, lower porosities indicate lower permeabilities, so the porosity loss probably offsets the larger ceramic particles which would otherwise tend to increase permeability. But the question remains: why did the permeability of the 75/25 mixture not fall like the 50/50 mixture did? By analogy to problems involving simultaneous flow of immiscible fluids, such as oil and water, it may be that the process is controlled by which material is the continuous 'phase'. In other words, the permeability of the packing may be controlled by which material comprises a continuous pathway from the inlet to the outlet. If there are continuous pathways available through both materials, then the permeability of the packing can be considered as equivalent to parallel flow through multiple layers of different permeability. However, if there is a continuous pathway through only one material, that material will be the dominant control on the permeability of the mixture. Applying this theory to the 75/25 mixture, the most likely situation is that there are continuous pathways in both sand and ceramic particles, which would be similar to parallel flow, or there are continuous pathways in neither material, which would be similar to series flow, and as such the resultant permeability is some weighted mean of the pure permeabilities. Conversely, in the 50/50 mixture, there are not enough ceramic particles to constitute a continuous path,

and as such the permeability is controlled strongly by the sand particles. This would explain the collapse of the 50/50 mixture to the pure sand permeability. This theory is supported by the pictures of the two mixtures after testing (Figures 4.12 – 4.15); in the 50/50 mixture, it appears that, especially in the middle of the packing, ceramic particles are primarily isolated from one another in such a way that fluid is forced through sand at least once during its voyage through the packing. Of course, the mixing and arrangement of particles is fundamentally a random phenomenon, and therefore other packing arrangements are possible. However, the natural tendency of mixtures of particles is toward that of maximum disorder, so it can be safely assumed that the sand and ceramic particles will not segregate. If the continuous pathway theory is correct, then there should be some threshold mass fraction that dictates when either material dominates the medium or there is quasi-parallel flow or series flow. For this instance, it must be somewhere between 50% ceramic and 75% ceramic. Not enough tests were performed to uncover a value which governs the distinction between quasi-parallel flow and flow dominated by ceramic.

20/40 Sand & 40/70 Sand

This particular mixture is homogeneous in the sense that there is no ceramic; therefore the above continuous pathway hypothesis does not apply in this case. It is evident from Figure 4.16 that the 50/50 mixture is not halfway between the bounding pure permeabilities, and is noticeably closer to the 40/70 permeability curve. This is

probably due to the mixture being created on the basis of weight fraction rather than number fraction; this mixture (initially) must have had more 40/70 grains than 20/40 grains, and so it is not surprising that the mixture permeability gravitates closer to the 40/70 curve. Little else can be said about this particular mixture.

20/40 Sand & 40/70 Ceramic

These mixtures are the most unpredictable of the set, as there are competing effects in play. The sand pack starts out with larger particles, and so should have a larger permeability at low stresses. Figure 4.18 confirms this, and shows that the 20/40 sand permeability falls below the 40/70 ceramic permeability at about 7,000 psi closure stress. It is not obvious what to expect from the behavior of mixtures of these two proppants. One peculiar aspect of Figure 4.18 is that the mixture permeability of 50% 20/40 sand and 50% 40/70 ceramic is actually below the 40/70 ceramic permeability at all stress levels. Initially the sand grains are larger, so one could reasonably expect that this mixture would be more permeable than the ceramic at low levels of stress, but this is not the case. As noted earlier, and implicit in the analytical models discussed in this paper, permeability is a function of porosity, which is in turn a function of sorting. Mixing of unlike sizes causes the grain size distribution to broaden and degree of sorting increases, which decreases porosity, and therefore decreases permeability. In this instance, the porosity loss must outweigh the effects of the larger grains introduced by the sand. Flow for this mixture is dictated primarily by the ceramic; in the context of the threshold mass

fraction concept introduced earlier, this means that more than 50% sand is needed to begin to see the behavior of the mixture show resemblance to the pure sand behavior.

The mixture of 75% sand and 25% ceramic also displays somewhat cryptic characteristics. The quasi-parallel flow theory, where fluid can traverse through either material without encountering the other, is somewhat cast in doubt by these results, although is later redeemed. Initially, at 2,000 psi stress, the mixture is behaving in accordance with the naïve expectation of linearly interpolating the permeability based on mass fraction. However, at 4,000 psi, its permeability is closer to that of the ceramic; at 6,000 psi, its permeability is intermediate between the two; at 8,000 psi, its permeability is closer to the sand; and at 10,000 psi, its permeability is closer to the ceramic. Part of this confusion is probably due to the large overlap in the error bars, which leave an unfortunately large amount of uncertainty in the accuracy of the measurements. However, some insight is gained by examining the cross-sectional view of the proppant pack after testing, shown in Figure 4.23. It is evident that there is a streak of ceramic sandwiched in between two regions of sand which starts at the beginning of the pack and runs all the way to the end, although it does become somewhat murky towards the end. This could explain the surprisingly high permeability of this mixture at 10,000 psi stress; the streak of ceramic essentially provides an effective path of least resistance. Of course, this streak may not exist throughout all of the other cross-sections of the packing, because otherwise the permeability of this packing should be identical to that of the 40/70 ceramic.

It is difficult to determine whether the results of this mixture enhance or refute the ideas of quasi-parallel flow and threshold mass fractions described earlier. This is partially due to the proximity of the permeabilities of the pure components, as the measurement uncertainties overlap, especially at higher stresses. The data show that the mixtures have noticeably higher permeabilities at high stresses than the pure sand packing; however, it is the author's opinion that, without the bizarre ceramic streak in the middle of the proppant pack in the 75/25 mixture, its permeability would fall much closer to the pure sand permeability than is shown.

20/40 Ceramic & 40/70 Sand

The expectation for these mixtures is that the 40/70 sand will severely degrade the permeability of the packing, as it both contains smaller grains initially and is less resistant to crushing. Figure 4.24 shows that this is true, even for a packing that has only 25% sand. Here, the weight percentages drastically increase the effect of the sand, because an equal weight of 40/70 sand grains combined with an equal weight of 20/40 ceramic grains will have a much higher number of sand grains, and the number of grains is the controlling factor in permeability. Figures 4.26 and 4.27 show pictures of the 50/50 mixture after testing, it is clear from both that the sand is the dominant 'phase', and that while ceramic particles are present, they are largely isolated from one another and are interspersed within the continuous sand medium. Even the pictures of the 75/25 mixture (Figures 4.28 and 4.29) appear to be dominated by ceramic, but in fact there is still a largely intact, highly continuous network of sand grains. Both mixtures are dominated by

the 40/70 sand; there is no evidence of quasi-parallel or series flow here. This means that there must be more than 75% ceramic to avoid severe permeability degradation for this pair of proppants.

40/70 Sand & 40/70 Ceramic

Finally, a 50/50 mixture of 40/70 sand and 40/70 ceramic is considered. Once again, the naïve expectation of the mixture permeability being exactly halfway between the two bounding permeabilities is not observed. Again, part of this is undoubtedly due to the fact that the number frequency distribution is the controlling parameter instead of the more convenient weight size distribution, and because of this there are more sand grains, and thus it is less likely for the ceramic to form an interconnected pathway when randomly mixed with sand. In this instance, the 50/50 mixture is much closer to the sand permeability that it is the ceramic permeability.

Areal Concentration

It was discovered that, for sand, a partial monolayer with about 90% areal coverage has a higher permeability than a full monolayer; and the multilayer permeability does not catch up to the 90% partial monolayer until about five layers of proppant have been deposited. However, if areal coverage of 90% is not attained, the permeability quickly plunges. For ceramics, the threshold may be smaller since ceramics are stronger, but the qualitative behavior should be similar. Also, after about 8 layers of proppant have

been deposited, the permeability attains a limiting value after which no increase will be observed with an increase in the number of layers.

The reason that the partial monolayer is more permeable than the full monolayer is that there is simply more space that is open to fluid flow compared to a full monolayer, and thus there are less frictional pressure losses. However, if the partial monolayer is too sparse, the confining stress will pulverize the proppant, resulting in a large permeability loss. For 40/70 sand, about 90% areal coverage is necessary to realize the full benefit of the partial monolayer.

SUMMARY

From a practical standpoint, there are a couple of rules of thumb which can be extracted from the experimental data. The first, and perhaps most important, is that if ceramic is used, it should probably not be used in conjunction with any sand. The only possible exception to this is when mixing 20/40 sand with 20/40 ceramic; and even here, at least 75% ceramic should be used to avoid excessive permeability loss. Another point to consider is that if mixtures are prepared on the basis of weight fractions, the results will skew towards the lighter density material, because the number frequency distribution is one of the fundamental controls on permeability, not the weight fraction distribution. Generally, the assumption of linearly interpolating the mixture permeability between the two pure components based on weight fractions is not valid.

From a theoretical standpoint, the data suggest that binary mixtures of unlike proppants can be characterized by two separate states. The first state is realized when

one of the components is interspersed within the other component, and the permeability of the mixture is dominated by the component which is continuous. The second state is realized when there are continuous pathways through both components, or there are continuous pathways through neither; the latter being more likely. The author suspects that for randomly mixed samples, there are threshold mass fractions that govern the transition between these two states.

Chapter 7: Correlations

An effort was made, using the data given in Chapter 4, to construct an algorithm that will predict the permeability of a proppant pack binary mixture (or single component) as a function of closure stress, grain sizes, materials, and weight fractions. This chapter reveals the results of the correlations after a discussion on their development and workflow.

DEVELOPMENT

Creating reliable correlations is a rather difficult task, because the tendency is to find equations that will perfectly match all of the data. However, as equations become more and more complicated and cumbersome, their predictive capability plummets. This is mostly due to the correlations deviating from a physics-based strategy to a data-fitting strategy. The challenge, then, is to find functions that obey the general physical phenomena but still honor the data, while keeping the functional form as simple as possible.

The first step is to consider the physics of the situation. Here, the most obvious observation is that the permeability of every proppant pack decreases monotonically with increasing stress. The simplest way to represent this would be with a decreasing linear function; but the data are not quite linear, and a linear correlation would eventually predict negative permeabilities for high stress values, which is obviously not physical and therefore unacceptable. From examining the data, it is evident that the rate of permeability decay decreases with increasing stress, i.e. permeability falls quicker at

lower stresses, and then levels off at higher stresses. A functional form that can accommodate this behavior is a hyperbolic decline function. This has the additional advantage that it will never predict a negative permeability. The proposed function has the following form:

$$k = A\left[B^{-\sigma/c}\right] \tag{7.1}$$

where k is the permeability in Darcies, σ is the closure stress in psi, and A, B, and C are constants to be determined. It is a trivial exercise to fit equations of this type to each sample, although, of course, not every sample exhibits a perfect hyperbolic shape.

The next step is to determine methods for producing A, B, and C for each sample. Again, the physics must be taken into account. In this case, A represents the permeability of the proppant at zero stress. The grain sizes will be the most critical factor here, since material will not matter much if no stress is applied. Ceramics may have a marginally higher permeability than sands at zero stress due to their relatively high degree of uniformity. In light of this, the A function should depend mostly on grain size. An adequate function, after trial and error, is found to be:

$$A = [Xd_{max} - Yd_{min}] \tag{7.2}$$

where X and Y are constants, and d is meant to be in units of microns (not the mesh numbers). Because the inherent assumption is that grain sizes are defined by their sieve boundaries, the equations have been constructed to accept a maximum grain size and minimum grain size for each component. The weight fractions are handled by simply using a linear combination of each term, illustrated in the following equation:

$$A = wf_1\left[Xd_{max,1} - Yd_{min,1}\right] + wf_2\left[Xd_{max,2} - Yd_{min,2}\right] \quad (7.3)$$

where the subscripts 1 and 2 correspond with components 1 and 2. The correlation is compared to the actual data in Figure 7.1:

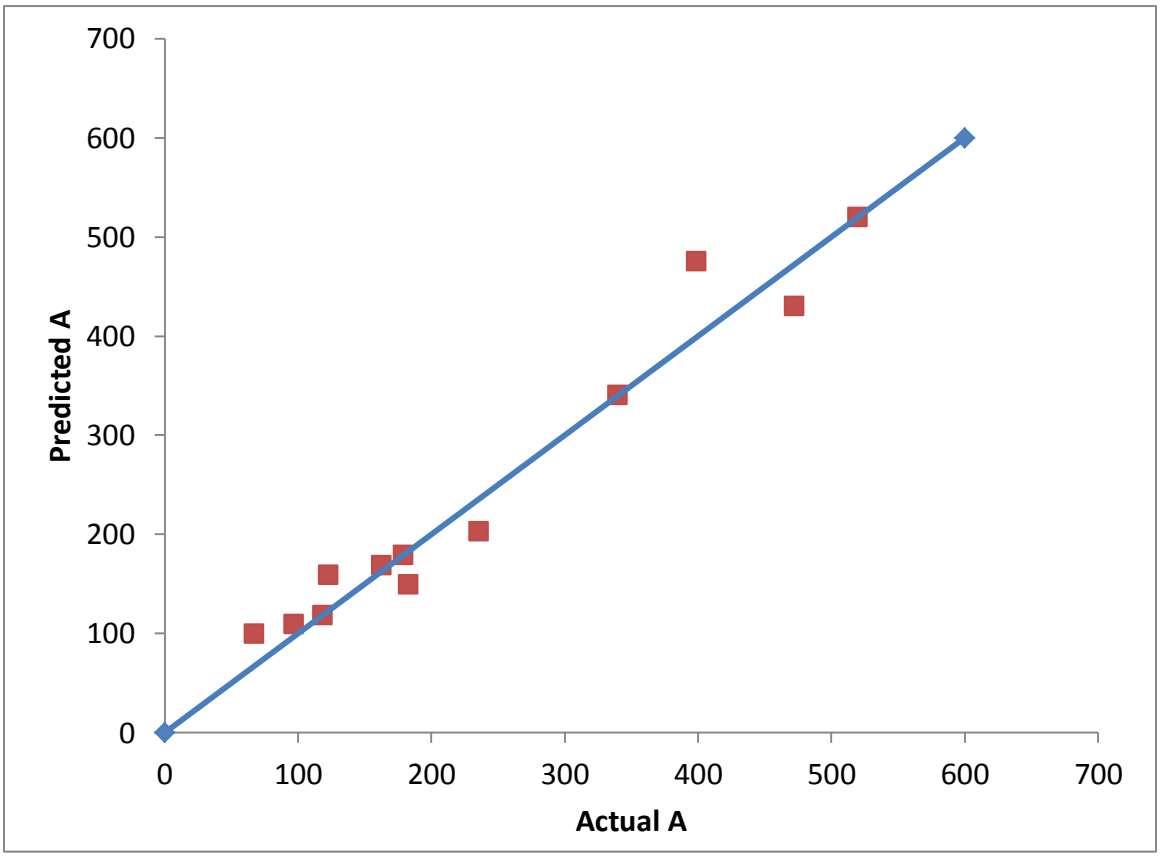

Figure 7.1: Predicted A values versus Actual A values.

The blue line in Figure 7.1 is representative of a perfect correlation; the red points correspond to each sample.

Finding a function for the parameter *B* is the next step. Mathematically speaking, as *B* increases in Equation 7.1, it is similar to pulling the curve towards the origin while keeping the endpoints fixed. Physically, this means that high *B* values should correspond with the proppant packs which have quick and significant drops in permeability at low

stress values. So, sand should have higher B values than ceramic because it is less resistant to stress. Also, larger grains should have higher B values because they have more permeability to lose than smaller grains.

Keeping these points in mind, the strategy here was to find a function which satisfied the pure ceramic proppants and a function which satisfied the pure sand proppants. Then mixtures of sand and ceramic can be dealt with by adding a mixing term to the weight fraction weighted linear combination of the pure sand and pure ceramic functions. Once again, a simple function was found for the pure ceramic case:

$$B = wf_c\, X\left[d_{min,c} + d_{max,c}\right] \tag{7.4}$$

where *wf* is the weight fraction and X is a constant (different from the X used in the A function). Note that when the weight fraction is one the equation simplifies to:

$$B = X\left[d_{min,c} + d_{max,c}\right] \tag{7.5}$$

which can be viewed simply as the average grain diameter multiplied by a constant $2X$.

The pure sand case did not allow itself to be represented by a linear function, and so a slightly more complicated logarithmic function was used. After trial and error, the equation came out to be:

$$B = Y\left[log_z(d_{min,s} + d_{max,s})\right] \tag{7.6}$$

where Y and Z are constants. Admittedly, this equation is dangerously encroaching upon the territory of data fitting, but it is the simplest formulation that could be found.

To account for mixing of sand and ceramic, again the physics must be considered. One scenario that will cause B to rise is large ceramic grains mixed with small sand grains; and likewise a scenario that will cause B to fall is small ceramic grains in general,

because these retard the rate of permeability decay. So, the mixing term was designed to mimic this behavior; it is given below:

$$wf_c wf_s C\left[d_{min,c} + d_{max,c} - d_{min,s} - d_{max,s}\right] \tag{7.7}$$

where C is a constant. If the term inside the brackets is positive, as will be the case with large ceramic grains and small sand grains, then B will rise. If we have small ceramic grains, B will decrease, unless the sizes are the same as the sand, in which case the mixing term will vanish. Note that if either weight fraction is zero, then the mixing term vanishes, as it should. Also note that the $wf_c wf_s$ product is a maximum when both are equal to 0.5. If the ratio is 90% to 10%, then that is not much of a mixture, and the mixing term is dampened, as it should be. The B function for mixtures of sand and ceramic is then:

$$\begin{aligned} B = {} & wf_c X\left[d_{min,c} + d_{max,c}\right] + wf_s Y\left[log_z(d_{min,s} + d_{max,s})\right] \\ & + wf_c wf_s C\left[d_{min,c} + d_{max,c} - d_{min,s} - d_{max,s}\right] \end{aligned} \tag{7.8}$$

At first glance, this looks overly cumbersome; but it is just a linear combination of the pure sand and pure ceramic functions plus a term to account for mixing. It is general; notice that if either weight fraction is zero, the equation collapses down to the base functions given in Equations 7.5 and 7.6.

The only contingency not accounted for here is a mixture of sands with different size distributions. Once again, it is a linear combination of the base sand function. However, due to the observation that the results tend towards the smaller component, an additional weighting factor is added to the term corresponding to the small component. It is basically the sum of the four grain sizes divided by the sum of the two larger grain

sizes. This assures that this factor will always be between 1 and 2. The equation is given below:

$$B = wf_l Y \log_z(d_{min,l} + d_{max,l}) + wf_s Y \log_z(d_{min,s} + d_{max,s}) \left(\frac{d_{min,l} + d_{max,l} + d_{min,s} + d_{max,s}}{d_{min,l} + d_{max,l}}\right) \quad (7.9)$$

where the subscripts *s* and *l* represent the small and large components, respectively.

A comparison of the actual *B* values against the *B* values predicted by Equations 7.8 and 7.9 is below:

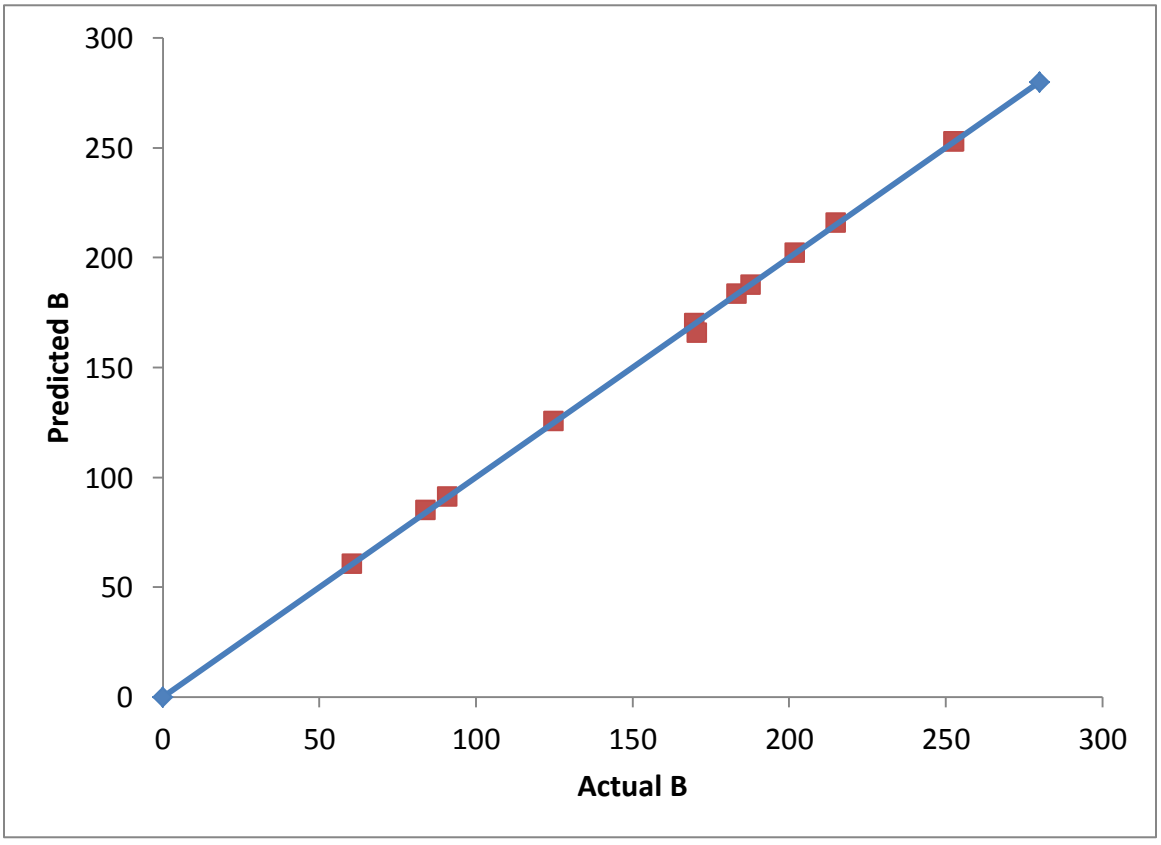

Figure 7.2: Predicted B values versus Actual B values.

As the figure shows, there is excellent agreement between the predicted and actual *B* values.

The final step is to find a function for the *C* parameter. This parameter has a similar function, mathematically and physically, to that of *B*. The main difference is that *C* behaves inversely in relation to *B*, e.g. high *C* values correspond with low *B* values. The same general strategy is employed; namely, functions are determined for both the pure sand and pure ceramic cases and a mixing term is added to account for sand and ceramic mixtures. For the pure ceramic, we have:

$$C = wf_c\left\{P + \left[wf_c\left(M + \frac{N}{\left(d_{max,c} + d_{min,c}\right)}\right)\right]\right\} \tag{7.10}$$

This looks cumbersome, but notice that when the weight fraction is one it reduces to:

$$C = (P + M) + \frac{N}{\left(d_{max,c} + d_{min,c}\right)} \tag{7.11}$$

P, *M*, and *N* are constants. For the pure sand, we have:

$$C = wf_s\left[W - V(d_{max,s} - d_{min,s})\right] \tag{7.12}$$

where *W* and *V* are constants.

The mixing term is more difficult for this case. There are two main observations that dictate the equation here: first, C increases with sand grain size *if* small ceramic is also present and second, the *difference* between the minimum ceramic grain size and minimum sand grain size controls C. If small sand grains are combined with large ceramic grains, C will fall. Thus the following expressions are intended to account for these effects:

$$\left[wf_s d_{max,s}\right]^R \tag{7.13}$$

$$Twf_c\left(d_{min,c} - d_{min,s}\right) \tag{7.14}$$

where R and T are constants. Finally, the sand/sand mixture needs to be dealt with. This was accomplished by using a linear combination of the base sand functions with an extra weighting factor applied to the small component. The equation is:

$$C = wf_l\left[W - V(d_{max,l} - d_{min,l})\right] + wf_s\left[Y\left[W - V\left(d_{max,s} - d_{min,s}\right)\right] + Z\right] \tag{7.15}$$

where the subscripts l and s denote large and small, and Y and Z are new constants.

In summary, for mixtures of sand and ceramic, we have:

$$C = wf_c\left\{P + \left[wf_c\left(M + \frac{N}{(d_{max,c} + d_{min,c})}\right)\right]\right\} + wf_s\left[W - V(d_{max,s} - d_{min,s})\right] + \left[wf_s d_{max,s}\right]^R + Twf_c\left(d_{min,c} - d_{min,s}\right) \tag{7.16}$$

which is a combination of Equations 7.10, 12, 13, and 14. The comparison of predicted C values versus actual C values is given below:

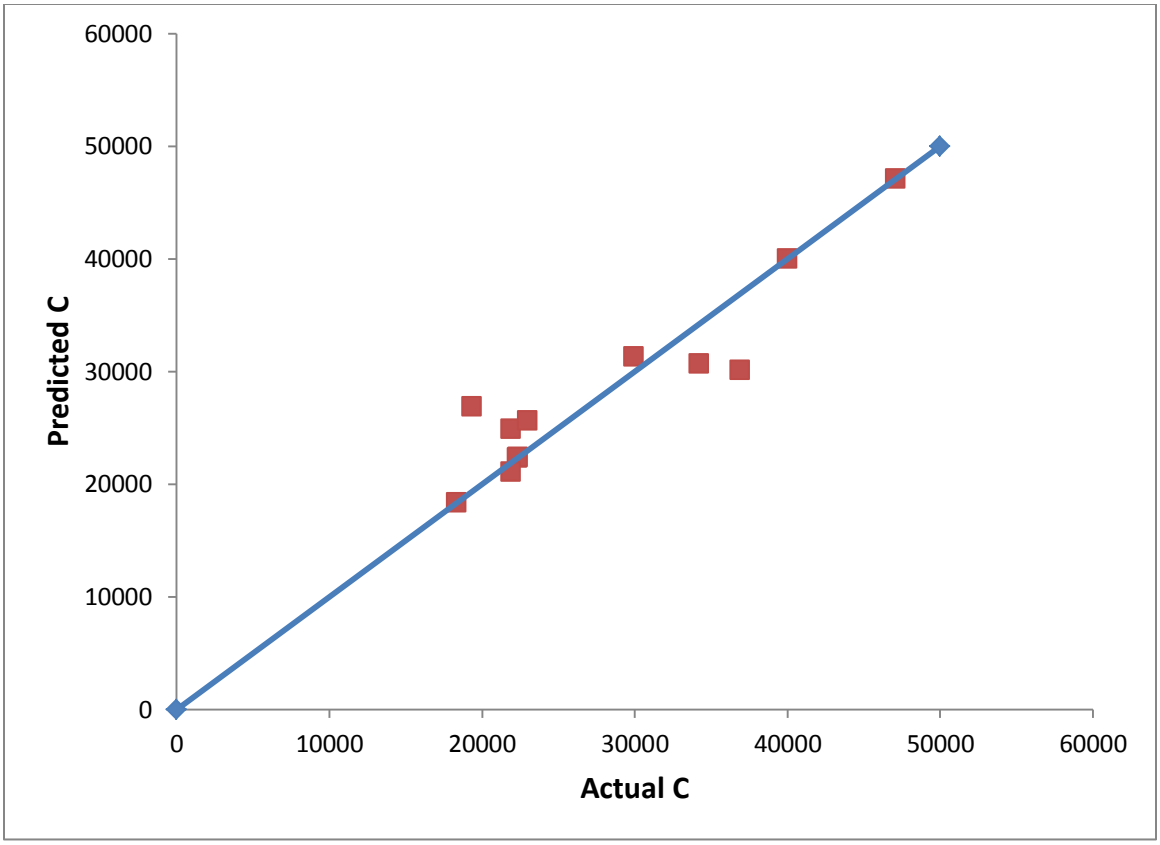

Figure 7.3: Predicted C values versus Actual C values.

This is the worst of the correlations, but it will suffice for the purposes of this study.

WORKFLOW

Since there are some contingencies to contend with, this section aims to provide a clear instruction on how to progress from a set of input variables to the final product. First, A, B, and C must be estimated, and then plugged into Equation 7.1 to generate permeability as a function of stress. It should be remembered that grain sizes should be entered in units of microns.

Correlation A

First, the constants determined for this correlation are revealed in Table 7.1 below:

Table 7.1: Constants for use with the correlation for A.

	20/40 only		Any 40/70 or smaller	
	Sand	Ceramic	Sand	Ceramic
X	0.407064	0.611844	0.255062	0.304119
Y	0.013921	0.000159	0.041382	0.05047

Notice that there are different constants for cases with only 20/40 mesh sizes and others for any scenario with particles smaller than the 40 mesh size. To determine the appropriate value for *A*, simply enter Equation 7.3 with the appropriate constants from Table 7.1.

Correlation B

For the *B* parameter, there are two different scenarios: a sand/sand mixture, and anything else. For the sand/sand mixture, Equation 7.9 should be used with the appropriate constants given in Table 7.2. For any other situation, Equation 7.8 should be used with the appropriate constants, again given in Table 7.2.

Table 7.2: Constants for use with the correlation for B.

	Sand/Ceramic Mixtures	Pure (only sand or only ceramic)
X	0.1700	0.1333
Y	1.2877	1.5423
Z	5.5979	1.0619
C	0.4564	-

Correlation C

This is the most cumbersome of the correlations, as there are four distinct cases: single component ceramic, single component sand, a sand/sand mixture, and a sand ceramic mixture. These are dealt with by using the appropriate constants, given in Table 7.3, with Equations 7.11, 12, 15, and 16, respectively.

Table 7.3: Constants for use with the correlation for C.

M	34123	R	1.438	W	22429
N	9008022	T	-19	Y	-0.1059
P	-1188	V	0.2348	Z	16688

The easiest way to calculate the appropriate values for A, B, and C is to create a spreadsheet that automatically decides which equations and which constants to use.

RESULTS

In this section, the predictions of the correlations described in the previous sections are compared against the actual data. Each plot is self-explanatory, so commentary will be withheld until the end of the section. First, the results of the single component proppants will be shown, followed by the mixtures.

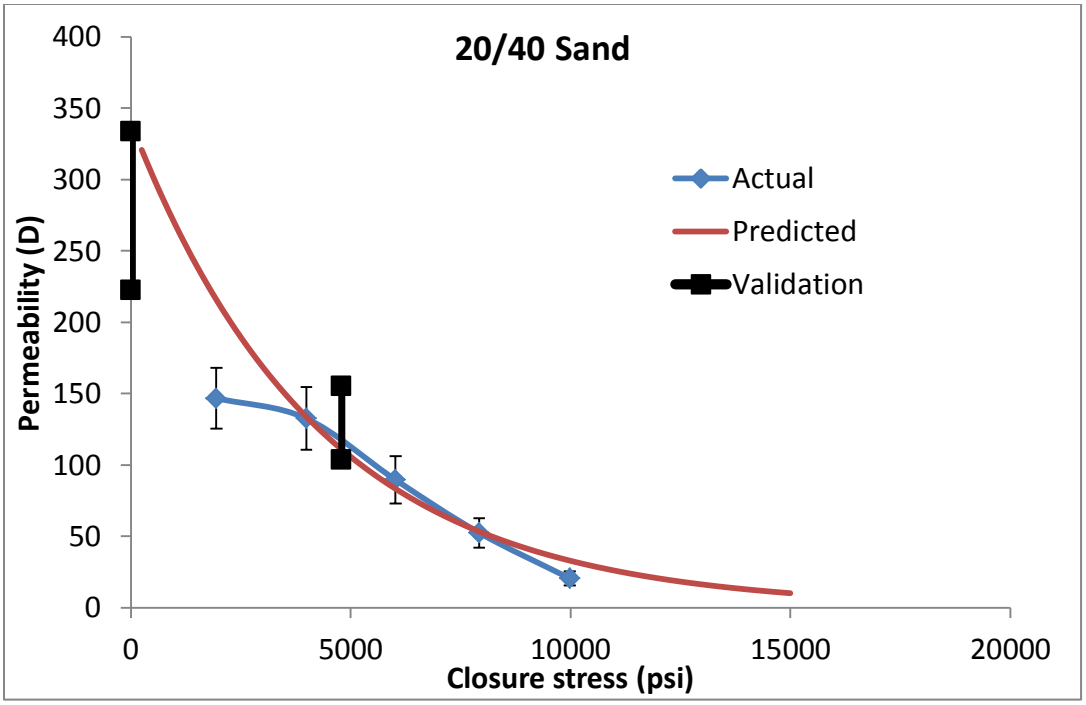

Figure 7.4: Comparison of prediction versus the actual data and the validation for 20/40 sand.

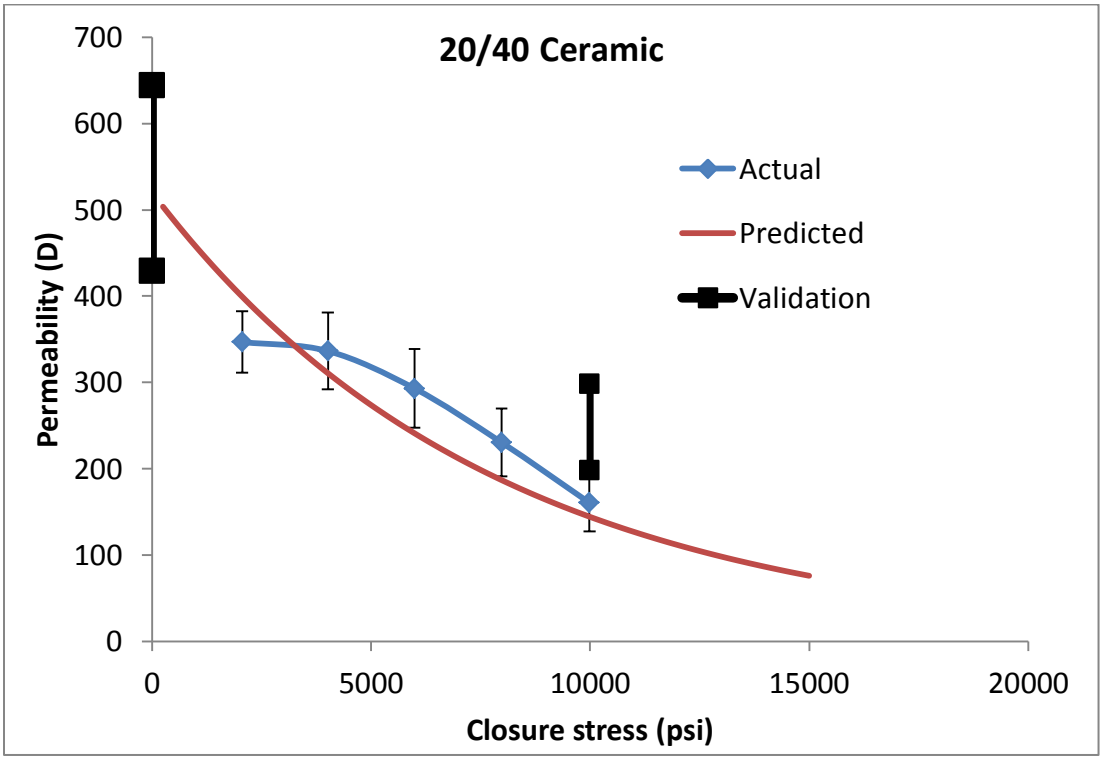

Figure 7.5: Comparison of correlation versus the actual data and the validation for 20/40 ceramic.

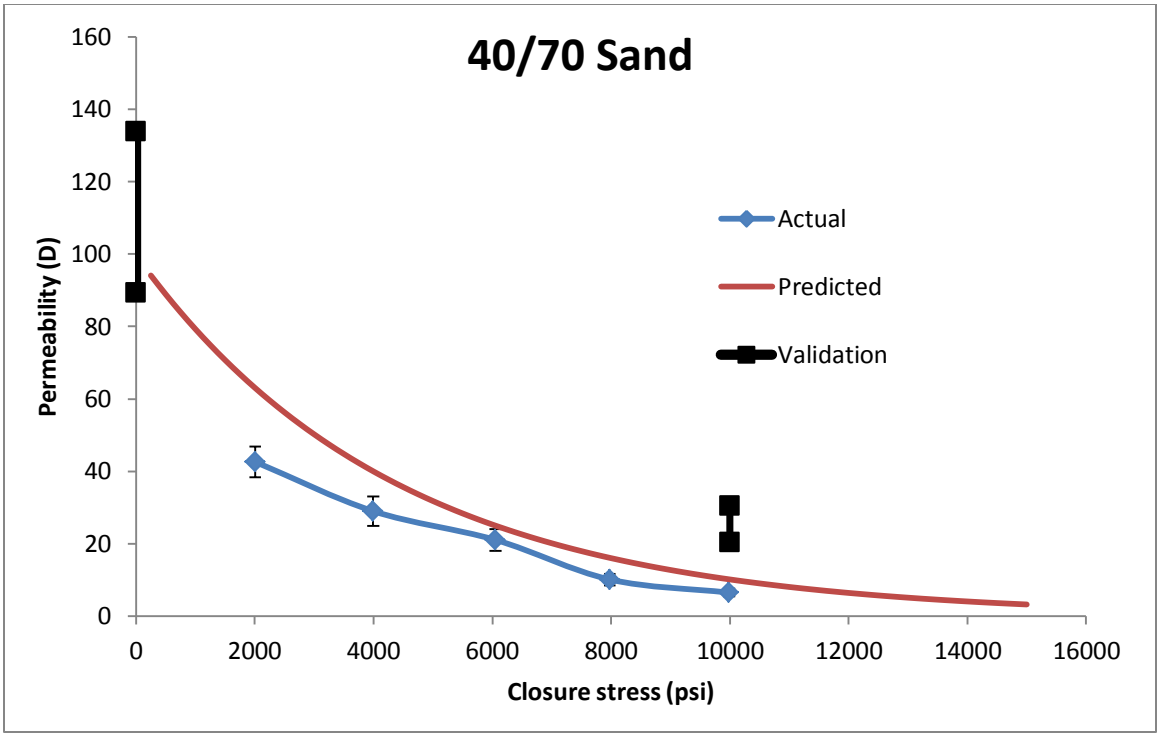

Figure 7.6: Comparison of correlation versus the actual data and the validation for 40/70 sand.

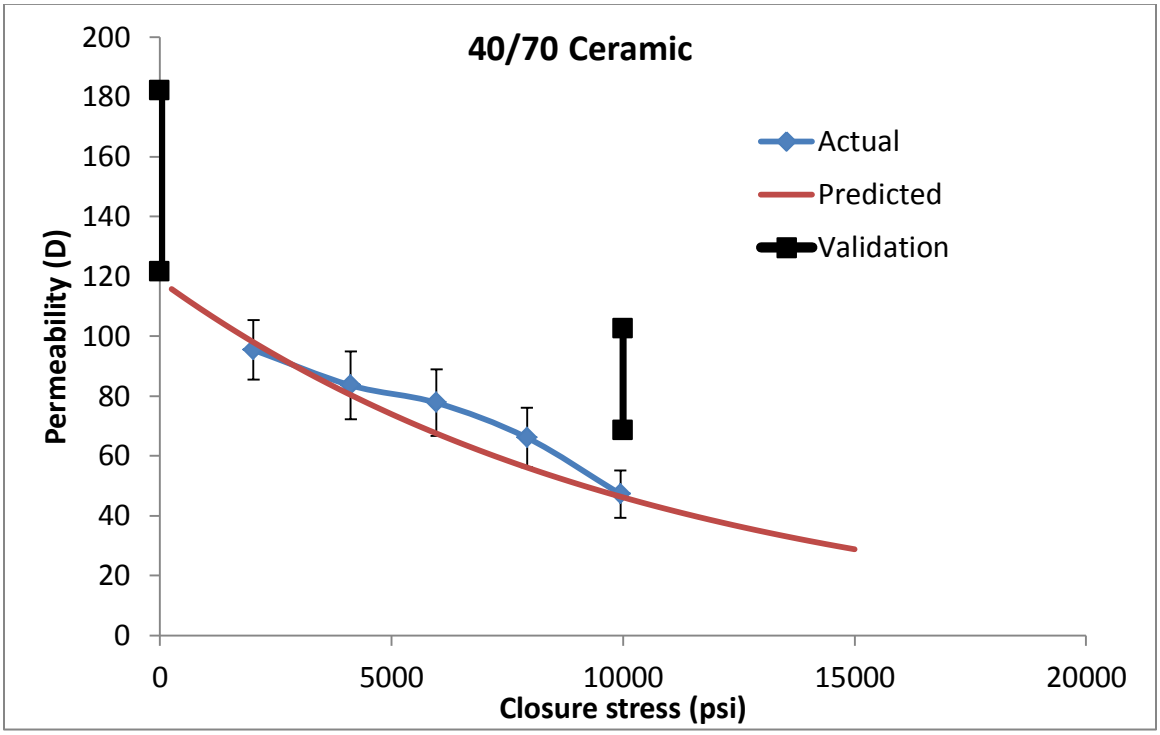

Figure 7.7: Comparison of correlation versus the actual data and the validation for 40/70 ceramic.

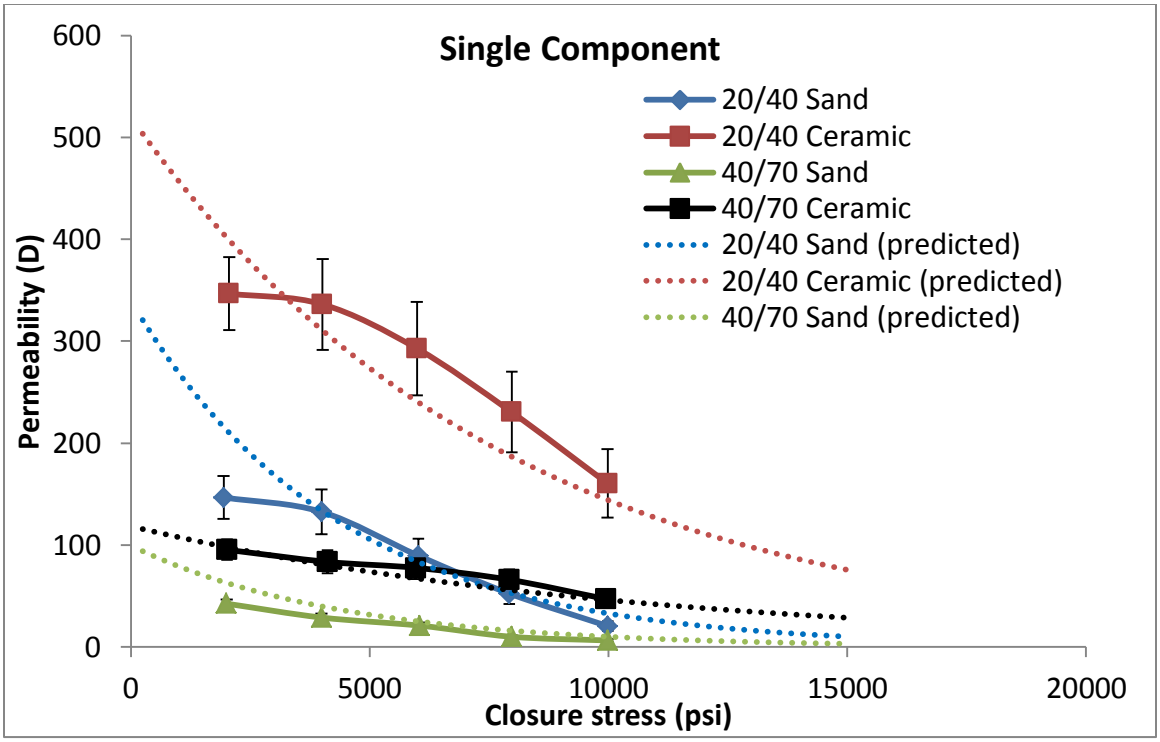

Figure 7.8: Comparisons of the single component predictions versus the actual data.

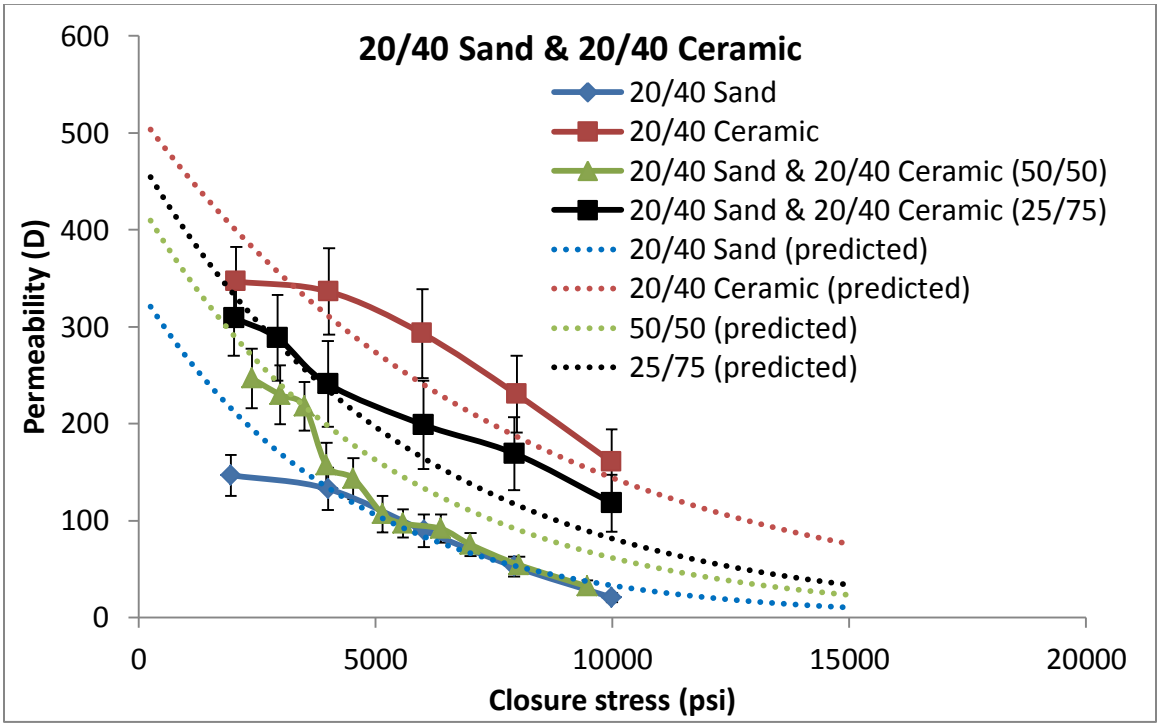

Figure 7.9: Comparisons of the predictions versus actual data for mixtures of 20/40 sand and 20/40 ceramic.

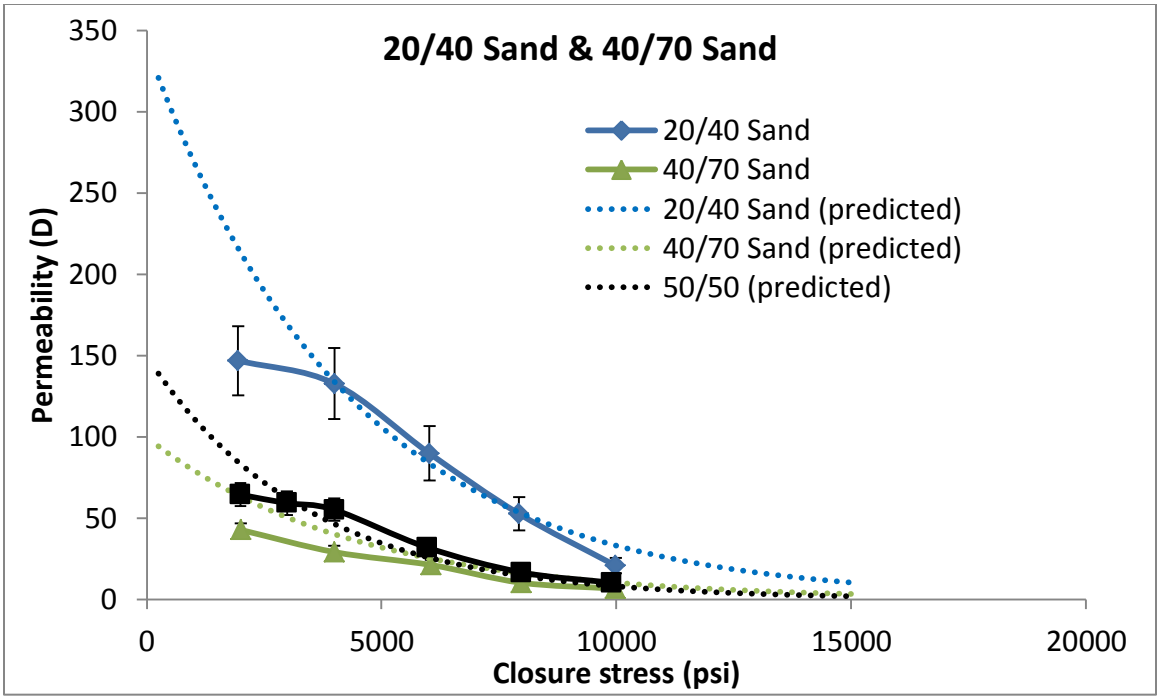

Figure 7.10: Comparisons of the predictions versus actual data for mixtures of 20/40 sand and 40/70 sand.

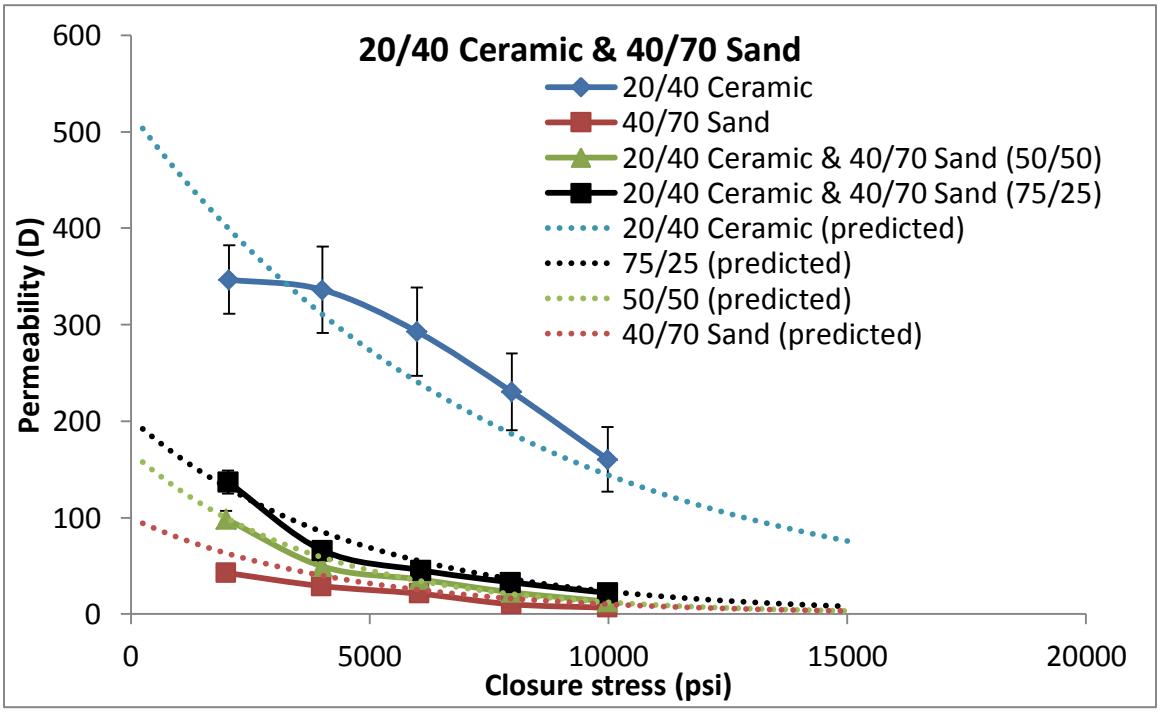

Figure 7.11: Comparisons of the predictions versus actual data for mixtures of 20/40 ceramic and 40/70 sand.

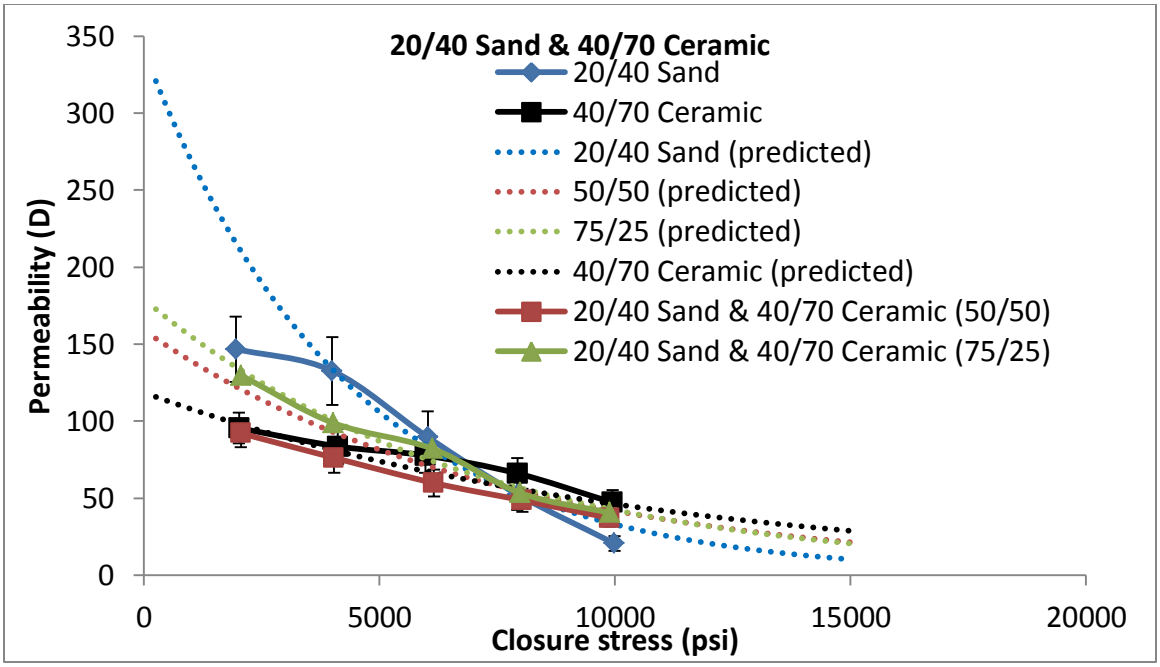

Figure 7.12: Comparisons of the predictions versus actual data for mixtures of 20/40 sand and 40/70 ceramic.

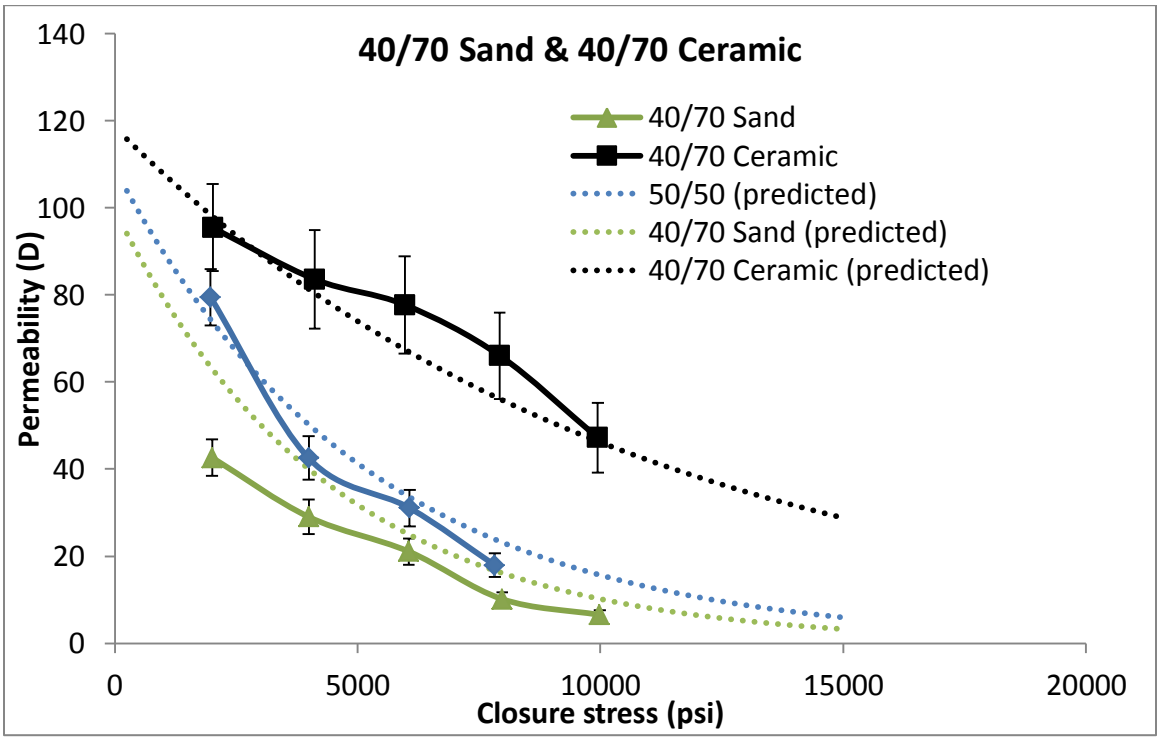

Figure 7.13: Comparisons of the predictions versus actual data for mixtures of 40/70 sand and 40/70 ceramic.

Based on Figures 7.4 through 7.13, the correlations are certainly not perfect, but they do approximate the data reasonably well. The biggest deviation is that of the equal mixture of 20/40 ceramic and 20/40 sand, as the correlation fails to predict the collapse down to the 20/40 sand curve at 4,000 psi stress. Another criticism that could justifiably be made against the correlations presented in this chapter is that they are too complicated, i.e. are too much of a data-fitting operation. This is a fair point, however I would respond that honoring the data is the first job of the correlation; in other words, agreement with the data is a necessary condition, but not sufficient. If the correlations do not agree with the data, they are equally as useless as the pure data fits. In spite of this, it is encouraging that the correlations generally agree with the non-stressed validation predictions, as shown in Figures 7.4 through 7.7.

Chapter 8: Conclusions and Future Directions

In this work, permeability and conductivity were measured for single and binary mixtures of proppants. The data was compared with a permeability model based on particle size distribution. Main conclusions are presented in the following section.

CONCLUSIONS

- Permeability decreases with increasing closure stress for all proppants and mixtures.
- The permeability reduction factor from 2,000 psi to 10,000 psi is approximately 2 for ceramics, 7 for sands, and 30 for the polymeric ULW.
- Permeability increases as grain size increases.
- The permeability of 20/40 sand is about 4 times higher than that of 40/70 sand at all stress levels.
- The permeability of 20/40 ceramic is about 3.5 times higher than that of 40/70 ceramic at all stress levels.
- For a given grain size and closure stress, the permeability of a proppant pack depends on the material.
- For a given grain size, the permeability of ceramic proppant ranges from 2 to 7 times as high as the sand permeability and 3 to 40 times as high as the ULW permeability.
- Proppant permeability is a function of areal concentration.

- As proppant concentration decreases from multiple layers to a single layer, the permeability decreases, then increases as it approaches a partial monolayer with about 80 to 90% coverage, then rapidly decreases.
- There is a maximum areal concentration beyond which the permeability will not increase further.
- For most cases, mixing an equal amount of proppants of two different sizes yields a mixture permeability closer to that of the smaller grain size permeability for stresses greater than 3,000 psi.
- Large sand mixed with smaller proppant is an exception to the previous statement; an equal mixture of these is approximately halfway between that of the two proppants.
- The analytical model successfully validated the experimental results.
- The mean grain diameter fell by a factor of 3 to 5 times after exposure to stress.
- The standard deviation of the size distributions increased after exposure to stress.
- The skewness of each sample before exposure to stress is about -0.6.
- The skewness of each sample after exposure to stress increased significantly.
- The porosity of each sample dropped from about 40% to 35% after exposure to. stress

FUTURE DIRECTIONS

The most natural and obvious way to extend the scope of this study is to experiment with more mixtures. Since it is not uncommon for smaller proppants to be

used at the beginning of fracture jobs, mixtures of 100 mesh grains with the more typical larger grain sizes would provide more insight. Obviously, we can predict with certainty that the 100 mesh proppants would decrease the overall permeability, but the magnitude of the decrease is not as obvious. Also, the mixtures of sand and ceramic presented in this study could be replicated, but with different weight fractions. These could help to verify or disprove the idea of threshold mass fractions which control the state of the mixture.

Another dimension that was not examined in this study is the effect of time at stress on the proppant permeability. This topic was discussed briefly in Chapter 2, but it would be interesting to measure the permeability immediately after stress is applied and repeat every couple of hours for the first day, and then once a day for approximately a week. There is sparse, if any, data on the permeability retention of proppants after a year of exposure to stress; this could be remedied by using simulation techniques to model the response of the grains to stress, obtaining the porosity and grain size distribution from the simulator, tuning the model to match the actual experimental data at early times, using the tuned model to simulate application of stress for a year or more, and finally obtaining the grain size distribution and porosity from the simulator and plugging them into Equation 5.1 to estimate the permeability. This is certainly a rigorous workflow, and construction of an accurate and capable numerical model is not trivial, but this could help answer questions about the long term permeability of proppant packings.

Appendix A: Diagnostic Plots

Most of the measurements that were performed are included in this appendix. The plots themselves are explained in Chapter 3, and so their origin will not be discussed further here, but their key trait is that the slope of the best-fit line is equivalent to the permeability (in units of Darcies) of the proppant packing; they are designed to facilitate usage of Equation 3.9. Each point represents a particular flow rate. Mixtures are in terms of weight percentage.

20/40 SAND

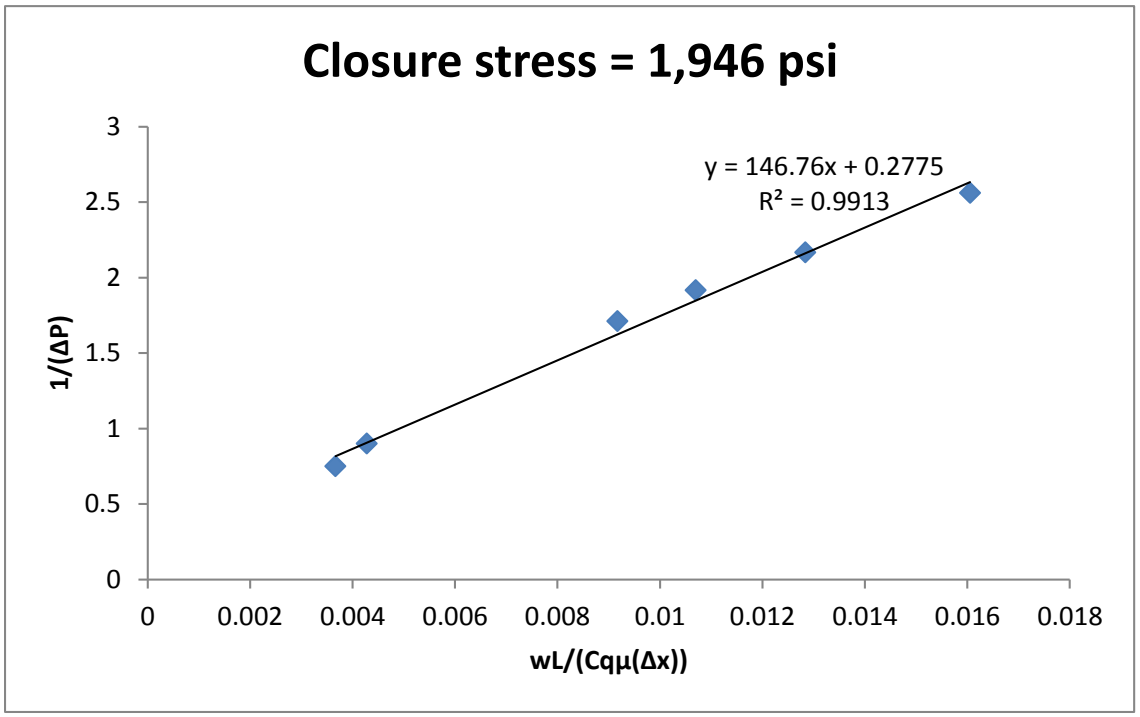

Figure A1: Diagnostic plot of 20/40 sand at 1,946 psi stress.

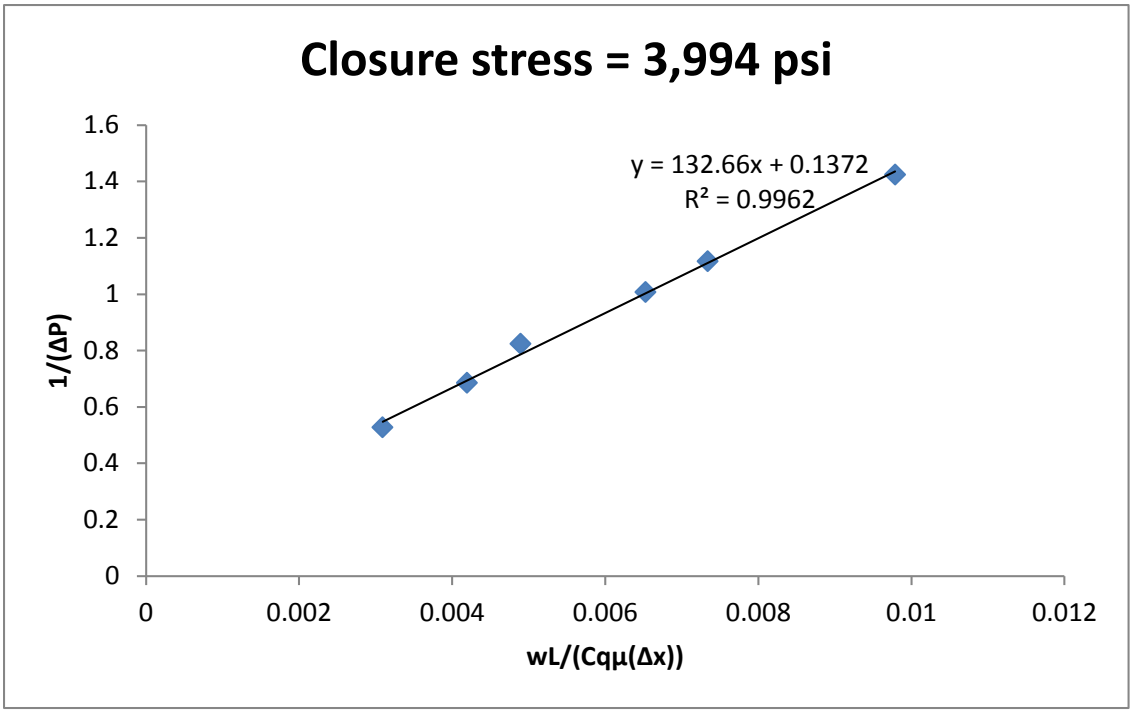

Figure A2: Diagnostic plot of 20/40 sand at 3,994 psi stress.

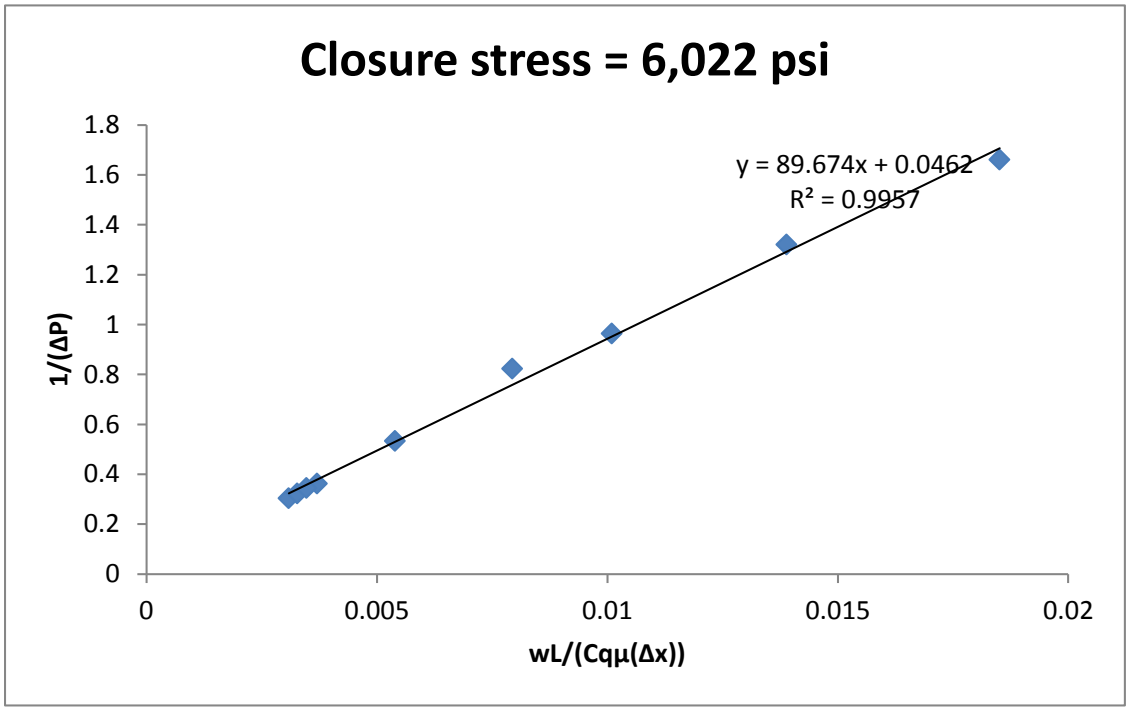

Figure A3: Diagnostic plot of 20/40 sand at 6,022 psi stress.

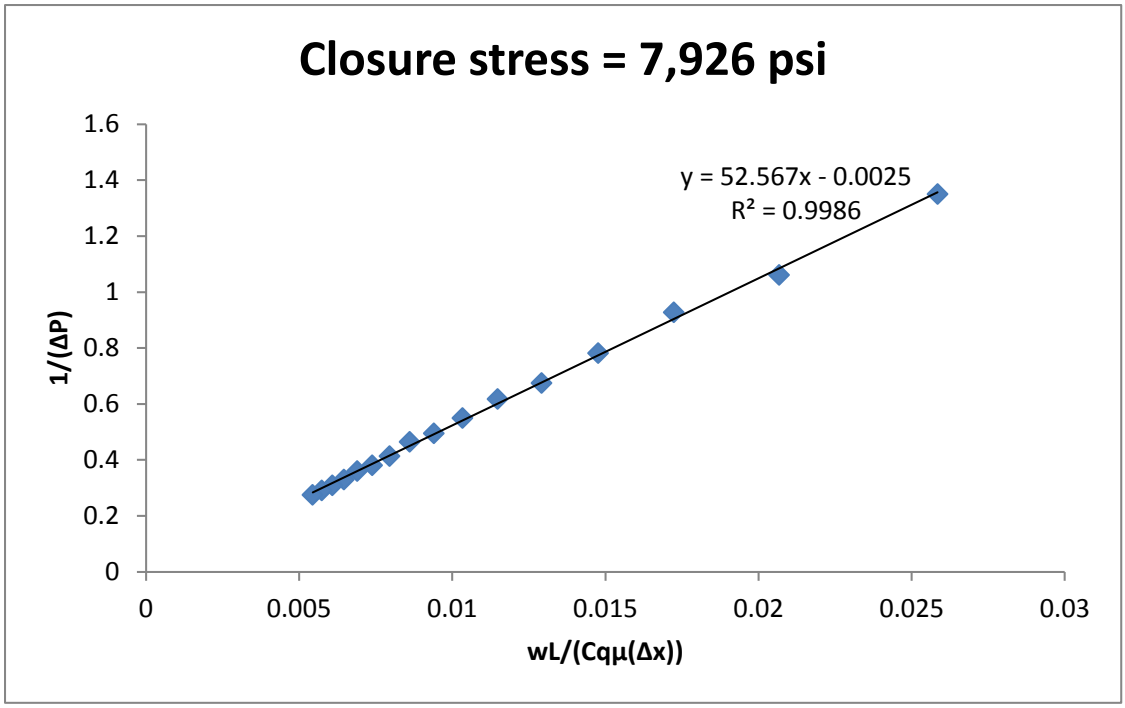

Figure A4: Diagnostic plot of 20/40 sand at 7,926 psi stress.

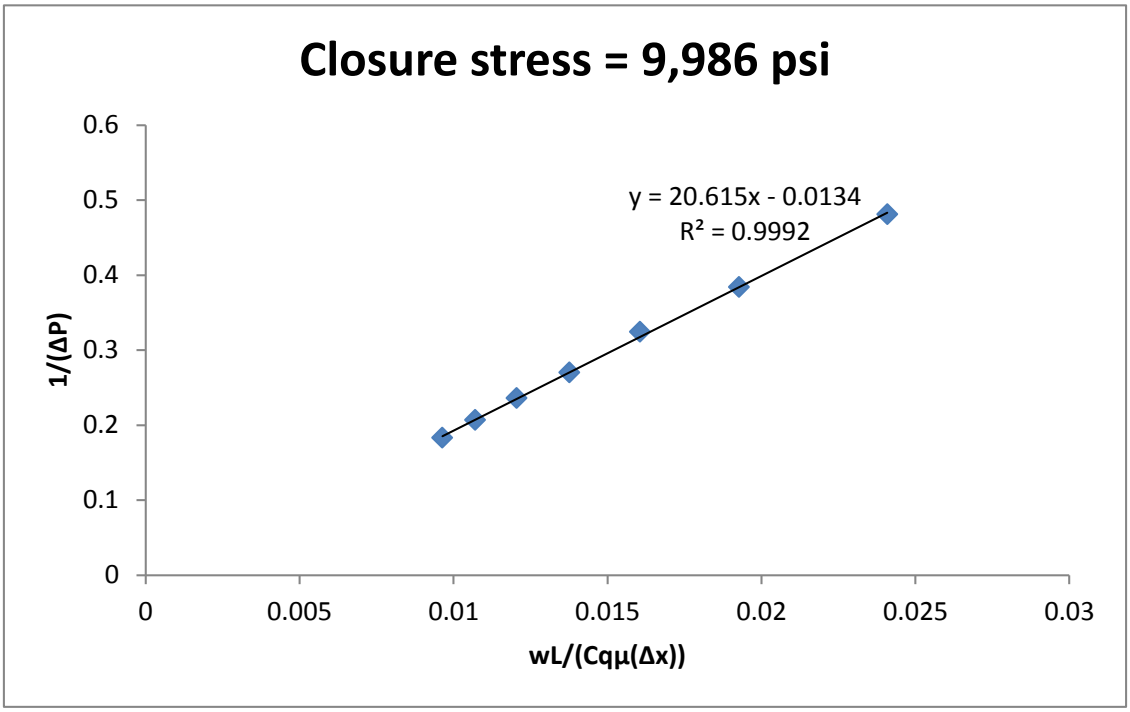

Figure A5: Diagnostic plot of 20/40 sand at 9,986 psi stress.

20/40 SAND & 20/40 CERAMIC (50/50)

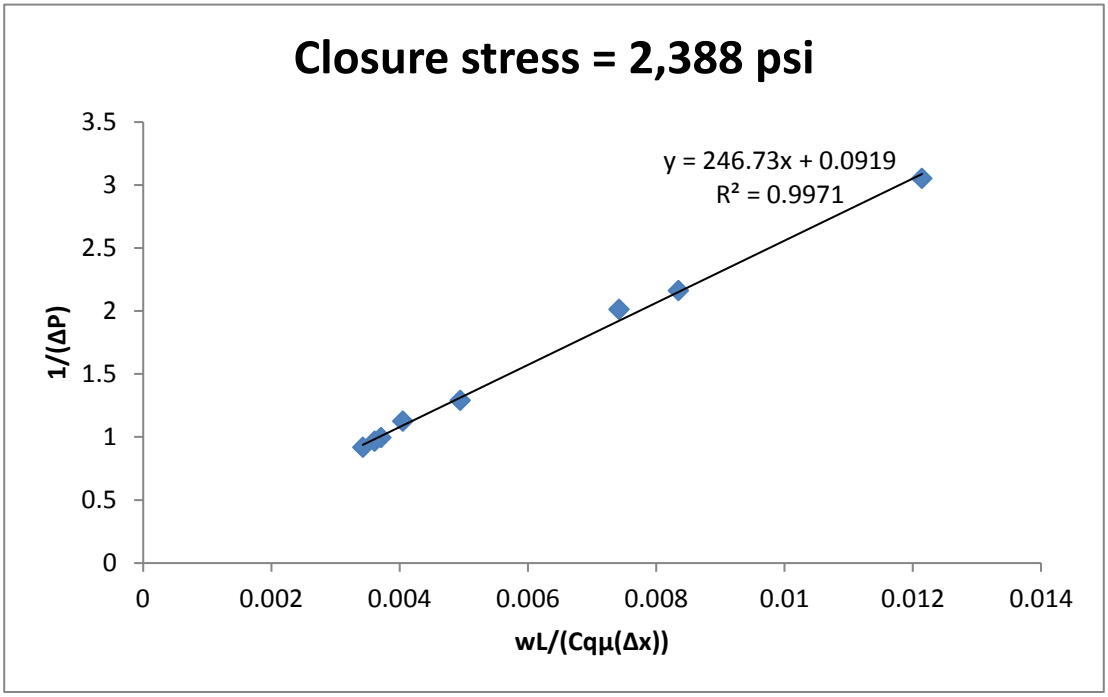

Figure A6: Diagnostic plot of mixture of 50% 20/40 sand and 50% 20/40 ceramic at 2,388 psi stress.

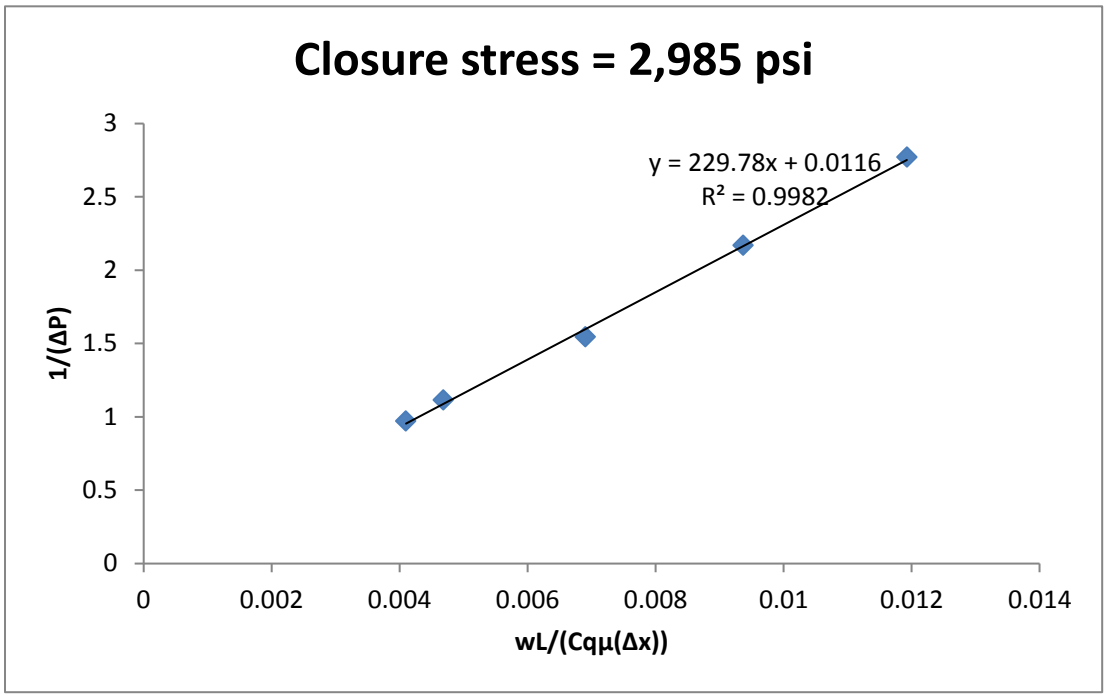

Figure A7: Diagnostic plot of mixture of 50% 20/40 sand and 50% 20/40 ceramic at 2,985 psi stress.

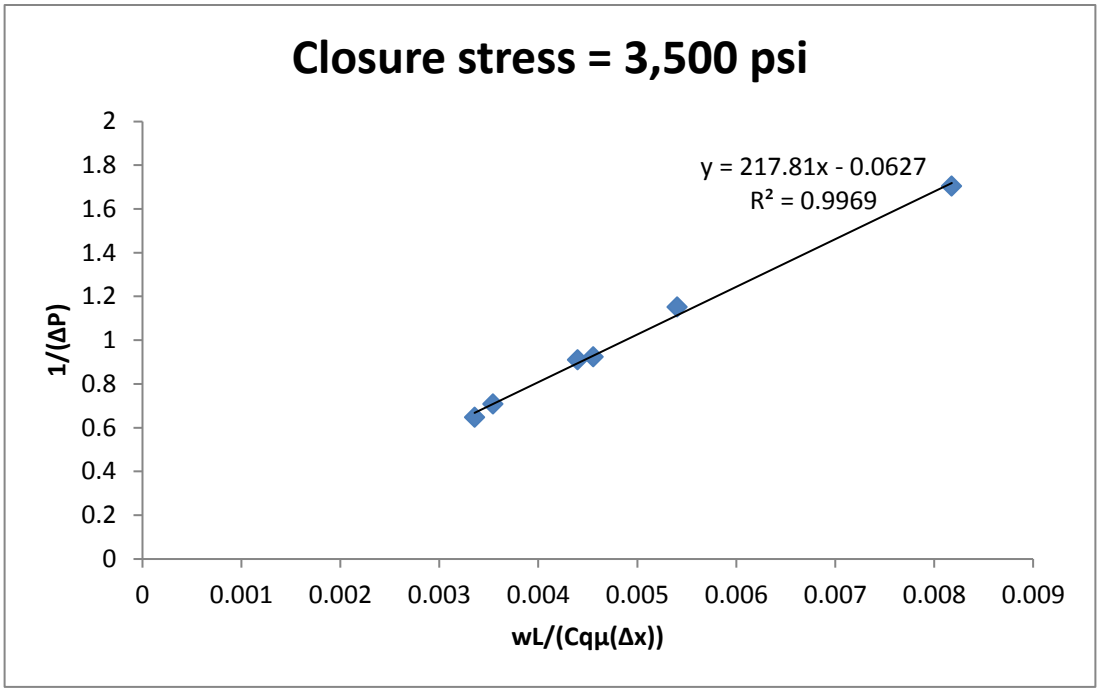

Figure A8: Diagnostic plot of mixture of 50% 20/40 sand and 50% 20/40 ceramic at 3,500 psi stress.

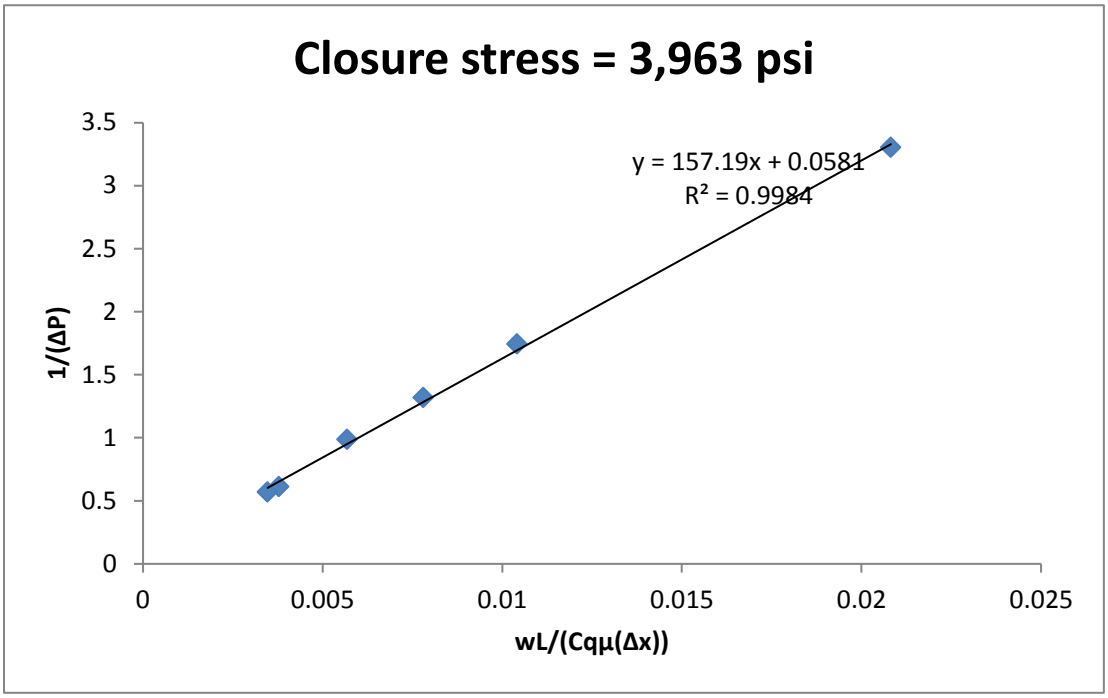

Figure A9: Diagnostic plot of mixture of 50% 20/40 sand and 50% 20/40 ceramic at 3,963 psi stress.

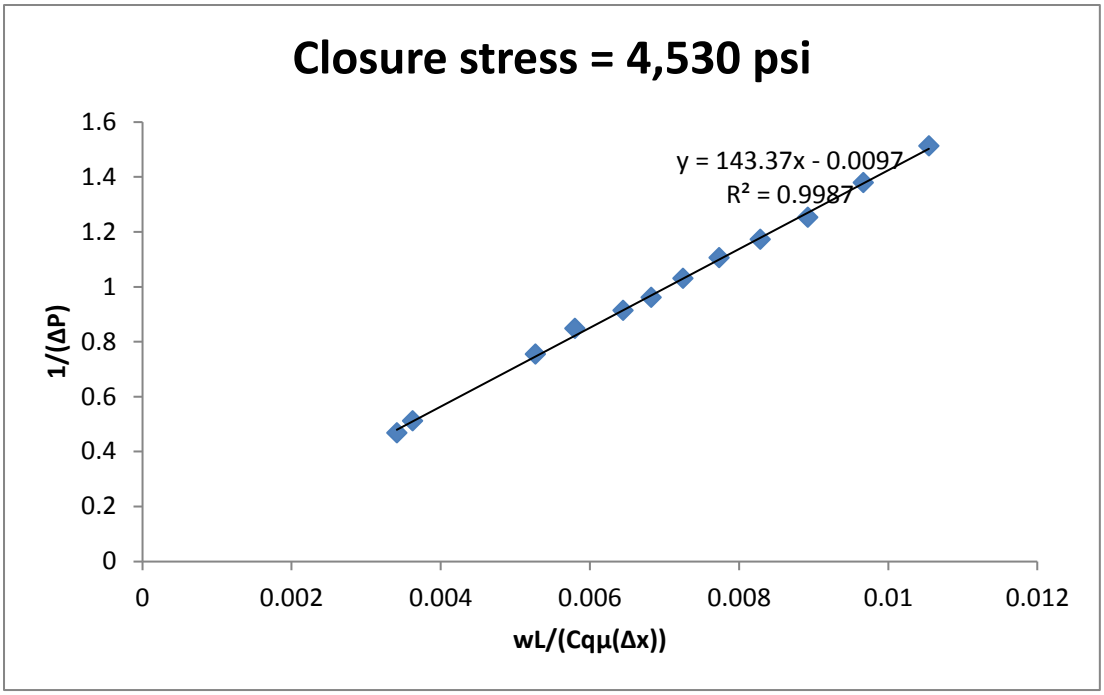

Figure A10: Diagnostic plot of mixture of 50% 20/40 sand and 50% 20/40 ceramic at 4,530 psi stress.

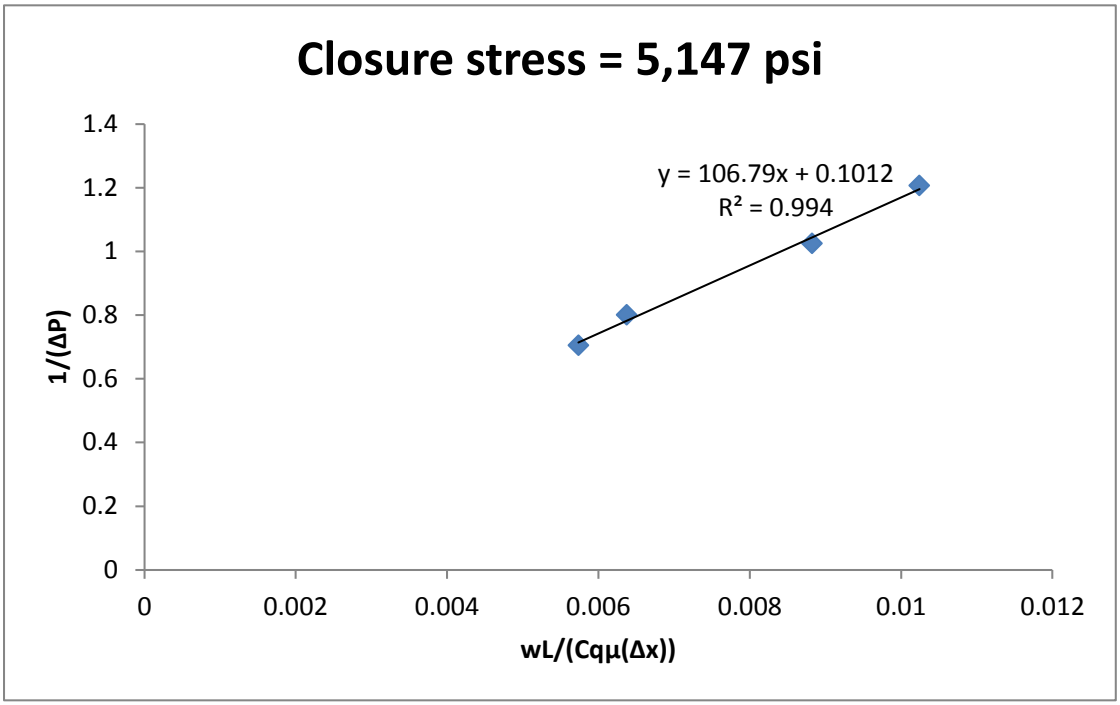

Figure A11: Diagnostic plot of mixture of 50% 20/40 sand and 50% 20/40 ceramic at 5,147 psi stress.

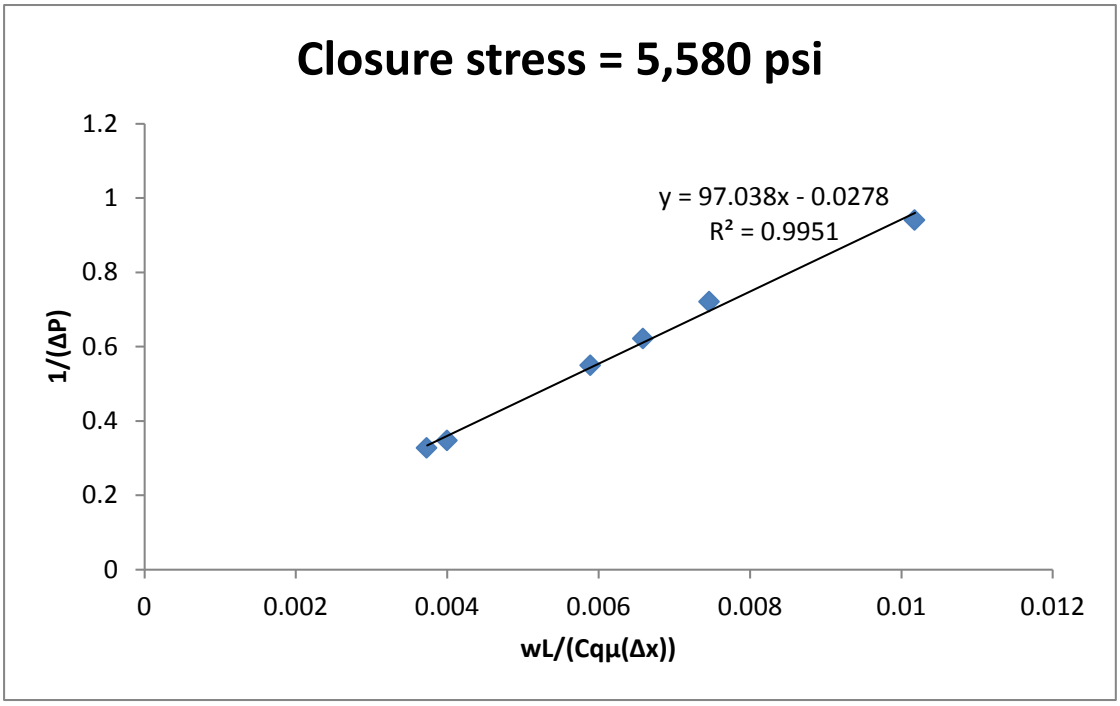

Figure A12: Diagnostic plot of mixture of 50% 20/40 sand and 50% 20/40 ceramic at 5,580 psi stress.

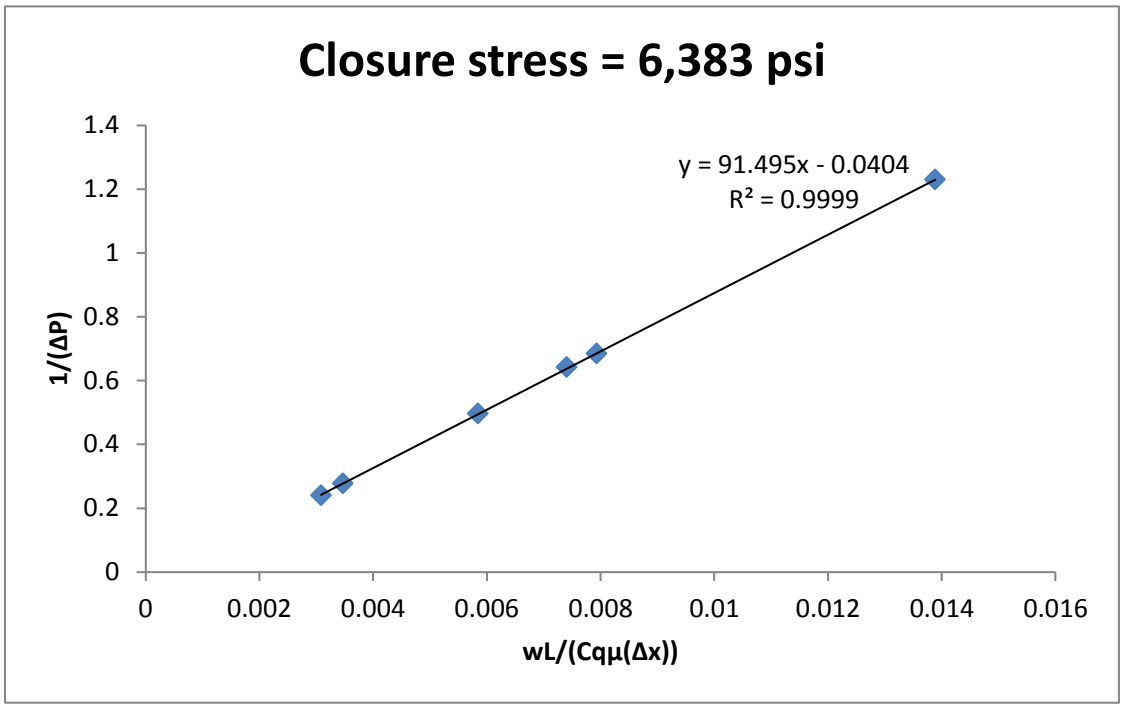

Figure A13: Diagnostic plot of mixture of 50% 20/40 sand and 50% 20/40 ceramic at 6,383 psi stress.

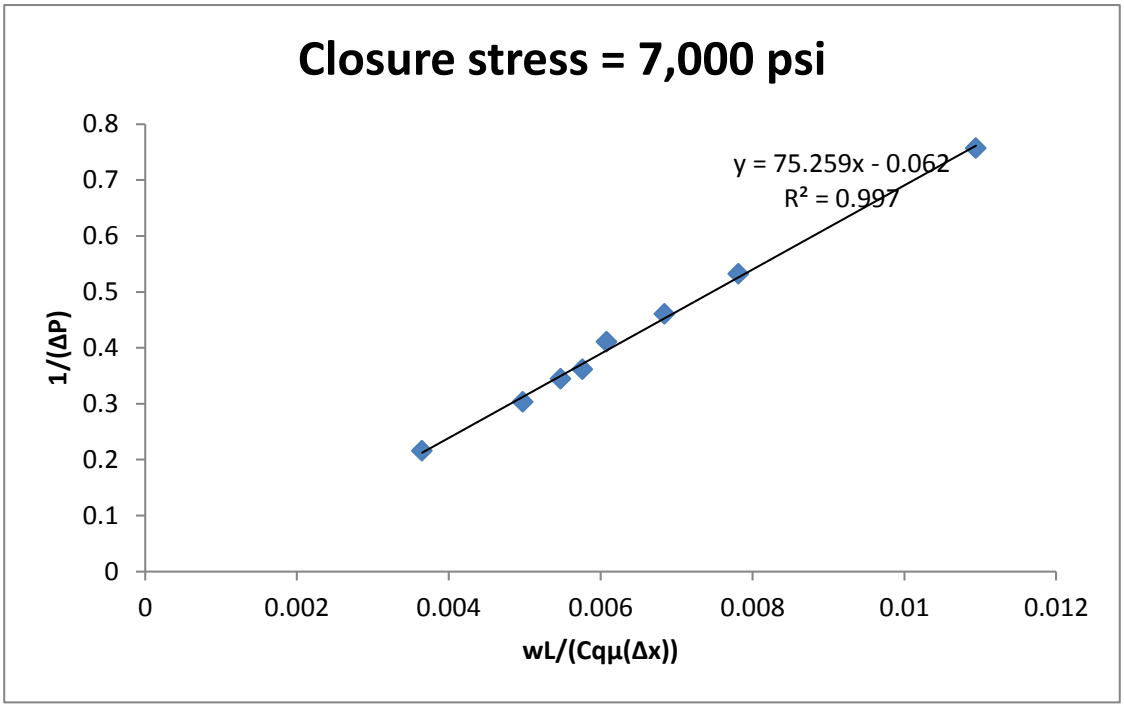

Figure A14: Diagnostic plot of mixture of 50% 20/40 sand and 50% 20/40 ceramic at 7,000 psi stress.

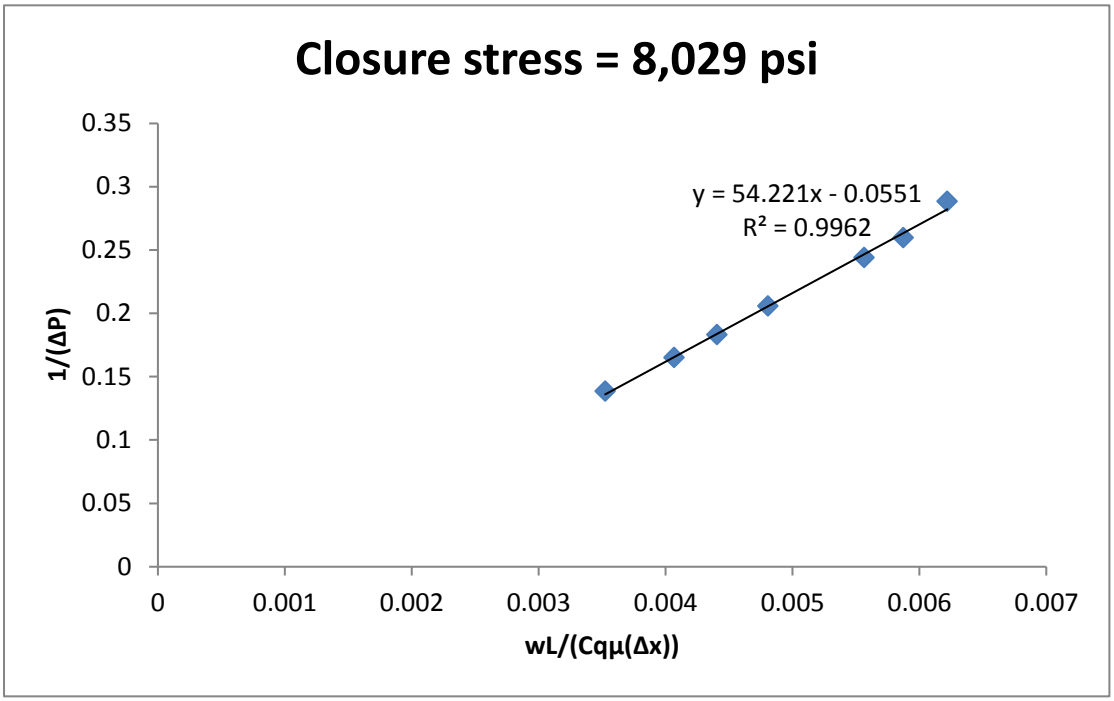

Figure A15: Diagnostic plot of mixture of 50% 20/40 sand and 50% 20/40 ceramic at 8,029 psi stress.

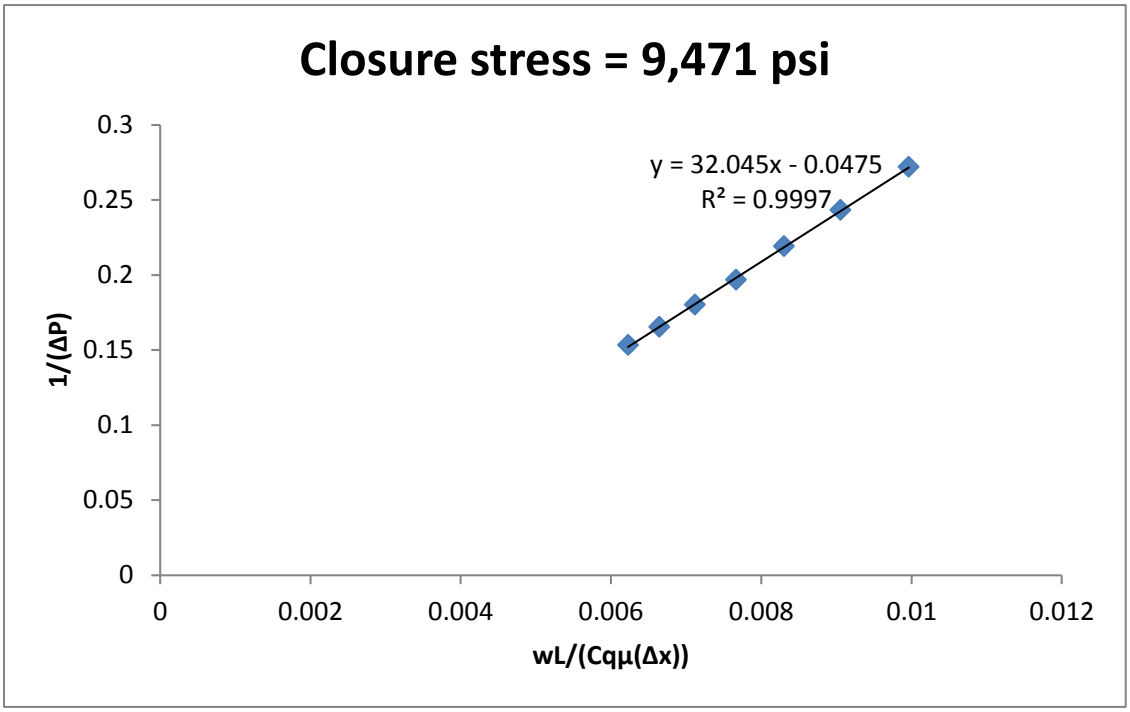

Figure A16: Diagnostic plot of mixture of 50% 20/40 sand and 50% 20/40 ceramic at 9,471 psi stress.

20/40 SAND & 20/40 CERAMIC (25/75)

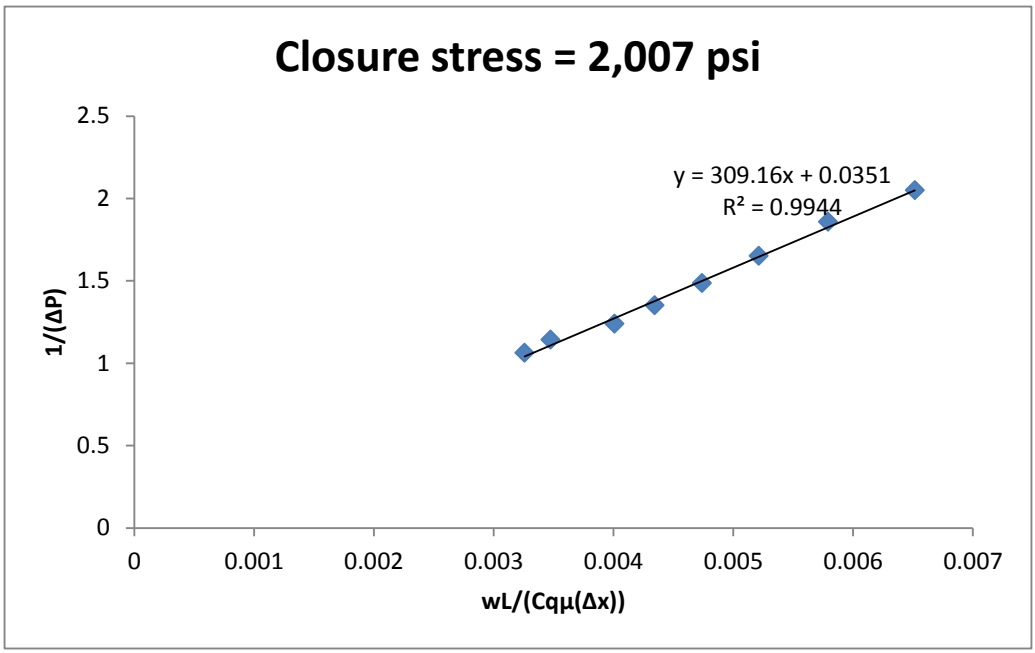

Figure A17: Diagnostic plot of mixture of 25% 20/40 sand and 75% 20/40 ceramic at 2,007 psi stress.

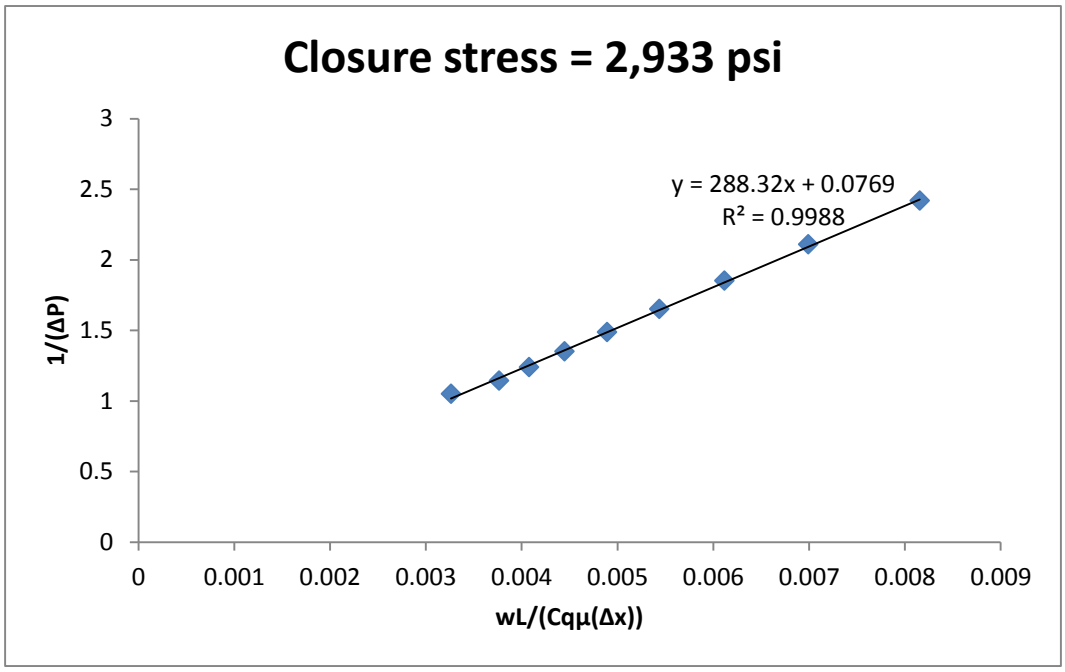

Figure A18: Diagnostic plot of mixture of 25% 20/40 sand and 75% 20/40 ceramic at 2,933 psi stress.

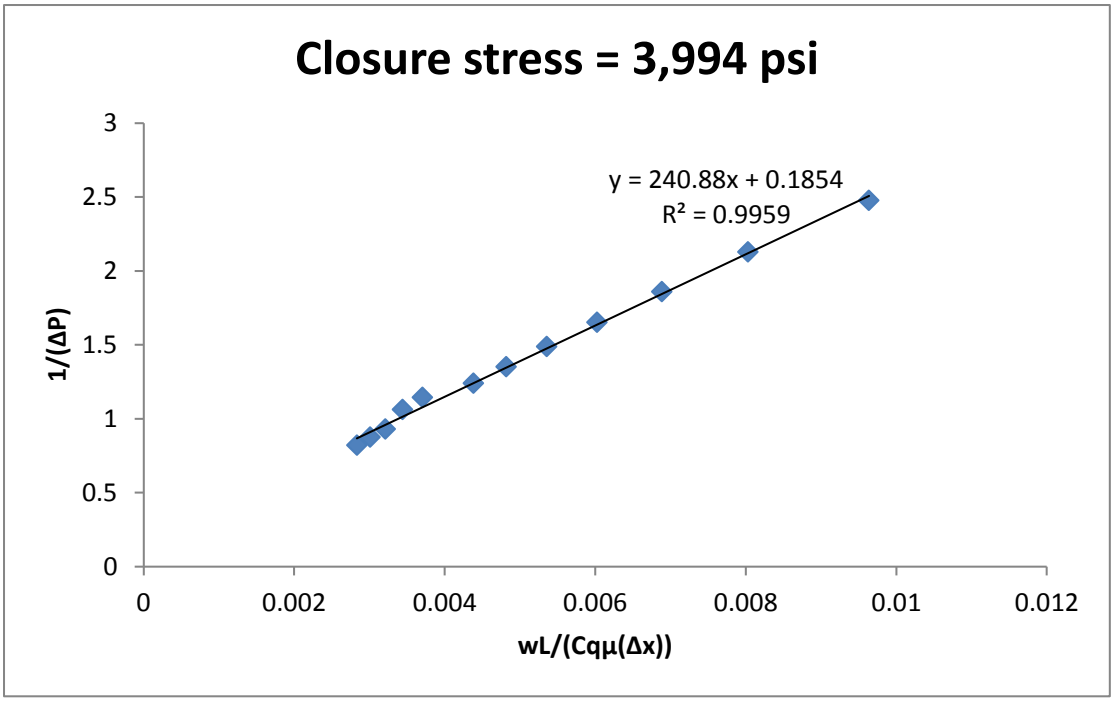

Figure A19: Diagnostic plot of mixture of 25% 20/40 sand and 75% 20/40 ceramic at 3,994 psi stress.

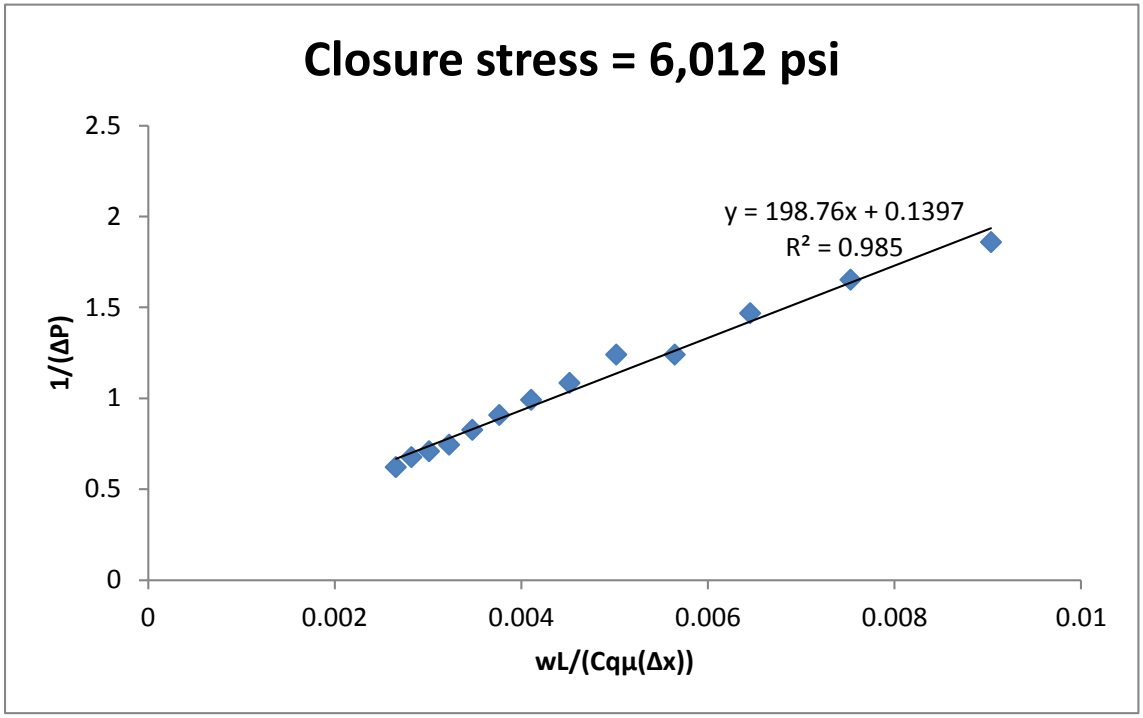

Figure A20: Diagnostic plot of mixture of 25% 20/40 sand and 75% 20/40 ceramic at 6,012 psi stress.

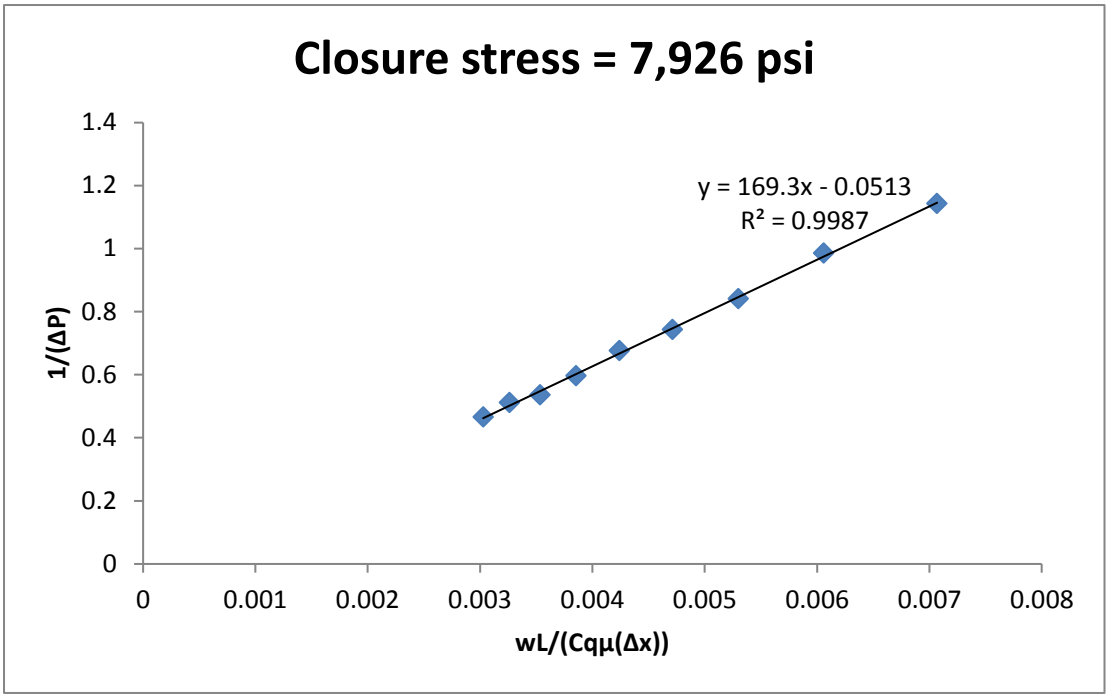

Figure A21: Diagnostic plot of mixture of 25% 20/40 sand and 75% 20/40 ceramic at 7,926 psi stress.

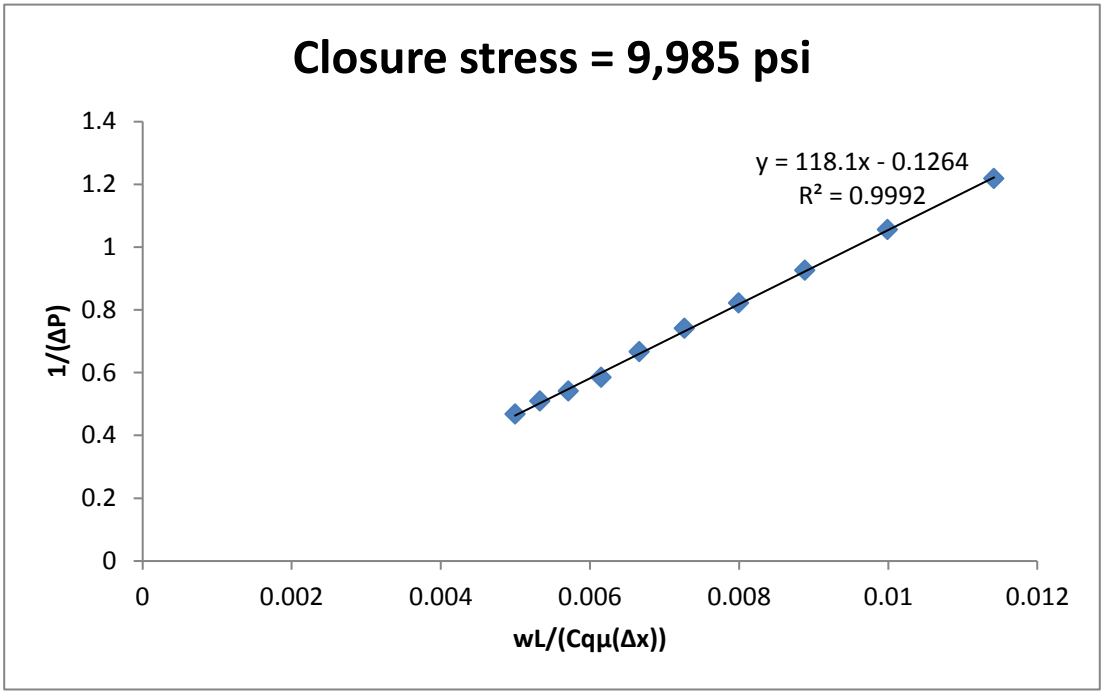

Figure A22: Diagnostic plot of mixture of 25% 20/40 sand and 75% 20/40 ceramic at 9,985 psi stress.

20/40 CERAMIC

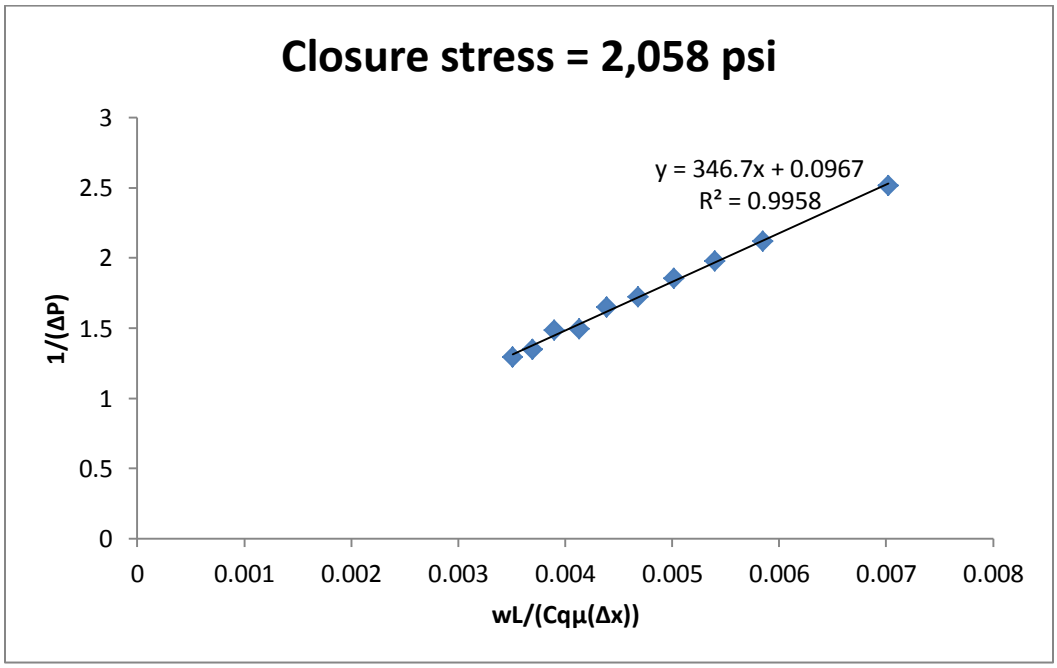

Figure A23: Diagnostic plot of 20/40 ceramic at 2,058 psi stress.

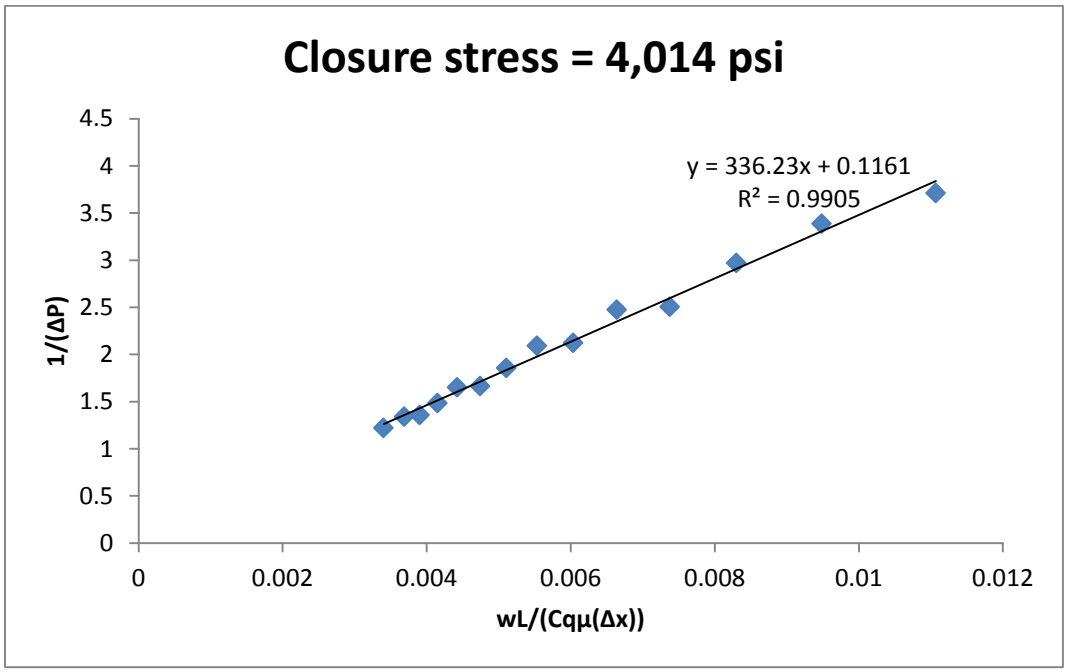

Figure A24: Diagnostic plot of 20/40 ceramic at 4,014 psi stress.

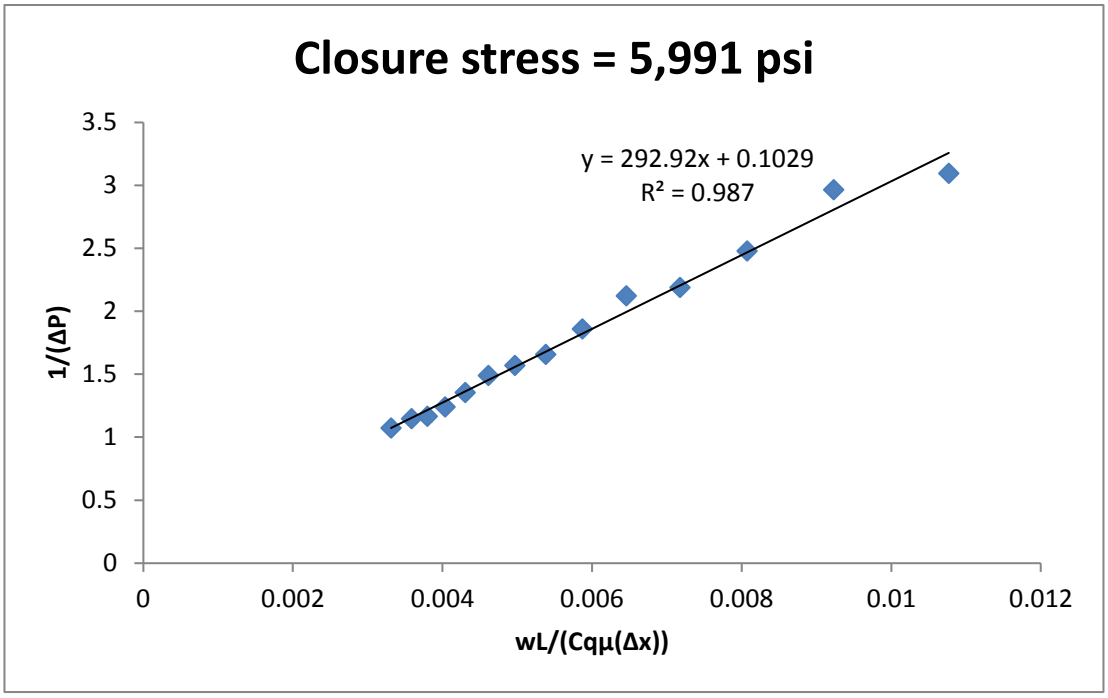

Figure A25: Diagnostic plot of 20/40 ceramic at 5,991 psi stress.

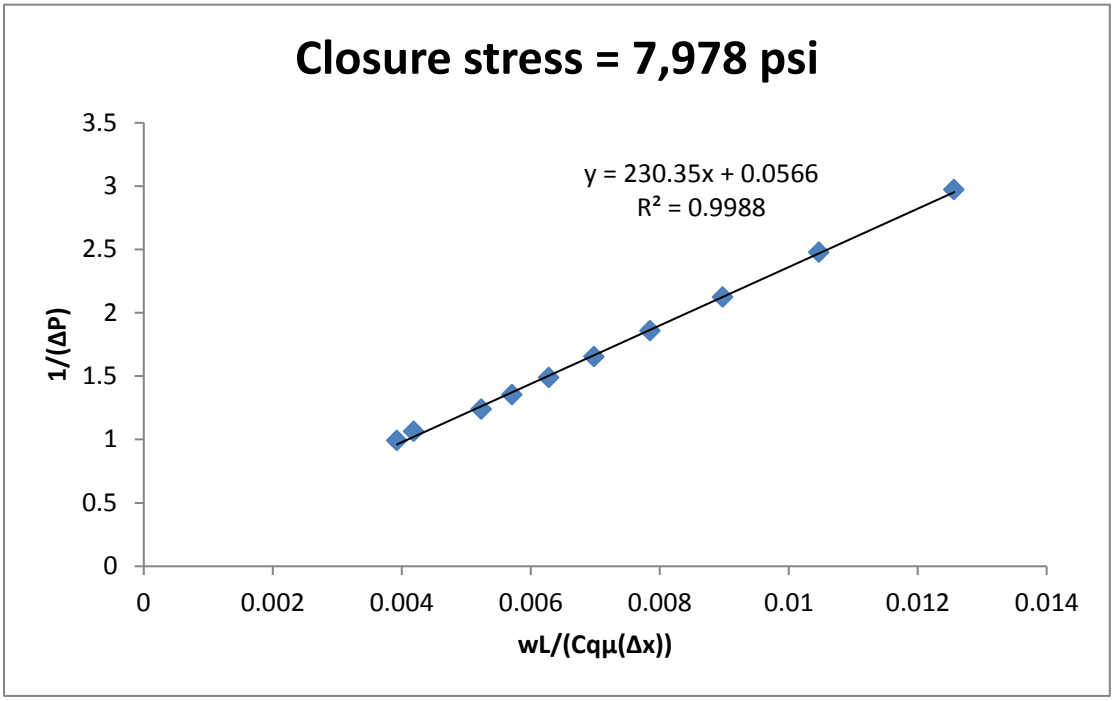

Figure A26: Diagnostic plot of 20/40 ceramic at 7,978 psi stress.

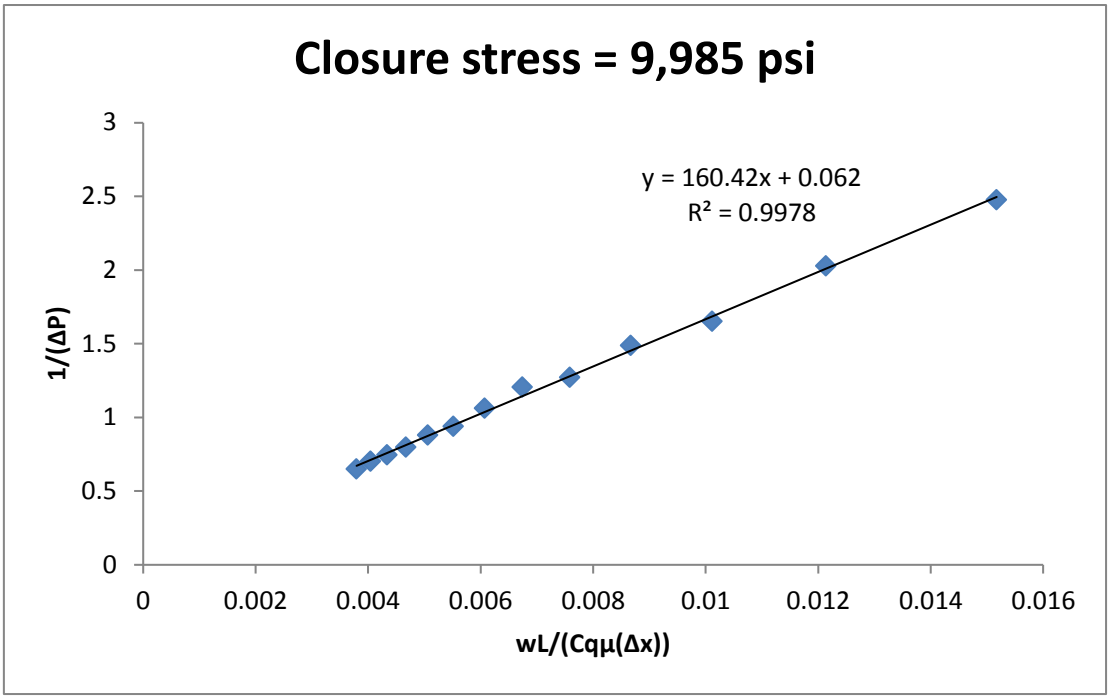

Figure A27: Diagnostic plot of 20/40 ceramic at 9,985 psi stress.

40/70 SAND

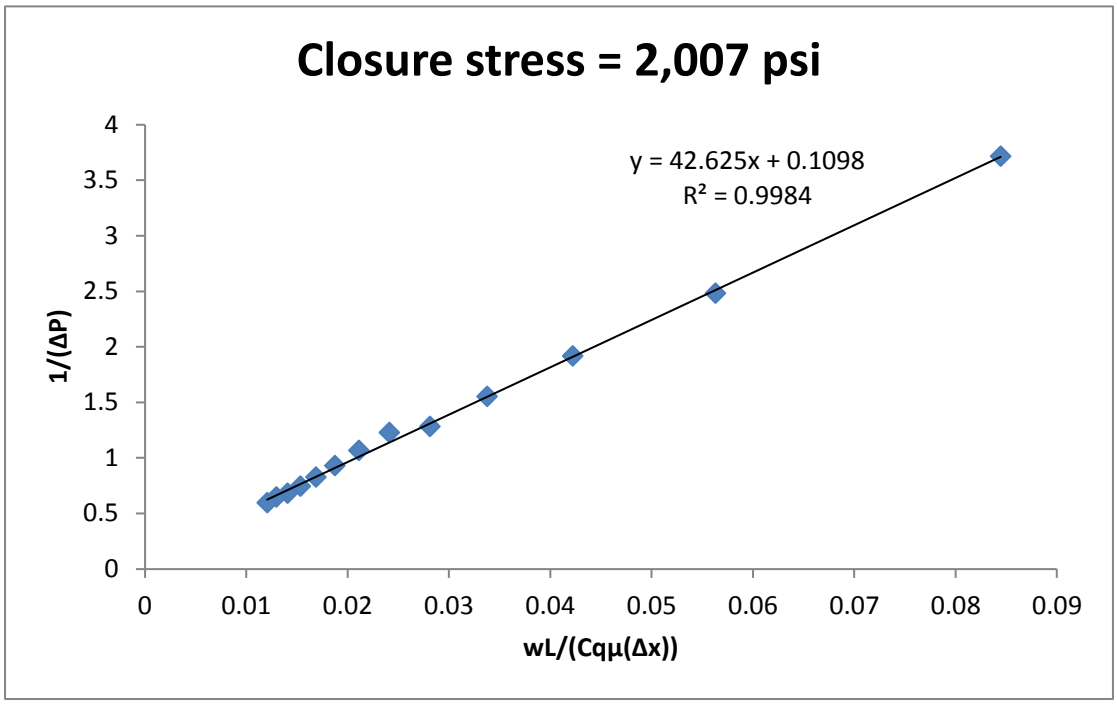

Figure A28: Diagnostic plot of 40/70 sand at 2,007 psi stress.

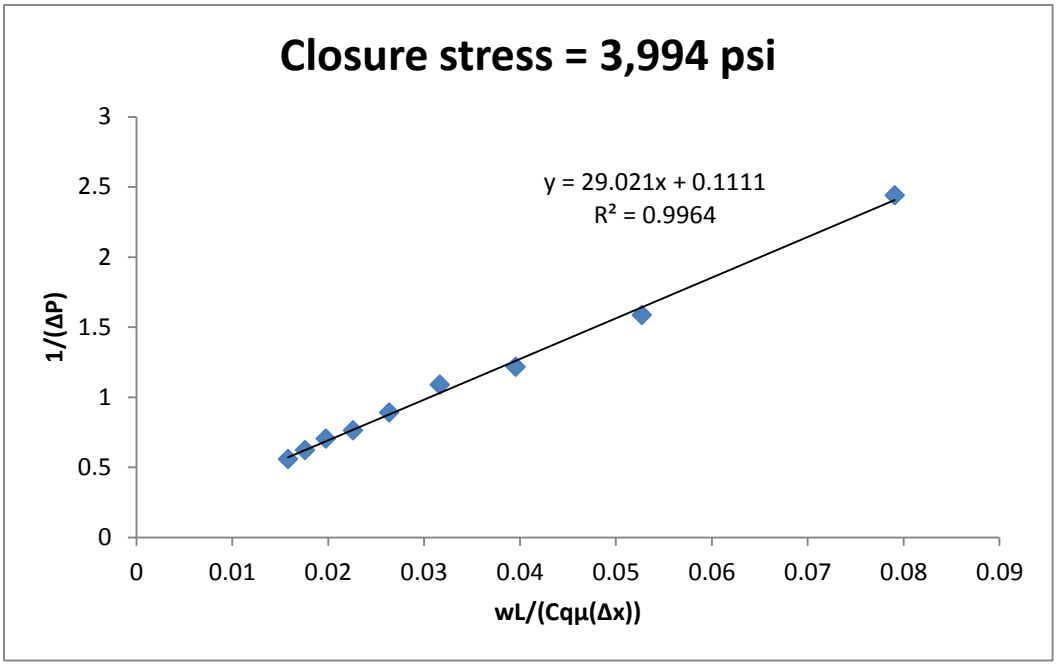

Figure A29: Diagnostic plot of 40/70 sand at 3,994 psi stress.

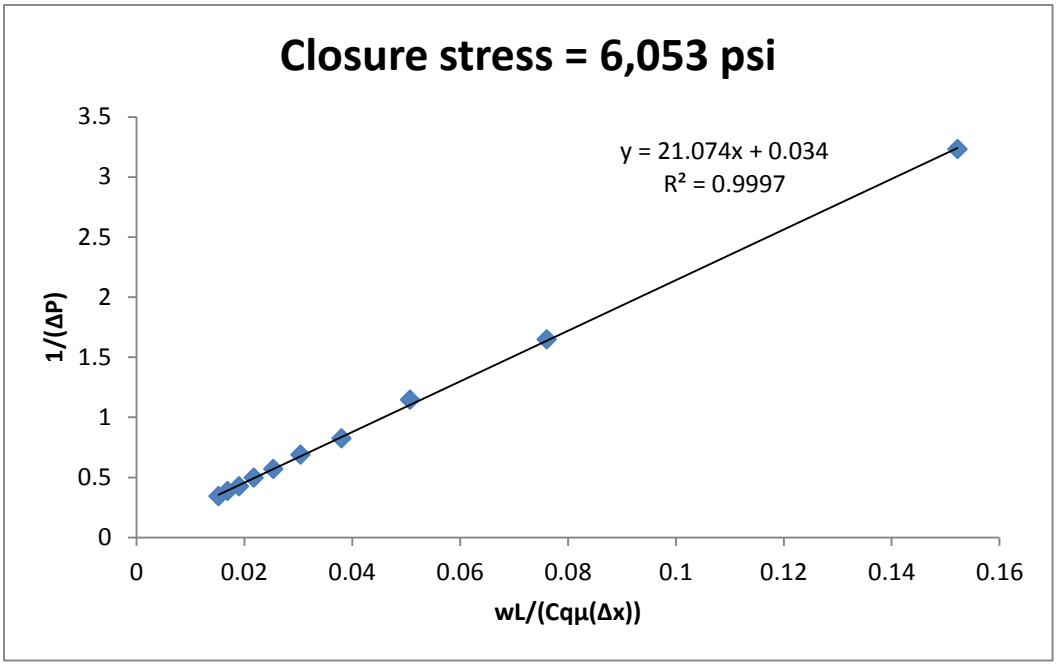

Figure A30: Diagnostic plot of 40/70 sand at 6,053 psi stress.

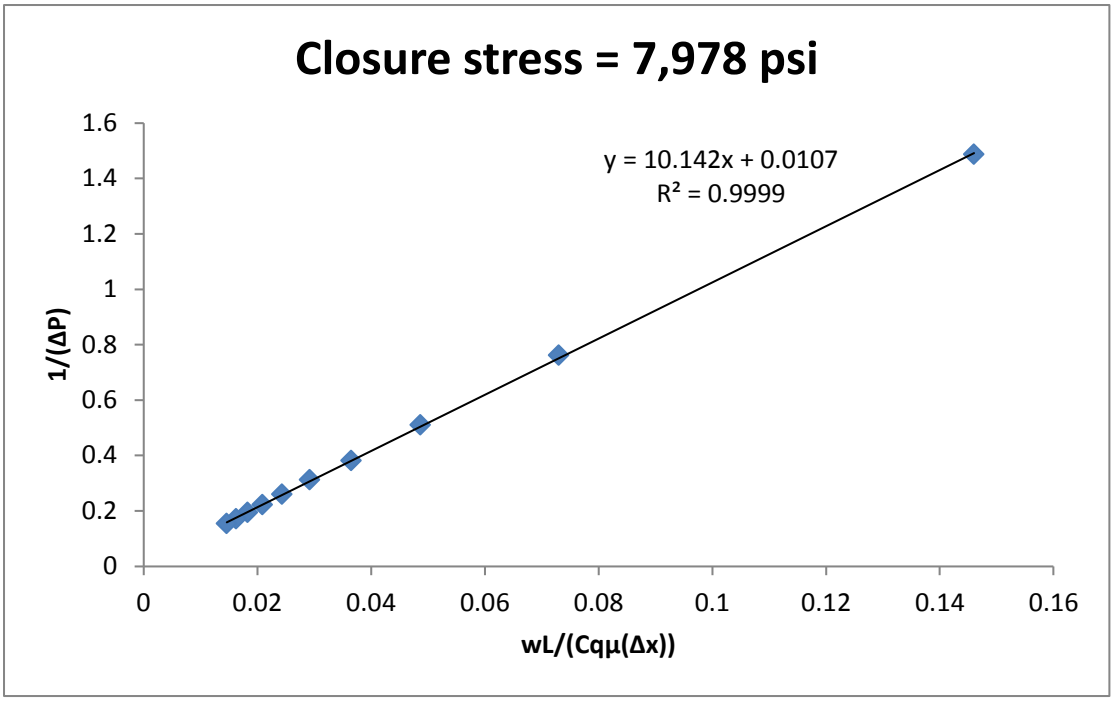

Figure A31: Diagnostic plot of 40/70 sand at 7,978 psi stress.

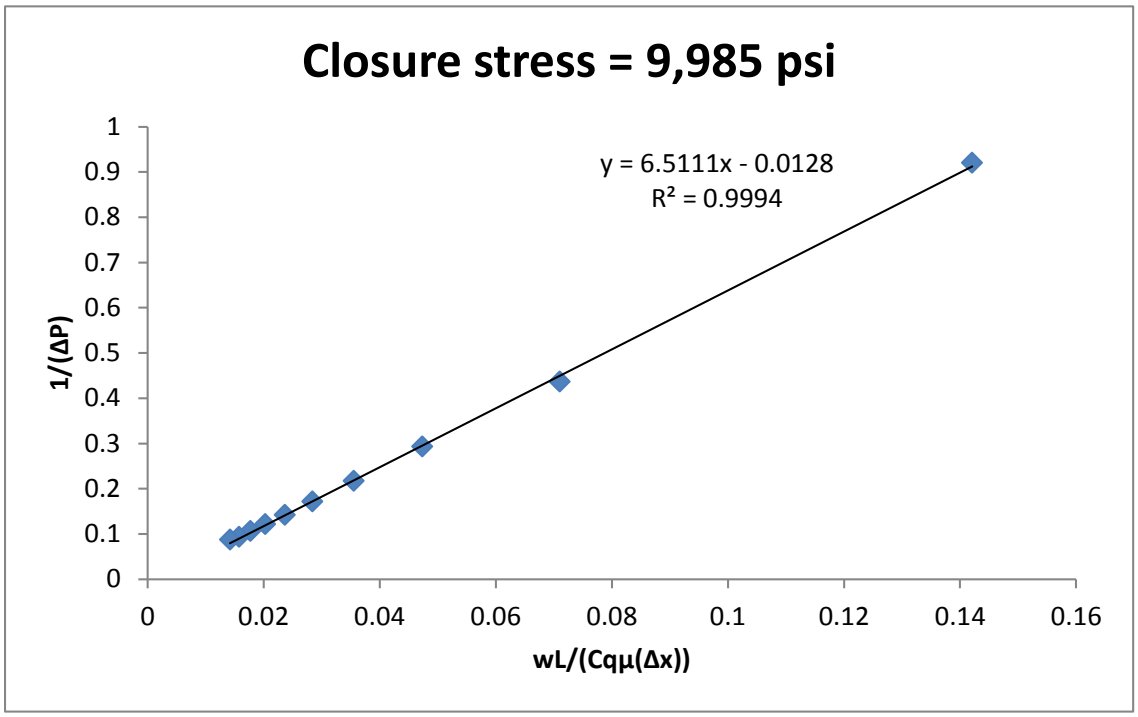

Figure A32: Diagnostic plot of 40/70 sand at 9,985 psi stress.

20/40 CERAMIC & 40/70 SAND (50/50)

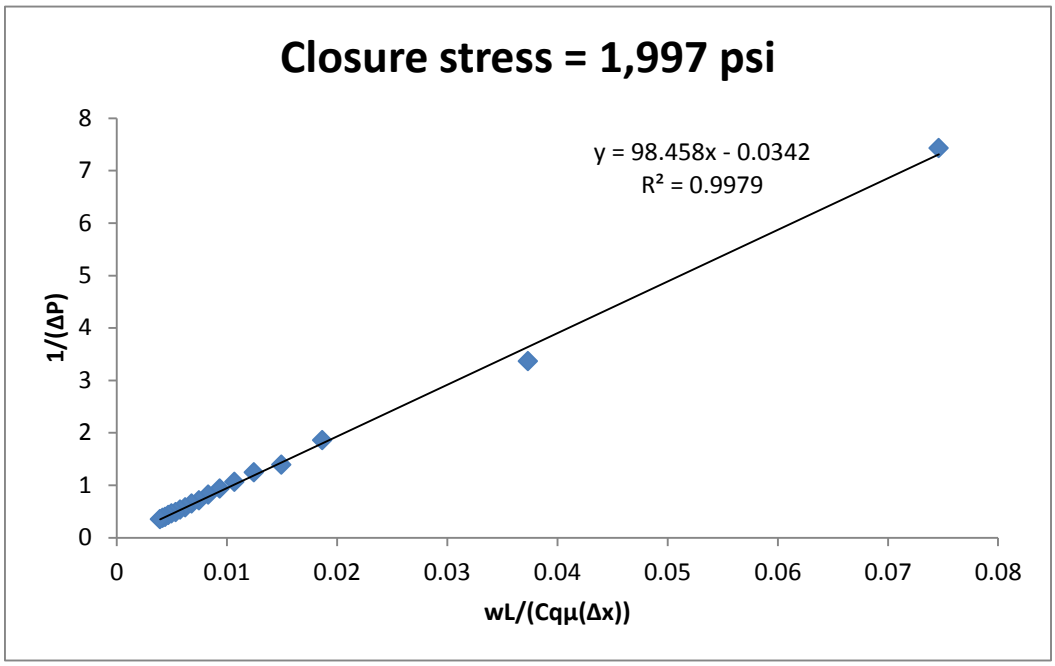

Figure A33: Diagnostic plot of mixture of 50% 20/40 ceramic and 50% 40/70 sand at 1,997 psi stress.

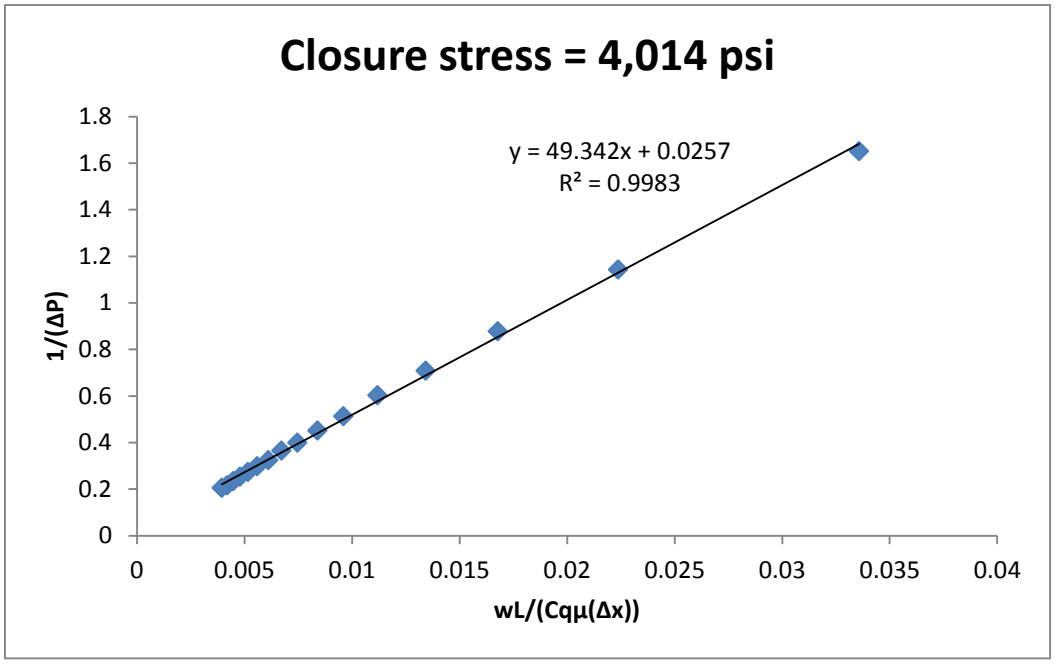

Figure A34: Diagnostic plot of mixture of 50% 20/40 ceramic and 50% 40/70 sand at 4,014 psi stress.

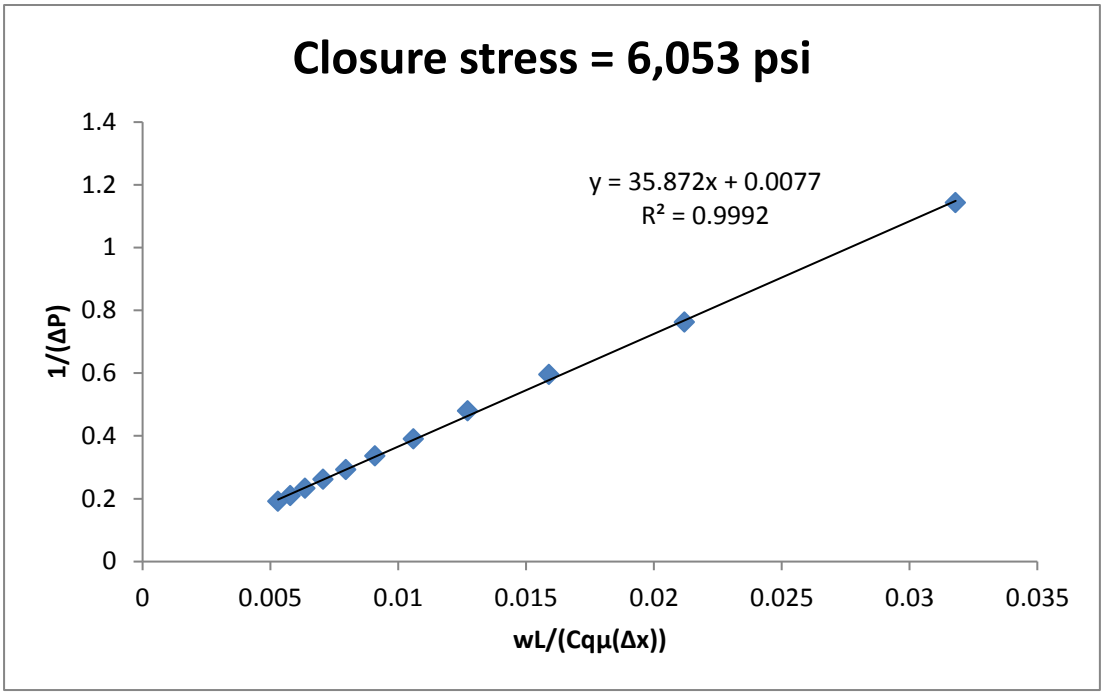

Figure A35: Diagnostic plot of mixture of 50% 20/40 ceramic and 50% 40/70 sand at 6,053 psi stress.

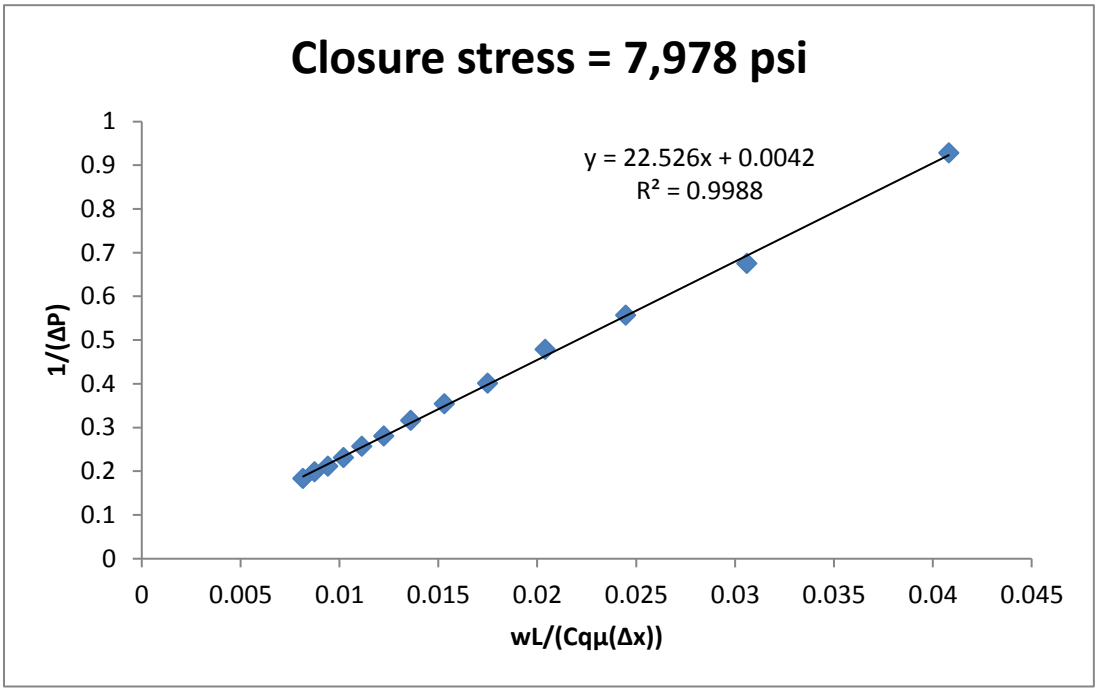

Figure A36: Diagnostic plot of mixture of 50% 20/40 ceramic and 50% 40/70 sand at 7,978 psi stress.

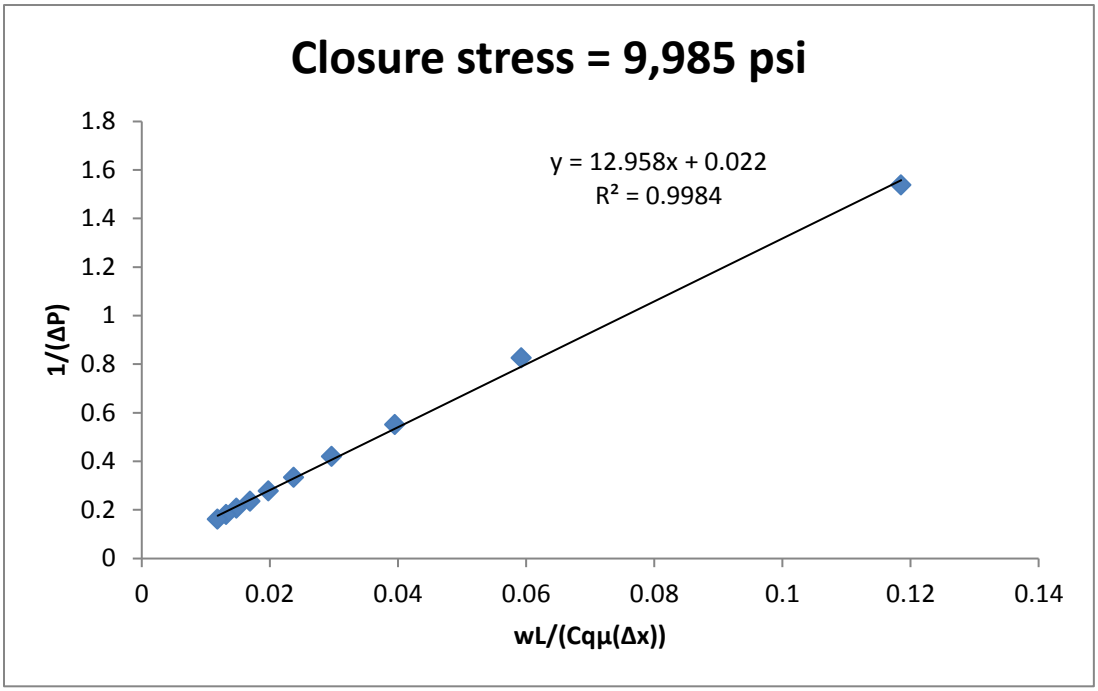

Figure A37: Diagnostic plot of mixture of 50% 20/40 ceramic and 50% 40/70 sand at 9,985 psi stress.

20/40 CERAMIC & 40/70 SAND (75/25)

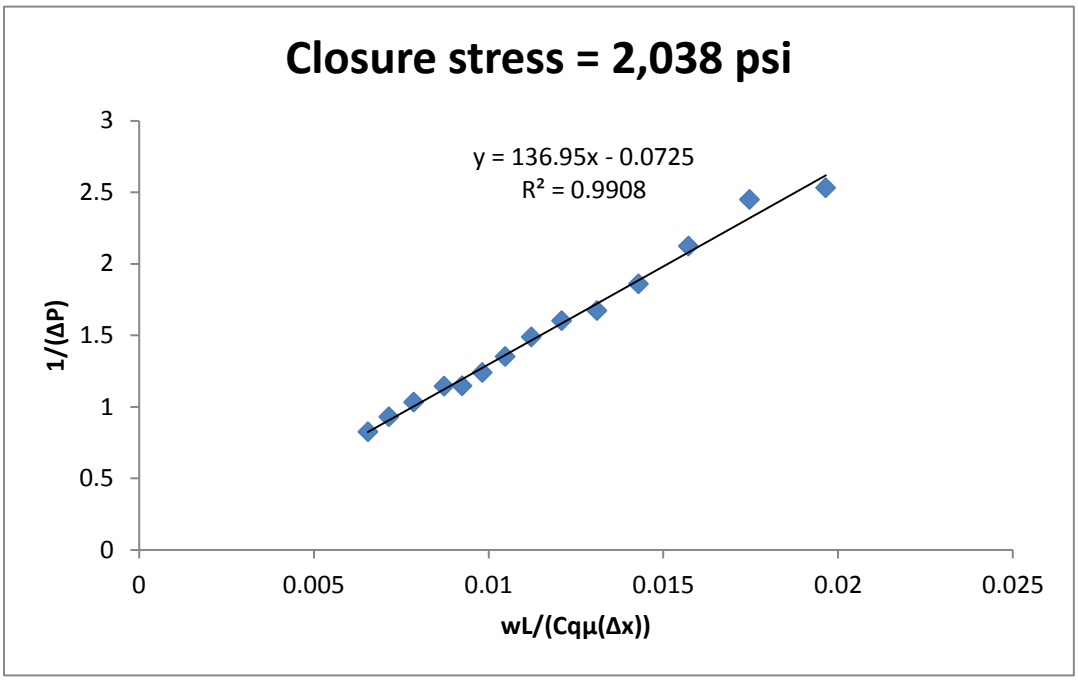

Figure A38: Diagnostic plot of mixture of 75% 20/40 ceramic and 25% 40/70 sand at 2,038 psi stress.

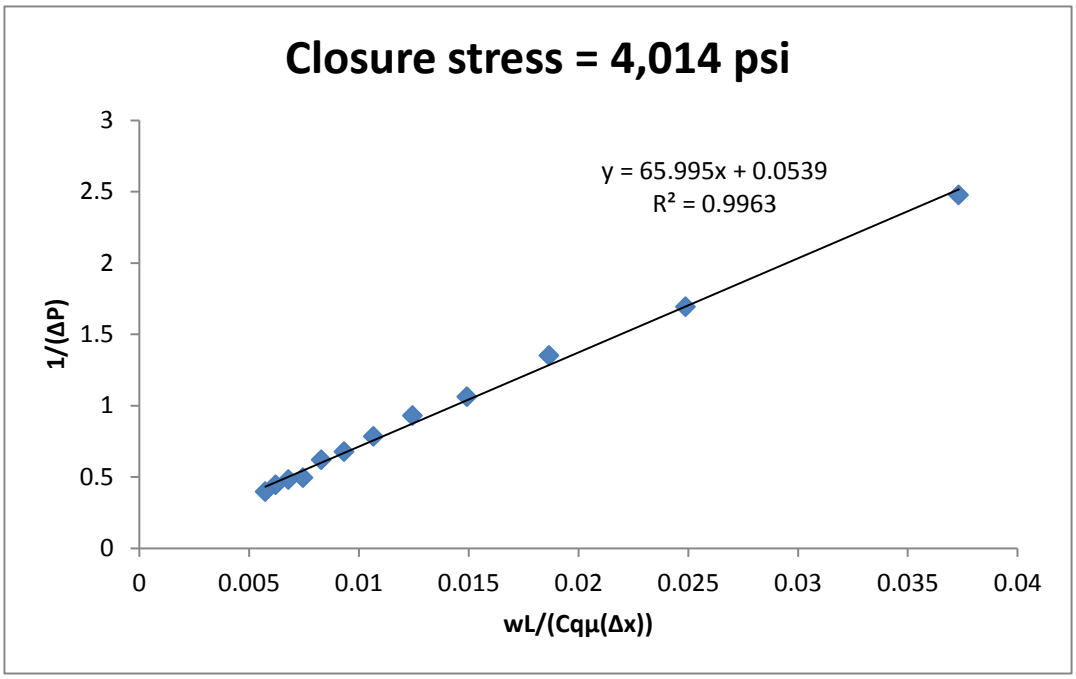

Figure A39: Diagnostic plot of mixture of 75% 20/40 ceramic and 25% 40/70 sand at 4,014 psi stress.

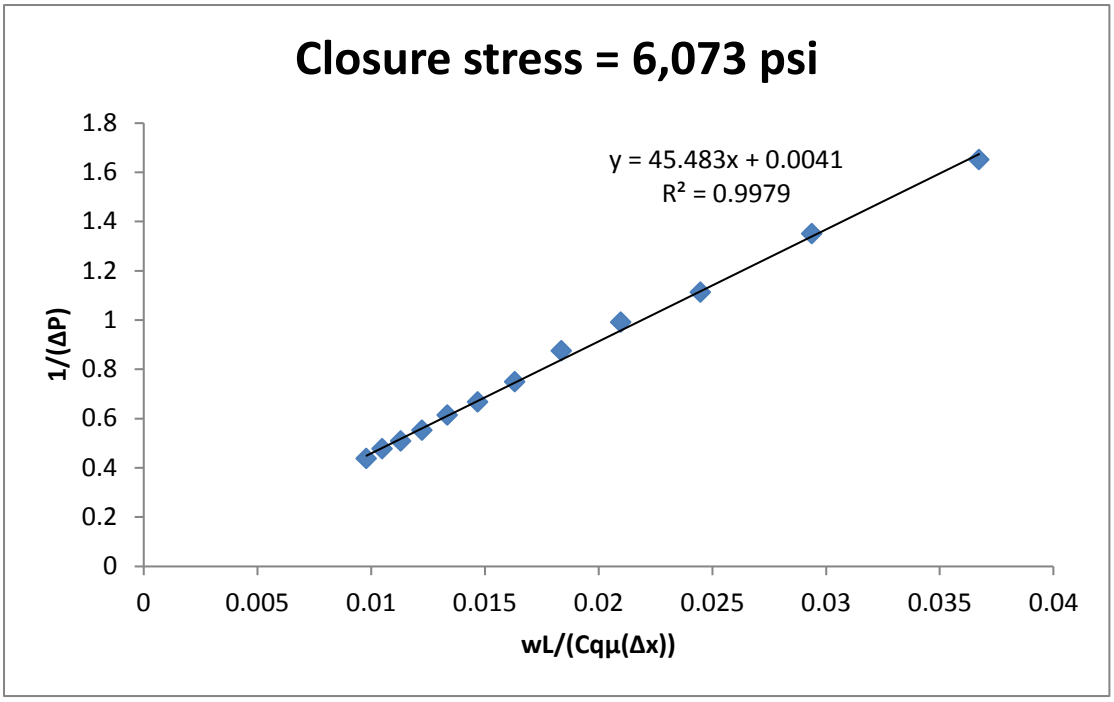

Figure A40: Diagnostic plot of mixture of 75% 20/40 ceramic and 25% 40/70 sand at 6,073 psi stress.

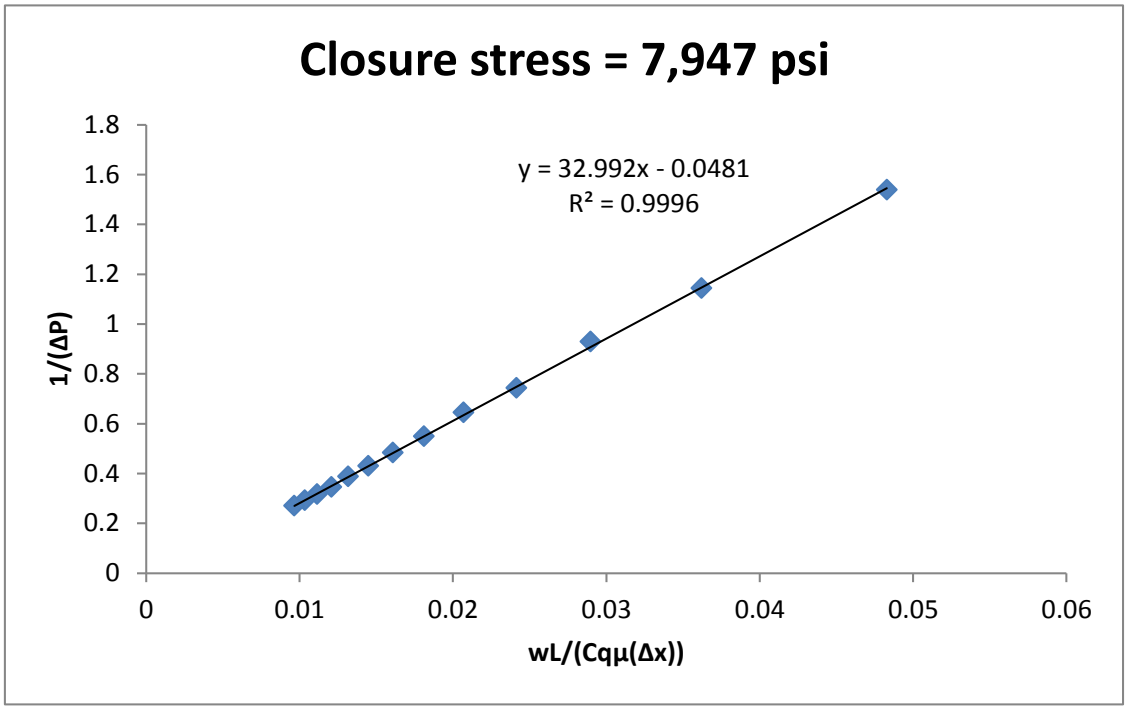

Figure A41: Diagnostic plot of mixture of 75% 20/40 ceramic and 25% 40/70 sand at 7,947 psi stress.

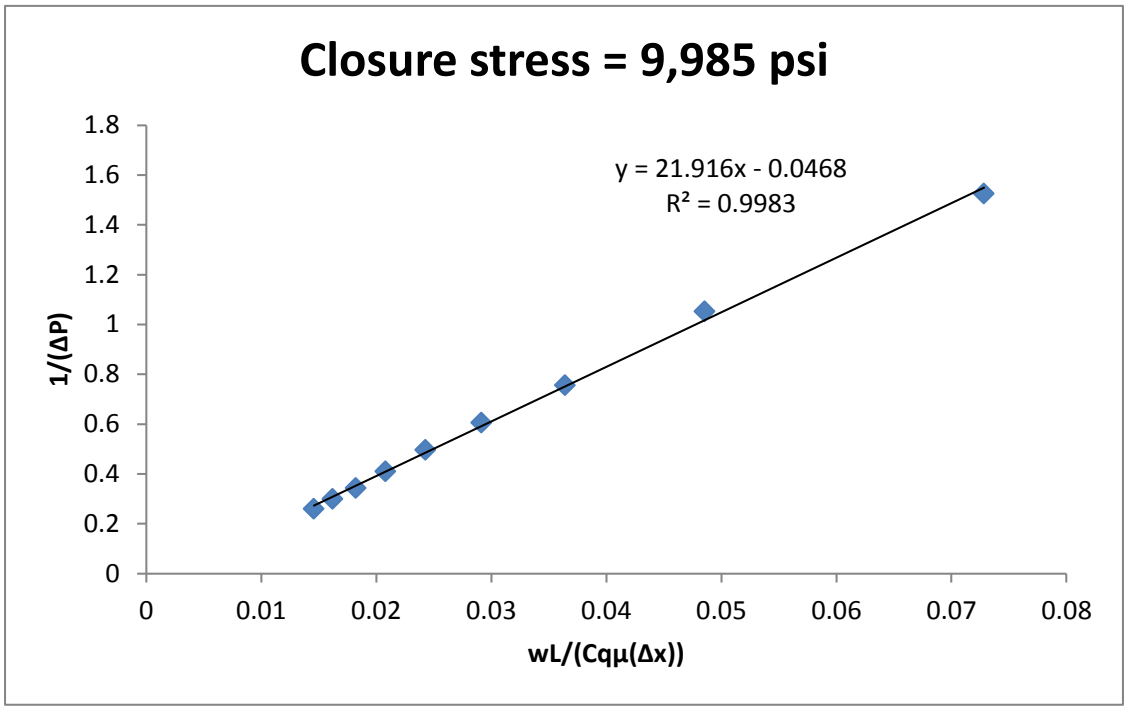

Figure A42: Diagnostic plot of mixture of 75% 20/40 ceramic and 25% 40/70 sand at 9,985 psi stress.

20/40 SAND & 40/70 SAND (50/50)

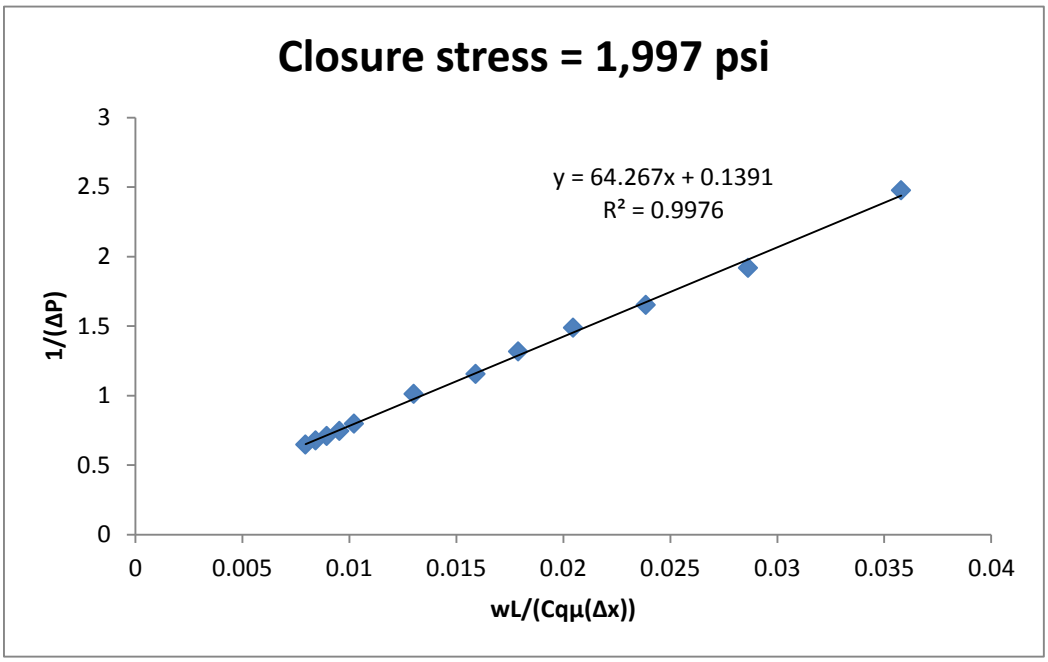

Figure A43: Diagnostic plot of mixture of 50% 20/40 sand and 50% 40/70 sand at 1,997 psi stress.

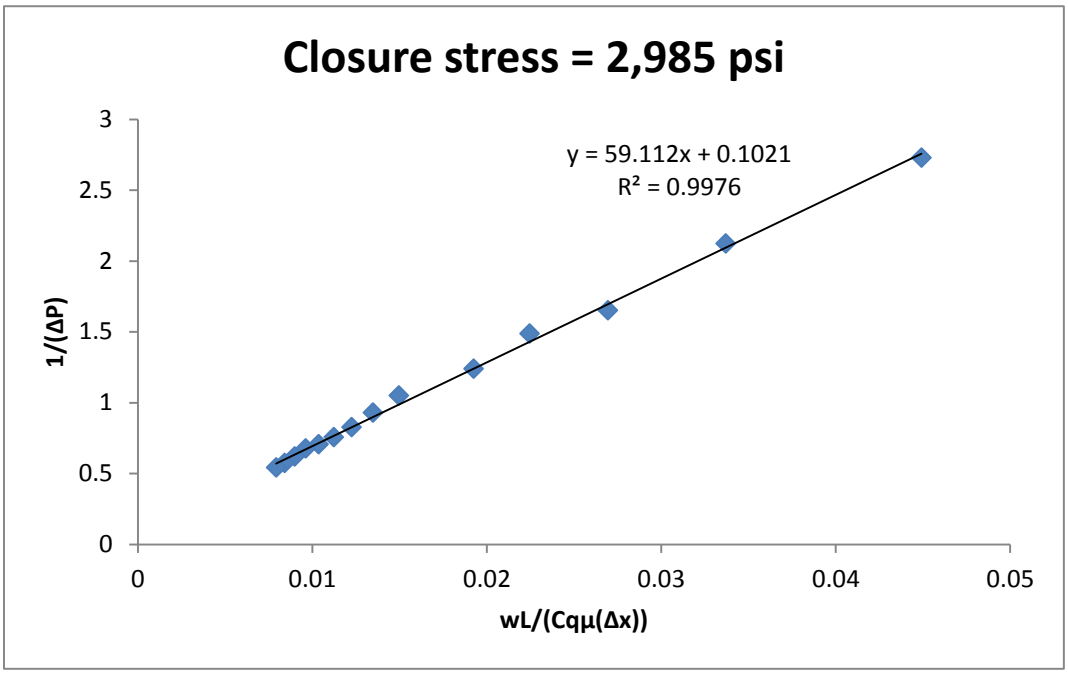

Figure A44: Diagnostic plot of mixture of 50% 20/40 sand and 50% 40/70 sand at 2,985 psi stress.

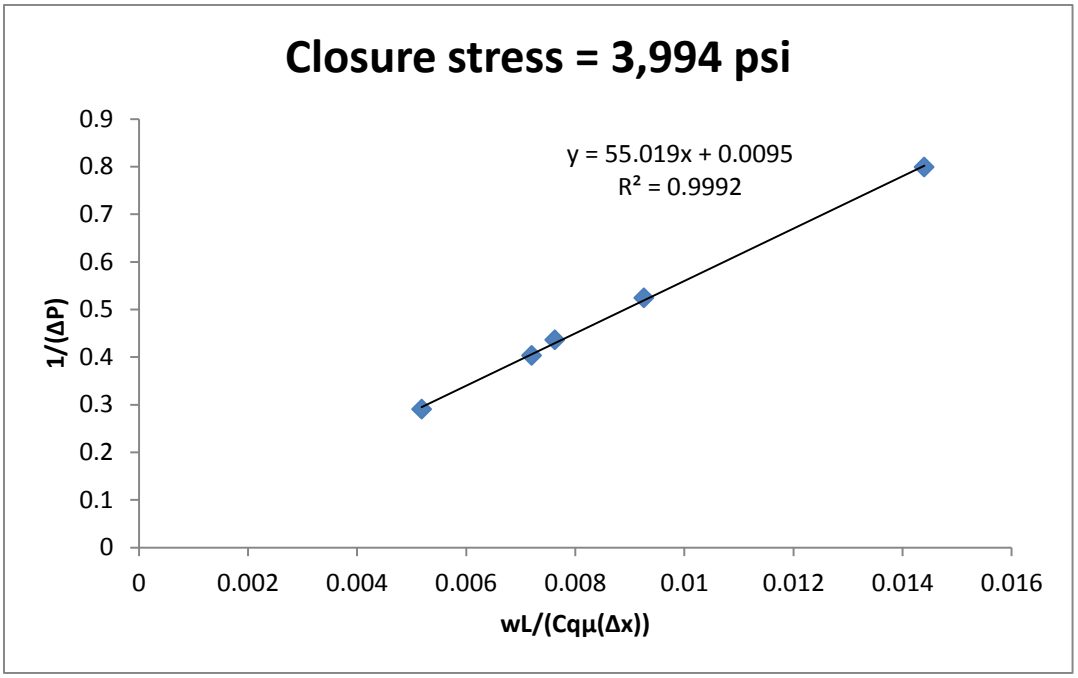

Figure A45: Diagnostic plot of mixture of 50% 20/40 sand and 50% 40/70 sand at 3,994 psi stress.

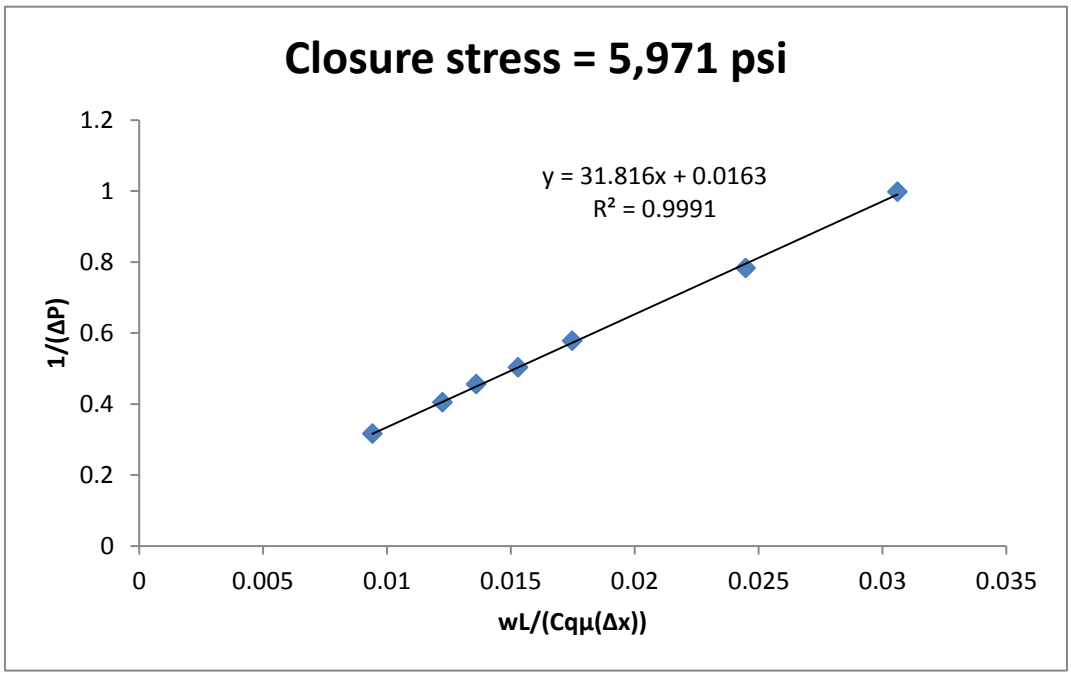

Figure A46: Diagnostic plot of mixture of 50% 20/40 sand and 50% 40/70 sand at 5,971 psi stress.

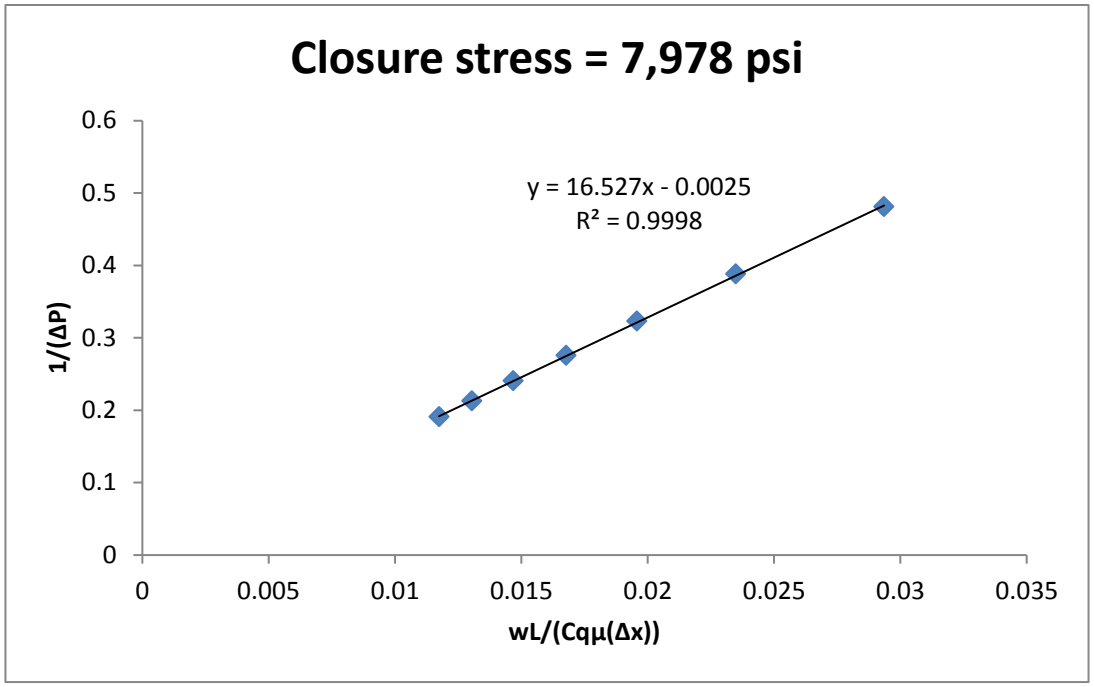

Figure A47: Diagnostic plot of mixture of 50% 20/40 sand and 50% 40/70 sand at 7,978 psi stress.

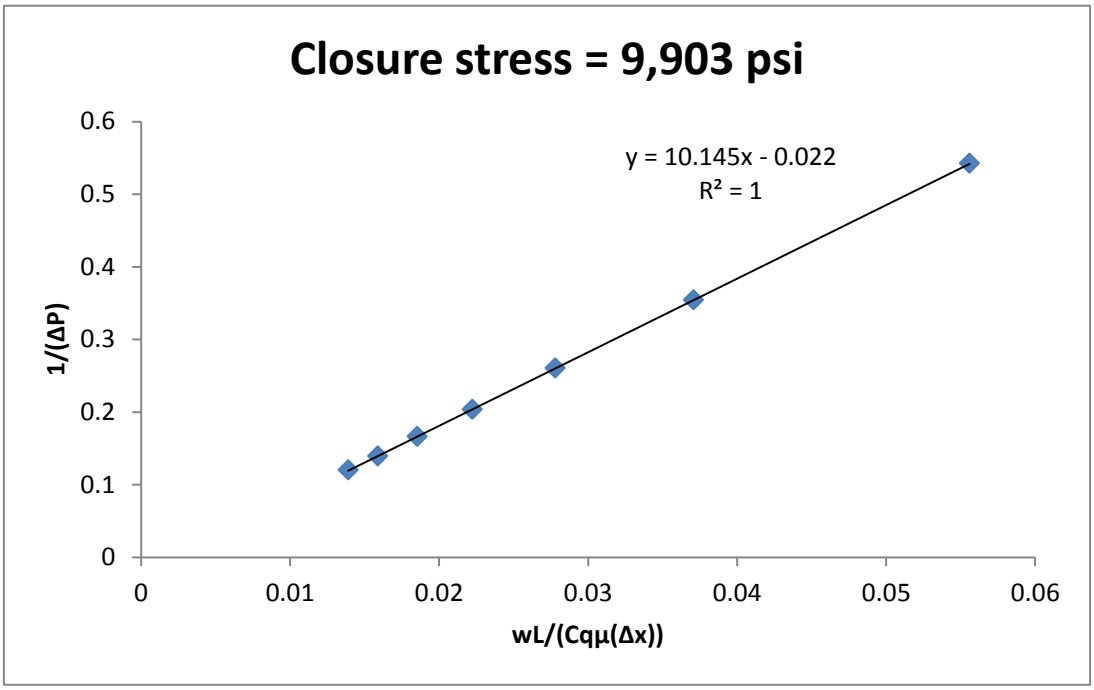

Figure A48: Diagnostic plot of mixture of 50% 20/40 sand and 50% 40/70 sand at 9,903 psi stress.

40/70 CERAMIC

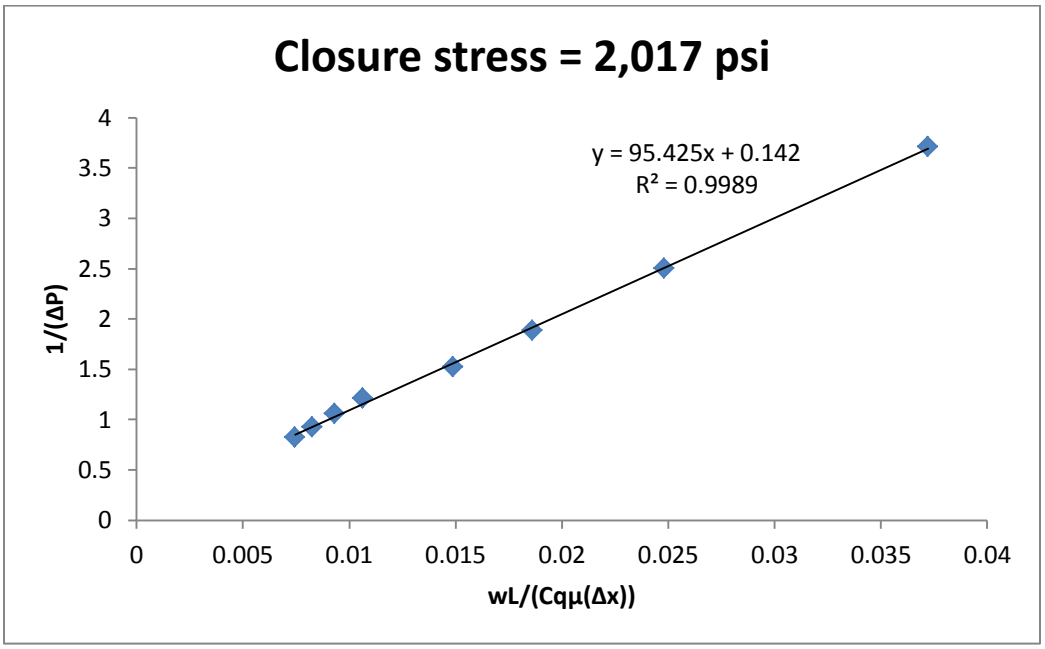

Figure A49: Diagnostic plot of 40/70 ceramic at 2,017 psi stress.

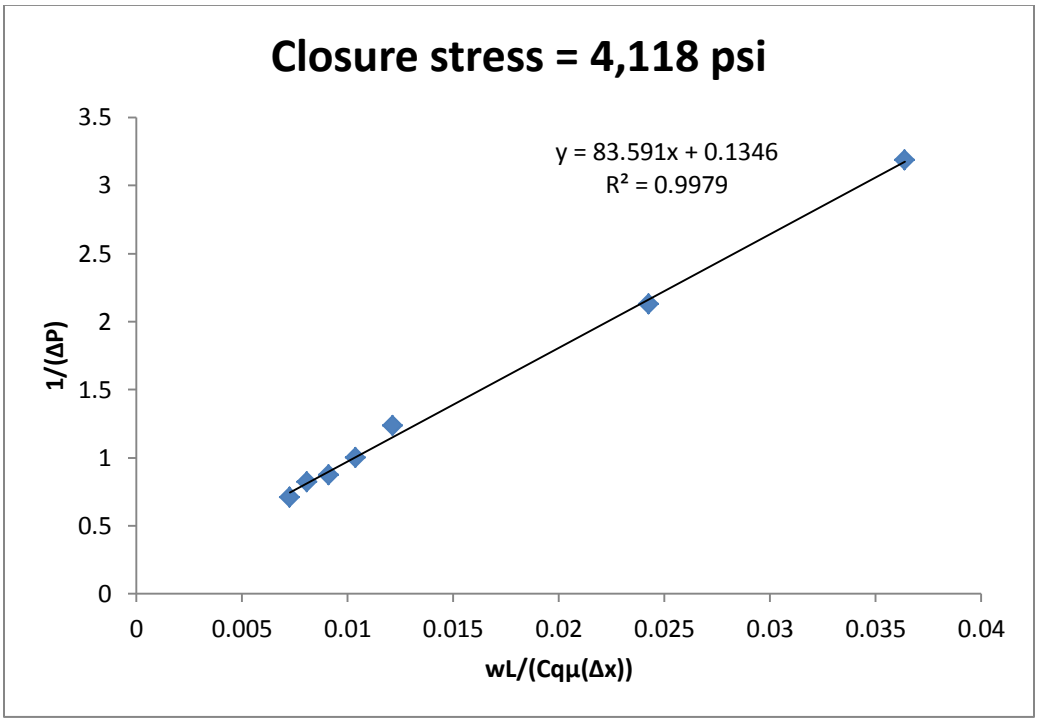

Figure A50: Diagnostic plot of 40/70 ceramic at 4,118 psi stress.

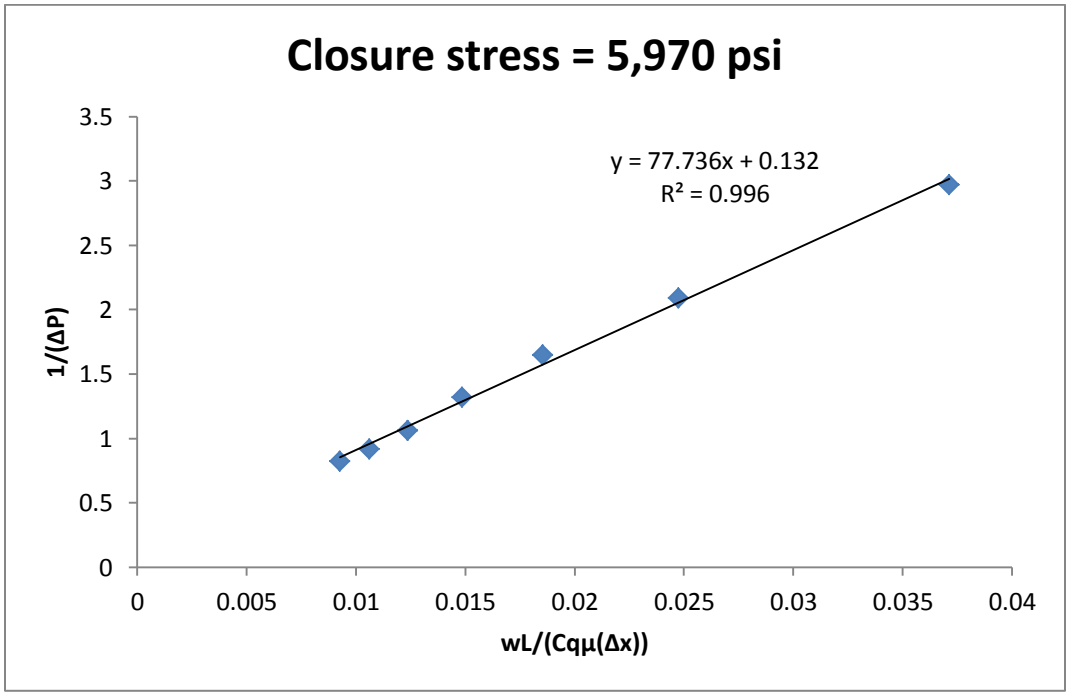

Figure A51: Diagnostic plot of 40/70 ceramic at 5,970 psi stress.

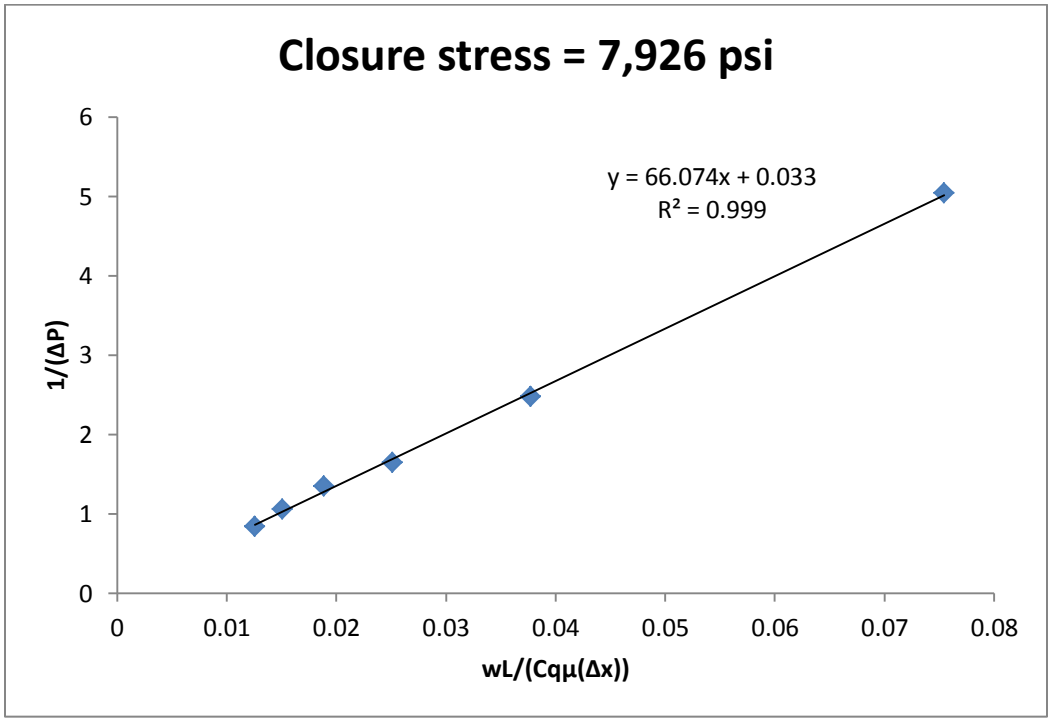

Figure A52: Diagnostic plot of 40/70 ceramic at 7,926 psi stress.

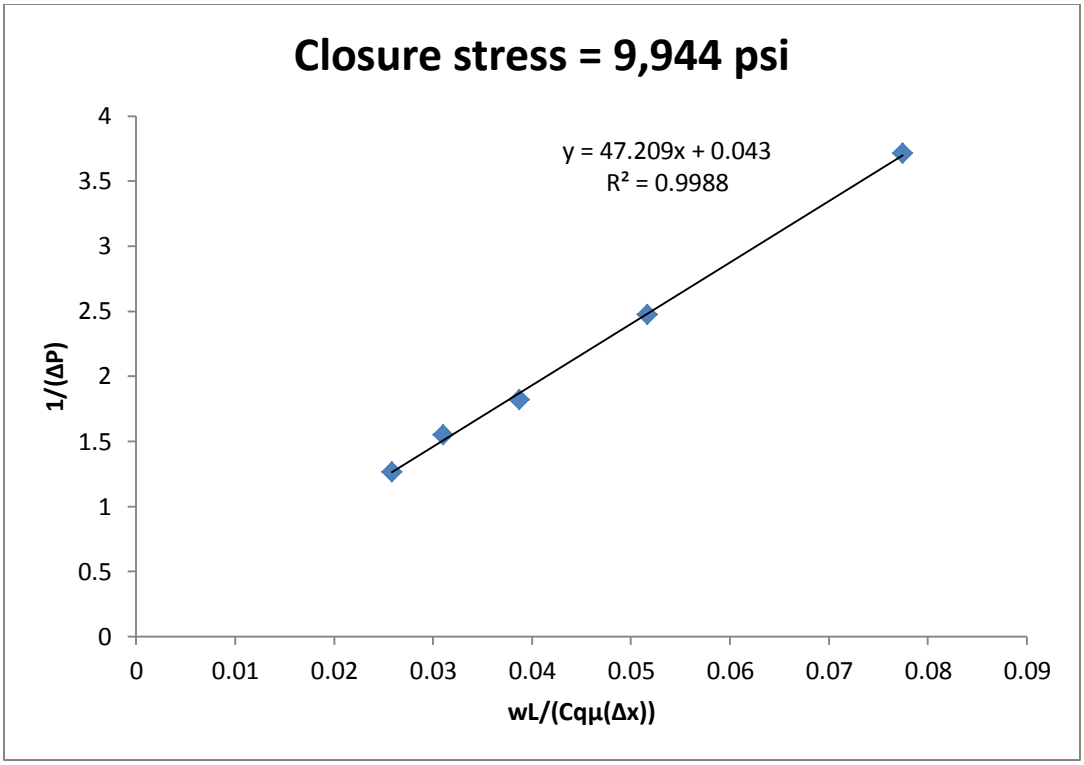

Figure A53: Diagnostic plot of 40/70 ceramic at 9,944 psi stress.

20/40 SAND & 40/70 CERAMIC (50/50)

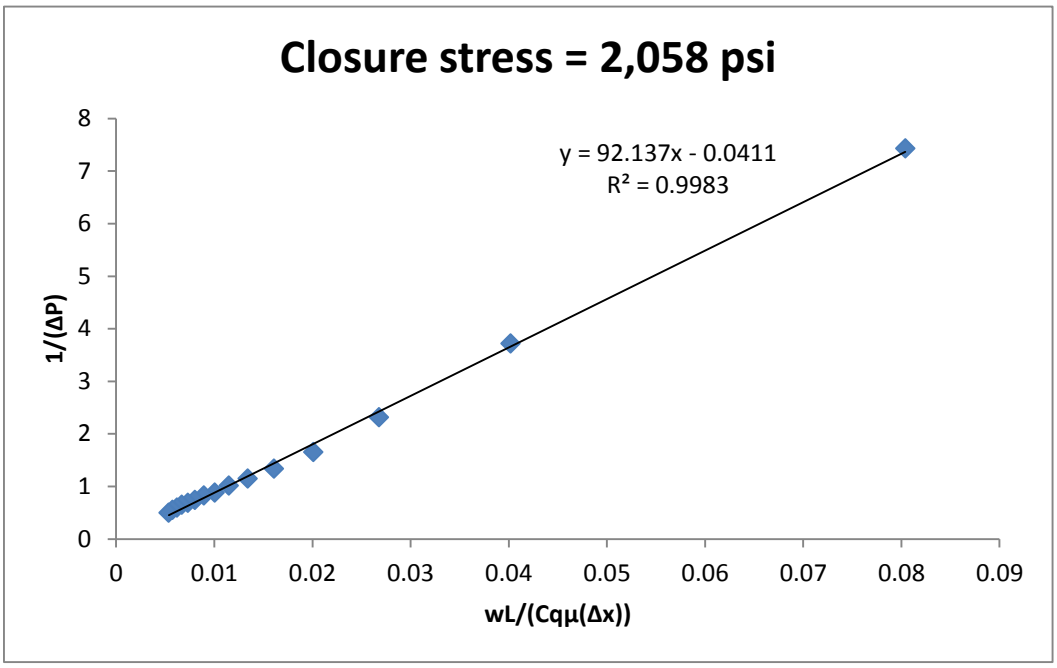

Figure A54: Diagnostic plot of 50% 20/40 sand and 50% 40/70 ceramic at 2,058 psi stress.

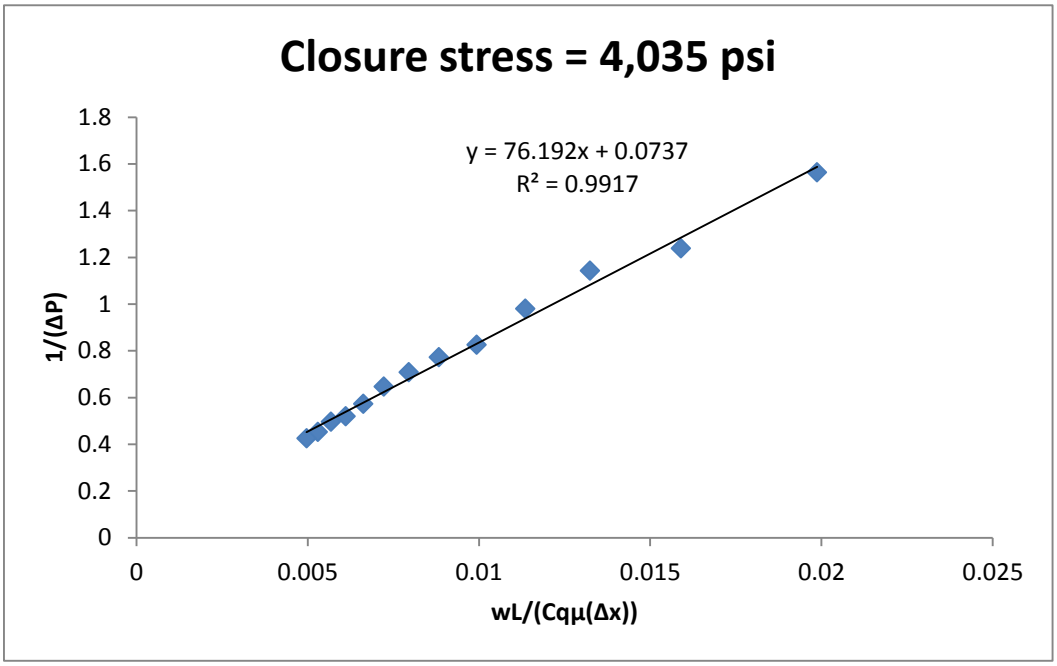

Figure A55: Diagnostic plot of 50% 20/40 sand and 50% 40/70 ceramic at 4,035 psi stress.

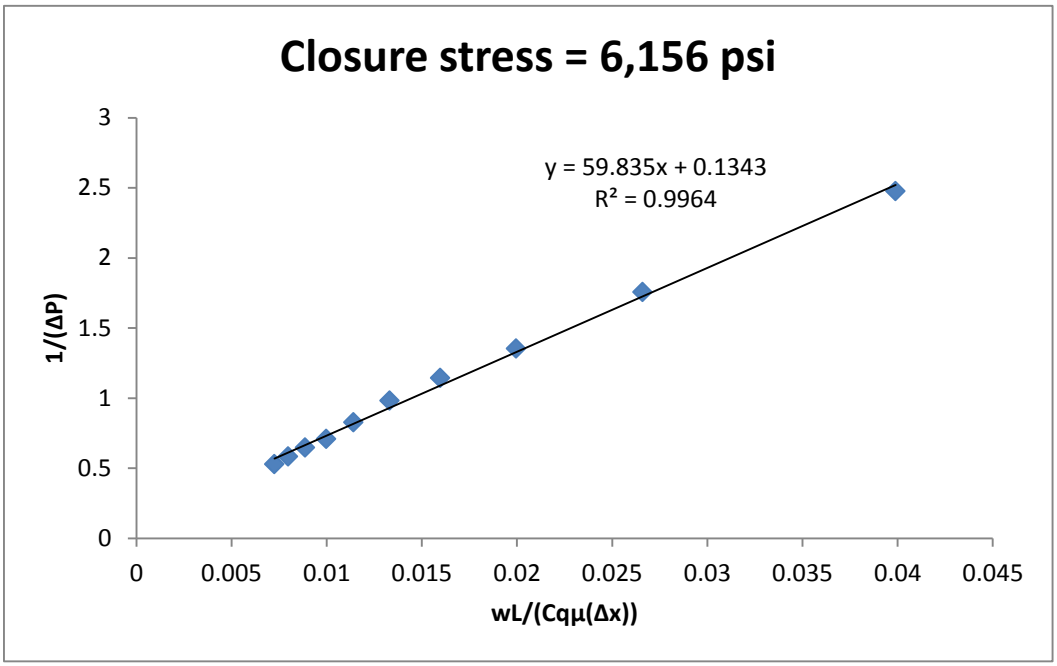

Figure A56: Diagnostic plot of 50% 20/40 sand and 50% 40/70 ceramic at 6,156 psi stress.

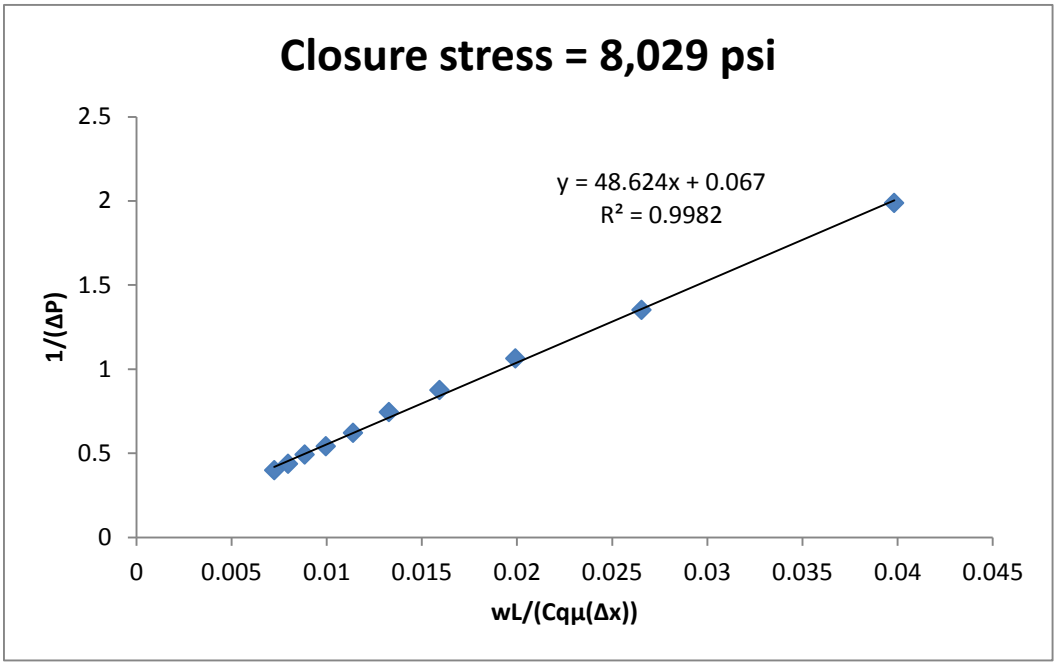

Figure A57: Diagnostic plot of 50% 20/40 sand and 50% 40/70 ceramic at 8,029 psi stress.

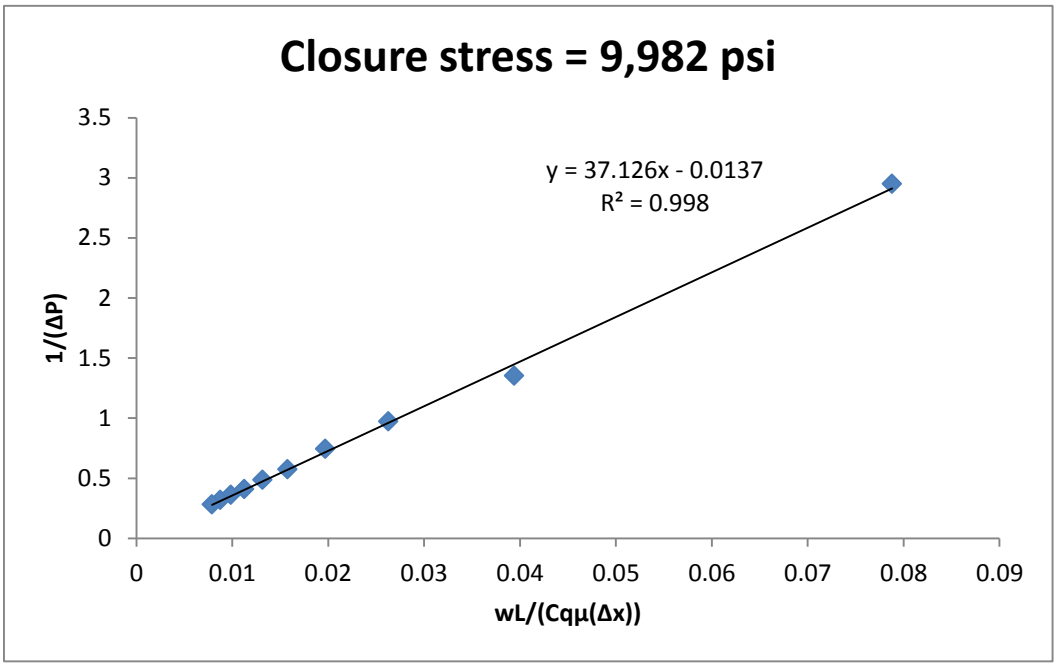

Figure A58: Diagnostic plot of 50% 20/40 sand and 50% 40/70 ceramic at 9,982 psi stress.

20/40 SAND & 40/70 CERAMIC (75/25)

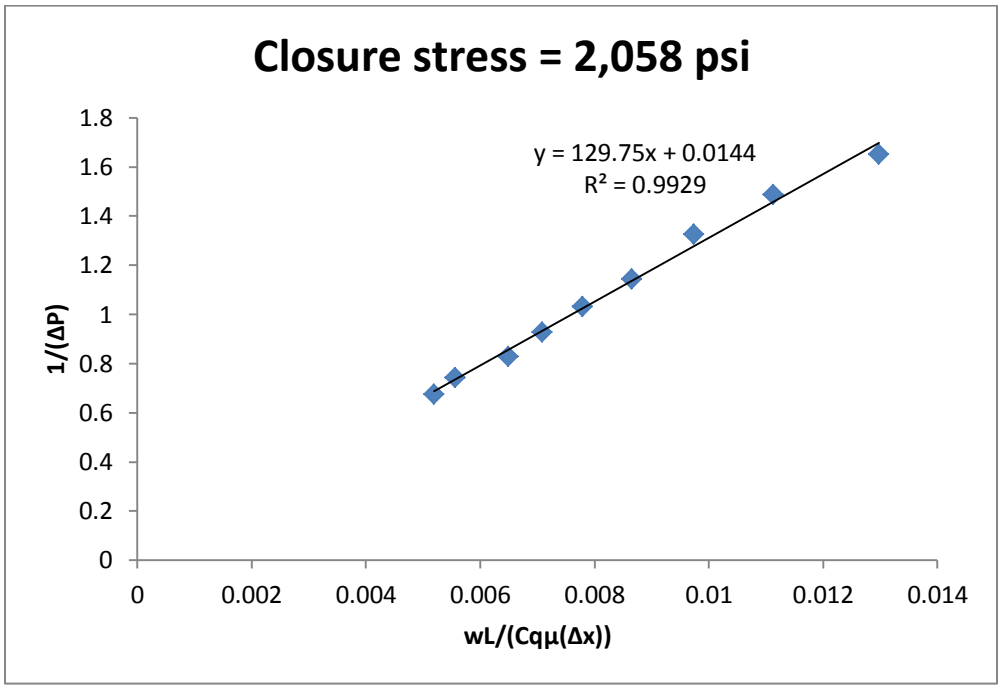

Figure A59: Diagnostic plot of 75% 20/40 sand and 25% 40/70 ceramic at 2,058 psi stress.

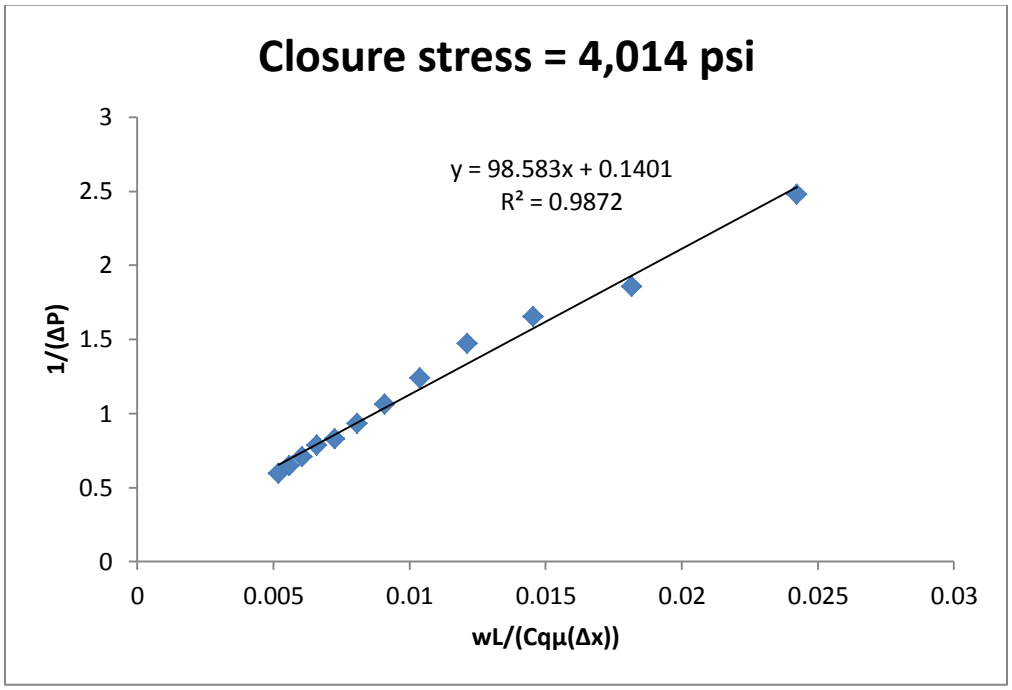

Figure A60: Diagnostic plot of 75% 20/40 sand and 25% 40/70 ceramic at 4,014 psi stress.

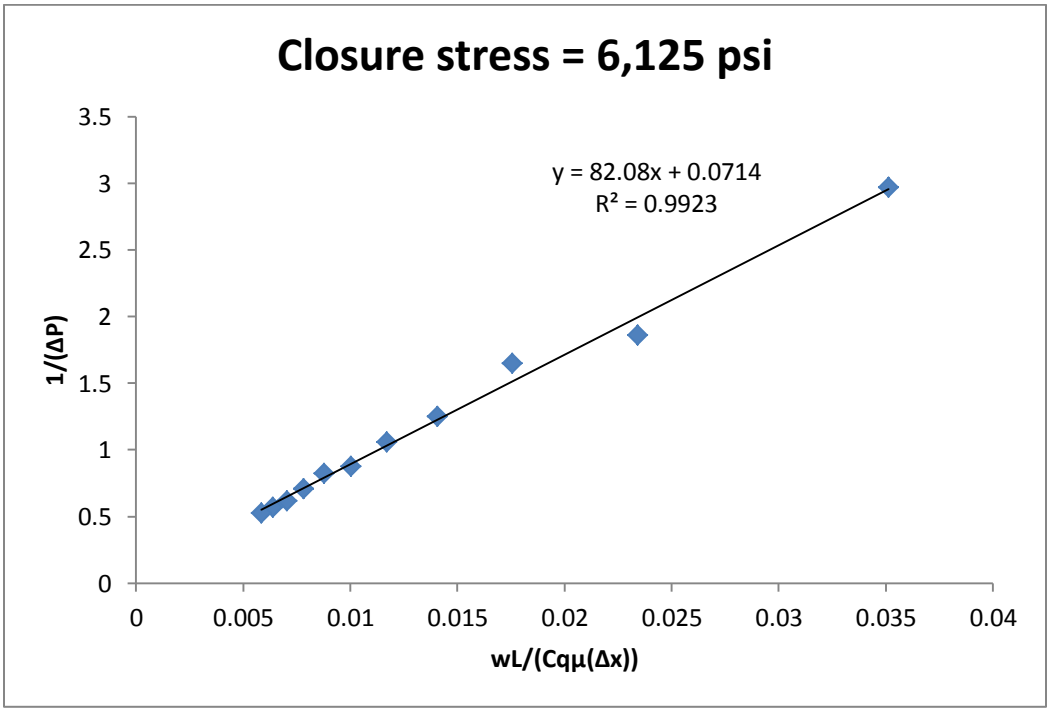

Figure A61: Diagnostic plot of 75% 20/40 sand and 25% 40/70 ceramic at 6,125 psi stress.

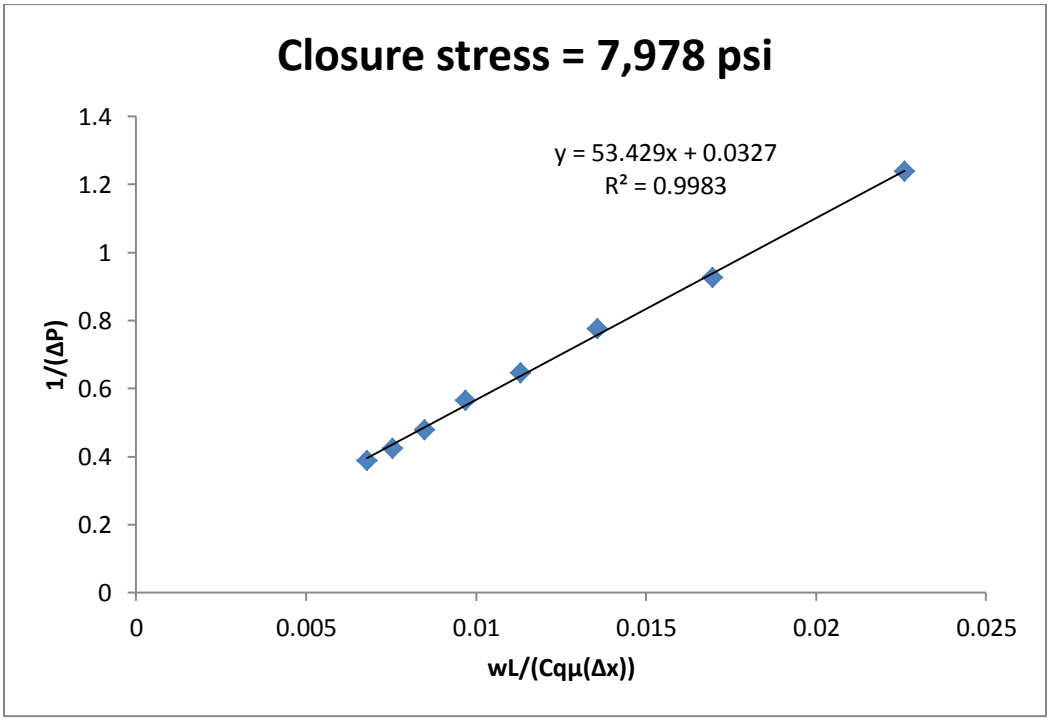

Figure A62: Diagnostic plot of 75% 20/40 sand and 25% 40/70 ceramic at 7,978 psi stress.

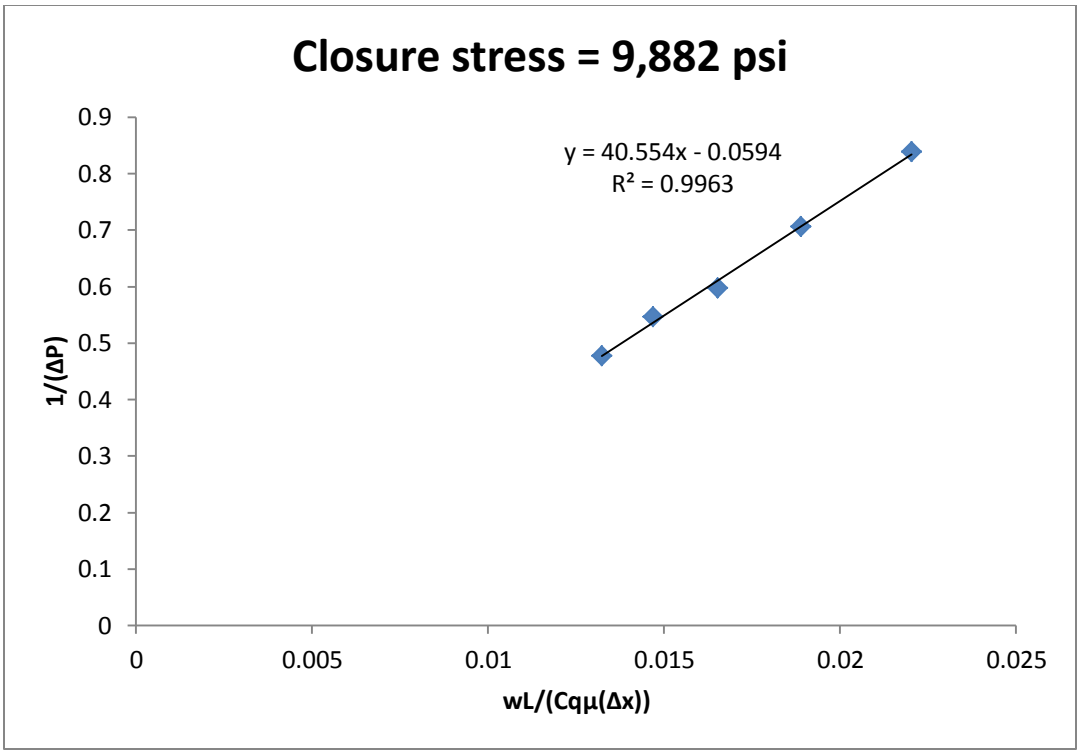

Figure A63: Diagnostic plot of 75% 20/40 sand and 25% 40/70 ceramic at 9,882 psi stress.

40/70 SAND & 40/70 CERAMIC (50/50)

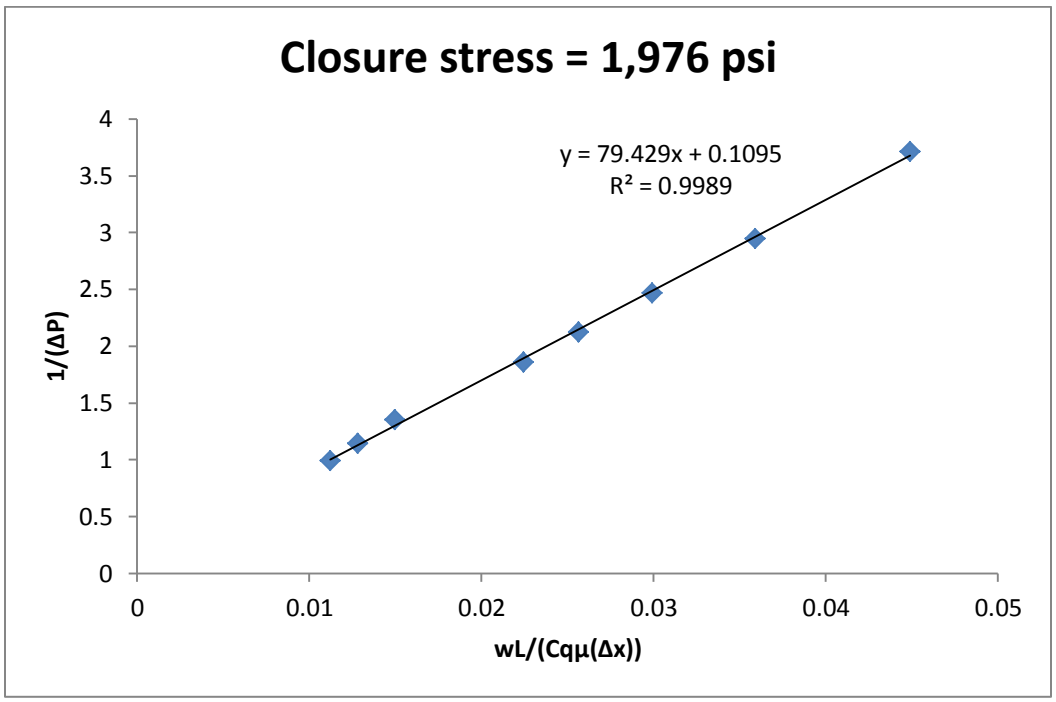

Figure A64: Diagnostic plot of 50% 40/70 sand and 50% 40/70 ceramic at 1,976 psi stress.

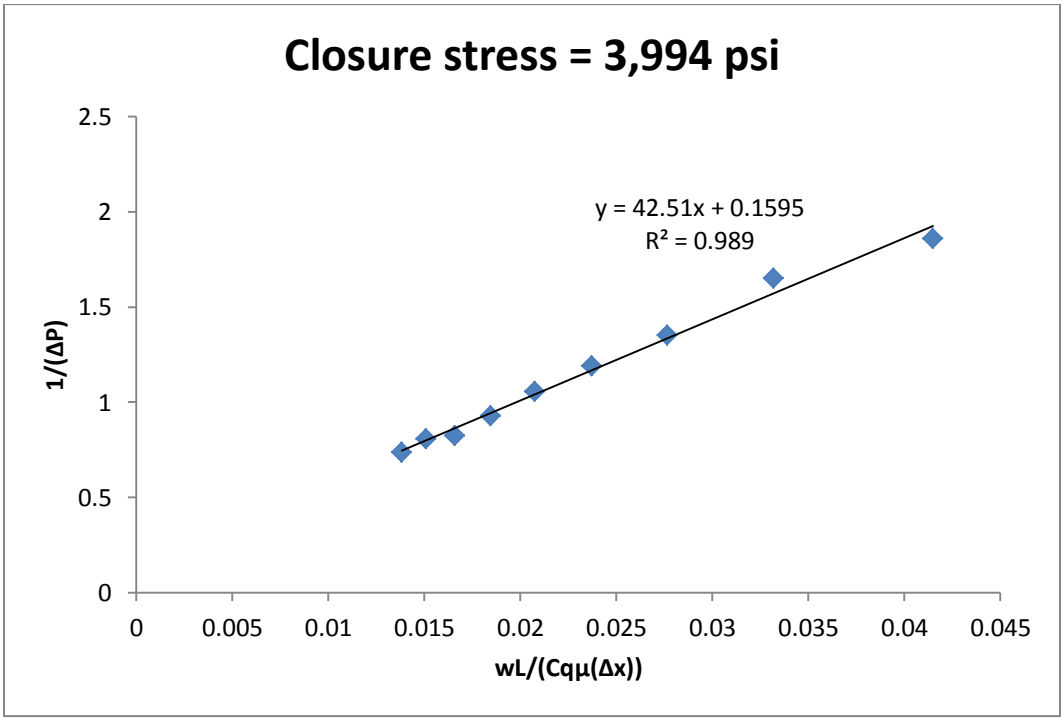

Figure A65: Diagnostic plot of 50% 40/70 sand and 50% 40/70 ceramic at 3,994 psi stress.

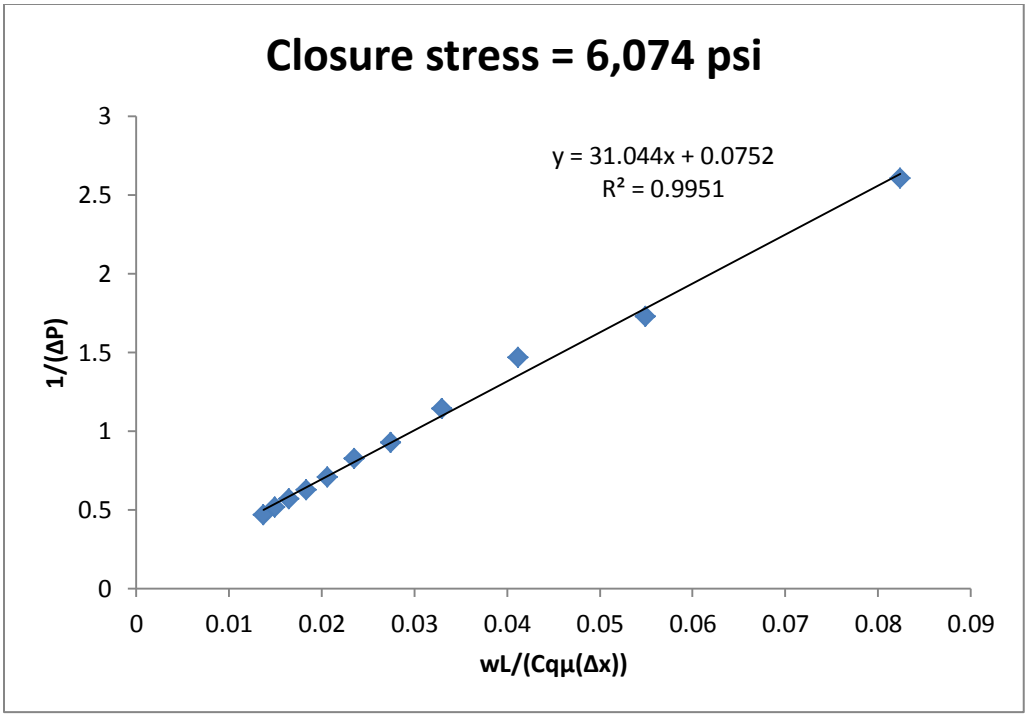

Figure A66: Diagnostic plot of 50% 40/70 sand and 50% 40/70 ceramic at 6,074 psi stress.

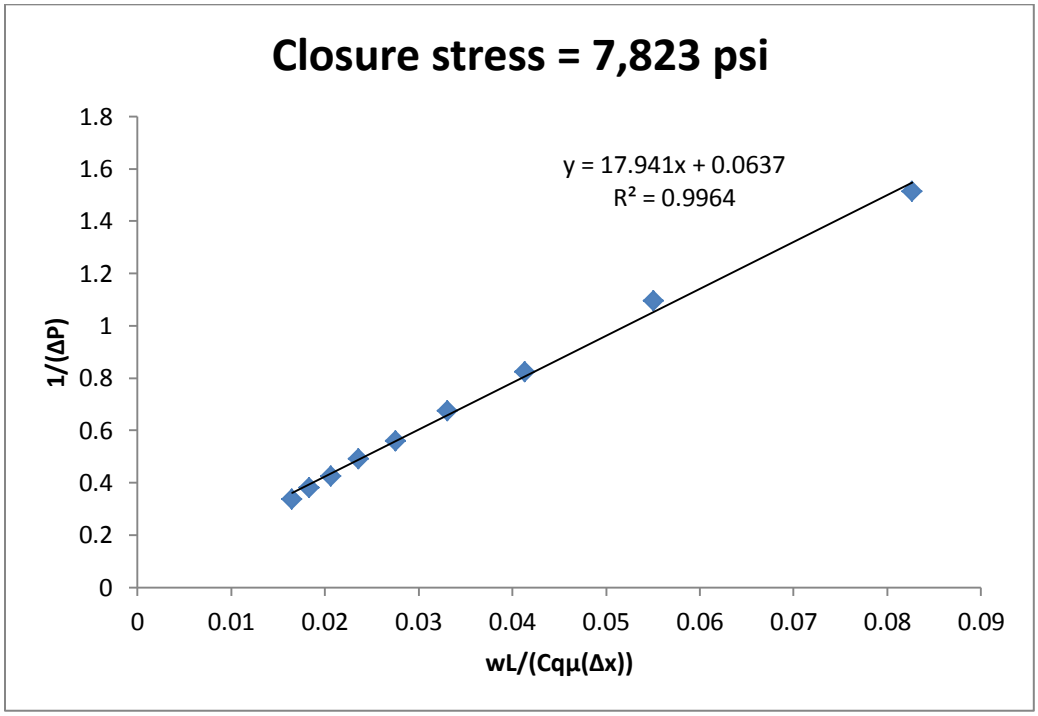

Figure A67: Diagnostic plot of 50% 40/70 sand and 50% 40/70 ceramic at 7,823 psi stress.

Appendix B: Grain Size Distribution Code

```
function[perm,mu,sigma,skew,nfd,wfd]=psd(mesh_range,wt,phi,
tau)

%Mesh_range input is a 1x2 vector with minimum and maximum
%meshes used from smallest to largest grain size e.g.[70
%20]
%Wt input is a vector that contains the weight in grams of
%each mesh, from smallest to largest.  import from excel.
%Phi is the measured porosity
%Tau is the tortuosity.  assume a value between 2 and 3.

mesh=[635 500 450 400 325 270 230 200 170 140 120 100 80 70
60 50 45 40 35 30 25 20];
d=[22.5 28.5 35 41.5 49 58 69 82.5 98 115.5 137.5 165 196
231 275 327 390 462 550 655 780 925];
rho=3.24;

for i=1:22
    if mesh(i)==mesh_range(1)
        j=i;
    end

    if mesh(i)==mesh_range(2)
        k=i;
    end
end

Mesh=zeros(1,k-j+1);
midpt=zeros(1,k-j+1);

for i=1:length(Mesh)
    Mesh(i)=mesh(j+i-1);
    midpt(i)=d(j+i-1);
end

astm=[635 500 450 400 325 270 230 200 170 140 120 100 80 70
60 50 45 40 35 30 25 20 18 16;
 20 25 32 38 45 53 63 75 90 106 125 150 180 212 250 300 355
425 500 600 710 850 1000 1180]';

for i=1:24
```

```
    if astm(i,1)== mesh_range(1)
        K=i;
    end
    if astm(i,1)== mesh_range(2)
        L=i;
    end
end

bin_edges=zeros(1,L-K+2);

for g=K:L+1
    bin_edges(g-(K-1))=astm(g,2);
end

N=zeros(1,length(Mesh));
F=10;  %F=divisor to reduce number of generated points
nfd=zeros(1,length(Mesh));

for i=1:length(N)
    N(i)=(10^12)*6*wt(i)/(F*pi*(d(i)^3)*rho);
end

for i=1:length(nfd)
    nfd(i)=N(i)/sum(N);
end

master_vec=linspace(bin_edges(1),bin_edges(2),N(1))';

for i=2:length(N)
    loopvec=linspace(bin_edges(i),bin_edges(i+1),N(i))';
    master_vec=vertcat(master_vec,loopvec);
end

mu=mean(master_vec);
sigma=std(master_vec);
skew=skewness(master_vec);
cdp=sigma/mu;
perm=((((skew*(cdp^3))+(3*(cdp^2))+1)^2)/((1+(cdp^2))^2))*(
mu^2)*(phi^3)/(((1-phi)^2)*tau*72);


wfd=wt/sum(wt);
wfd(length(bin_edges),1)=0;
bar(bin_edges,wfd,'histc')
```

```
nfd(1,length(bin_edges))=0;
hold on
bar(bin_edges,nfd,'histc')
xlabel('Grain Diameter (microns)')
ylabel('Frequency')
h=findobj(gca,'Type','patch');
display(h)
set(h(1),'FaceColor','r','EdgeColor','k','facealpha',0.75);
set(h(2),'FaceColor','b','EdgeColor','k','facealpha',0.75);
legend([h(1) h(2)],{'Number Frequency','Weight
Frequency'});
nfd=nfd';
```

Bibliography

Alramahi, B., M.I. Sundberg. 2012. Proppant Embedment and Conductivity of Hydraulic Fractures in Shales. Presented at the US Rock Mechanics/Geomechanics Symposium held in Chicago, Illinois, U.S.A., 24-27 June 2012. American Rock Mechanics Association paper #12-291.

ASTM International. 2011. Standard Specification for Woven Wire Test Sieve Cloth and Test Sieves.

Barree, R.D., S.A. Cox, V.L. Barree, M.W. Conway. 2003. Realistic Assessment of Proppant Pack Conductivity for Material Selection. Presented at the SPE Annual Technical Conference and Exhibition held in Denver, Colorado, U.S.A., 5-8 October 2003. SPE 84306.

Beard, D.C., P.K. Weyl. 1973. Influence of Texture on Porosity and Permeability of Unconsolidated Sand. *AAPG Bulletin*, Vol. 57, No.2, pp. 349-369.

Bedinger, M.S. 1961. Relation Between Median Grain Size and Permeability in the Arkansas River Valley. U.S.G.S. Professional Paper 424-C, p C-31 to C-32.

Bird, R. Byron, Warren E. Stewart, Edwin N. Lightfoot. 2007. *Transport Phenomena* (2^{nd} ed.). New York: John Wiley & Sons.

Brannon, Harold D., Mark R. Malone, Allan R. Rickards, William D. Wood, J. Randall Edgeman, Josh L. Bryant. 2004. Maximizing Fracture Conductivity with Proppant Partial Monolayers: Theoretical Curiosity or Highly Productive Reality? Presented at the SPE Annual Technical Conference and Exhibition held in Houston, Texas, U.S.A., 26-29 September 2004. SPE 90698.

Carbo Ceramics. 2013. Carbo-Prop: Cost-effective, intermediate-density proppant.

Carman, P.C. 1937. Fluid Flow Through a Granular Bed: Transactions of the Institution of Chemical Engineers, London, Vol. 15, pp. 150-167.

Cobb, S.L., J.J. Farrell. 1986. Evaluation of Long-Term Proppant Stability. Presented at the International Meeting on Petroleum Engineering held in Beijing, China, 17-20 March 1986. SPE 14133.

Cutler, R.A., D.O. Enniss, A.H. Jones, S.R. Swanson. 1983. Fracture Conductivity Comparison of Ceramic Proppants. Presented at the SPE/DOE Symposium on Low Permeability held in Denver, 14-16 March 1983. SPE 11634.

Darcy, Henry. 1856. *Les Fontaines publiques de la ville de Dijon*. Paris: Victor Dalmont.

Dvorkin, Jack. 2009. Kozeny-Carman Equation Revisited.

Fieller, N.R.J., E.C. Flenley, W. Olbricht. 1990. Statistics of Particle Size Data. *Journal of the Royal Statistical Society. Series C (Applied Statistics)*, Vol. 41, No.1, pp. 127-146. *JSTOR*. Accessed 6 December 2013.

Friedman, Gerald M. 1962. On Sorting, Sorting Coefficients, and the Lognormality of the Grain-Size Distribution of Sandstones. *The Journal of Geology*, Vol. 70, No. 6, pp. 737-753. *JSTOR*. Accessed 1 January 2014.

Gaurav, Abhishek. 2010. Ultra Light Weight Proppants in Shale Gas Fracturing: Master's thesis, University of Texas at Austin.

Gidley, John L., Stephen A. Holditch, Dale E. Nierode, Ralph W. Veatch Jr. 1989. "Fracture Treatment Design". *Recent Advances in Hydraulic Fracturing*, Vol. 12, pp. 124-27, 235 Richardson, TX: Monograph Series, SPE

Huang, H., J. Ayoub. Applicability of the Forchheimer Equation for Non-Darcy Flow in Porous Media. 2007. Presented at the SPE Annual Technical Conference and Exhibition held in San Antonio, Texas, U.S.A, 24-27 September 2006. SPE 102715.

Hubbert, M. King. 1940. The Theory of Ground-Water Motion. *The Journal of Geology*, Vol. 48, No. 8, Part 1, pp. 785-944. *JSTOR*. Accessed 14 December 2013.

Hubbert, M. King, David G. Willis. 1956. Authors' Reply to Discussion of 'Mechanics of Hydraulic Fracturing'. Presented at Petroleum Branch Fall Meeting in Los Angeles, California, U.S.A., 14-17 October 1956.

Kaufman, Phillip B., Harold D. Brannon, Robert W. Anderson, Mark Ziegler, Aidner Neves, Mark A. Parker, Kathy Abney, Gabriel Warwick Kerr de Paiva Cortes, Sara Joyce, Glenn S. Penny. Introducing New API/ISO Procedures for Proppant Testing. 2007. Presented at the SPE Annual Technical Conference and Exhibition held in Anaheim, California, U.S.A., 11-14 November 2007. SPE 110697.

Keech, C.F., P.G. Rosene. 1964. Ground-Water Conditions in the Proposed Waterfowl Refuge Area Near Chapman, Nebraska. *U.S. Department of the Interior*, Geological Survey Water-Supply Paper 1779-E.

Kozeny, J. 1927. Uber kapillare Leitung des Wassers im Boden: Sitzungsbericht der Akademie der Wissenschaften, Wien, Vol. 136, pp. 271-306.

Krumbein, W.C., G.D. Monk. 1942. Permeability as a Function of the Size Parameters of Unconsolidated Sand. *Petroleum Technology*, pp. 153-163.

Lehman, Lyle V., Mark A. Parker, Matt E. Blauch, Randy Haynes, Alan Blackmon. 1999. Proppant Conductivity – What Counts and Why. Presented at the Mid-Continent Operations Symposium, held in Oklahoma City, Oklahoma, U.S.A., 29-31 March 1999. SPE 52219.

Likhachev, E.R. 2002. Dependence of Water Viscosity on Temperature and Pressure. *Technical Physics*, Vol. 48, No. 4, pp. 514-15.

McDaniel, B.W. 1986. Conductivity Testing of Proppants at High Temperature and Stress. Preesented at the 56th California Regional Meeting of the Society of Petroleum Engineers held in Oakland, California, U.S.A., 2-4 April 1986. SPE 15067.

McDaniel, Robert R., John R. Willingham. 1978. The Effect of Various Proppants and Proppant Mixtures on Fracture Permeability. Presented at the Annual Fall Technical Conference and Exhibition held in Houston, Texas, U.S.A., 1-3 October 1978. SPE 7573.

Mokadam, R.G. 1961. Thermodynamic Analysis of the Darcy Law. Presented at the Summer Conference of the Applied Mechanics Division, Chicago, Illinois, U.S.A. 14-16 June 1961. ASME No. 61-APM-5.

Neuman, S.P. 1977. Theoretical Derivation of Darcy's Law. *Acta Mechanica*, Vol. 25 pp. 153-170. *Springer*.

Panda, Manmath N., Larry W. Lake. 1994. Estimation of Single Phase Permeability from Parameters of Particle Size Distribution. *AAPG Bulletin*, Vol. 78, No.7, pp. 1028-1039.

Rickards, Allan R., Harold D. Brannon, William D. Wood, Christopher J. Stephenson. 2003. High Strength, Ultra-Lightweight Proppant Lends New Dimensions to Hydraulic Fracturing Applications. Presented at the SPE Annual Technical Conference and Exhibition held in Denver, Colorado, U.S.A., 5-8 October 2003. SPE 84308.

Schubarth, S.K., S.L. Cobb, R.G. Jeffrey. 1997. Understanding Proppant Closure Stress. Presented at the SPE Production Operations Symposium held in Oklahoma City, Oklahoma, U.S.A., 9-11 March 1997. SPE 37489.

Shepherd, Russell G. 1989. Correlations of Permeability and Grain Size. *Ground Water,* Vol. 27, No. 5, pp. 633-638.

Stephens, W.T., S.K. Schubarth, K.R.Dickson, E.M. Snyder, K.J. Doles, D.C. Herndon. 2007. Behavior of Proppants Under Cyclic Stress. Presented at the SPE Hydraulic Fracturing Technology Conference held in College Station, Texas, U.S.A., 29-31 January 2007.

Zoback, Mark D. 2010. *Reservoir Geomechanics*. New York: Cambridge University Press.